University of August 20th 1955-Skikda
Faculty of science
Department of Chemistry

Thesis

Submitted to the Department of Chemistry

For the Requirement for PhD Degree (LMD) in Chemistry

Specialty: Materials chemistry

Presented by

HAYOUNE ASMA

Elaboration and characterization of functionalized Djebel Debbagh KDD3 clay by magnetite and photocatalysts oxides and their application for removal of methylene blue.

Elaboration et caractérisation de l'argile de Djebel Debbagh KDD3 fonctionnalisée par la magnétite et les oxydes photocatalyseurs et leur application dans la dégradation du bleu de méthylène.

Presented publicly on: July 14th 2022

Jury composed of:

Halladja Sabrina	Full Professor	President	University of Skikda
Akkari Hocine	Full Professor	Supervisor	University of Batna-2.
Chebli Derradji	Full Professor	Examiner	University Ferhat Abbas Setif-1
Boughettoucha Abdellah	Full Professor	Examiner	University Ferhat Abbas Setif-1
Chiha Mahdi	Full Professor	Examiner	University of Skikda
Chettah AbdElhak	Full Professor	Examiner	University of Skikda

Skikda : 2021/2022

Acknowledgment

It is with great pleasure and enthusiasm that I am writing this page. Much more than the final point of the scientific writing, this page represents a meditation on a period relating, five years of life very rich in events. Personally, the doctoral thesis was a real exercise and a great experience in every way. In the beginning, I imagined what defined a thesis: a professional springboard, a personal investment, perseverance, intellectual perseverance, an intellectual adventure.

From the bottom of my heart, I would like to thank **ALLAH** for his great blessing and his immense mercy which accompanied me throughout my school to a university career, and for the Strength, he gave me to complete this thesis work.

At the outset, I would like to express my sincere gratitude to my supervisor Professor **Hocine Akkari** (université Batna 2) who started by proposing this Ph.D. project and believing in my capacity to accomplish it. I am very thankful for his permanent support, scientific guidance, constant optimism, and encouragement throughout this long walk. I deeply appreciate his careful revision of all my work.

I am also very grateful to jury president Professor **Halladja Sabrina** (université 20 août 1955- Skikda), and the jury members; Professor **Derradji Chebli** (université Ferhat Abbas Sétif 1), Professor **Abdallah Bouguettoucha** (université Ferhat Abbas Sétif 1), Professor **Mahdi Chiha** (université 20 août 1955- Skikda) and Professor **Abdellhak Chettah** (université 20 août 1955- Skikda), whom kindly gave me the honor, for examining my work and for chairing the juries of my thesis.

I would like to express my deepest gratitude to Professor **Vincenzo Vaiano** (università degli Studi di Salerno, Italy) who helped me to do the tests of photocatalysis. I am grateful for the invaluable help he has given me. His scientific knowledge has strongly contributed to the scientific quality of this work.

Within the framework of the PNE scholarship; I warmly thank Professor Nicoleta Ravasio (Università degli Studi di Milano, Italy) who welcomed me into her laboratory in Milan she made me discover her universe with good mood and kindness. Without forgetting, Professor **Francisco de Paula Martin Jimenez** (Universidad de Málaga, Spain) contributed to this research work with his expertise in the techniques of analyses. I thank him for all the experiences explanations and light that you brought to me.

Within the framework of the ERASMUS grant, I thank Dr. **Jia Yang** and Dr. **Muhammed Zubair** (Norwegian University of Science and Technology) for welcoming me into their laboratory.

My last thanks go to the people without whom I could not have overcome the obstacles of life, my family, especially my guide in life, the symbol of tenderness, my dear mother, and my generous father. My parents have always supported me despite the distance, my sisters and my brothers, I adore you and thank you for having been for being there for me. I thank very warmly all the people I have had the pleasure of knowing during these years. I will not forget my friends for their encouragement over the years. Thank you for keeping me entertained and supporting me to the end.

Table of contents

List of figures

List of tables

List of acronyms

AOPs	Advanced oxidation processes
BET	Brunauer, Emmett, and Teller
C_0	Initial concentration
Ce	Equilibrium Concentration of dye in solution
EDX	Energy dispersive x-rays analysis
E_g	Band gap energy
FTIR	Fourier-transform infrared spectroscopy
HKDD3	Halloysite Kaolin Djebel Debbagh 3
HNT	Halloysite clay
HRTEM	High resolution transmission electronic microscopy
JCPDS	Joint Committee on Powder Diffraction Standards
K_1	Pseudo-First-Order Rate Constant
K_2	Pseudo-second-Order Rate Constant
K	kinetic constant
KDD3	Kaolin Djebel Debbagh
MB	Methylene blue
NPs	Nanoparticles
PFO	Pseudo-first-order
pH_{pzc}	Point of zero charge
PSO	Pseudo-second-order
q max	Maximum quantity adsorbed
qe	Quantity adsorbed at Equilibrium

qt	Adsorption Capacity at any Time
SE	Standard error
SEM	Scanning electron microscope
SEM	Scanning electronic microscopy
SSA	Specific surface area
T	Tetrahedral sheet
HKDD3	Halloysite Kaolin Djebel Debbagh
TOC	Total organic carbon
Uv-visible DRS	Diffuse reflectance spectroscopy,
wt%	Weight percent
XPS	X-ray photoelectron spectroscopy
XRD	X-ray diffraction
ΔG^0	Standard Gibbs free energy change
ΔH^0	Standard enthalpy change
ΔS^0	Standard entropy change

Introduction

Water means life, the earth doesn't exist without it. Water covers 71% of the planet's surface **[1]**. The protection of the environment and the remediation of environmental problems are major challenges for an effective improvement of the quality of life and sustainable development. Water is used in multiple human activities such as domestic use agriculture and industry. At the global level, 70% of water consumption is for the agricultural sector, 11% is for urban needs and 19% is for industrial needs. The almost exponential growth of the human population and the intensification of agricultural and industrial activities lead to a continuous increase in the demand for freshwater. The protection of natural water resources and the development of new technologies for water and wastewater treatment have become the main environmental challenges of the 21st century

Water pollution is caused by different categories of chemical and biological toxic substances. Heavy metals and organic dyes are known to be common pollutants that threaten human health and the environment. Around 2.3 billion people worldwide suffer from diseases linked to water pollution, with over 95% of them living in a poor countries (e.g. India, and Pakistan) **[2]**. The discharge of dyes in effluents causes toxicity to aquatic organisms and can be carcinogenic, mutagenic, and can cause serious damage to humans (brain, central nervous system, reproductive system**) [3]**. Several techniques have been used for the removal of dyes from water such as adsorption, coagulation-flocculation, precipitation, exchange, and membrane separation **[4].** However, these processes have certain limitations such as the inability to eliminate certain elements and the generation of secondary waste that require additional treatment. This can be overcome by the application of advanced oxidation processes (AOPs) which are considered to be weak creators of toxic waste during treatment **[5]**.

Heterogeneous photocatalysis is one of the advanced oxidation promising processes which can be applied to water and air disinfection and surface development, self-cleaning and self-decontaminating materials. Also can be used for the removal and degradation of pollutants (pesticides, dyes, volatile organic compounds (VOCs), etc.) **[6]**. their applications are very broad, due to their benefits in particular simple conditions (at room temperature and atmospheric pressure), clean, safe (low or non-polluting energy source, absence of oxidizing chemicals and discharges pollutants), inexpensive and easy **[7]**.

Numerous strategies have been studied in order to develop heterogeneous photocatalysis to increase the efficiency of the process and to make it more convenient and economical. Among these strategies, the immobilization of the photocatalyst is a very important point **[8]**. It is known that the separation of fine photocatalyst particles after the treatment consumes more energy and time, which results in a significant reduction in the benefits of this technology in the water treatment industries. To avoid this problem, photocatalyst particles are immobilized on a surface such as glass, carbonous materials, or clay **[9]**. Moreover, the combination of these materials with magnetite nanoparticles provides a desirable route for direct separation **[10].**

The application of porous materials is considered a source with an advantageous economic potential for wastewater treatment. They show an aptitude particular to the elimination of hazardous substances, either by adsorption or by exclusion size. The presence of pores facilitates their important uses in various fields such as ions exchange, catalysis, detection, isolation, and biological purification molecular. The major advantages of using these materials are low cost and affordability. Several studies have focused on the use of porous materials to remove different contaminants (organic and inorganic chemicals, heavy metals, microorganisms).

Among the porous materials available, natural clay minerals have recently made considerable attention as alternative materials that are less expensive, non-toxic, abundant, and possess multifunctional properties depending on the type of clay. The application of clay minerals in the field of heterogeneous photocatalysis for the processing of wastewater was exploited with special attention.

In recent decades, particular attention has been paid to the use of magnetic adsorbents, and more specifically magnetic iron nanoparticle adsorbents, in the field of environmental science. These compounds have unique magnetic properties, as they are often superparamagnetic **[11]** and can thus be easily manipulated and separated by an external magnetic field without the need for the time-consuming and energy-consuming steps of filtration, decantation, or centrifugation following the decontamination process. Magnetic nanoparticles also present remarkable properties compared to their analogs in mass such as a high specific surface [**12]** which has the effect of limiting the resistance to internal diffusion leading to a high adsorption capacity [**13]**, biocompatibility, low toxicity, and high stability **[14]**. TiO_2/clay has advantages over commercial photocatalysts such as high specific surface area, and low economic cost **[15-17]**. The titanium oxide immobilization process often

involves several chemical and thermal interactions, hence the porous clay materials that have a very stable structure are often the most demanded as supports for the catalysts **[18-20]**.

The objective of this study is the valorization of natural clay of Algerian origin, the Kaolin Djebel Debbagh, by exploring the possibilities of their functionalization by magnetite nanoparticles and photocatalyst materials, with the aim of the development of supported photocatalyst materials that can degrade effectively organic pollutants in aqueous media, particularly under visible irradiation.

After the general introduction, **the first chapter** reports a bibliographical synthesis. It consists of three parts. The first part is devoted to highlighting the importance of properties of clay minerals focused on halloysite clay. The second part focused on heterogeneous photocatalysis by presenting the principle, the effects of operating parameters on the efficiency of the process, a generality of the supported photocatalysts, and a brief overview of photocatalytic treatment. In the third part, we are interested in the combination of iron oxide particles (magnetite) onto clay and their application for the removal of pollutants organics. **The second chapter** presents the materials and products used, the preparation protocol HKDD3 with magnetite and titanium dioxide, and the principle of characteristic analysis which are performed in work. **The third chapter** focused on the characterization of purified clay HKDD3 and its application for the removal of methylene blue. **The fourth one** focused on the comparative study between adsorption and sono-adsorption of MB dye using magnetite-HKDD3 clay. **The fifth chapter** is related to the results of characterization and photocatalytic tests for MB removal from the aqueous medium of two types of photocatalysts: TiO_2 doped with silver and iron supported on magnetic HKDD3 clay. **The sixth chapter** is devoted to the synthesis and characterization of iron sulfide loaded on HKDD3 clay and its removal for MB dye. Finally, **the general conclusion** of this manuscript provides a global summary of all the results obtained in this study at the end of which the main perspectives opened by this work are identified.

References

[1] J. Gloser, Miller, G.T.: Living in the Environment. Principles, Connections, and Solutions, Biologia Plantarum. 45 (2002) 128–128. https://doi.org/10.1023/A:1015199330106.

[2] Q. Wang, Z. Yang, Industrial water pollution, water environment treatment, and health risks in China, Environ Pollut. 218 (2016) 358–365. https://doi.org/10.1016/j.envpol.2016.07.011.

[3] M.A.M. Salleh, D.K. Mahmoud, W.A.W.A. Karim, A. Idris, Cationic and anionic dye adsorption by agricultural solid wastes: A comprehensive review, Desalination. 280 (2011) 1–13. https://doi.org/10.1016/j.desal.2011.07.019.

[4] A. Ahmad, S.H. Mohd-Setapar, C.S. Chuong, A. Khatoon, W.A. Wani, R. Kumar, M. Rafatullah, Recent advances in new generation dye removal technologies: novel search for approaches to reprocess wastewater, RSC Adv. 5 (2015) 30801–30818. https://doi.org/10.1039/C4RA16959J.

[5] G. Matafonova, V. Batoev, Recent advances in application of UV light-emitting diodes for degrading organic pollutants in water through advanced oxidation processes: A review, Water Research. 132 (2018) 177–189. https://doi.org/10.1016/j.watres.2017.12.079.

[6] U.I. Gaya, Heterogeneous Photocatalysis Using Inorganic Semiconductor Solids, Springer Netherlands, Dordrecht, 2014. https://doi.org/10.1007/978-94-007-7775-0.

[7] E. Pelizzetti, N. Serpone, eds., Homogeneous and Heterogeneous Photocatalysis, Springer Netherlands, Dordrecht, 1986. https://doi.org/10.1007/978-94-009-4642-2.

[8] N. Yahya, F. Aziz, N.A. Jamaludin, M. A. Mutalib, A.F. Ismail, W.N. W. Salleh, J. Jaafar, N. Yusof, N. A. Ludin, A review of integrated photocatalyst adsorbents for wastewater treatment, Journal of Environmental Chemical Engineering. 6 (2018) 7411–7425. https://doi.org/10.1016/j.jece.2018.06.051.

[9] N.V.S. Praneeth, S. Paria, Clay-Semiconductor Nanocomposites for Photocatalytic Applications, in: Clay Minerals: Properties, Occurrence and Uses, 2017.

[10] J. Chang, J. Ma, Q. Ma, D. Zhang, N. Qiao, M. Hu, H. Ma, Adsorption of methylene blue onto Fe3O4/activated montmorillonite nanocomposite, Applied Clay Science. 119 (2016) 132–140. https://doi.org/10.1016/j.clay.2015.06.038.

[11] H. Cao, J. He, L. Deng, X. Gao, Fabrication of cyclodextrin-functionalized superparamagnetic Fe3O4/amino-silane core–shell nanoparticles via layer-by-layer method, Applied Surface Science. 255 (2009) 7974–7980. https://doi.org/10.1016/j.apsusc.2009.04.199.

[12] B. Szczepanik, P. Rogala, P. M. Słomkiewicz, D. Banaś, A. Kubala-Kukuś, and I. Stabrawa, "Synthesis, characterization and photocatalytic activity of TiO2-halloysite and Fe2O3-halloysite nanocomposites for photodegradation of chloroanilines in water," Appl. Clay Sci., vol. 149, pp. 118–126, Dec. 2017, doi: 10.1016/j.clay.2017.08.016.

[13] P. Zheng, Y. Du, D. Liu, and X. Ma, "Synthesis, adsorption and photocatalytic property of halloysite-TiO2-Fe3O4 composites," Desalination Water Treat., vol. 57, no. 47, pp. 22703–22710, Oct. 2016, doi: 10.1080/19443994.2015.1137498.

[14] P. Xu, G.M. Zeng, D.L. Huang, C.L. Feng, S. Hu, M.H. Zhao, C. Lai, Z. Wei, C. Huang, G.X. Xie, Z.F. Liu, Use of iron oxide nanomaterials in wastewater treatment: A review, Science of The Total Environment. 424 (2012) 1–10. https://doi.org/10.1016/j.scitotenv.2012.02.023.

[15] A. Gołąbiewska, M. P. Kobylański, and A. Zaleska-Medynska, "Fundamentals of metal oxide-based photocatalysis," in Metal Oxide-Based Photocatalysis, Elsevier, 2018, pp. 3–50. doi: 10.1016/B978-0-12-811634-0.00002-0.

[16] M. E. Borges, M. Sierra, E. Cuevas, R. D. García, and P. Esparza, "Photocatalysis with solar energy: Sunlight-responsive photocatalyst based on TiO2 loaded on a natural material for wastewater treatment," Sol. Energy, vol. 135, pp. 527–535, Oct. 2016, doi: 10.1016/j.solener.2016.06.022.

[17] G. Jing, Z. Sun, P. Ye, S. Wei, and Y. Liang, "Clays for heterogeneous photocatalytic decolorization of wastewaters contaminated with synthetic dyes: a review," Water Pract. Technol., vol. 12, no. 2, pp. 432–443, Jun. 2017, doi: 10.2166/wpt.2017.046.

[18] Y. Du and P. Zheng, "Adsorption and photodegradation of methylene blue on TiO2-halloysite adsorbents," Korean J. Chem. Eng., vol. 31, no. 11, pp. 2051–2056, Nov. 2014, doi: 10.1007/s11814-014-0162-8.

[19] Z.-L. Cheng and W. Sun, “Preparation and Solar Light Photocatalytic Activity of N-Doped TiO2-Loaded Halloysite Nanotubes Nanocomposites,” J. Mater. Eng. Perform., vol. 24, no. 10, pp. 4090–4095, Oct. 2015, doi: 10.1007/s11665-015-1699-3.

[20] D. Wu et al., “Improved photoelectric performance via fabricated heterojunction g-C3N4/TiO2/HNTs loaded photocatalysts for photodegradation of ciprofloxacin,” J. Ind. Eng. Chem., vol. 64, pp. 206–218, Aug. 2018, doi: 10.1016/j.jiec.2018.03.017.

CHAPTER I Bibliographic study

This chapter is composed of three parts: The first one presents the main concepts of clay minerals and their classification, and application for the elimination of organic contaminants. A bibliographical synthesis gathering the main techniques best adapted for the elimination of dyes, in particular the methods based on adsorption and photocatalytic activity, will be presented thereafter. The second part of the chapter describes iron oxide nanomaterials in water treatment. The third part focused on heterogeneous catalysis especially titanium dioxide nanoparticles their doping, and application. The effects of the operating parameters on the efficiency of the process, a generalization of the supported photocatalysts, and a brief overview of photocatalytic treatment.

I.1 Clays

Clays are fine-grained minerals that are plastic in nature, may solidify when dried or burned, and contain the appropriate quantity of water. Although most clays contain phyllosilicates, the additional components may contribute to plasticity or hardness when fried or dried **[1]**. Clays are distinguished from other fine-grained soils by differences in mineralogy and size. Several definitions have been proposed **[2]**, varying according to the criteria chosen, but often difficult to elaborate. A concise definition referring to clay behavior. We will retain here only the mineralogical and granulometric definitions.

a- Mineralogical definition

The clay minerals are included in the family of phyllosilicates and they are constituted by a bidimensional tetrahedral layer of composition T_2O_5, T can be Si^{4+}, Al^{3+}. These tetrahedrons are linked in the same plane by three of their vertices, the fourth being oriented in another direction **[3]**. The tetrahedral layers are linked in the structure to octahedral layers or groups of ordered or independent cations.

b- Granulometric definition

A clay, in the agronomic sense of the term, is the mineral fraction of a soil whose particles have dimensions lower than 2µm. The raw clay is generally constituted of a basic mineral component (kaolinite, montmorillonite, etc...) and some secondary impurities as quartz, calcite, and organic matter **[4]**. Kaolin is commonly used to produce materials including rubber, plastic, paper, ceramics, catalysts, cosmetics, and adsorbent materials because of its strong chemical and mechanical stability, layered structure, and high cation exchange potential **[5]**. Also, it can be used as a scavenger in the atmosphere by eliminating contaminants either by ion exchange or through adsorption **[6]**.

I.1.1 Composition of clays

Clays are the result of the physical or mechanical disintegration of the rocks, followed by a chemical transformation that usually contains phyllosilicates (silicates in sheets). It can also contain some impurities (quartz for example) and organic matter. Phyllosilicates are one of the main components of the earth's crust. Clays are always accompanied by impurities such as **[7]**:

- Silicon oxides and hydroxides: (quartz and cristobalite).

- Iron-bearing minerals: hematite Fe_2O_3, magnetite Fe_3O_4.
- Carbonates: calcite $CaCO_3$, dolomite $CaMg(CO_3)_2$
- Aluminum oxides and hydroxides: gibbsite $Al(OH)_3$.
- Organic matter

In recent years, the interest granted to the study of clays by numerous researchers in the world justifies by (Pedro, 1994) **[8]**:

- Their abundance in nature
- The importance of the surfaces (the presence of electrical charges on these surfaces)
- The exchangeability of the inter-foliar cations is responsible for hydration and swelling which gives these clays hydrophilic properties.

Most clay minerals are in sheet form (phyllosilicates); tetrahedral and octahedral

- Tetrahedral sheets: are arranged in hexagonal meshes and consist of oxygen tetrahedrons surrounding a silicon atom. The tetrahedral silica group is arranged in a hexagonal network that repeats itself to form a composition sheet $Si(OH)_4$ it is the different combination between the octahedral sheet of silica and the alumina sheet **[9]**, as presented in **figure I.1.**

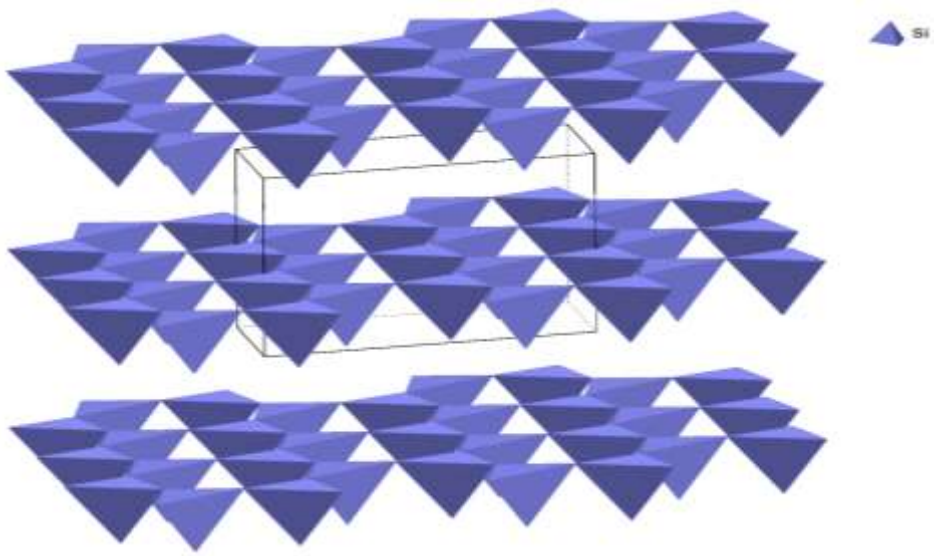

Figure I. 1 Tetrahedral sheet.

- Octahedral sheets are composed of octahedrons formed by two planes of oxygen-hydroxyl framing larger atoms such as Al, Fe, Mg, Li, etc. **[10]** as shown in **figure I.2**

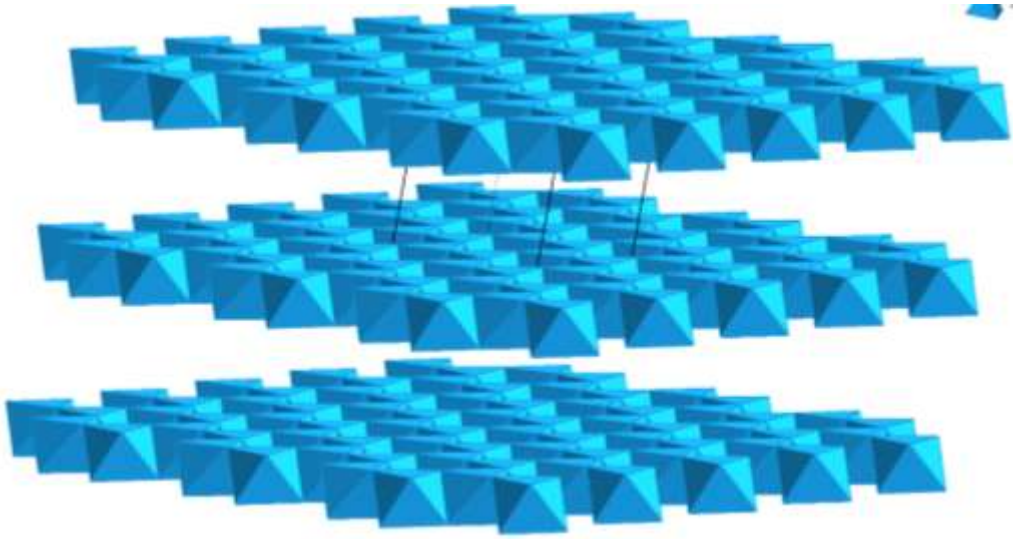

Figure I. 2 Octahedral sheets.

I.1.2 Classification of clay minerals

Grim and Guven are the first who classify clay minerals **[9] b**ased on the structural composition of clays. Kaolinite, Illite, Smectite, and Vermiculite are classified into four categories.

Type of layer, **i.e., 1:1 or 2:1 of tetrahedral silicates sheets and octahedral hydroxides sheets** type 1:1 (or T-O): which combine two layers: Octahedral and tetrahedral (examples kaolinite $Al_2(Si_2O_5)(OH)_4$); type1:2 (or T-O-T) which contain three layers: T silica / O gibbsite/ T silica. The O layer is surrounded by two T layers (hence the formula containing (Si_4O_{10}) (examples pyrophyllite $Al_2(Si_4O_{10})(OH)_4$ **[11]**. The classification of mineral clays is listed in **Table I.1**

Table I. 1 classification of clay minerals

Type	**Group of clay**	**Clay minerals**	**structure**
1/1	kaolinite	kaolinite	T-O
		halloysite	
		Dickite	
	smectites	montmorillonite	T-O-T

		saponite	
2/1		Beidellite	
		Nontronite	
	illites	illite	
	Vermiculite	vermiculite	
	micas	biotite	
		muscovite	
2/1/1	Chlorites	Chlorites	T-O-T-O

I.1.3 Properties of clay minerals

I.1.3.1 Hydration and swelling

The hydration phenomenon leads to the phenomenon of swelling by increasing the number of layers of water solvating compensating cations in space interfoliar. The degree of swelling depends on the nature of the clay and ions which are fixed on the clay, the water molecule contains three possibilities to contract the ions fixed on the clay, and the water molecule contains three possibilities to contract the bindings:

- It is a dipole, so it can establish electrostatic character bonds.
- The two hydrogens ensure the formation of hydrogen bonds.
- The oxygen atom has two pairs of free electrons which are used to form coordination bonds.

I.1.3.2 Specific surface area

The specific surface area is an essential property in the characterization of porous materials. It describes all the surfaces accessible to ionic particles, it is expressed by m^2 /g. it can distinguish:

- The surfaces of the external planes forming the bases of the particles, these are the external surfaces.
- The cumulative surfaces of all the planes of the sheets, which limit the interfoliar spaces, are called internal surfaces.
- The surfaces that laterally mark the boundaries of the sheets are the lateral areas.

I.1.3.3 pH_{pzc}

The surface charge is produced by the hydrolysis of silanol (Si-OH) and aluminol (Al-OH) groups in the clay lattice. Based on the silica composition and pH of the solution, the net surface charge could

be positive or negative. When the pH is less than pHpzc, the clay has an anion exchange capacity, $SiOH + H^+ \rightarrow SiOH^{2+}$

And when the pH is more than pHpzc, the clay has a cation exchange capacity..

$SiOH + OH^- \rightarrow SiO^- + H_2O$

The clay used in this study is kaolin extracted from Djebel Debbagh zone 3 Guelma.

The origin term of kaolin is from china which comes from "KAOLING", the name of a hill located near Yaochao-Fu in Kiangsi province. Kaolin is rocks composed largely of kaolinite, halloysite **[12]**, dickite **[13]**, and nacrite **[14]**.

I.1.4 Kaolinite and Halloysite

I.1.4.1 Kaolinite

Kaolinite is a di-octahedral TO phyllosilicate, consisting of a regular sheets composed of a tetrahedral layer (T) siliceous alternating with an octahedral (O) aluminous layer under the formula chemical: $Si_2O_5Al_2$ $(OH)_4$ forming hexagonal shape. Kaolinite has a wide range of physical and chemical characteristics that make it valuable in a variety of industries, including cement, paper, ceramic, paint, plastic, rubber, refractory, automotive, chemical, environmental, and textile. As a result, a thorough understanding of kaolinite's properties is critical for improving structural features and expanding application possibilities.

I.1.4.2 Halloysite

Berthier (1826) is the first one who described halloysite as a dioctahedral mineral clay of type 1:1 of the kaolin family. The name comes from Omalius d'Halloy, who was found in Belgium. The term halloysite (10A°) is ascribed to the hydrated mineral and halloysite (7A°) for the dehydrated form as recommended by the AIPEA Nomenclature comity.

I.1.4.2.1 Geological occurrence of halloysite

It generally comes from the transformation or alteration of primary silicates or volcanic rocks. Halloysite usually needs lower temperatures (<100°C) than Kaolinite (> 100°C) to crystallize in hydrothermal conditions. For example, New Zealand's halloysite, for example, is produced by low-temperature hydrothermal alteration of volcanic rocks., which means it contains quartz, cristobalite, and feldspar **[15]**.

Table I. 2 Specific surface area and mineralogy of halloysite from different regions in the world [16].

Country	Name of zone	Morphology	BET (m^2/g)
China	Longyan	Tube/platy	-
United States	Dragon Mine	tube	57.3
Turkey	Turkish	Tube/platy	72.2
Australia	Camel lake	tube	74.6
New Zeland	Matauri Bay	Tube/platy	22.1
Algeria	Djebel Debbagh 3	tube	71.71

I.1.4.2.2 Structure and morphology of Halloysite

Halloysite clay has various morphology: tubular, platy, and spheroidal. The dominant shape is tubular. The length and width of halloysite tubules was varied from 0.4 to 2 um, and 0.05 to 0.2 um, respectively. whereas inner lumen diameter and outer diameter is ranging 10–70 nm and 20–200 nm, respectively **[17]**.

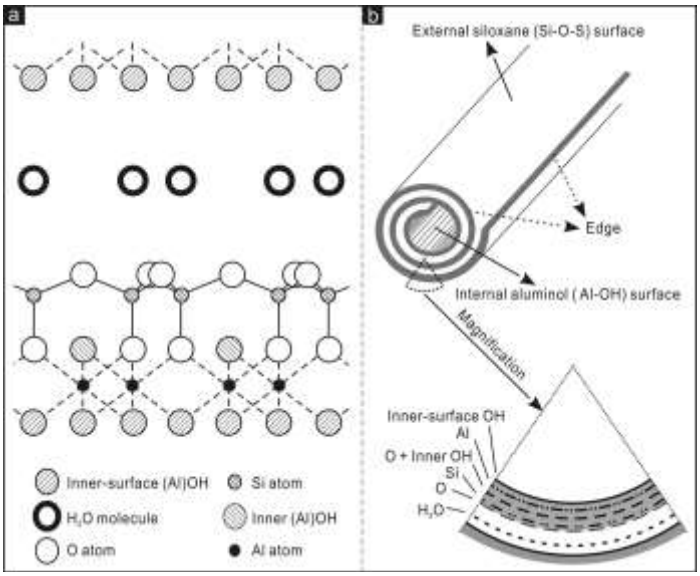

Figure I. 3 Structure of halloysite [18].

I.1.4.2.3 Properties of Halloysite

The halloysite has a specific surface area of 60–70 m^2/g **(table I.2).** During drying, the wall multilayer spacing reduces from 1.0 to 0.7 nm. The outside surface is consists of siloxane groups, and

the inner lumen is composed of aluminol groups. While, halloysite nanotubes are ionized in aqueous environments, the inner and outer surfaces of the tubes acquire opposing charges. This charge separation is retained in water with a pH range of 3.0 to 8.5, and may be explained by comparing negative and positive electrical-potential values of silica and alumina in water. The pore SSA and pore diameter of halloysite particles increased with increasing pH, but the overall surface area and surface area of the mesopores dropped when the pH increased **[19]**. The halloysite aggregated in acidic solution, and numerous mesopores between the halloysite nanotubes were closed, resulting in reduced pore volumes and diameters, also the pore area decreases with increasing pH. While the halloysite nanotubes were effectively dispersed in the basic solution, the surface area of the interior space expanded due to the opening of the halloysite nanotubes' mesopores.

I.1.4.2.4 Application of halloysite clay

The fields of application of clays are numerous: In the raw state, the production of ceramics (porcelain, earthenware, etc.). For modified states, clay is used in paper, cosmetics, the pharmaceutical industry (manufacture of drugs, such as Smecta and Bedelix), and in the adsorption of pollutants compounds. Furthermore, in catalysis, medicine, and sensors. In particular, halloysite clay has been commonly used for antibacterial **[20]**, catalytic **[21]**, optical **[22]**, electrical **[23**], magnetic **[24]** and energy storage **[25]** applications.

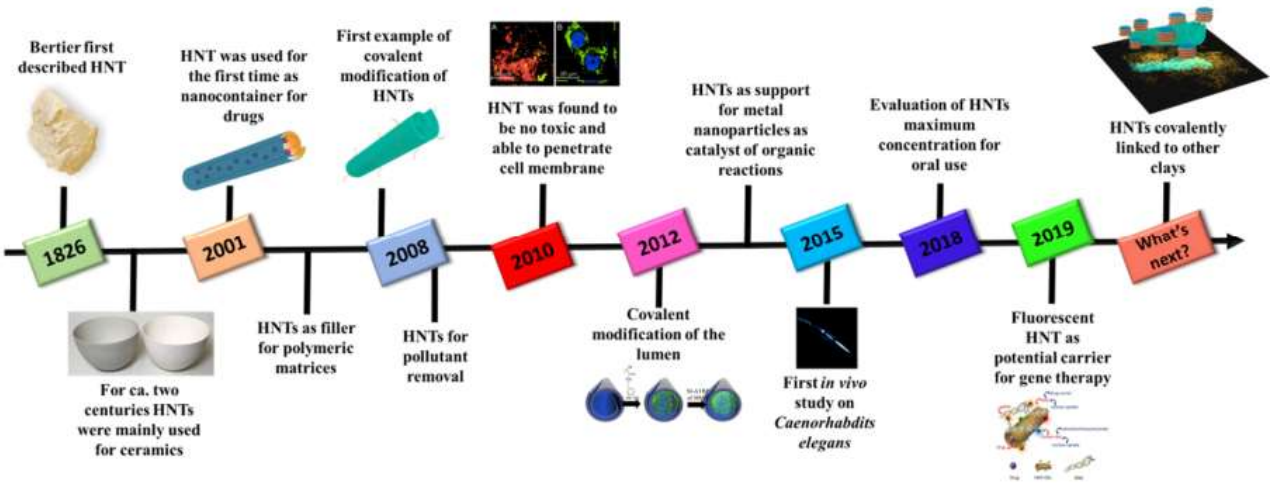

Figure I. 4 A brief timeline for the development of halloysite clay **[26]**.

I.1.5 Clay and environment

Due to the adsorption properties of clays and their capacity to form organo-mineral complexes, they intervene in the elimination of pollutants in natural water and the environment. These pollutants can be quickly trapped, the effectiveness of adsorption depends on the properties and concentration of the latter and other factors (pH, temperature).

For the elimination of crystal violet and brilliant green dyes, B.K.Nandi et al utilized commercial kaolin. To get the best conditions for adsorption of a large number of pollutants, certain factors such as starting dye concentration, mass of adsorbent, pH, and temperature were investigated. For crystal violet and brilliant green, the efficiency rate was 47.27 mg/g and 65.42 mg/g, respectively **[27]**. Peng Luo et al. collected halloysite clay from Hebei Province (China), milled, sieved, and dried for 24 hours at 373 K. The neutral red dye was removed with it. At 298, 308, and 318 K, the rate of adsorbed dye was 54.85, 59.24, and 65.45 mg/g, respectively, at pH 7. The adsorption was spontaneous and endothermic, according to the thermodynamic analysis **[28].** Novel composite (kaolinite incorporated into poly(acrylamide co-acrylic acid) was fabricated by Adel A.El-Zahhar et al for adsorption of bromophenol blue (BPB) dye. The thermodynamics results exhibited that the process is a spontaneous and exothermic chemical reaction. Furthermore, the adsorption rate was 5.89 mg/g **[29]**.

Montmorillonite clay was extracted from the northeast of Brazil. This adsorbent has been shown highly effective removal of methylene blue, about 292.15 mg/g at pH 11. The equilibrium adsorption was attained about 30 min. the thermodynamics parameters were showed that the adsorption exothermic and spontaneous **[30].**

The bentonite clay was treated by thermal and acid activation which was utilized for Congo red removal. The results showed that the adsorption reached 95% at pH 5.5. while the thermodynamic study revealed that the adsorption was spontaneous and exothermic **[31]**.

I.2 Processes of pollutants organics degradation

I.2.1 Generality about dyes

There are many sources of pollution and environmental contamination. The consequences on human health and the environment (respiratory diseases, gastroenteritis, risks of cancers...) of these pollutants, whether chemical volatile organic compounds (VOC), heavy metals, dyes…) or biological (bacteria, viruses) **[32]**. The use of dyes in human life dates back to antiquity. The ancient Egyptians

and Prussian used them to dye the rocks and ceramics. At the time, the coloring matters used before were extracted from plants such as indigo or animals such as carmine which is extracted from the cochineal. The use of these natural dyes lasted until the first half of the 19th century. Afterward, they were gradually replaced by synthetic dyes. Today, dyes have a great interest in our life in many industries (leather, textile, paper, plastics, pharmaceuticals, cosmetics...etc) **[33]**. The spillage of dyes into the environment is a huge problem. The presence of these types of contaminants which are aesthetically unpleasant in water even at low concentrations generates a negative effect on human health. In the following section, the different families of dyes will be presented in **table I.3** and their risks to the environment and the organism.

Table I. 3 classification of textile dyes and their health effects**[34]**, **[35]**.

Dyes	**examples**	**Textile industrial products**	**Health effect**
Acid dyes	Acid blue 25, methyl orange, congo red	Polyamide, fibers, polyurethane, modified acrylics, nylon	Skin and mucous membrane irritation and burns
Basic dyes	Basic red 46, malachite green, methylene blue	Silk, moderant acrylic, polyster	Carcinogers, allergic skin reactions, mutation, cancer
Direct dyes	Direct orange, direct black, direct blue	Leather, cotton, paper	Bladder cancer carcinogen
Disperse dyes	DisperseYellow, Disperse blue, Disperse red	Polyamide,acrylic fibers, cellulos	DNA damage, induction of bladder cancer in humans
Reactive dyes	Remazol, reactive black 5	Nylon, wool, cellulose, cotton	Allergic respiratory problem
Vat dyes	indigo, vat blue	Wool, rayon fibers, flax wool cotton	Severe burns, skin and mucous membrane irritation

Basic or cationic dyes have a positively charged auxochrome that will, during electrolysis, move towards the cathode (-) The character of acid or base applying to auxochrome does not imply necessarily the acid or basic character of the dye solution **[36]**. Furthermore, they are salts of organic amines, which means that they have good solubility in water. The bonds are made between the cationic sites of the dyes and the anionic sites of the fibers. In the process of disappearing in the dyeing of the wool and silk, these dyes have benefited from a renewed interest in the appearance of the acrylic fibers, on which they allow very vivid and resistant shades. In this study, we are interested in a basic dye, which is Methylene blue.

I.2.1.1 Methylene blue

It is a cationic dye from phenothiazine derivative **[37]**, It is a dark green powder that comes in many hydrated forms: monohydrate, di-hydrate, tri-hydrate, and penta-hydrate **[38],** with the tri-hydrate being the most prevalent. Because of its stable molecular structure, it is frequently used as a model of organic contamination. It's widely utilized in a variety of disciplines, including chemistry, medicine, dentistry, and the dye industry.

- it speeds up the elimination of methemoglobins
- it stains cotton, wood, silk, and paper it accelerates the reduction of methemoglobins **[39]**;
- it's an antibacterial and antirheumatic;
- it's an optical limiter coupled with a polymer for eye protection against powerful lasers, an active photosensitizer used in the treatment of cancer; therapy of toxic methemoglobinemia;

I.2.1.2 Toxicity of synthetic dyes

Discharge of effluents dyestuffs in aquatic environments is a huge problem. These compounds are known for their toxicity related to their complex structures and their high molecular weights, which are the main reasons for their resistance to biodegradation, in addition to their accumulation. The diazo dyes are considered the most toxic [40]. According to numerous studies, azo dyes have carcinogenic effects on humans. This carcinogenic effect is mainly due to the formation of aromatic amines by chemical or enzymatic disruption of bonds azoic. These aromatic amines can be absorbed percutaneous by inhalation of dust and possibly by ingestion. The risk of absorption of these compounds is increased by the fact that they are virtually all fat-soluble. The toxicity of azo dyes and their derivatives is aggravated by substitution in the aromatic nucleus in particular by the methylated,

nitro, and halogen group [41]. On the other hand, the presence of other substitutions such as sulfonate groups (SO_3H) decreases their toxicity. For their part of triphenyl methane derivatives are as risky as the other triphenylmethane derivatives. It causes eczema and gastric disorders. Their injection can cause even carcinogenic effects.

I.2.2 Dye removal processes

Dyes effluent combined with wastewater might pose a risk to the environment **[42]**. For the treatment of wastes of environmental significance, many physicochemical methods have been developed **[43]**. photocatalytic and Photolysis processes are chemical treatments, whereas biological and aerobic degradation are biological treatments, and physiochemical treatments include electro chemical coagulation, adsorption, and membrane filtering **[44]**. Based on design, cost and dye separation efficiency, each technique has its own set of limitations **(table I.4) [45]**. There are a large number of processes that can be applied to the removal and recovery of dyes present in industrial effluents.

Table I. 4 advantages and drawbacks of processes of removal dyes in industrial effluents.

separation technique	Advantages	Disadvantages
photocatalysis	Operational cost is low and economically feasible	generation a toxic products for some photocatalyst
Fenton reagent	Low-cost reagent and quick process	Disposal issues and sludge production
Anaerobic degradation	Byproducts can be utilized as energy resources	Under aerobic conditions require more treatment and produce of hydrogen sulfide and methane
Aerobic degradation	In the removal of azo dyes, the operational cost is slow and effective.	Create a favorable environment for the growth of microorganisms and proceed at a slow rate.
Adsorption	All dyes have a high adsorption capacity.	Low surface area for some adsorbents, high cost of adsorbents
Ion exchange	No sorbents are lost.	ineffective for disperse dyes
Membrane filtration	With high-quality effluents, it is effective for all dyes.	Suitable for low-volume treatment and sludge production.

I.2.3 Adsorption

Adsorption is one of the most significant industrial waste treatment separation techniques. It is a mass transfer technique in which a solid material (adsorbent) attracts dissolved components to its surface, allowing them to be selectively extracted from an aqueous solution. This includes the accumulation of concentrated components at the process's surface or during the interphase. The adsorbent might be a liquid, a solid, a gas, or a dissolved solute. Adsorption can be chemical or physical **(table I.5)**; in the former, the adsorbate is chemically bonded to the surface, involving the exchange of electrons. In the latter approach, physical forces including hydrogen bonding, polarity, and Vander Waals forces are used to bind waste molecules to the adsorbent surface. This separation thechnique is widely used to remove colors from an aqueous medium and is often considered the best approach. The effectiveness of this technique is determined by the chemical and physical

characteristics of the adsorbate and adsorbent, as well as their cost, availability, convenience of use, surface area, and toxicity**[46]**. The low-cost adsorbents were divided into five classes by Gisi et al. **[47]**: (i) domestic wastes and agricultural (ii) industrial by-products, (iii) marine materials, (iv) sludge, (v) ore materials and soil, and (vi) low-cost innovative adsorbents.

Table I. 5 Comparatives between physisorption and chemisorption.

Physisorption [48]	**Chemisorption [49]**
Weak liaison (van der Waals)	Strong covalent bonds
Low temperature, constantly lower than the adsorbate critical temperature	High temperature
Reversible (nonselective surface attachment)	irreversible (Selective surface attachment)
Low enthalpy H < 20kjmol	High enthalpy H=40Kj/ mol
Low activation energy	High activation energy
Multilayer adsorption	Monomolecular adsorption

I.2.3.1 Main factors influencing adsorption

The adsorption equilibrium between adsorbent /adsorbate depends on many factors, the main ones of which are described below:

- Specific surface area (SSA): adsorption has a direct relationship with the surface area **[50]**.
- Nature of adsorbate: The less a substance is soluble in the solvent, the better it is adsorbed.
- Hydrogen potential (pH): Adsorption is strongly dependent on the pH of the solution and therefore will influence the loading of the adsorbent surface, the degree of ionization, and adsorbate speciation. The acid-base characteristics of Functional groups on the surface change with pH. They become basic in character for $pH < pH_{PZC}$ by adsorption of H^+ ions (PZC: zero charge point) and become acidic for $pH > pH_{PZC}$ by adsorption of OH- ions **[51]**.
- Polarity: A polar solute will have more affinity for the solvent or the adsorbent.
- Temperature: For economic reasons, adsorption takes place at room temperature. The temperature influences both the adsorption rate and the equilibrium concentration **[52]**.

I.2.3.2 Applications of adsorption

The adsorption separation technology is nowadays one of the most popular methods of separation. It is widely used for the separation and purification of gases and liquids in a wide variety of fields,

from industries oil, petrochemical, and chemical industries, environmental applications **[53]**, and pharmaceutical companies. Air, water, and effluent treatment for the disposal of pollutants, drying, drug production, etc. In the case of water treatment, the applications are multiple. One finds by example:

- Drinking water treatment to remove residual tastes and odors
- The discoloration of liquors
- The elimination of pollutants in wastewater.

I.2.4 Sono assisted adsorption

Ultrasound has recently gained popularity in environmental protection for the destruction of harmful contaminants. The use of ultrasound in combination with the adsorption process has been discovered to be a promising approach in the field **[54].** Many researchers have examined ultrasound's effects on the adsorption of organic molecules by various sorbents **[55]**. It has been observed that combining two methods is more effective in removing dyes than doing so sequentially **[56]**. The collapse of tiny bubbles has been ascribed to the chemical and mechanical effects of ultrasound **[57]**. Ultrasonic vibration reduces the thickness of liquid films connected to the solid phase, simplifies sorbate species transport through the interface, improves mass transfer, and destroys sorbate-sorbent affinity **[58]**. A high-speed jet of liquid is produced by the asymmetric collapse of the cavity near the solid surface. Strong forces are striking the surface as a result of these jets. This procedure causes severe destruction at the point of impact, highly reactive surfaces, and produces newly exposed. Furthermore, the ultrasonic energy may fluctuate depending on the adsorption/desorption system's equilibrium characteristics and the equilibrium time of the adsorption decreased **[59].** Despite the various advantages of the sonochemical degradation process, its rate of degradation of many organic pollutants is very low. This is attributed to the low effectiveness of reactive radical training **[60]**. Consequently, the degradation of organic pollutants using this method takes several hours and, therefore, the energy and the cost are high **[61]**.

Among researches which were combined the adsorption and ultrasonication, Hamza et al. used Sono-assisted adsorption to remove CV from a laden aqueous solution onto Raw Tunisian Smectite Clay. The impact of several variables such as contact time, starting CV concentration, sorbent dosage, and pH on the Sono-assisted adsorption of CV pigment was investigated in adsorption studies **[62]**.

Owing to the synergistic process achieved in this combined system, using a combined ultrasound/activated charcoal process resulted in a higher CV decolorization than using adsorption or sonolysis alone. Experiments were carried out using various pigment concentrations and temperatures as the starting point. 50.1 mg/g was the maximum monolayer adsorption capacity **[63]**.

I.3 Iron oxide nanomaterial in water treatment

Iron is the fourth common element on the surface of the earth and it is found in the aquatic and terrestrial environment. At different pH, the element occurs in many various oxidation states and minerals, including goethite **[64]**, hematite **[65]**, magnetite **[66]**, and maghémite **[67].** They are produced for use in several applications. In particular magnetite nanoparticles are the subject of many reviews for their potential in the rapidly emerging field of nanotechnology**[68]** due to their characteristics, such as superparamagnetism, large specific surface area and so on. Furthermore, iron oxide nanoparticles might be useful in the creation of high-capacity adsorbents and photocatalysts. Magnetic iron oxide-based nanocomposites with saturation magnetization offer a cost-effective solution for adsorption and photocatalysis due to their reusability and simplicity of recovery. The rising push for environmental and economically more efficient technologies is in part fuelling the drive towards functional nanomaterials as well as for their potential use as materials for medical, computational, industrial process, and groundwater remediation **[69]**. In recent years, there is more attention on using magnetic iron oxide/clay was in the SCOPUS database **(Figure I.5).**

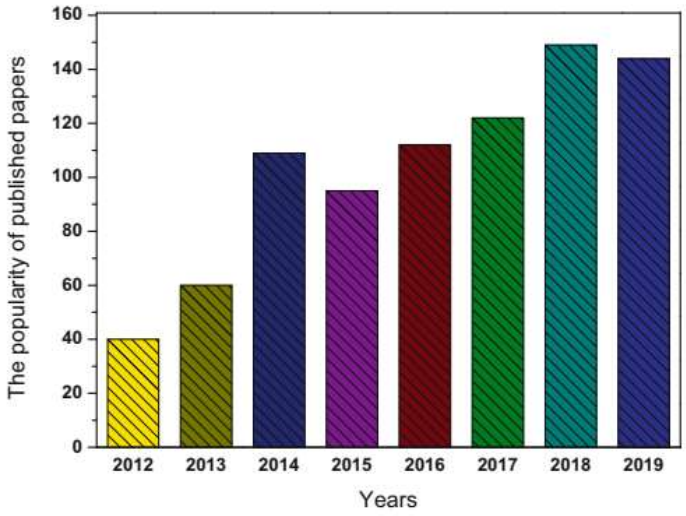

Figure I. 5 the using magnetic iron oxide/clay nanocomposite for removal of organic pollutants (source Scopus, 2012-2019).

I.3.1 Magnetite

Magnetite Fe_3O_4 is a black ferrous-iron oxide. It is a naturally occurring iron ore, and it is represented as a spinel class **[70]**. It is a black solid with a metallic luster. Today, magnetite-based materials are widely used in industrial applications, as permanent magnets, high-frequency magnetic components, and recently as components of high magneto-resistance components.

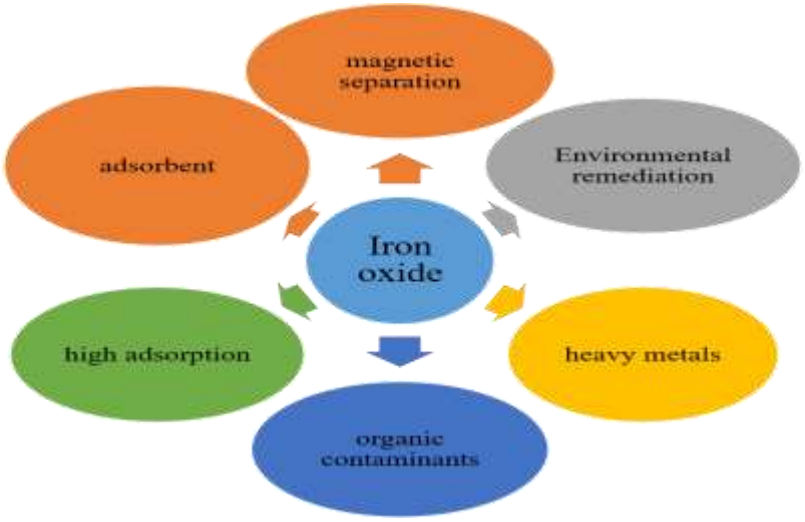

Figure I. 6 Application of iron oxide**.**

I.3.1.1 Limitation of nanoparticles of magnetite

Due to their high adsorption efficiency and biocompatibility, magnetite are defined highly qualified as sorbents for the elimination of different types of pollutants, fast removal, and ease of aqueous removal processes. However, the oxidation and agglomeration susceptibility of magnetite particles restricts its usage as an adsorbent material in aqueous media, necessitating surface capping of these Fe_3O_4 nanoparticles for optimal adsorption performance. Furthermore, the discharge of iron oxide and its influence on aquatic ecosystems. For example, the combination of iron oxide with clays increases the performance of these composites as adsorbents, and researchers have exhibited an effective application in adsorption operations **[71].**

I.3.2 Magnetic adsorbent for water treatment

Four key characteristics can be included to classify that material as sorbent, according to a study report (1) The potential to eliminate larger concentrations of toxins, (2) high reactivity, (3) high porosity, and (4) non-toxicity in water remediation. The cost is a very important factor, higher environmental stability and effectiveness, higher potential for adsorption, and non-toxicity of iron

oxide nanomaterial make them suitable for water treatment **[72]**. The field of polluted water adsorption is another distinctive feature that favors the use of nanomaterials from iron oxide in magnetism. The separation feature also allows the process, including filtration and centrifuging, to avoid these conventional separation techniques. Usually, there is a lot of support using in the loading of magnetite nanoparticles such as carbon adsorbent particles, mineral adsorbent particles, and modified polymers. In the below section we focus on modified magnetic clay support for removing organic contaminants via adsorption which are more dominant than advanced oxidation processes (AOPs).

I.3.3 Application of magnetic iron oxides clays as sorbent in adsorption of organic pollutants

Clays have several limitations that have resulted in a variety of changes to improve their adsorption capacities. Clay modification refers to the addition of a foreign substance to clay matrices in order to increase their adsorption capacity. Pillaring, mechanochemical modification, ion exchange, organo-modification, and sonochemical treatment are all examples of clay modification methods. **A** variety of studies have reported on the modifications of clay such as modification by magnetite nanoparticles **[73]**.

Magnetic Fe_3O_4/C core-shell nanoparticles were prepared by Zhang and Kong to eliminate cresol red (CR) and methylene blue (MB) from an aqueous solution, the adsorption capacity of Fe_3O_4/C nanoparticles with an average size of 250 nm was checked. the adsorption capacities for CR and MB are 11.22 mg/g and 44.38 mg/g respectively **[74]**.

Wu et al. synthesized Fe_3O_4 rectorite nanoparticles to fabricate an adsorbent that was studied to adsorb methyl orange (MO), methylene blue (MB), and neutral red (NR). Results of characterizations revealed that REC was bound to clusters of Fe_3O_4 nanoparticles **[75]**.

Xie et al developed a magnetic sorbent HNT– Fe_3O_4 with iron oxide nanoparticles loaded on the halloysite nanotube (HNT) for removal: methyl orange, methylene blue, and neutral red. For MB, the adsorbed quantity was 18.44 mg/g, whereas, for neutral red dye, it was 13.62 mg/g **[76]**.

Wu et al prepared via solvothermal process, Graphene-Fe_3O_4 nanocomposite was synthesized and analyzed for adsorption of organic pararosaniline dye. The experimental adsorption results are correctly represented by the Langmuir isotherm and pseudo-second-order model. The adsorption potential for pararosaniline removal was 198.23 mg/g **[77].**

Magdy et al synthesized **Fe_3O_4**/kaolin by co-precipitation method for investigation of removal Direct Red 23 dye and anionic C.I. from aqueous media. The results showed that the quantity adsorbed reached 22.88 mg/g. The adsorption process is endothermic, and spontaneous **[78].**

The magnetic Kaolinite nanotube (KNTs) was synthesized by solvothermal method for adsorption of methylene blue with high removal of 35.91 $mg.g^{-1}$ at 298 K which was reported by Xu, H et al **[79].** The Fe_3O_4/bentonite was synthesized via the coprecipitation route by Hashem et al **[80]** with a maximum adsorption capacity was 1600 mg/g.

I.4 Generality of heterogeneous catalysis

Kato and F. Masuo published a paper in 1964 that described the oxidation of tetralin in the liquid phase using TiO_2 as a photocatalyst and UV irradiation. Furthermore, several researchers have observed reactions in the gas phase employing UV-illuminated semiconducting TiO_2, including Steinbach, Teichner, Tanaka, Yoneyama, and others **[81]**. K. Honda and A. Fujishima developed the photosensitization of a TiO_2 electrode as a photoanode and Pt metal electrode as a cathode for the electrolysis of H_2O into H_2 and O_2 under UV light irradiation **[82]**, in 1972. In recent years several types of research focus on semiconductors and their application in different fields. Among them, titanium dioxide was a benchmark semiconductor due to its precious properties and applications. The main drawback of TiO_2 is to absorb in the UV region. For this reason, TiO_2 was modified by doping with metals and no-metals elements.

I.4.1 Principle of heterogeneous photocatalysis

Heterogeneous photocatalysis involves the photoexcitation of a semiconductor by absorption light. It can be defined as the catalysis of a photochemical reaction and involves a solid/gas interface, or solid/liquid **[83]**. The photocatalytic process can be divided into five independent steps **[84]**:

1. Diffusive migration of the reagents from the fluid phase to the surface of the photocatalyst, including in the porosity of the photocatalyst
2. Adsorption of reagent at least one reagent on the catalyst surface
3. Adsorbed phase reaction (the stage in which the photocatalytic reaction at strictly speaking)
4. Desorption of products
5. Diffusional migration of products from the catalyst surface to the fluid phase

I.4.2 Criteria of choosing of photocatalyst

Several criteria must be considered when selecting a semiconductor material to be used as a photocatalyst **[85]**:

- The energy of the incident photons (UV or visible radiation) should be greater than the energy of the bandgap, to allow activation of the semiconductor. The redox potential of the conduction band must be more negative than the potential of reduction of chemical species, and the redox potential of the valence band must be more positive than the oxidation potential of the chemical species
- Chemically inert and photo-stable in air or water according to the application
- Low toxicity or nontoxic

I.4.3 Application of TiO_2

The extensive research on TiO_2 material has yielded many potential applications in varied fields from photovoltaic and photocatalysis to photo electrochromic and sensors. These applications may be divided into two categories: "energy" and "environmental," with many of them relying on more than just the TiO_2 material's characteristics **[86].**

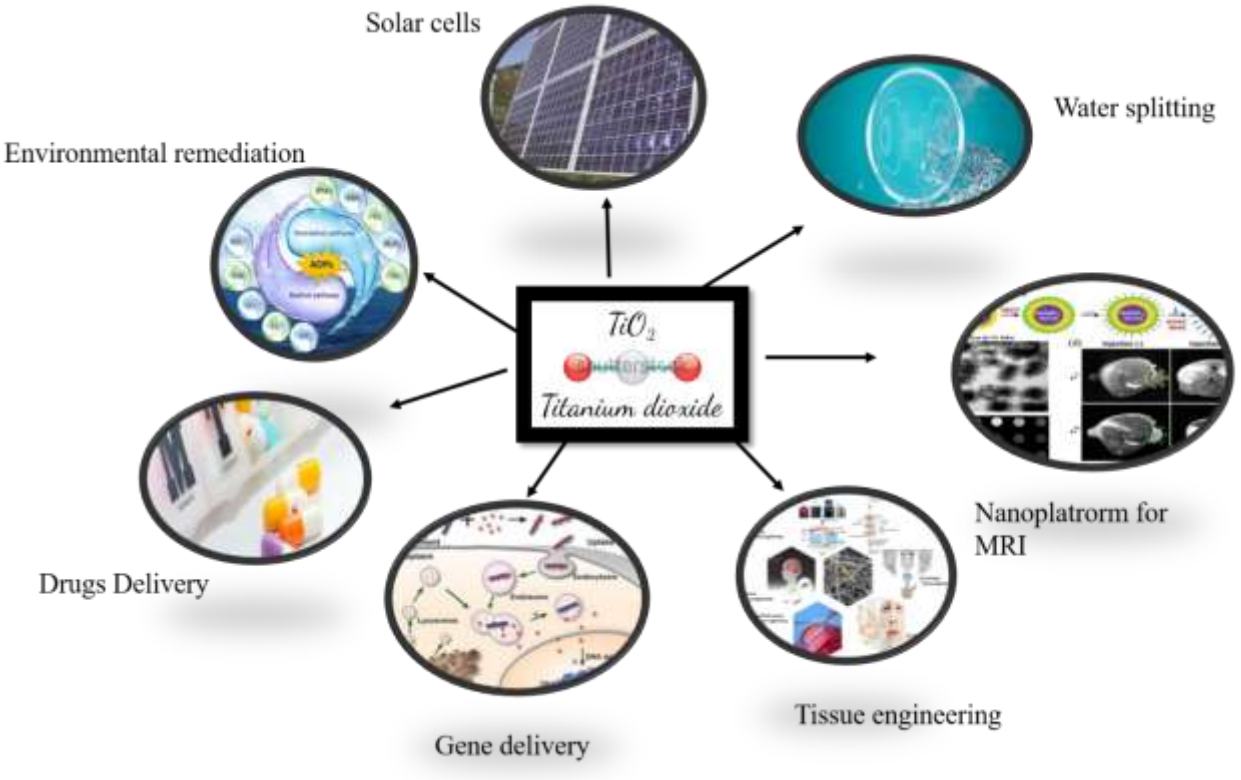

Figure I. 7 Application of TiO_2.

I.4.4 Titanium Dioxide Doping

Currently, most photocatalysis applications use titanium dioxide in its predominantly Anatase form, which has very good semiconductor properties. However, this activity can be summarized by the use of UV radiation, which represents 3 to 5% of the sunlight reaching the earth.

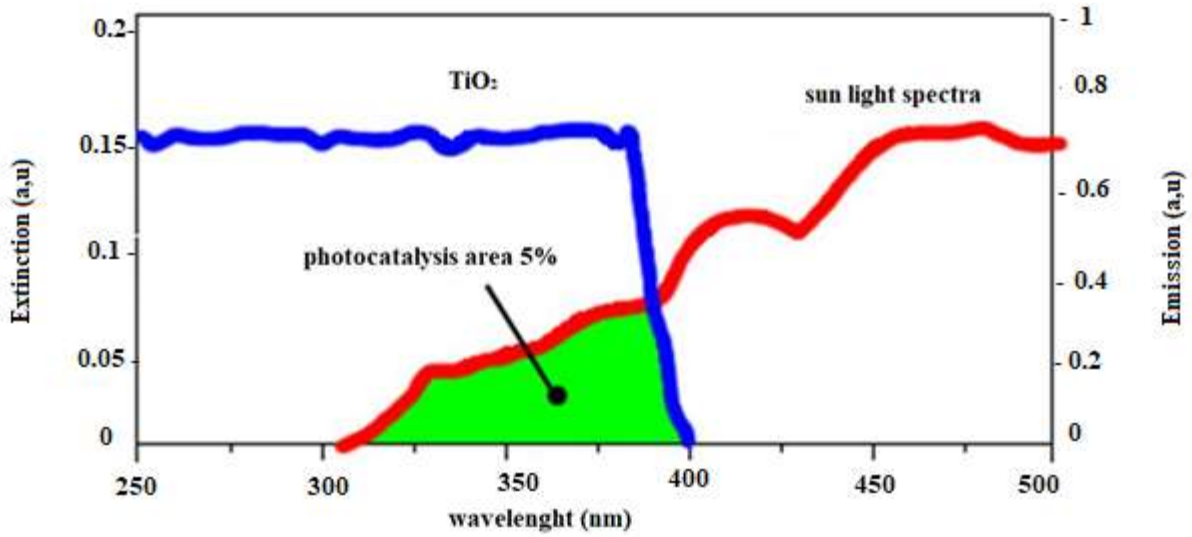

Figure I. 8 Comparison of the solar spectrum with the fundamental absorption spectrum.

To modify the optical TiO_2, there are two methods according to Chen

a- **Sensitization surface chemical modification:** is to treat the TiO_2 to enable the production of photocurrent. This sensitizer may be a metallic, inorganic, or organic material. A variety of inorganic and organic dyes have been studied as sensitizers for TiO_2,

b- **doping bulk chemical modification:** the implantation of transition metal ions such as V, Cr, Fe, Co, Ni in a network of TiO_2 could allow a large change in the absorption band of this crystalline TiO_2 photocatalyst to the visible regions, with different levels of efficiency photocatalytic **[87]**. However, the majority of these works adhere to the fact that this modification increases the recombination of charges (electrons and holes). In parallel, Sato et al. began to perform anionic doping. The doping of TiO_2 with nitrogen, carbon, sulfur, or boron (anionic doping) allows a displacement of the TiO_2 from the absorption band to the visible spectral range **[88]**. Indeed, when these elements bond with titanium, orbital changes occur and lead to a decrease in the width of the photocatalyst's bandgap.

I.4.5 Chalcogenide

The oxides of titanium, zinc, tin, iron, zirconium and cerium have been widely used to degrade various organic contaminants **[89]**. However, the wide band gap of these metal oxides limits their photocatalytic application in UV light. In addition, the rapid recombination of electron-hole pairs is another important issue **[90]**. Consequently, chalcogenide photocatalysts (sulphides, selenides, and tellurides) have turned into consideration owing to their crucial properties which are active under visible light irradiation **[91]**. Among them FeS which is a semiconductor that has applications in photocatalysis, batteries, and solar cells. Iron sulfide nanoparticles were used as a reducing agent having the benefits of being a cost-effective, high-efficiency, and environmentally friendly material. This substance has the potential to create a substantial amount of Fe^{2+} and S^{2-} ions are present. They demonstrated that dyes in solution may be treated with iron sulfide by adsorption, photodegradation.

I.4.6 Limitation of using TiO_2 in water treatment

The use of TiO_2 in suspension in water involves two major problems: the separation of the photocatalyst from the treated water and the reuse of TiO_2 particles. The particle size of TiO_2 is around 30 nm, the price required for the separation makes the process more difficult with high cost. Furthermore, the costs of filtration of the catalyst. The decantation process could be a solution, but this would require the use of huge reservoirs for suspension storage and delayed use of treated water. One of the solutions to this problem is to fix the photocatalyst on a suitable support. Some works have been focused on using different supports (tubes, glass or carbon fibers, glass or stainless steel plates, clays ...). on the other hand, the choice of suitable support of Titanium dioxide should have the following properties:

- Favour strong Physico-chemical bonds with the catalyst particles without have a negative effect on reactivity;
- Large surface area **[92]**;
- Good capacity to adsorb organic compounds to be degraded;
- Physical configuration favoring the solid/treated water separation;
- Be chemically inert;

Concerning the deposit of photocatalyst, two following conditions are imperative:

- There must be good catalyst/support adhesion;
- The catalyst fixation process must not disturb the photocatalytic activity.

Two main ways have been explored to fix TiO_2 on different supports. The first is to immobilize the catalyst after synthesizing it. The second is to generate the in-situ catalyst. In the following paragraphs, we'll give a quick overview of the loading TiO_2 on clays (photocatalyst/support).

I.4.7 Loading TiO_2 nanoparticles

Inorganic substrates, such as silica, polymers, and natural porous materials, can support TiO_2, which has high photocatalytic activity in wastewater purification. Some natural mineral materials, such as zeolites and clay, are gaining popularity because of their porous structure, low cost, and large storage capacity. Furthermore, due to their low polar surface and wide surface area, as well as their strong adsorption ability for non-polar organic contaminants, these natural materials are ideal options for titania support **[93].**

TiO_2-clay composites have several benefits over commercial photocatalysts, including a large specific surface area, excellent hydrophobicity, and a cheap cost. Because the titanium oxide immobilization process frequently includes several chemical and thermal interactions, porous clay materials with a relatively stable structure are frequently requested as catalyst supports **[94]**.

I.4.8 Works focus on loading TiO_2 on clay

I.4.8.1 TiO_2 HNTs

TiO_2-halloysite (TiO_2-HNT) composites were prepared by Yuanyuan Du and Pengwu Zheng. with the sol-gel approach under calcination treatment at different temperatures 100, 200, 300, and 500°C. The composites were characterized by transmission electron microscopy (TEM), Fourier transform infrared spectroscopy (FTIR), and X-Ray diffraction (XRD). TiO_2 particles agglomerated in clusters of 10-30 nm were placed on HNT, the crystalline of anatase became more perfect. However, at 500 °C, the structure of HNT might be damaged by raising the calcination temperature. Methylene blue adsorption and photocatalytic activity were evaluated. Adsorption kinetics followed the pseudo-second-order and Langmuir isotherms. MB has adsorption capabilities ranging from 38.57 to 54.29 mg/g. The greatest photodegradation was seen at 300 °C calcination when 81.6 percent of the MB was destroyed after 4 hours of UV exposure **[95]**.

The TiO_2- and Fe_2O_3-halloysite nanocomposites were fabricated by using the acid treatment for halloysite from Poland. The first sample (TiO_2-halloysite) was prepared under hydrothermal treatment at 65 °C using titanium isopropoxide as a precursor. The second sample (Fe_2O_3-halloysite)

nanocomposite was synthesized by the sol-gel method. Gelatinous ferric hydroxide was used as a ferric precursor. The acid treatment was performed to halloysite with sulfuric acid (3M) under stirring for 4 hours at 80°C. The photocatalytic performance of TiO_2- and Fe_2O_3-halloysite nanocomposites for chloroaniline, and 2,6-dichloroaniline under the UV irradiation for 300min exhibited a good result for decomposing pollutants compared to commercial TiO_2, commercial photocatalyst P25 **[96]**.

The halloysite-TiO_2 composites were produced using the sol-gel technique, followed by the coprecipitation approach for magnetite deposition. Transmission electron microscopy, energy-dispersive X-ray spectroscopy, a particular surface analyzer, and X-ray diffraction were used to characterize the HNT- TiO_2-Fe_3O_4 composites. Methylene blue (MB) photodecomposition by HNT-TiO_2 and HNT- TiO_2- Fe_3O_4 exhibited a good discoloration of MB. Under UV light irradiation for 12 hours, which removed almost 100 % MB. The kinetic adsorption was ascribed to the pseudo-second-order model and the isotherm data fitted the Langmuir model well. The photocatalytic activity of 4-nitrophenol exhibited about 98% of degradation for HNT- TiO_2-Fe_3O_4 and was repeated for five cycles **[97]**.

The HNTs/N-doped TiO_2 nanocomposites were synthesized by a novel method of chemical vapor deposition in an autoclave (HNTs powder, $(NH_4)_2CO_3$ solid (N-TiO_2/HNTs(S) sample) or a saturated solution (N-TiO_2/HNTs(L) sample), and $TiCl_4$, at temperature 100 °C, calcination at 550 °C) [98]. The photocatalytic performance was studied by the degradation of phenol under simulated solar light radiation. The photocatalytic degradation of phenol by N-doped TiO_2/HNTs(L) nanocomposite exhibits the highest photocatalytic activity under simulated solar light about 70% after 150min compared with N-doped TiO_2/HNTs(S) which attaints 40%.

D. Wu, et al **[99]** prepared a novel photocatalyst coupling g-C3N4 with TiO_2 supported on HNTs by sol-gel and calcination methods. The introduction of HNTs and the g-C3N4-TiO_2heterojunction effectively enhanced the charge transfer and separation efficiency of photogenerated electron-hole pairs, which endued the g-C3N4/TiO_2/HNTs hybrid material with outstanding photoelectric performance and good stability. And an enhanced photocatalytic activity was exhibited by photodegradation of ciprofloxacin compared with pure TiO_2. Furthermore, the main active species were detected through trapping experiment and ESR spin-trap technique with DMPO, which confirmed that the O_2 and the h^+ were the main active species in the photocatalytic system.

I.4.8.2 TiO_2/MMT

The preparation of TiO_2 / MMT nanocomposite by impregnating $TiCl_4$ with calcination at 350° C was investigated by Djellabi et al. On the surface of clay developed crystalline TiO_2 Anatase. Five cationic colors, such as crystal violet, MB, RhB, methyl orange (MO), and Congo red, are degraded and photoactivity has been examined under UV-A light. The degradation rates were shown as follows: violet-crystal (97.1%) > MB (93.2%), RhB (79.8%) > MO (36.1%) > red Congo (22.6 %) **[100].**

Mishra et al TiO_2 / bentonite nanocomposites synthesized under microwave conditions (180 °C), contributing to the creation of TiO_2 anatase NPs within 10 minutes on the bentonite surface. Bentonite nanocomposites of 50% TiO_2 by weight was tested for the degradation of methylene blue due to its SSA (70 m^2/g) and pore size (0.3455 cm^3/g) **[101]**.

Ag/TiO_2 loaded on bentonite by impregnating has been further prepared AgNPs (0.5-3%) **[102]**. The Ag-TiO_2 bentonite nanocomposite demonstrated higher photocatalytic behavior under simulated solar radiation. The phenol removal performance was higher than TiO_2 and Ag-TiO_2 nanoparticles.

I.4.8.3 Kaolinite

A nanocomposite composed of mixed-phase TiO_2 NPs was prepared by Zhang et al **[103]** using a simple method involving stirring and low-temperature aging of the material for 12-24 hours. The layered structure of kaolinite was destroyed to some degree during the synthesis, contributing to the creation of a dual mesoporous structure due to the integration of TiO_2 into kaolinite. The HRTEM showed various lattice fringes that allowed various TiO_2 phases to be identified. The nanocomposite showed excellent photoactivity relative to red-G acid degradation and 4-Nitrophenol (4-NP) as compared to commercial P25. The mesoporous structure, high area and heterojunction formation between anatase-brookite and anatase-rutile TiO_2 resulted in high photocatalytic activity in TiO_2 / kaolinite nanocomposite.

I.5 Conclusion

In this chapter, we summarized the main concepts of clay minerals and their application for removal of organic contaminants through adsorption and photocatalysis processes. The abundance of current research accessible in the literature demonstrates that there is a growing interest in the use of iron nanoparticles for water and wastewater treatment. Modification clays by magnetite particles is

one of interesting materials which can be easily separated due to the action of an external magnetic field. Moreover, the functionalization of clays by titanium dioxide have a great interest for photodegradation of many contaminants. According to the studies consulted in the bibliography**,** halloysite clay was considered as a promising materials for removal contaminants due to their tubular shape, low cost, and affordable substance. Furthermore, combined with oxides (Fe_3O_4, TiO_2, ZnO …) have proved efficiency in removal of organics contaminants under visible light irradiation.

References

[1] A. A. Adeyemo, I. O. Adeoye, and O. S. Bello, “Adsorption of dyes using different types of clay: a review,” Appl. Water Sci., vol. 7, no. 2, pp. 543–568, May 2017, doi: 10.1007/s13201-015-0322-y.

[2] F. Hubert, L. Caner, A. Meunier, and E. Ferrage, “Unraveling complex <2 m clay mineralogy from soils using X-ray diffraction profile modeling on particle-size sub-fractions: Implications for soil pedogenesis and reactivity,” Am. Mineral., vol. 97, no. 2–3, pp. 384–398, Feb. 2012, doi: 10.2138/am.2012.3900.

[3] B. B. Lázaro, “HALLOYSITE AND KAOLINITE: TWO CLAY MINERALS WITH GEOLOGICAL AND TECHNOLOGICAL IMPORTANCE,” p. 32.

[4] O. Ochieng, “Characterization and classification of clay minerals for potential applications in Rugi Ward, Kenya,” Afr. J. Environ. Sci. Technol., vol. 10, no. 11, pp. 415–431, Nov. 2016, doi: 10.5897/AJEST2016.2184.

[5] C. H. Zhou, L. Z. Zhao, A. Q. Wang, T. H. Chen, and H. P. He, “Current fundamental and applied research into clay minerals in China,” Appl. Clay Sci., vol. 119, pp. 3–7, Jan. 2016, doi: 10.1016/j.clay.2015.07.043.

[6] Mohd. Rafatullah, O. Sulaiman, R. Hashim, A. Ahmad, Adsorption of methylene blue on low-cost adsorbents: A review, Journal of Hazardous Materials. 177 (2010) 70–80. https://doi.org/10.1016/j.jhazmat.2009.12.047

[7] S. Guggenheim and R. T. Martin, “Definition of Clay and Clay Mineral: Joint Report of the Aipea Nomenclature and CMS Nomenclature Committees,” Clays Clay Miner., vol. 43, no. 2, pp. 255–256, Apr. 1995, doi: 10.1346/CCMN.1995.0430213.

[8] M. Alvarez-Silva, A. Uribe-Salas, M. Mirnezami, J.A. Finch, The point of zero charge of phyllosilicate minerals using the Mular–Roberts titration technique, Minerals Engineering. 23 (2010) 383–389. https://doi.org/10.1016/j.mineng.2009.11.013.

[9] R. E. Grim, “Clay Mineralogy: The clay mineral composition of soils and clays is providing an understanding of their properties,” Science, vol. 135, no. 3507, pp. 890–898, Mar. 1962, doi: 10.1126/science.135.3507.890.

[10] S. Ismadji, F. E. Soetaredjo, and A. Ayucitra, "Natural Clay Minerals as Environmental Cleaning Agents," in Clay Materials for Environmental Remediation, S. Ismadji, F. E. Soetaredjo, and A. Ayucitra, Eds. Cham: Springer International Publishing, 2015, pp. 5–37. doi: 10.1007/978-3-319-16712-1_2.

[11] F. Bergaya, M. Jaber, and J.-F. Lambert, "Clays and Clay Minerals as Layered Nanofillers for (Bio)Polymers," in Environmental Silicate Nano-Biocomposites, L. Avérous and E. Pollet, Eds. London: Springer, 2012, pp. 41–75. doi: 10.1007/978-1-4471-4108-2_3.

[12] I. R. Wilson, "Kaolin and halloysite deposits of China," Clay Miner., vol. 39, no. 1, pp. 1–15, Mar. 2004, doi: 10.1180/000985543910116.

[13] C. O. Choo and S. J. Kim, "Dickite and Other Kaolin Polymorphs from an Al-rich Clay Deposit Formed in Volcanic Tuff, Southeastern Korea," Clays Clay Miner., vol. 52, no. 6, pp. 749–759, Dec. 2004, doi: 10.1346/CCMN.2004.0520610.

[14] M. D. Ruiz Cruz, "Dickite, Nacrite and Possible Dickite/Nacrite Mixed-Layers from the Betic Cordilleras (Spain)," Clays Clay Miner., vol. 44, no. 3, pp. 357–369, Jun. 1996, doi: 10.1346/CCMN.1996.0440305.

[15] V. Reyes-Zamudio, C. Angeles-Chávez, and J. Cervantes, "Clay minerals in historic buildings," J. Therm. Anal. Calorim., vol. 104, no. 2, pp. 405–413, May 2011, doi: 10.1007/s10973-010-1041-0.

[16] "Read Nanosized Tubular Clay Minerals Online by Elsevier Science | Books." https://www.scribd.com/book/315409779/Nanosized-Tubular-Clay-Minerals-Halloysite-and-Imogolite (accessed Aug. 19, 2021).

[17] D. Rawtani, Y.K. Agrawal, MULTIFARIOUS APPLICATIONS OF HALLOYSITE NANOTUBES: A REVIEW, *Rev. Adv. Mater. Sci*, *30*(3), 282-295.

[18] Y. Zhang, A. Tang, H. Yang, and J. Ouyang, "Applications and interfaces of halloysite nanocomposites," Appl. Clay Sci., vol. 119, pp. 8–17, Jan. 2016, doi: 10.1016/j.clay.2015.06.034.

[19] Y. Joo, J. H. Sim, Y. Jeon, S. U. Lee, and D. Sohn, "Opening and blocking the inner-pores of halloysite," Chem. Commun., vol. 49, no. 40, pp. 4519–4521, Apr. 2013, doi: 10.1039/C3CC40465J.

[20] K. M. Rao, S. Nagappan, D. J. Seo, and C.-S. Ha, "pH sensitive halloysite-sodium hyaluronate/poly(hydroxyethyl methacrylate) nanocomposites for colon cancer drug delivery," Appl. Clay Sci., vol. 97–98, pp. 33–42, Aug. 2014, doi: 10.1016/j.clay.2014.06.002.

[21] M. Zieba, J. L. Hueso, M. Arruebo, G. Martínez, and J. Santamaría, "Gold-coated halloysite nanotubes as tunable plasmonic platforms," New J. Chem., vol. 38, no. 5, pp. 2037–2042, Apr. 2014, doi: 10.1039/C3NJ01127E.

[22] "Highly dispersed polyamide-11/halloysite nanocomposites: Thermal, rheological, optical, dielectric, and mechanical properties - Prashantha - 2013 - Journal of Applied Polymer Science - Wiley Online Library." https://onlinelibrary.wiley.com/doi/abs/10.1002/app.39160 (accessed Dec. 29, 2020).

[23] Z. Rozynek, T. Zacher, M. Janek, M. Čaplovičová, and J. O. Fossum, "Electric-field-induced structuring and rheological properties of kaolinite and halloysite," Appl. Clay Sci., vol. 77–78, pp. 1–9, Jun. 2013, doi: 10.1016/j.clay.2013.03.014.

[24] Y. Zhang, J. Ouyang, and H. Yang, "Metal oxide nanoparticles deposited onto carbon-coated halloysite nanotubes," Appl. Clay Sci., vol. 95, pp. 252–259, Jun. 2014, doi: 10.1016/j.clay.2014.04.019.

[25] "Preparation of stearic acid/halloysite nanotube composite as form-stable PCM for thermal energy storage - Mei - 2011 - International Journal of Energy Research - Wiley Online Library." https://onlinelibrary.wiley.com/doi/abs/10.1002/er.1874 (accessed Dec. 29, 2020).

[26] M. Massaro, R. Noto, and S. Riela, "Past, Present and Future Perspectives on Halloysite Clay Minerals," Molecules, vol. 25, no. 20, p. 4863, Oct. 2020, doi: 10.3390/molecules25204863.

[27] B. Nandi, A. Goswami, and M. Purkait, "Removal of cationic dyes from aqueous solutions by kaolin: Kinetic and equilibrium studies," Appl. Clay Sci., vol. 42, no. 3–4, pp. 583–590, Jan. 2009, doi: 10.1016/j.clay.2008.03.015.

[28] P. Luo, Y. Zhao, B. Zhang, J. Liu, Y. Yang, and J. Liu, "Study on the adsorption of Neutral Red from aqueous solution onto halloysite nanotubes," Water Res., vol. 44, no. 5, pp. 1489–1497, Mar. 2010, doi: 10.1016/j.watres.2009.10.042.

[29] A. A. El-Zahhar, N. S. Awwad, and E. E. El-Katori, "Removal of bromophenol blue dye from industrial waste water by synthesizing polymer-clay composite," J. Mol. Liq., vol. 199, pp. 454–461, Nov. 2014, doi: 10.1016/j.molliq.2014.07.034.

[30] C. A. P. Almeida, N. A. Debacher, A. J. Downs, L. Cottet, and C. A. D. Mello, "Removal of methylene blue from colored effluents by adsorption on montmorillonite clay," J. Colloid Interface Sci., vol. 332, no. 1, pp. 46–53, Apr. 2009, doi: 10.1016/j.jcis.2008.12.012.

[31] M. Toor and B. Jin, "Adsorption characteristics, isotherm, kinetics, and diffusion of modified natural bentonite for removing diazo dye," Chem. Eng. J., vol. 187, pp. 79–88, Apr. 2012, doi: 10.1016/j.cej.2012.01.089.

[32] R. D. Combes and R. B. Haveland-Smith, "A review of the genotoxicity of food, drug and cosmetic colours and other azo, triphenylmethane and xanthene dyes," Mutat. Res., vol. 98, no. 2, pp. 101–248, Mar. 1982, doi: 10.1016/0165-1110(82)90015-x.

[33] Y. Anjaneyulu, N. Sreedhara Chary, and D. Samuel Suman Raj, "Decolourization of Industrial Effluents – Available Methods and Emerging Technologies – A Review," Rev. Environ. Sci. Biotechnol., vol. 4, no. 4, pp. 245–273, Nov. 2005, doi: 10.1007/s11157-005-1246-z.

[34] F. Dawood, C. K. Loo, and W. H. Chin, "Incremental on-line learning of human motion using Gaussian adaptive resonance hidden Markov model," in The 2013 International Joint Conference on Neural Networks (IJCNN), Dallas, TX, USA, Aug. 2013, pp. 1–7. doi: 10.1109/IJCNN.2013.6706826.

[35] F. M. D. Chequer et al., "The azo dyes Disperse Red 1 and Disperse Orange 1 increase the micronuclei frequencies in human lymphocytes and in HepG2 cells," Mutat. Res. Toxicol. Environ. Mutagen., vol. 676, no. 1–2, pp. 83–86, May 2009, doi: 10.1016/j.mrgentox.2009.04.004.

[36] U. Pagga and D. Brown, "The degradation of dyestuffs: Part II Behaviour of dyestuffs in aerobic biodegradation tests," Chemosphere, vol. 15, no. 4, pp. 479–491, Jan. 1986, doi: 10.1016/0045-6535(86)90542-4.

[37] S. Rani, M. Aggarwal, M. Kumar, S. Sharma, and D. Kumar, "Removal of methylene blue and rhodamine B from water by zirconium oxide/graphene," Water Sci., vol. 30, no. 1, pp. 51–60, Apr. 2016, doi: 10.1016/j.wsj.2016.04.001.

[38] T. Rager, A. Geoffroy, R. Hilfiker, and J. M. D. Storey, "The crystalline state of methylene blue: a zoo of hydrates," Phys. Chem. Chem. Phys., vol. 14, no. 22, pp. 8074–8082, 2012, doi: 10.1039/C2CP40128B.

[39] J. Gülen and F. Zorbay, "Methylene Blue Adsorption on a Low Cost Adsorbent—Carbonized Peanut Shell," Water Environ. Res., vol. 89, no. 9, pp. 805–816, Sep. 2017, doi: 10.2175/106143017X14902968254836.

[40] B. Lellis, C. Z. Fávaro-Polonio, J. A. Pamphile, and J. C. Polonio, "Effects of textile dyes on health and the environment and bioremediation potential of living organisms," Biotechnol. Res. Innov., vol. 3, no. 2, pp. 275–290, Jul. 2019, doi: 10.1016/j.biori.2019.09.001.

[41] K.-T. Chung, "Azo dyes and human health: A review," J. Environ. Sci. Health Part C Environ. Carcinog. Ecotoxicol. Rev., vol. 34, no. 4, pp. 233–261, Oct. 2016, doi: 10.1080/10590501.2016.1236602.

[42] M. Iqbal and J. Nisar, "Cytotoxicity and mutagenicity evaluation of gamma radiation and hydrogen peroxide treated textile effluents using bioassays," J. Environ. Chem. Eng., vol. 3, no. 3, pp. 1912–1917, Sep. 2015, doi: 10.1016/j.jece.2015.06.011.

[43] H. N. Bhatti, A. Jabeen, M. Iqbal, S. Noreen, and Z. Naseem, "Adsorptive behavior of rice bran-based composites for malachite green dye: Isotherm, kinetic and thermodynamic studies," J. Mol. Liq., vol. 237, pp. 322–333, Jul. 2017, doi: 10.1016/j.molliq.2017.04.033.

[44] M. Toor, B. Jin, S. Dai, and V. Vimonses, "Activating natural bentonite as a cost-effective adsorbent for removal of Congo-red in wastewater," J. Ind. Eng. Chem., vol. 21, pp. 653–661, Jan. 2015, doi: 10.1016/j.jiec.2014.03.033.

[45] T. S. Anirudhan and M. Ramachandran, "Adsorptive removal of basic dyes from aqueous solutions by surfactant modified bentonite clay (organoclay): Kinetic and competitive adsorption

isotherm," Process Saf. Environ. Prot., vol. 95, pp. 215–225, May 2015, doi: 10.1016/j.psep.2015.03.003.

[46] O. Duman, S. Tunç, and T. G. Polat, "Determination of adsorptive properties of expanded vermiculite for the removal of C. I. Basic Red 9 from aqueous solution: Kinetic, isotherm and thermodynamic studies," Appl. Clay Sci., vol. 109–110, pp. 22–32, Jun. 2015, doi: 10.1016/j.clay.2015.03.003.

[47] S. De Gisi, G. Lofrano, M. Grassi, and M. Notarnicola, "Characteristics and adsorption capacities of low-cost sorbents for wastewater treatment: A review," Sustain. Mater. Technol., vol. 9, pp. 10–40, Sep. 2016, doi: 10.1016/j.susmat.2016.06.002.

[48] L. W. Bruch, M. W. Cole, and E. Zaremba, Physical Adsorption: Forces and Phenomena. Courier Dover Publications, 2007.

[49] M. Králik, "Adsorption, chemisorption, and catalysis," Chem. Pap., vol. 68, no. 12, pp. 1625–1638, Dec. 2014, doi: 10.2478/s11696-014-0624-9.

[50] Y. Lu et al., "Mesoporous activated carbon materials with ultrahigh mesopore volume and effective specific surface area for high performance supercapacitors," Carbon, vol. 124, pp. 64–71, Nov. 2017, doi: 10.1016/j.carbon.2017.08.044.

[51] H. Molavi, A. Pourghaderi, and A. Shojaei, "Experimental Study on the Influence of Initial pH, Ionic Strength, and Temperature on the Selective Adsorption of Dyes onto Nanodiamonds," J. Chem. Eng. Data, vol. 64, no. 4, pp. 1508–1514, Apr. 2019, doi: 10.1021/acs.jced.8b01091.

[52] A. Kausar, H.N. Bhatti, Adsorptive Removal of Uranium from Wastewater: A Review, *J. Chem. Soc. Pak*, 2013.

[53] L. R. Marcelo, J. S. de Gois, A. A. da Silva, and D. V. Cesar, "Synthesis of iron-based magnetic nanocomposites and applications in adsorption processes for water treatment: a review," Environ. Chem. Lett., vol. 19, no. 2, pp. 1229–1274, Apr. 2021, doi: 10.1007/s10311-020-01134-2.

[54] A. Wang, W. Guo, F. Hao, X. Yue, and Y. Leng, "Degradation of Acid Orange 7 in aqueous solution by zero-valent aluminum under ultrasonic irradiation," Ultrason. Sonochem., vol. 21, no. 2, pp. 572–575, Mar. 2014, doi: 10.1016/j.ultsonch.2013.10.015.

[55] M. H. Entezari and T. R. Bastami, “Influence of ultrasound on cadmium ion removal by sorption process,” Ultrason. Sonochem., vol. 15, no. 4, pp. 428–432, Apr. 2008, doi: 10.1016/j.ultsonch.2007.05.004.

[56] M. H. Entezari and T. Soltani, “Cadmium and lead ions can be removed simultaneously from a binary aqueous solution by the sono-sorption method,” Ultrason. Sonochem., vol. 16, no. 4, pp. 495–501, Apr. 2009, doi: 10.1016/j.ultsonch.2008.12.001.

[57] W. Liu, J. Zhang, C. Cheng, G. Tian, and C. Zhang, “Ultrasonic-assisted sodium hypochlorite oxidation of activated carbons for enhanced removal of Co(II) from aqueous solutions,” Chem. Eng. J., vol. 175, pp. 24–32, Nov. 2011, doi: 10.1016/j.cej.2011.09.004.

[58] M. Dastkhoon, M. Ghaedi, A. Asfaram, A. Goudarzi, S. M. Mohammadi, and S. Wang, “Improved adsorption performance of nanostructured composite by ultrasonic wave: Optimization through response surface methodology, isotherm and kinetic studies,” Ultrason. Sonochem., vol. 37, pp. 94–105, Jul. 2017, doi: 10.1016/j.ultsonch.2016.11.025.

[59] Z. Eren, “Ultrasound as a basic and auxiliary process for dye remediation: A review,” J. Environ. Manage., vol. 104, pp. 127–141, Aug. 2012, doi: 10.1016/j.jenvman.2012.03.028.

[60] Y. Zhai et al., “Effective sonocatalytic degradation of organic dyes by using Er3+:YAlO3/TiO2–SnO2 under ultrasonic irradiation,” J. Mol. Catal. Chem., vol. 366, pp. 282–287, Jan. 2013, doi: 10.1016/j.molcata.2012.10.006.

[61] J. Wang et al., “Study on inorganic oxidants assisted sonocatalytic degradation of Acid Red B in presence of nano-sized ZnO powder,” Sep. Purif. Technol., vol. 67, no. 1, pp. 38–43, May 2009, doi: 10.1016/j.seppur.2009.03.005.

[62] W. Hamza, N. Dammak, H. B. Hadjltaief, M. Eloussaief, and M. Benzina, “Sono-assisted adsorption of Cristal Violet dye onto Tunisian Smectite Clay: Characterization, kinetics and adsorption isotherms,” Ecotoxicol. Environ. Saf., vol. 163, pp. 365–371, Nov. 2018, doi: 10.1016/j.ecoenv.2018.07.021.

[63] S. M. Yakout, M. R. Hassan, A. A. Abdeltawab, and M. I. Aly, "Sono-sorption efficiencies and equilibrium removal of triphenylmethane (crystal violet) dye from aqueous solution by activated charcoal," J. Clean. Prod., vol. 234, pp. 124–131, Oct. 2019, doi: 10.1016/j.jclepro.2019.06.164.

[64] M. Legodi and D. Waal, "The preparation of magnetite, goethite, hematite and maghemite of pigment quality from mill scale iron waste," Dyes Pigments, vol. 74, pp. 161–168, Dec. 2007, doi: 10.1016/j.dyepig.2006.01.038.

[65] M. C. Pereira, L. C. A. Oliveira, and E. Murad, "Iron oxide catalysts: Fenton and Fentonlike reactions – a review," Clay Miner., vol. 47, no. 3, pp. 285–302, Sep. 2012, doi: 10.1180/claymin.2012.047.3.01.

[66] A. Mahdieh, A. R. Mahdavian, and H. Salehi-Mobarakeh, "Chemical modification of magnetite nanoparticles and preparation of acrylic-base magnetic nanocomposite particles via miniemulsion polymerization," J. Magn. Magn. Mater., vol. 426, pp. 230–238, Mar. 2017, doi: 10.1016/j.jmmm.2016.11.091.

[67] M. M. Can, M. Coşkun, and T. Fırat, "A comparative study of nanosized iron oxide particles; magnetite (Fe3O4), maghemite (γ-Fe2O3) and hematite (α-Fe2O3), using ferromagnetic resonance," J. Alloys Compd., vol. 542, pp. 241–247, Nov. 2012, doi: 10.1016/j.jallcom.2012.07.091.

[68] M. Namdeo, "Magnetite Nanoparticles as Effective Adsorbent for Water Purification-A Review," Adv. Recycl. Waste Manag., vol. 02, no. 03, 2018, doi: 10.4172/2475-7675.1000135.

[69] "Vassilis Inglezakis, Stavros Poulopoulos - Adsorption, Ion Exchange and Catalysis_ Design of Operations and Environmental Applications (2006) (2006, Elsevier Science).pdf."

[70] P. Xu et al., "Use of iron oxide nanomaterials in wastewater treatment: A review," Sci. Total Environ., vol. 424, pp. 1–10, May 2012, doi: 10.1016/j.scitotenv.2012.02.023.

[71] A. Pratt, "Environmental Applications of Magnetic Nanoparticles," Front. Nanosci., vol. 6, pp. 259–307, Dec. 2014, doi: 10.1016/B978-0-08-098353-0.00007-5.

[72] R. A. Crane and T. B. Scott, "Nanoscale zero-valent iron: future prospects for an emerging water treatment technology," J. Hazard. Mater., vol. 211–212, pp. 112–125, Apr. 2012, doi: 10.1016/j.jhazmat.2011.11.073.

[73] G. Fadillah, S. P. Yudha, S. Sagadevan, I. Fatimah, and O. Muraza, "Magnetic iron oxide/clay nanocomposites for adsorption and catalytic oxidation in water treatment applications," Open Chem., vol. 18, no. 1, pp. 1148–1166, Sep. 2020, doi: 10.1515/chem-2020-0159.

[74] Z. Zhang and J. Kong, "Novel magnetic Fe3O4@C nanoparticles as adsorbents for removal of organic dyes from aqueous solution," J. Hazard. Mater., vol. 193, pp. 325–329, Oct. 2011, doi: 10.1016/j.jhazmat.2011.07.033.

[75] D. Wu, P. Zheng, P. Chang, and X. Ma, "Preparation and Characterization of Magnetic Rectorite/Iron Oxide Nanocomposites and Its Application for the Removal of the Dyes," Chem. Eng. J. - CHEM ENG J, vol. 174, pp. 489–494, Oct. 2011, doi: 10.1016/j.cej.2011.09.029.

[76] Y. Xie, D. Qian, D. Wu, and X. Ma, "Magnetic halloysite nanotubes/iron oxide composites for the adsorption of dyes," Chem. Eng. J., vol. 168, no. 2, pp. 959–963, Apr. 2011, doi: 10.1016/j.cej.2011.02.031.

[77] Q. Wu, C. Feng, C. Wang, and Z. Wang, "A facile one-pot solvothermal method to produce superparamagnetic graphene-Fe3O4 nanocomposite and its application in the removal of dye from aqueous solution," Colloids Surf. B Biointerfaces, vol. 101, pp. 210–214, Jan. 2013, doi: 10.1016/j.colsurfb.2012.05.036.

[78] A. Magdy, Y. O. Fouad, M. H. Abdel-Aziz, and A. H. Konsowa, "Synthesis and characterization of Fe 3 O 4 /kaolin magnetic nanocomposite and its application in wastewater treatment," J. Ind. Eng. Chem., vol. 56, pp. 299–311, Dec. 2017, doi: 10.1016/j.jiec.2017.07.023.

[79] H. Xu, J. Liu, P. Chen, Preparation of Magnetic Kaolinite Nanotubes for the Removal of Methylene Blue from Aqueous Solution. J Inorg Organomet Polym **28,** 790–799 (2018). https://doi.org/10.1007/s10904-017-0728-0

[80] F. S. Hashem, "REMOVAL OF METHYLENE BLUE BY MAGNETITE- COVERED BENTONITE NANO-COMPOSITE," *European Chemical Bulletin*, 2013, vol. 2, no 8, p. 524-529.

[81] J. Schneider et al., "Understanding TiO2 Photocatalysis: Mechanisms and Materials," Chem. Rev., vol. 114, no. 19, pp. 9919–9986, Oct. 2014, doi: 10.1021/cr5001892.

[82] A. Fujishima, T. N. Rao, and D. A. Tryk, "Titanium dioxide photocatalysis," J. Photochem. Photobiol. C Photochem. Rev., vol. 1, no. 1, pp. 1–21, Jun. 2000, doi: 10.1016/S1389-5567(00)00002-2.

[83] M. Castellote and N. Bengtsson, "Principles of TiO2 Photocatalysis," in Applications of Titanium Dioxide Photocatalysis to Construction Materials, Y. Ohama and D. Van Gemert, Eds. Dordrecht: Springer Netherlands, 2011, pp. 5–10. doi: 10.1007/978-94-007-1297-3_2.

[84] H. Xu, "Recent advances in TiO2-based photocatalysis," Journal of Materials Chemistry A, 2014, vol. 2, no 32, p. 12642-1266

[85] K. Maeda and K. Domen, "Photocatalytic Water Splitting: Recent Progress and Future Challenges," J. Phys. Chem. Lett., vol. 1, no. 18, pp. 2655–2661, Sep. 2010, doi: 10.1021/jz1007966.

[86] A. J. Haider, Z. N. Jameel, and I. H. M. Al-Hussaini, "Review on: Titanium Dioxide Applications," Energy Procedia, vol. 157, pp. 17–29, Jan. 2019, doi: 10.1016/j.egypro.2018.11.159.

[87] H. Park, Y. Park, W. Kim, and W. Choi, "Surface modification of TiO2 photocatalyst for environmental applications," J. Photochem. Photobiol. C Photochem. Rev., vol. 15, pp. 1–20, Jun. 2013, doi: 10.1016/j.jphotochemrev.2012.10.001.

[88] M. V. Dozzi and E. Selli, "Doping TiO2 with p-block elements: Effects on photocatalytic activity," J. Photochem. Photobiol. C Photochem. Rev., vol. 14, pp. 13–28, Mar. 2013, doi: 10.1016/j.jphotochemrev.2012.09.002.

[89] P. K. Labhane, S. H. Sonawane, G. H. Sonawane, S. P. Patil, and V. R. Huse, "Influence of Mg doping on ZnO nanoparticles decorated on graphene oxide (GO) crumpled paper like sheet and its high photo catalytic performance under sunlight," J. Phys. Chem. Solids, vol. 114, pp. 71–82, Mar. 2018, doi: 10.1016/j.jpcs.2017.11.017.

[90] "Metal oxide semiconducting interfacial layers for photovoltaic and photocatalytic applications | SpringerLink." https://link.springer.com/article/10.1007/s40243-015-0054-9 (accessed Jan. 18, 2021).

[91] G. Chen et al., "Highly efficient removal of U(VI) by a novel biochar supported with FeS nanoparticles and chitosan composites," J. Mol. Liq., p. 114807, Nov. 2020, doi: 10.1016/j.molliq.2020.114807.

[92] A. Gołąbiewska, M. P. Kobylański, and A. Zaleska-Medynska, "Fundamentals of metal oxide-based photocatalysis," in Metal Oxide-Based Photocatalysis, Elsevier, 2018, pp. 3–50. doi: 10.1016/B978-0-12-811634-0.00002-0.

[93] M. E. Borges, M. Sierra, E. Cuevas, R. D. García, and P. Esparza, "Photocatalysis with solar energy: Sunlight-responsive photocatalyst based on TiO2 loaded on a natural material for wastewater treatment," Sol. Energy, vol. 135, pp. 527–535, Oct. 2016, doi: 10.1016/j.solener.2016.06.022.

[94] G. Jing, Z. Sun, P. Ye, S. Wei, and Y. Liang, "Clays for heterogeneous photocatalytic decolorization of wastewaters contaminated with synthetic dyes: a review," Water Pract. Technol., vol. 12, no. 2, pp. 432–443, Jun. 2017, doi: 10.2166/wpt.2017.046.

[95] Y. Du and P. Zheng, "Adsorption and photodegradation of methylene blue on TiO2-halloysite adsorbents," Korean J. Chem. Eng., vol. 31, no. 11, pp. 2051–2056, Nov. 2014, doi: 10.1007/s11814-014-0162-8.

[96] B. Szczepanik, P. Rogala, P. M. Słomkiewicz, D. Banaś, A. Kubala-Kukuś, and I. Stabrawa, "Synthesis, characterization and photocatalytic activity of TiO2-halloysite and Fe2O3-halloysite nanocomposites for photodegradation of chloroanilines in water," Appl. Clay Sci., vol. 149, pp. 118–126, Dec. 2017, doi: 10.1016/j.clay.2017.08.016.

[97] P. Zheng, Y. Du, D. Liu, and X. Ma, "Synthesis, adsorption and photocatalytic property of halloysite-TiO2-Fe3O4 composites," Desalination Water Treat., vol. 57, no. 47, pp. 22703–22710, Oct. 2016, doi: 10.1080/19443994.2015.1137498.

[98] Z.-L. Cheng and W. Sun, "Preparation and Solar Light Photocatalytic Activity of N-Doped TiO2-Loaded Halloysite Nanotubes Nanocomposites," J. Mater. Eng. Perform., vol. 24, no. 10, pp. 4090–4095, Oct. 2015, doi: 10.1007/s11665-015-1699-3.

[99] D. Wu et al., "Improved photoelectric performance via fabricated heterojunction g-C3N4/TiO2/HNTs loaded photocatalysts for photodegradation of ciprofloxacin," J. Ind. Eng. Chem., vol. 64, pp. 206–218, Aug. 2018, doi: 10.1016/j.jiec.2018.03.017.

[100] R. Djellabi et al., "Photoactive TiO2–montmorillonite composite for degradation of organic dyes in water," J. Photochem. Photobiol. Chem., vol. 295, pp. 57–63, Dec. 2014, doi: 10.1016/j.jphotochem.2014.08.017.

[101] A. Mishra, M. Sharma, A. Mehta, and S. Basu, "Microwave Treated Bentonite Clay Based TiO2 Composites: An Efficient Photocatalyst for Rapid Degradation of Methylene Blue," J. Nanosci. Nanotechnol., vol. 17, no. 2, pp. 1149–1155, Feb. 2017, doi: 10.1166/jnn.2017.12674.

[102] A. Mishra, A. Mehta, M. Sharma, and S. Basu, "Impact of Ag nanoparticles on photomineralization of chlorobenzene by TiO2/bentonite nanocomposite," J. Environ. Chem. Eng., vol. 5, no. 1, pp. 644–651, Feb. 2017, doi: 10.1016/j.jece.2016.12.042.

[103] Y. Zhang, H. Gan, and G. Zhang, "A novel mixed-phase TiO2/kaolinite composites and their photocatalytic activity for degradation of organic contaminants," Chem. Eng. J., vol. 172, no. 2, pp. 936–943, Aug. 2011, doi: 10.1016/j.cej.2011.07.005.

Chapter II Materials and methods

This chapter is devoted to the description of the clay considered in this study and the synthesis methods (coprecipitation, hydrothermal) which allowed to obtain Fe_3O_4, TiO_2 and their doping with metals such as iron and silver which supported on HKDD3 clay. Afterward, we will discuss on fixation of iron sulfide FeS nanoparticles to use for photocatalytic. Then, we have described the range of instrumental techniques that we used to characterize, analyze and study the different materials elaborated as well as the conditions in which the measurements and the analyses were carried out. In the same way, we have presented the different and varied effects (concentration, mass loading, pH, and scavengers) used to study the photocatalytic activity, adsorption, and sono-sorption.

II.1 Materials

II.2 Kaolin Djebel Debbagh

The most common mineral in sediments is kaolin, which has a residual or hydrothermal origin. The geological conditions under which kaolin was generated, its mineralogical constitution, and its physical and chemical properties are all factors that influence its features. The major mineral phases of the kaolin group ($Al_2Si_2O_{10}(OH)_4$) are kaolinite and halloysite, which are composed of dioctahedral 1:1 layers **[1]**. Kaolin of Djebel Debbagh is located in the North-East of Algeria. It is known, and exploited kaolin for almost a century; it has been extracted from a mine located in Djebel Debbagh (wilaya of Guelma, Algeria). This deposit is hydrothermal it was suggested hydrothermal alteration at higher temperatures. The Djebel Debbagh deposit covers an area of 391 km^2. It is 17 Km away from the city of Hammam Debbagh **[2]**. Kaolin is generally of the color white and can have other colors (yellow, gray, red, or green). This coloration is due to the presence of impurities such as MgO, FeO(OH), CaO, Na_2O, K_2O, and TiO_2 **[3]**. Halloysite clay is a natural substance extracted from over the world, including in China and New Zealand **[4]**. Our halloysite was collected from the Djebel Debbagh region. The appropriate technique of purification will be determined by the kind of impurities present in the raw sample, as well as the functionalization or surface modification.

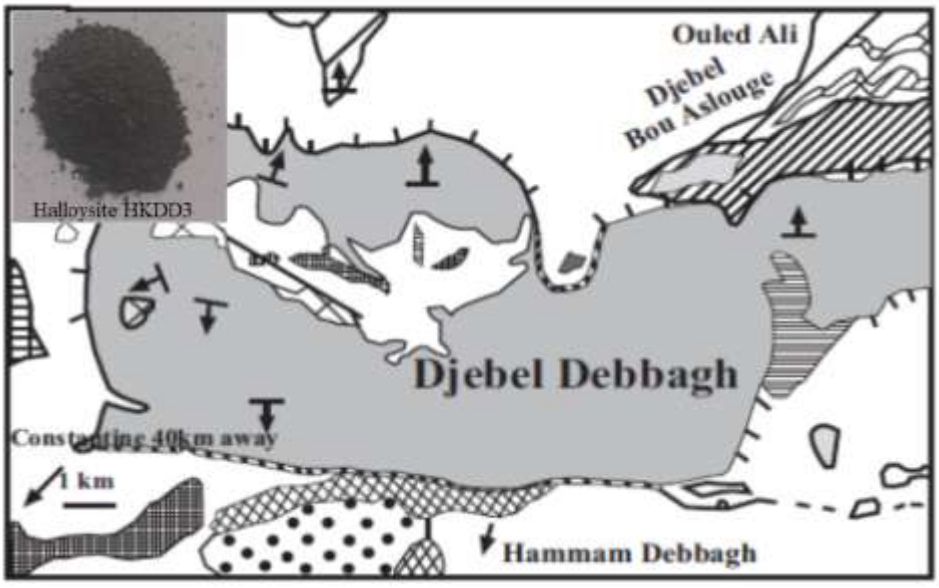

Figure II. 1 Geologic location of kaolin Djebel Debbagh

The kaolin of Djebel Debbagh (KDD3) is very rich in alumina 36 to 40%, but contains a high level of manganese oxide (MnO) ranging from 0.56 to 3% and gives a grey color to more than 80% of the deposit's kaolin. The quality of kaolin varies greatly with the extraction deposit. Some deposits give pure kaolin with a concentration of metal oxide impurities of less than 1% in weight and sometimes concentrations below 0.5% by weight (kaolin KDD1), this type of kaolin has a very white appearance **[5]**.

II.3 Purification of HKDD3 clay

The treatment of natural clay (HKDD3) consists of removing impurities (quartz, calcite, organic matter). The followed steps were performed:

- **Grinding**

An agate mortar was used to grind the block of clay into powder clay.

- **Purification with hydrogen peroxide**

In order to remove organic matter from clay, hydrogen peroxide (H_2O_2) purification can be carried out in a variety of ways. But in general, a large quantity of clay (HKDD3) is dispersed in 10% H_2O_2, and magnetically stirred for 30 minutes, then it was applied the sedimentation to get the clay which was in suspension **[6]**.

- **Drying in the oven**

The clay was dried in an oven at T=100°C for the removal of adsorbed water, for 4 hours.

II.4 Preparation of samples

II.4.1 Synthesis methods

Besides its advantages, each technique has certain limitations **(Table.II.1).** For the production of nanoparticles (magnetite, titanium dioxide) with the desired characteristics, the methods coprecipitation, sol-gel, hydrothermal and thermal decomposition **(figure II.2)** are employed **[7].** Firstly, due to the simplicity, cheap cost, and scalable yield, co-precipitation seems to be the most efficient approach.

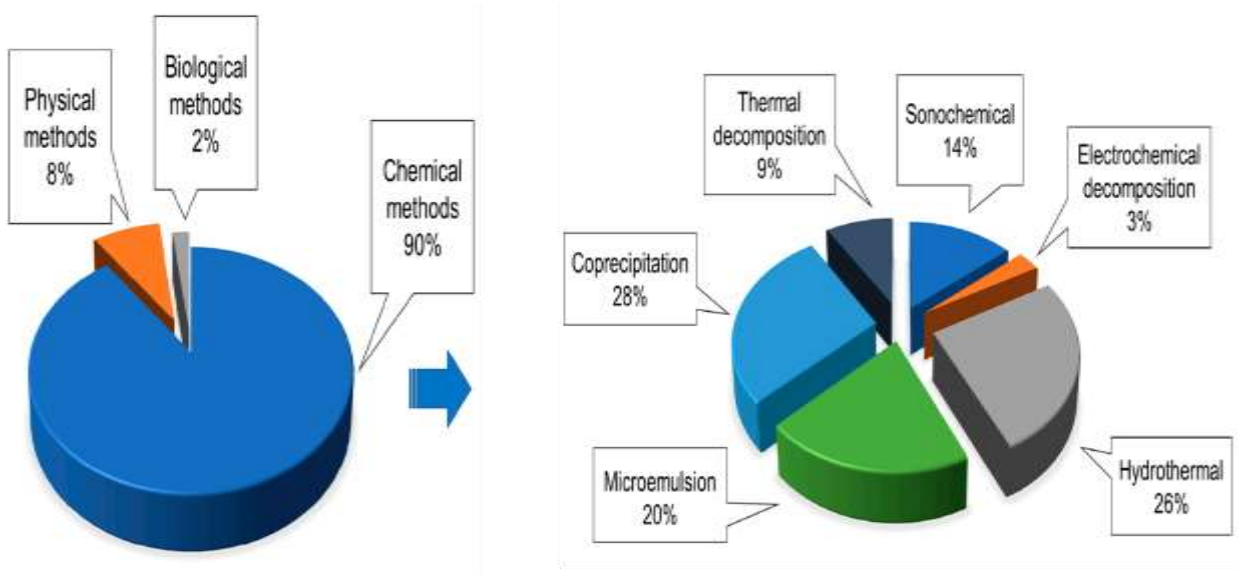

Figure II. 2 synthesis methods for oxides particles **[8]**

Nevertheless, agglomerations can also prevent and reduce the interfacial area of the nanoparticles. Moreover, this technique makes it difficult to generate tiny, crystalline nanoparticles. Secondly, sol-gel is seen as an alternate method with environmental conditions and good nanoparticle size control. Nevertheless, due to the significant amount of ethanol emitted throughout the process, this synthesis technique demands consideration of safety. Annealing at high temperatures and vacuum seems to be a costly therapy after treatment because of the significant energy consumption. Finally, the hydrothermal approach produces smaller sizes (less than 50 nm) at higher temperatures (200-300°C) and under high pressure, although hydrothermal techniques still need the development of facilities **[9]**. Finally, the thermal decomposition technique may be used to generate a tiny size distribution of particles with a high crystalline structure that is highly monodispersed. However, due to the higher temperature required throughout the process, it is also considered a costly approach **[10]**.

Table II. 1 Comparison of different chemical methods used in the preparation of magnetite nanoparticles

	Coprecipitation	**hydrothermal**	**Sol-gel**	**Thermal decomposition**
conditions	Easy, inert atmosphere	Relatively easy, higher pressure	Complicated, ambien	Complicated, inert atmosphere
Temperature (°C)	25 to 70	130 to 250	25 to 80	100 to 350
time	Minutes/hours	hours	Minutes/ hours	Days /hours
Size distribution	Relatively narrow	narrow	Very narrow	Very narrow
Shape control	Not well	Very well	well	Very well
Advantages	Easy and efficient - Safer procedure -High production efficiency - Lower cost	High Control of size and shape	High control of microstructure; internal structure homogeneity; size; shape and aspect ratio	-High crystallinity - Simple control of shape and particle size

II.4.2 Synthesis of Fe_3O_4-HKDD3 nanocomposite by coprecipitation

The **Fe_3O_4-KDD3** nanocomposite was synthesized by the co-precipitation method **[11]**. A quantity of HKDD3 clay was dispersed in 200 ml of a solution containing 1.16 g $FeCl_3.7H_2O$ and 0.5 g $FeSO_4$ dissolved in distilled water, under inert gas (N_2). A quantity of ammonia solution was added dropwise. The mixture was kept under stirring for 3h at 70°C after that the black prepared nanocomposite was watched several times and dried at 100 °C in the oven.

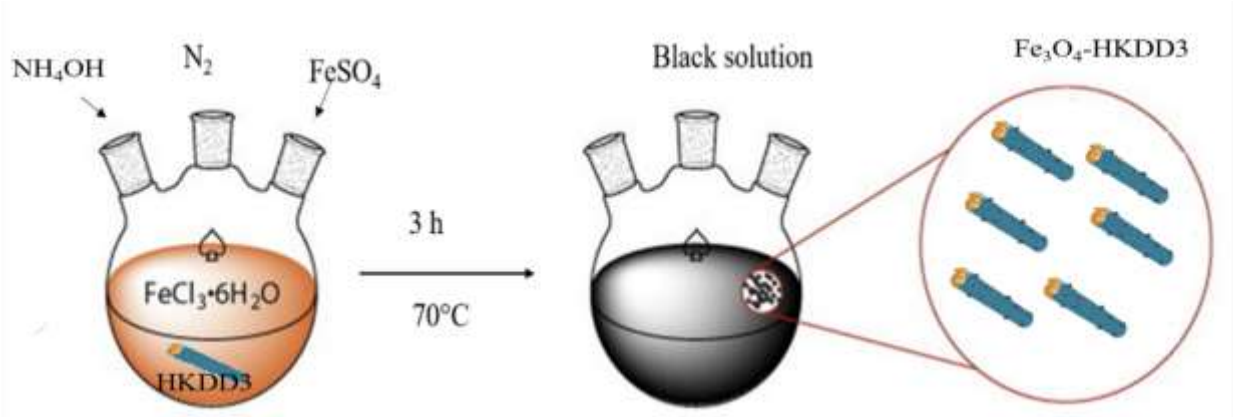

Figure II. 3 Schema of the preparation method of Fe_3O_4-HKDD3 nanocomposite

II.4.3 Synthesis of photocatalysts based on HKDD3 clay by solvothermal method

We elaborate different samples of TiO_2 and doped TiO_2 loaded on magnetic HKDD3 clay as cited below

1- 30% TiO_2- Fe_3O_4- HKDD3
2- 2%Ag doped TiO_2- Fe_3O_4- HKDD3
3- 1%Fe doped TiO_2- Fe_3O_4- HKDD3
4- 2%Ag- 1% Fe doped TiO_2- Fe_3O_4- HKDD3

II.4.3.1 30% TiO_2- Fe_3O_4- KDD3

An amount of M-HKDD3 was dispersed in 9.6 ml of isopropanol $(CH_3)_2CHOH$ to obtain the precursor solution under stirring for 15 min. then 0.4 ml of TTIP ($Ti[OCH(CH_3)_2]_4$) was added dropwise. Next, The solution was then transferred to a Teflon-lined stainless steel autoclave and solvothermal treated for 24 hours at 160 °C. The precipitates were rinsed with deionized water and ethanol several times after cooling to room temperature before being dried in a vacuum oven at 60 °C.

In the case of doping with iron and silver the same procedure with adding the amount of silver nitrate and iron nitrate after the addition of titanium precursor.

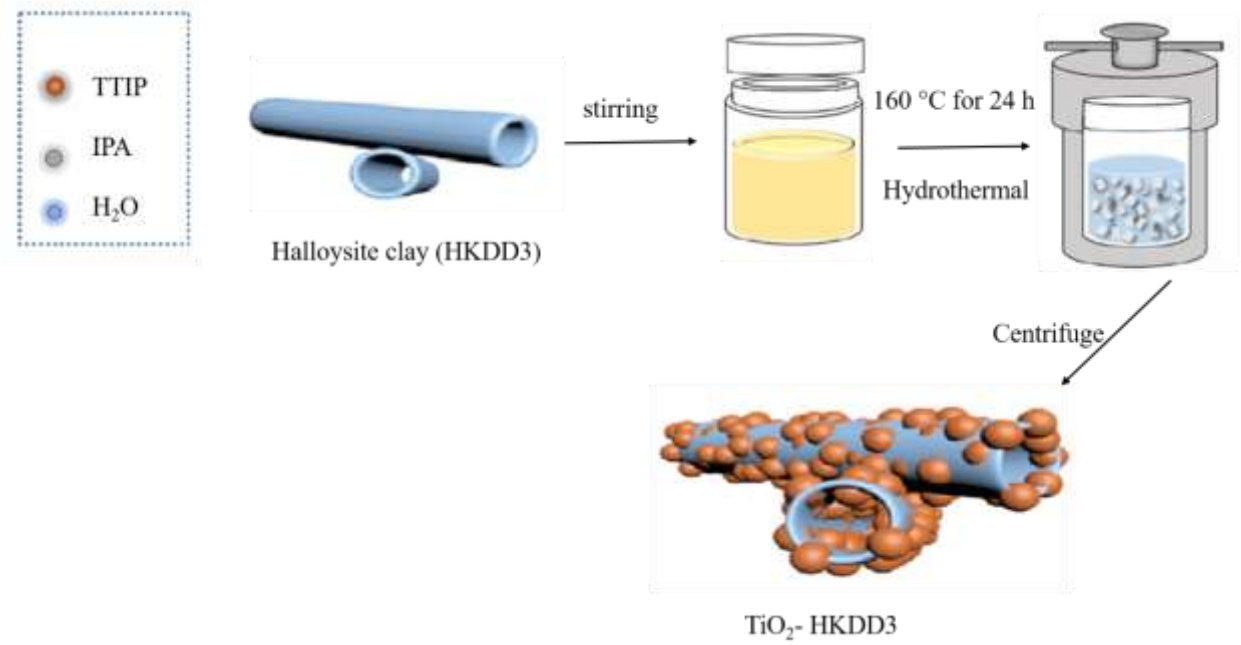

Figure II. 4 Schema of the preparation of photocatalyst TiO_2- HKDD3

II.4.4 Synthesis of FeS-HKDD3 catalyst

A simple hydrothermal technique was used to make catalyst. 0.9 g of $FeSO_4.7H_2O$ was dissolved in 20 ml distilled water and dropped into a solution containing 0.5 g of HKDD3 clay distributed in 30 ml for 30 minutes while stirring. After that, 2.3 g of thiourea were dissolved in 20 ml of distilled water. The mixture stayed under stirring for 1 h and then transferred to an autoclave reactor for 18 h at 180°C. The as-prepared powder was washed several times with distilled water then it was centrifuged and dried in the oven at 80°C. The FeS nanoparticles were synthesized with the same method without adding HKDD3 clay.

Firstly, Fe^{2+} was absorbed through electrostatic interactions on the halloysite surface when $FeSO_4$ aqueous solution was applied dropwise under magnetic stirring into the halloysite clay suspension (stage I). Secondly, under continuous magnetic stirring, $(NH_2)_2CS$ solution was added dropwise into the mixture to be distributed homogeneously (stage II). At the beginning of reaction at 180°C, H_2S was produced by $(NH_2)_2CS$ hydrolytic reaction and reacted with Fe^{2+} via the following equations (stage III) to form FeS particles:

$$\mathbf{(NH_2)_2CS + 2H_2O = CO_2 + H_2S + 2NH_3} \quad \mathbf{(1)}$$

$$\mathbf{Fe^{2+} + S^{-2} = FeS} \quad \mathbf{(2)}$$

II.5 Preparation of methylene blue solution

In this work, we used one type of pollutant, which is cationic dye methylene blue as an organic pollutant. The solution is made by dissolving the appropriate quantity of the substance in distilled water without first purification. The pH was adjusted to different values using hydrochloride acid or hydroxide sodium. The characteristic of methylene blue dye is shown in **Table II.2**

Table II. 2 physicochemical properties of methylene blue dye

Dye	Methylene blue
Formula	$C_{16}H_{18}ClN_3S$
Molecular mass (g/mol)	319.85
λ_{max} (nm)	663

The maximum absorption of MB is 663 nm. The choice of this cationic dye is justified, by its adsorption on the clay minerals because of the electrostatic attraction between the negatively charged clay particles and the cationic entities of the dye.

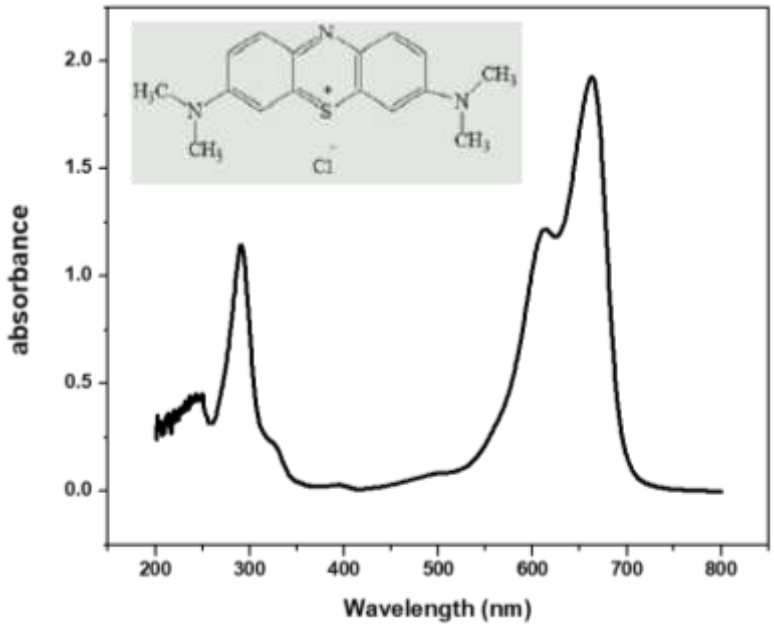

Figure II. 5 Absorption spectra of methylene blue dye (C=10 $mg.L^{-1}$).

II.6 Methods of measurement and analysis

II.6.1 UV-visible spectrophotometry

UV-visible spectrophotometry is a method of quantitative analysis that allows to measure the absorbance of a chemical substance dissolved in a solution and can be used to follow the kinetics of its discoloration using a previously calibrated spectrophotometer. The concentration of a substance is proportional to its absorbance according to the Beer-Lambart law, it is evaluated using calibration curves.

$$\mathbf{A = \varepsilon\, l\, C} \qquad \textbf{(3)}$$

With: A: absorbance, ε: specific extinction coefficient of the solute. L: the thickness of the optical cell and C: concentration of the solute. The wavelength of the absorption maximum of MB (λmax) is 663 nm.

The substrate removal rate was calculated using the following relationship: C_0-C_t

$$\mathbf{R}(\%) = \frac{(\mathbf{C0-Ct})}{\mathbf{C0}} * \mathbf{100} \qquad \textbf{(4)}$$

II.6.2 Measurement of total organic carbon

Total organic carbon (TOC) is an important parameter for the evaluation of the organic load of water. TOC measurement allows the user to know the total organic carbon content present in a sample that contains different organic compounds. The usefulness of this measurement is to check whether the pollutants undergo partial or total mineralization after their treatment. Indeed, its concept is to use a powerful oxidant in an acid media to fully oxidize all organic materials into CO_2 and H_2O, with the amount of CO_2 produced is measured by an infrared detector. The TOC content was tested to confirm the mineralization of the contaminants following photocatalytic treatment. The total organic carbon (TOC) content of the treated solutions was used to estimate the level of mineralization. The TOC of solutions was determined using CO_2 produced by catalytic combustion at a high temperature (680°C) **[12].**

The TOC removal (mineralization efficiency) and MB discoloration efficiency at the generic irradiation time were evaluated using the following relationship:

$$\textbf{Mineralization efficiency}\,(\mathbf{t}) = \left(\mathbf{1} - \frac{\mathbf{TOC(t)}}{\mathbf{TOC_0}}\right)\mathbf{100} \qquad \textbf{(5)}$$

Where TOC(t) is the total organic carbon at the generic irradiation time (mg/l), TOC_0 is the initial total organic carbon (mg/l), c(t) is the MB concentration at the generic irradiation time (mg/l), c_0 is the initial MB concentration (mg/l).

II.7 Procedure of adsorption MB

To conduct the dye adsorption studies on the nanocomposite, 100 mg of magnetic HKDD3 was added to a volume of 100 mL of each starting dye concentration and stirred until equilibrium was reached. A sample was separated by centrifugation and analyzed in a UV-Vis spectrophotometer. The adsorption capacity at time t, q_t (mg/g) was calculated using the following expression:

$$q_t = \frac{(C_0 - C_t) * V}{m} \quad \textbf{(6)}$$

Where C_o and C_t are the initial concentration and the concentration at time (t) of adsorbate solution respectively (mg/L); V is the volume of dye solution (L) and m is the weight of the used adsorbent (g). In the sono-adsorption process, an ultrasonic bath (D-78224 Singen/Htw; typ S30, Germany) was used to produce the ultrasound waves at a fixed frequency of 50/60 Hz and an ultrasonic power of 80 W.

II.8 Parameters study on adsorption process of MB dye

II.8.1 Effect of contact time and initial concentration

At different initial dye concentrations (10, 20, 30, and 40 $mg.L^{-1}$), 0.1 g of adsorbent was added to solutions at room temperature and free pH. The mixture was kept under stirring at different intervals of time ranging from 0 to 120 min.

II.8.2 Effect of pH

To study the effect of pH on MB adsorption on M-HKDD3, experiments were carried out on 30 mg/L initial dye concentration at varying pH ranges of 4.0 to 9.0 in presence of 0.1g adsorbent at room temperature (±25°C). The pH of the MB solution was adjusted using 1 $mol.L^{-1}$ of HCl and1 $mol.L^{-1}$ of NaOH.

II.8.3 Effect of temperature

To study the influence of thermodynamic parameters, a series of experiments were conducted at different temperatures in the range of (303-323 K). The entropy (ΔS), enthalpy (ΔH), and Gibbs free energy (ΔG) were calculated by the following equations.

$$\Delta G° = -RT\ln K_e \quad (7)$$

$$\Delta G° = \Delta H° - T\Delta S° \quad (8)$$

$$\ln K_e = -\frac{\Delta H°}{RT} + \frac{\Delta S°}{R} \quad (9)$$

$$K_e = \frac{qe}{Ce} \quad (10)$$

Where R is the universal gas constant (8.314 J/mol K) and T is the absolute temperature (K). K_e is the adsorption equilibrium constant.

II.8.4 Isotherm models

An adsorption isotherm is a variation of the adsorbed quantity qe ($mg.g^{-1}$) on a solid as a function of the Ce concentration ($mg.L^{-1}$) i.e. the interaction adsorbate with adsorbent. The isotherms model was obtained by varying the initial concentrations of MB (from 5 to 40 $mg.L^{-1}$) at room temperature and free pH. In this study, the adsorption equilibrium is analyzed by application of the Langmuir and Freundlich models which are commonly used **[13]**

The **Langmuir model** depends on the assumption of monolayer adsorption. Where that the adsorption of a specific atom on given adsorption does not rely upon the control of the following adsorption site. The Langmuir model was expressed by the following equation:

$$q = \frac{q_e K_l C_e}{1 + K_l C_e} \quad (11)$$

Where; C_e is the equilibrium concentration (mg/L); qe is the quantity adsorbed at equilibrium (mg/g); K_l is the equilibrium constant relative to the Langmuir model;

The **Freundlich** equation is used to describe heterogeneous systems, where the interaction between molecules adsorbed in solid bulk is not limited to the formation of a monolayer.
It is an empirical equation, characterized by the factor 1/n of heterogeneity. It can be described by the following equation (nonlinear) **[14]:**

$$qe = K_f Ce^{1/n} \quad (12)$$

Where; K_F is the equilibrium constant relative to the Freundlich model (L/g); 1/n is the heterogeneity factor is ranging between 0.1 and 1.

II.8.5 Kentic models

The kinetic models provide us with information about the adsorption mechanism and the mode of solute transfer from the liquid phase to the solid phase. The literature reported several models such as the pseudo-first-order model (PFO), the pseudo-second-order kinetic model (PSO), and Weber and Morris model or intraparticle diffusion model. The nonlinear plots of data regression of PFO and PSO were represented to determine kinetics.

The adsorption rate constant K_1 is given by the following relation:

$$\frac{dq}{dt} = K_1 (q_e - q) \quad \textbf{(13)}$$

In the pseudo-second-order model, the adsorption rate constant K_2 is given by the following relation: $K_2(qe-q)^2$

$$\frac{dq}{dt} = K_2 (q_e - q)^2 \quad \textbf{(14)}$$

Where; q_e is the quantity of dye adsorbed at equilibrium (g/mg); q_t is the quantity of dye adsorbed at time t (g/mg); t is the contact time (min); K_1 is the adsorption rate constant for the pseudo-first-order (min^{-1}); K_2 is the adsorption rate constant for pseudo-second-order (g/mg.min).

The intra-particle model was defined by the equation $q_t = K_{id} * t^{0.5} + C.$ **(15)**

Where qt is the amount of adsorbate per unit weight of adsorbent.

C (mg/g) is a constant which gives information about the boundary layer and Kid ($mg.g^{-1}.min^{-1/2}$) is the intraparticle rate constant and t is time contact.

II.9 Photocatalytic performance of methylene blue degradation

A Pyrex cylindrical reactor (ID = 2.6 cm, L_{TOT}= 41 cm, and V_{TOT}= 200 mL) with an air distributor device (flowrate of 142 N cm^3 min) was used for the photocatalytic studies. The visible-LED strip (nominal power: 10 W; provided by LED lighting hut; emission in the range 400–800 nm; light intensity: 13 mW cm^{-2}) was placed against the photoreactor's exterior surface. To achieve the adsorption-desorption phenomena, the MB dye solution was exposed to visible light for 3 hours after being kept in the dark for 2 hours. About 3 mL of the solution was removed from the photoreactor and centrifuged to remove the catalyst at various intervals. The aqueous solution was examined using a UV-Vis spectrophotometer (Thermo Scientific Evolution 201). The highest absorbance value at 663nm was used to evaluate the elimination of MB dye in further detail. The total organic carbon

(TOC) content of the treated solutions was used to estimate the mineralization level. The TOC of solutions was determined using CO_2 produced by catalytic combustion at a high temperature (680°C) **[12].**

$$\textbf{Discoloration efficiency}\ (t) = \left(1 - \frac{c(t)}{c_0}\right) 100 \quad \textbf{(16)}$$

The Langmuir–Hinshelwood model is usually used to describe the kinetics of the photocatalytic process **[15]**. The derivation is based on the degradation rate (*r*), which is expressed as follows:

$$r = -\frac{dc}{dt} = \frac{k_r K_{ad} c}{1 + K_{ad} c} \quad \textbf{(17)}$$

Where k_r, K_{ad}, and *c* are the intrinsic kinetic constant, adsorption equilibrium constant and, dye concentration, respectively.

Assuming that adsorption is weak and the concentration of compounds is low, the equation above can be simplified to the first-order kinetics expression with an apparent discoloration kinetic constant (K_{app}):

$$\ln\left(\frac{c_0}{c}\right) = k_r K_{ad} t = K_{app} t \quad \textbf{(18)}$$

The value of the apparent discoloration kinetic constant can be calculated by the slope of the zero-passing straight line obtained from plotting $\ln(c_0/c)$ vs time t.

II.10 Parametric study of photocatalytic study

A parametric study was carried out to investigate the influence of different parameters on the efficiency of the photocatalytic reaction, as the catalyst dose, the pH of the solution, and the initial pollutant concentration (Co).

II.10.1 Effect of the catalyst dose

According to the literature, the efficiency of the photocatalytic reaction is influenced by the variation of the catalyst dose. Therefore, knowledge of the optimal dose is important. The influence of the catalyst dose varying from 0.3 to 1.25 $g.L^{-1}$ for photocatalyst on the photodegradation of the MB dye with a Co concentration fixed at 7 $mg.L^{-1}$ and free pH (without adjustment) has been studied.

II.10.2 Effect of the pH of the solution

The effect of pH on the efficiency of the photodegradation process is an important parameter to study. During our study the influence of pH was studied for values set at 4; 5; 6.7; 8. a Co concentration of 7 $mg.L^{-1}$ and an optimal dose of 0.9 $g.L^{-1}$ of the photocatalyst. The pH adjustment was performed by adding HCl and NaOH (0.1 or 1 M).

II.10.3 Effect of the initial concentration of the pollutant (C_0)

It is interesting to study the influence of the variation of the initial Co concentration on the efficiency of photocatalytic degradation. This approach was carried out by maintaining the other parameters (pH and catalyst dose) at their optimal values for different Co values ranging from 7 to 28 $mg.L^{-1}$. The experiments were conducted under visible light radiation, at free pH, and a catalyst mass of 0.9 $g.L^{-1}$.

II.10.4 Effect of scavengers

When exposing a photocatalyst to radiation, several active species are generated, namely: holes (h^+), electrons (e-), radicals; hydroxyl ($OH^\bullet$), and superoxide radicals (O_2^-).

We used four inhibitors (scavengers). The role of these inhibitors is to trap these species and subsequently inhibit the photocatalytic reaction. 2-propanol, Benzoquinone, and Na_2EDTA were used to trap respectively: $OH^\bullet$, $O_2^{-\bullet}$ and h^+. These experiments were carried out at a Co concentration of 7 $mg.L^{-1}$, with mass catalyst 0.9 $g.L^{-1}$, at pH 6.7.

II.11 Characterization methods

Different techniques have been used to characterize raw Kaolin (KDD3) and modified Kaolin, including X-ray diffraction (XRD) to identify phase and structure, diffuse reflectance to measure the optical gap (UV-DRS), scanning electron microscopy (SEM-EDS), transmission electron microscopy (TEM) to visualize morphology, infrared spectroscopy (FTIR), and XPS to detect chemical bona fide vibrations. As well as the BET analysis to know the specific surface area and pores of prepared materials. These techniques and their principles of operation are described as follows:

II.11.1 X-ray diffraction

In materials research, X-ray diffraction is perhaps the most extensively used method. It is based on the matter's diffraction of X-rays. It only works on crystalline materials and allows the size of the lattice and crystallites to be determined. This technique is based on a set of reticular planes (hkl)

that are positioned at an angle to the incident beam **(Figure II.6)**. By observing lines from which the reticular distances d_{hkl}, typical of a specific crystalline substance, can be calculated, this is converted into the diffractogram, which represents intensity as a function of angle. Small angle XRD spectra demonstrate the d-spacing and Bragg's law is used for the calculation. The small-angle peak shifts towards the lower 2θ indicate an increase in d-spacing. Wide-angle XRD is used to find the crystallinity of the clay mineral and the semiconductors along with their crystallite size using the Scherrer equation. Peaks of different phases, complexes, and peak shifts for modifications as doping and ion treatment can also be observed by XRD spectra.

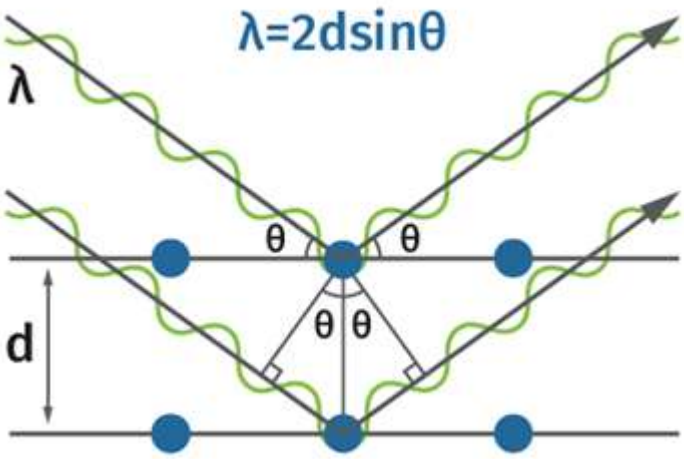

Figure II. 6 schema of Bragg's law.

Experimental conditions

X-ray diffraction (XRD) patterns were collected on a PANanalytical X'Pert Pro automated diffractometer. Powder patterns were recorded in Bragg-Brentano reflection configuration by using a Ge(111) primary monochromator (Cu Kalfa1) and the X'Celerator detector with a step size of 0.0167º (2θ). The powder patterns were recorded between 4 and 70 º in 2θ with an equivalent counting time of ~60 s/step. The crystalline phases were identified by using the diffraction patterns of the joint committee on powder diffraction standards (JCPDS) of the international center for diffraction Data (ICDD).

II.11.2 Microscopy

Electron microscopes such as scanning electron microscope (SEM) and transmission electron microscope (TEM) are used to obtain direct evidence related to size, shape, morphology, elemental composition with distribution, lattice structures, etc.

II.11.2.1 Scanning Electron Microscopy (SEM)

This approach is based on the interaction between an electron beam produced by the electron cannon and a crystalline matrix, the secondary beam of which is rasterized with the electron beam of a cathode ray tube (CRT or television image tube) which is attracted by the collector. The topography (surface feature) and morphology (shape and size) of samples may be determined using this method. SEM provides surface morphology information, allowing the distribution of semiconductor material over the clay to be observed. At the same time, particle agglomeration or inappropriate loading can be verified.

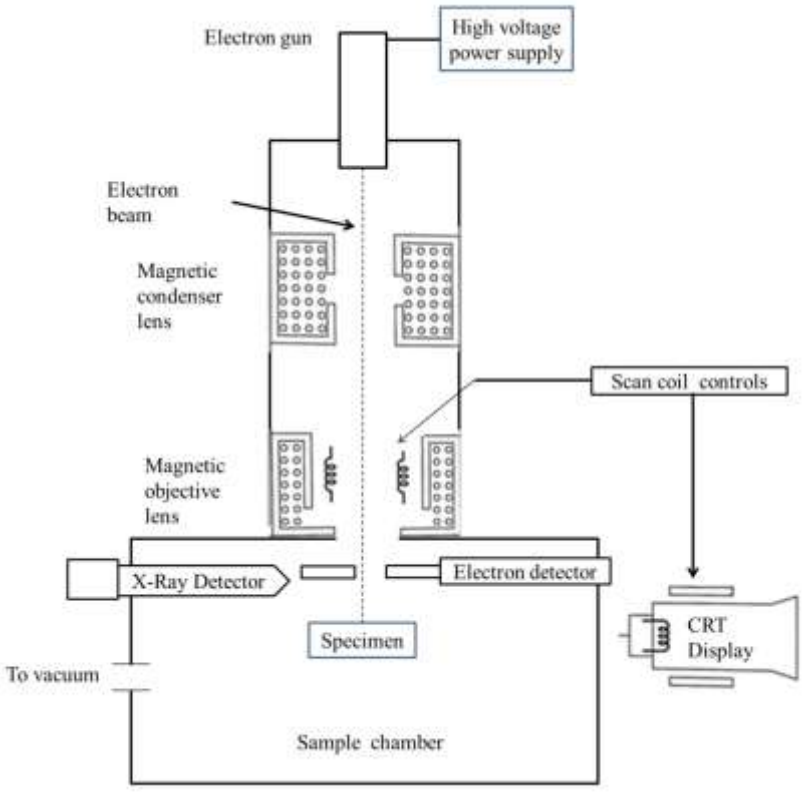

Figure II. 7 Schematic diagram of SEM-EDX instrument **[16].**

II.11.2.2 Energy Dispersive X-ray Spectroscopy (EDX)

EDX is used to analyze the chemical composition of a sample. The system is coupled to the SEM. The principle of microanalysis is based on the detection of X-photons emitted by the sample under electron bombardment. The electrons of the incident beam interact with the core electrons of the sample atoms and when an atom is ionized, a very fast radiative excitation occurs. An electron from the upper layers of the atom joins the unoccupied layer of lower energy. In order to maintain an overall energy balance, an X-photon is emitted simultaneously. The energy of this photon is characteristic of the ionized atom. The X emission spectrum is, therefore, representative of the chemical constituents of the sample.

II.11.2.3 Transmission electronic microscopy (TEM)

Transmission electron microscopy (TEM) has been widely utilized to determine the size of tiny metal particles. The electron microscope employs an electron beam (1–40 keV); the electron cannon is made up of a tungsten anode and beam aperture control. At the point where the electron beam impacts the specimen, an electron lens system may concentrate it with an extremely tiny cross-section. The transmitted electrons travel through another set of electron optics before falling on a fluorescent screen, which produces an image that may be captured on photographic film. The particle size and distribution are shown in TEM images. The picture is projected onto a screen, and particles of various sizes are counted.

- **Experimental conditions**

Field Emission (FE) - Scanning electron microscopy (SEM) images were obtained by using an FEI, Helios Nanolab 650, and the Energy dispersive spectroscopy (EDS) and High-resolution transmission electronic microscopy (HRTEM) images by using an FEI, Talo.

II.11.3 The Fourier transforms infrared spectroscopy (FT-IR)

The basic principle of infrared (IR) spectrometry is based on the interaction of the IR electromagnetic radiation with the material at different frequencies. In the spectrum general electromagnetic radiation, the field of IR radiation is included between 12800 and 10 cm^{-1} which breaks down into three parts: near, medium, and far IR. We are particularly interested in the mid-infrared (MIR) region which corresponds to the wavenumber range [4000 - 400 cm^{-1}]. When a molecule is irradiated with IR radiation, it can absorb partially and selectively this radiation. As a result, it is excited (vibrational and rotational energy) which are modified with an increase of its

amplitudes. The energy of the incident IR radiation is decreased after the interaction, which leads to the appearance of an absorption band at this frequency. The absorbed energy is characteristic of each chemical bond of the sample analyzed.

- **Experimental conditions**

The system used was a Bruker Vertex70 spectrometer. Samples were recorded without prior sample preparation. A standard spectral resolution of 4 cm^{-1} in the spectral range 4000-500 cm^{-1} was used for spectrum acquisition.

II.11.4 Brunauer-Emmett-Teller (BET) surface area analysis:

In catalytic applications, the surface area of a material is crucial. The idea is based on Braunauer, Emmett, and Teller's isothermal theory of adsorption isotherm in multilayer gas adsorption, which was developed in 1938. The entire surface area per unit mass of the product accessible to atoms and molecules is known as the specific surface area. The physical principle for the determination of the mass area is based on the adsorption of gas at low temperatures. The phenomenon of adsorption is achieved thanks to weak links (Van der Waals forces) on the surface of the solid; these forces act on the surface of the solid to the outside, especially on gas molecules surrounding the sample to be analyzed.

- **Experimental condition**

The particles' specific surface was estimated by measuring nitrogen (N_2) absorption-desorption isotherms and applying the theory proposed by Brunauer-Emmett-Teller (B.E.T) on a Micromeritics ASAP 2010 apparatus. After a degassing at 300°C under vacuum for 2 h, the samples were cooled and submitted to adsorption-desorption analysis.

II.11.5 UV vis DRS:

For powdered or crystalline materials, diffuse reflectance is an effective sampling technique. This method is beneficial for identifying the catalyst's absorption edge. In the case of atoms, ions, or molecules, it provides information on the electronic transition between orbitals or bands. The formation of the clay/catalyst is often established when the absorption spectra of the clay semiconductor nanocomposite match those of the semiconductor material. In addition, shifting the absorbance spectra as a function of time can be used to determine the time required for the complete formation of the semiconductor material on the clay. The shift of the absorbance peak can also be used to validate the doping of another element.

- **Experimental conditions**

High-performance UV-Vis-NIR spectrometer. It provides excellent resolution throughout the UV-Vis-NIR spectrum, from 170 to 3300 nm. It has a double-plane Littrow monochromator; double diffraction grating of 1200 lines/mm with the blaze at 250 nm and 300 lines/mm blaze at 1192 nm; automatic polarizers; and four detectors consisting of one four detectors consisting of a photomultiplier tube, a PbS detector, and the Si/InGaAs multilayer Si/InGaAs detector.

This equipment is complemented by a wide range of sampling accessories:

- Kit of cells for powder.
- Film holder.
- Solid sample holders.
- Cell holders for standard and specialized cuvettes.

Diffuse reflectance spectra were measured in powder using BaSO4 as a blank. The support used was of small size, as well as the slit used.

II.11.6 X-ray photoelectron spectroscopy (XPS):

Surface examination using X-ray photoelectron spectroscopy is a non-destructive method. X photons produced by a monochromatic Mg or Al source excite the elements of the surface layers. Each element's photoelectrons reflect the chemical environment in which it exists. X-ray photoelectron spectroscopy (XPS) has long been known as a valuable technique for detecting chemical species on solid surfaces. The catalyst surface may be characterized directly using this method. Before and after the reaction test, it provides information on the elemental composition and oxidation states of the elements on the solid surface.

- **Experimental conditions**

XPS analyses were performed using a K-alpha spectrometer from Thermo Scientific using an Al Kα anticathode at 1486.6 eV. The spectra are recalibrated relative to the free carbon used as a reference (284.7 0.1 eV). Semiquantitative analyses could also be performed.

All of these characterization tests were performed at Central Research Support Service (SCAI) in Malaga, Spain.

II.12 Conclusion

During this chapter**,** we have tried to outline the characteristics of used samples and devices, as well as the methods of preparation and characterization of nanomaterials. On the other hand, we have described the experimental protocols as adsorption and photocatalysis processes. Besides, the factors include pH, mass loading, concentration, and temperature that influence on the removal of dyes from an aqueous solution.

References

[1] H. G. Dill, "Kaolin: Soil, rock and ore," *Earth-Science Reviews*, vol. 161, pp. 16–129, Oct. 2016, doi: 10.1016/j.earscirev.2016.07.003.

[2] B. Nait Amara, D. E. Aissa, S. Maouche, M. Braham, D. Machane, and N. Guessoum, "Hydrothermal alteration mapping and structural features in the Guelma basin (Northeastern Algeria): contribution of Landsat-8 data," *Arab J Geosci*, vol. 12, no. 3, p. 94, Feb. 2019, doi: 10.1007/s12517-019-4224-4.

[3] K. Ibrahim, M. Moumani, and S. Mohammad, "Extraction of γ-Alumina from Low-Cost Kaolin," *Resources*, vol. 7, no. 4, p. 63, Sep. 2018, doi: 10.3390/resources 7040063.

[4] E. Joussein, S. Petit, J. Churchman, B. Theng, D. Righi, and B. Delvaux, "Halloysite clay minerals — a review," *Clay miner.*, vol. 40, no. 4, pp. 383–426, Dec. 2005, doi: 10.1180/0009855054040180.

[5] M. Laraba, "Characterization of Algerian kaolins for utilization as a raw material in electrical insulators," *Cerâmica*, vol. 65, no. 374, pp. 267–273, Jun. 2019, doi: 10.1590/0366-69132019653742556.

[6] K.-M. Ng, Y.-T. R. Lau, C.-M. Chan, L.-T. Weng, and J. Wu, "Surface studies of halloysite nanotubes by XPS and ToF-SIMS," *Surface and Interface Analysis*, vol. 43, no. 4, pp. 795–802, 2011, doi: https://doi.org/10.1002/sia.3627.

[7] A.-G. Niculescu, C. Chircov, and A. M. Grumezescu, "Magnetite nanoparticles: Synthesis methods – A comparative review," *Methods*, p. S1046202321001109, Apr. 2021, doi: 10.1016/j.ymeth.2021.04.018.

[8] S. Ansari *et al.*, "Magnetic Iron Oxide Nanoparticles: Synthesis, Characterization and Functionalization for Biomedical Applications in the Central Nervous System," *Materials*, vol. 12, no. 3, p. 465, Feb. 2019, doi: 10.3390/ma12030465.

[9] H. Bouakaz, M. Abbas, R. Brahimi, and M. Trari, "Physical properties of the delafossite CuCoO2 synthesized by co-precipitation /hydrothermal route," *Materials Science in Semiconductor Processing*, vol. 136, p. 106132, Dec. 2021, doi: 10.1016/j.mssp.2021.106132.

[10] A. V. Rane, K. Kanny, V. K. Abitha, and S. Thomas, "Methods for Synthesis of Nanoparticles and Fabrication of Nanocomposites," in *Synthesis of Inorganic Nanomaterials*, Elsevier, 2018, pp. 121–139. doi: 10.1016/B978-0-08-101975-7.00005-1.

[11] Y. Xie, D. Qian, D. Wu, and X. Ma, "Magnetic halloysite nanotubes/iron oxide composites for the adsorption of dyes," *Chemical Engineering Journal*, vol. 168, no. 2, pp. 959–963, Apr. 2011, doi: 10.1016/j.cej.2011.02.031.

[12] Franco, Sacco, De Marco, and Vaiano, "Zinc Oxide Nanoparticles Obtained by Supercritical Antisolvent Precipitation for the Photocatalytic Degradation of Crystal Violet Dye," *Catalysts*, vol. 9, no. 4, p. 346, Apr. 2019, doi: 10.3390/catal9040346.

[13] K. Y. Foo and B. H. Hameed, "Insights into the modeling of adsorption isotherm systems," *Chemical Engineering Journal*, vol. 156, no. 1, pp. 2–10, Jan. 2010, doi: 10.1016/j.cej.2009.09.013.

[14] R. Ezzati, "Derivation of Pseudo-First-Order, Pseudo-Second-Order and Modified Pseudo-First-Order rate equations from Langmuir and Freundlich isotherms for adsorption," *Chemical Engineering Journal*, vol. 392, p. 123705, Jul. 2020, doi: 10.1016/j.cej.2019.123705.

[15] C.-H. Wu and J.-M. Chern, "Kinetics of Photocatalytic Decomposition of Methylene Blue," *Ind. Eng. Chem. Res.*, vol. 45, no. 19, pp. 6450–6457, Sep. 2006, doi: 10.1021/ie0602759.

[16] D. A. Skoog, S. R. Crouch, and F. J. Holler, *Principles of instrumental analysis.* Belmont, CA: Thomson Brooks/Cole, 2007.

CHAPTER III
Characterization of HKDD3 clay: removal of MB dye

This chapter presents the characterization results of HKDD3. The mineralogical composition of the pristine HKDD3 clay was performed by X-ray diffraction. Transmission and scanning electron microscopy was used to identify the morphology of HKDD3. The Fourier transform infrared spectroscopic and textural analysis (BET) completes the physicochemical study by identification of various forms of the minerals present in the clay and the specific surface area. Thus, the HKDD3 clay was tested by adsorption of MB dye.

III.1 Characterization of HKDD3

III.1.1 Chemical composition by fluorescence X (XRF)

The chemical composition of HKDD3 clay was performed by fluorescence X. The main oxides in the sample **(Table III.1)** are consistent with a large fraction of kaolin group minerals **[1]**. According to the results, the alumina and silica contents were about 38.48%, and 36.11%, respectively. The SiO_2/Al_2O_3 mass ratio is 0.94. In addition to the presence of impurities content (Fe_2O_3, MgO, CaO) less than 3%. The percentage of alumina is greater than silica. The report of silica/alumina is less than 1 which means that HKDD3 is not pure i.e a mixture of kaolinite and halloysite phase as XRD measurement confirmed. The MnO content is relatively high compared to the other oxides in HKDD3, which can be explained by its grey color.

Table III. 1 Chemical composition of HKDD3

Element	**Al_2O_3**	**SiO_2**	**Fe_2O_3**	**CaO**	**MgO**	**Na_2O**	**K_2O**	**MnO**
W/W%	38.48	36.11	0.13	0.42	0.16	0.26	0.03	0.46-1.34

III.1.2 X-ray diffraction analysis (XRD)

X-ray diffraction analysis shows that kaolin HKDD3 consists of halloysite and kaolinite **(Figure III.1)**. The pattern obtained is practically similar to the one obtained by T. Imai et al **[2]** in their study of an Algerian halloysite. This suggests that the HKDD3 in this study is halloysite clay. The XRD pattern was recorded from 4 to 80°. The characteristics peaks at 2θ = 11.71°, 19.98° 24.53°,34.96°, 37.69°, 38.28°, 54.69°, and 62.62° correspond to the halloysite (7A°) structure (JCPDS 29-1487) **[3]**. The other peaks at positions 9.27°, 19.98, 34.96°, 37.69°, 38.8°, 48.19°, 54.69°, and 62.62° were ascribed to Kaolinite (JCPDS 80-0886) **[4]**. The Kaolin extracted from Djebel Debbagh 3 is a mixture of kaolinite and halloysite **[5]**.

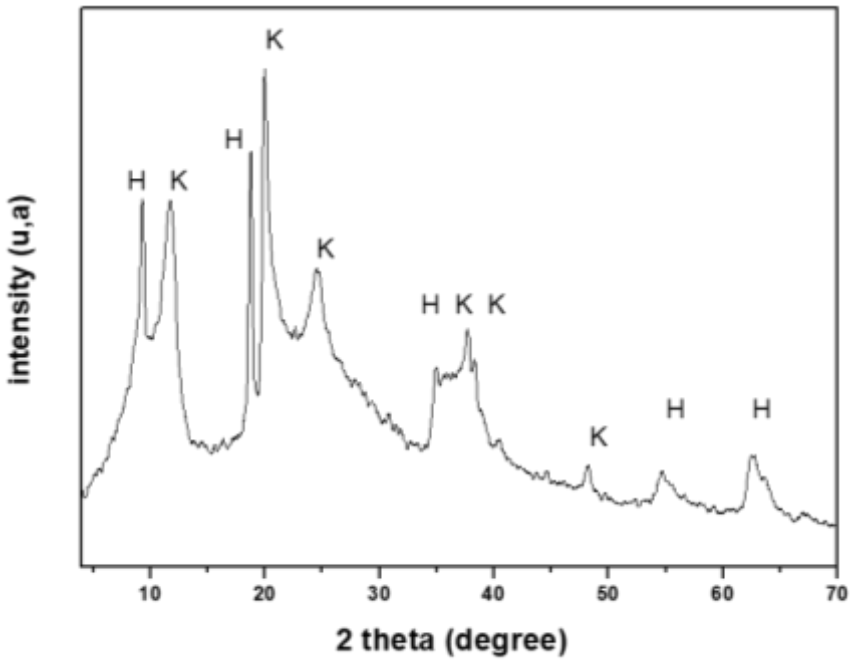

Figure III. 1 XRD pattern of HKDD3 clay, K: kaolinite; H: halloysite.

For the indexing of the X-ray diffraction pattern, the following methods are used conventional investigations of the inter-reticular distances of diffraction (d_{hkl}) planes corresponding to each diffraction line (**Table III.2**). The diffraction angles of the different planes of each phase are compared with the JCPDS files. The analysis of the XRD pattern is a bit difficult because the raw kaolin contains mineral phases and impurities. The pattern represents the essential phases which are kaolinite and halloysite.

Table III. 2 Positions of the major phases that appear in the HKDD3 clay.

Pos. [°2Th.]	d-spacing [Å]	mineral	Plans (d_{hkl})
9.30	9.50	H	001
11.81	7.50	K	001
18.75	4.73	H	001
19.88	4.46	H	110
24.70	3.60	K+H	002
34.89	2.57	H	200
37.70	2.39	H	013
48.17	1.89	K	$\bar{1}\bar{3}3$
54.60	1.68	H	301
62.33	1.49	H	$\bar{3}\bar{3}1$

III.1.3 Scanning electron microscopy and Edx mapping

In general, the solid phase of the mineral clay can be described in three units according to the scale of size: the sheet, the particle, and the aggregate. The particle is made up of several sheets and is usually more than 8 nanometers thick. In addition, the aggregate is a set of primary particles oriented in all directions. The aggregates vary in size from 0.1 to 10 microns. **Figure III.2** shows the micrographs obtained by SEM. The image (at 2 µm) represents that the HKDD3 clay is a halloysite clay with a tubular shape. SEM analysis revealed that the sample's content was uniform, with numerous tubules and the presence of occasional particle agglomerates.

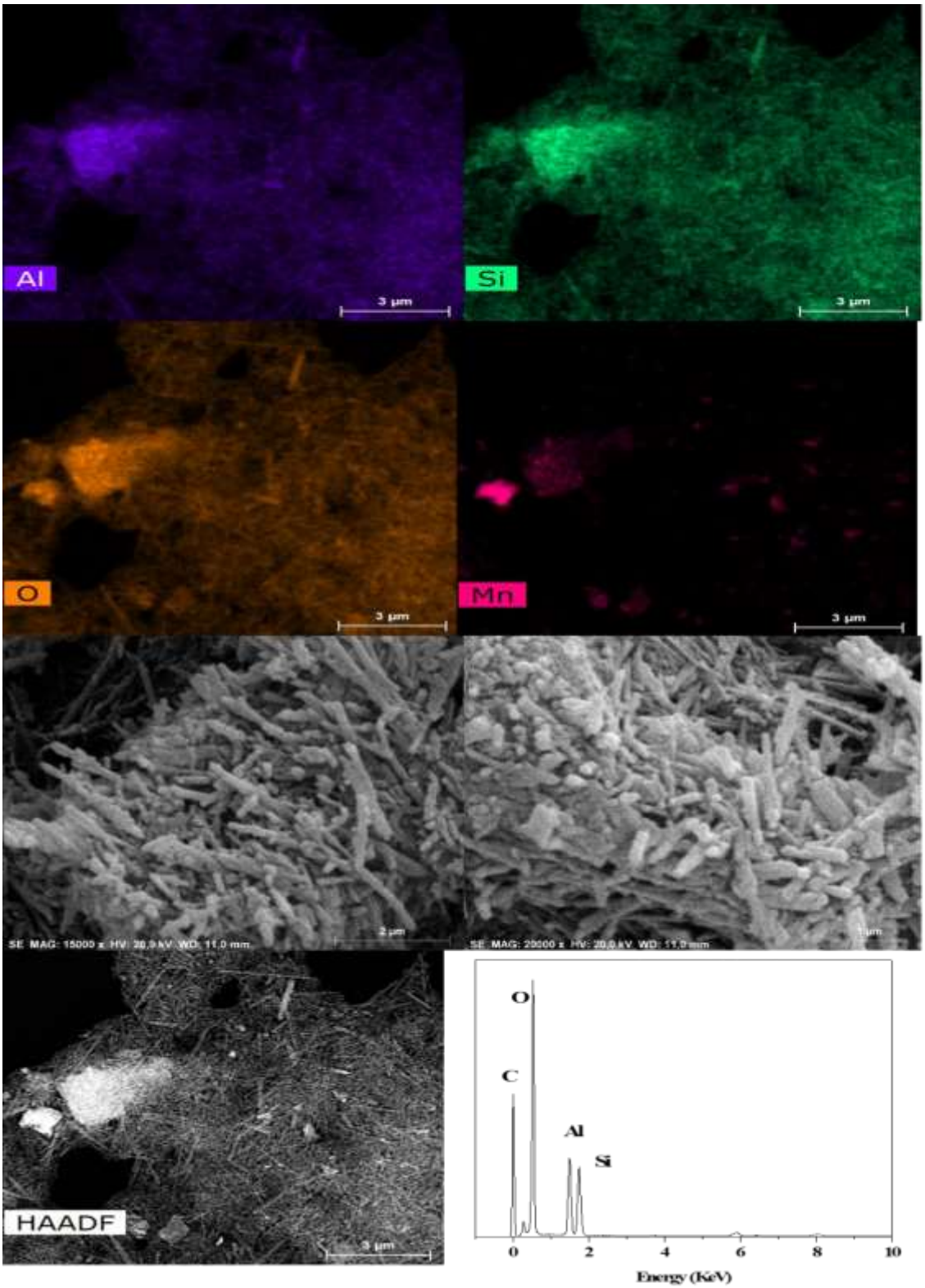

Figure III. 2 SEM images of purified clay HKDD3.

III.1.4 Analysis by transmission electron microscopy (HRTEM)

The sample HKDD3 has a characteristic tubular shape, with long open-ended tubes ranging in length from 0.5 to 5 µm and diameters ranging from 20 to 50 nm. The length is ranged from 1 to 3.5 µm, and the diameter is between 20-50 nm **(According to image J software) [6].** TEM images (**Figure III.3**) indicate that the lumen of the halloysite was empty.

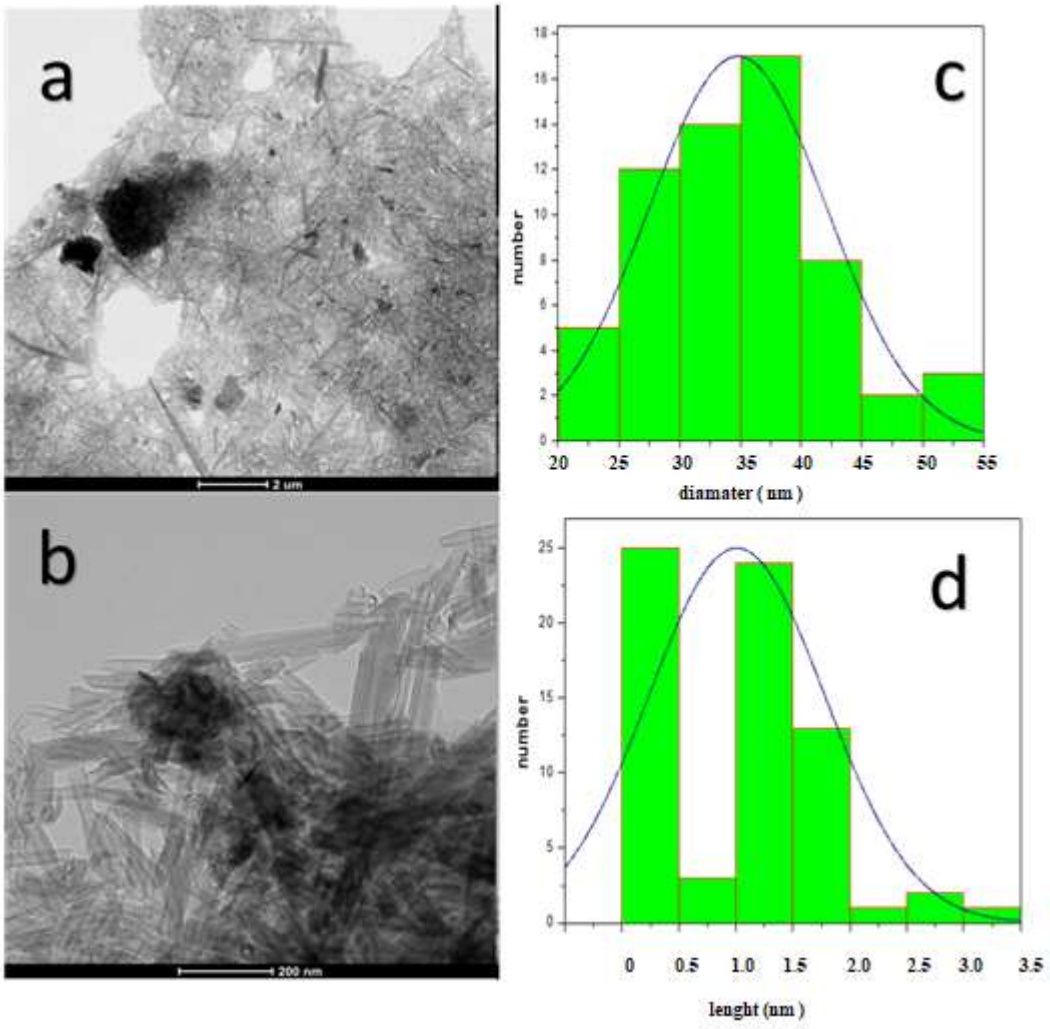

Figure III. 3 TEM images of HKDD3 clay (a), (b); histogram of length and diameter (c), (d).

III.1.5 BET analysis

The porosity and specific surface area were confirmed by the pore analysis based on adsorption-desorption of N_2 gas measurement as represented in **Figure III.4**. The isotherm has a type IV, with an apparent H3 hysteresis loop **[7]**. Consequently, HKDD3 clay has an essentially mesoporous and macroporous structure **[8]**. The size of the pores is less well segmented, and the peaks obtained are less distinct. This proves that porosity is irregular, and heterogeneous, inside the halloysite. The average value is practically of the same order of magnitude approximately 12.41 nm and the total pore volume is 0.222 cm^3/g as shown in **table III.3.** While the surface area indicates the value of 71.71 m^2.

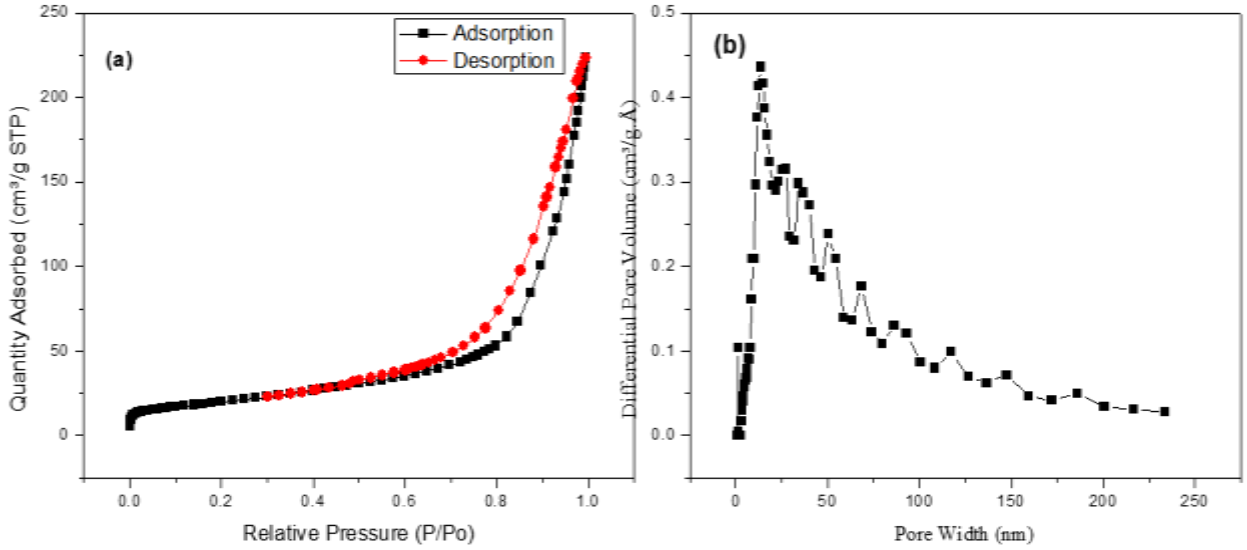

Figure III. 4 Isotherms of adsorption-desorption of N_2 of HKDD3 (a), Pore size distribution of HKDD3 clay (b).

According to table **III.2**, compared to other types of halloysite the HKDD3 has a good specific surface and average pore volume. While the pore diameter was higher about 12.41 nm.

Table III. 3 specific surface areas of different halloysite clay were extracted from several regions**.**

Halloysite	**Dragonite DG Dragon Mine, Utah, North America**	**Camel Lake CLA 63 km E of Maralinga, South Australia**	**Te Puke TP Bay of Plenty, New Zealand**	**Djebel Debbagh 3 (easten of Algeria)**
SSA (m^2/g)	57.30	74.66	33.31	71.71
BJH pore volume cm^3/g	0.12	0.17	0.09	0.22
BJH pore diameter (nm)	8.15	8.91	9.38	12.41
reference	**[9]**	**[10]**	**[11]**	**This work**

III.1.6 Fourier Transform Infrared Spectroscopy (FTIR)

A pure phyllosilicate's infrared spectrum is divided into many regions:

1/ Region of vibration of the hydroxyl groups **[12]**:

Between 3750 and 3400 cm^{-1} for the valence vibration bands.

Between 950 and 600 cm^{-1} for the angular deformation bands.

2/ Vibration region of the silicate anion:

Between 1200 and 700 cm^{-1} for the valence vibration bands.

Between 600 and 400 cm^{-1} for the deformation bands.

3/ Region of vibration of the hydration water of the interfoliar cations:

The bands of vibration of valence are between 3640 and 3400 cm^{-1} and are superimposed on the OH valence bands of the clay. The deformation bands are between 1650 and 1610 cm^{-1}

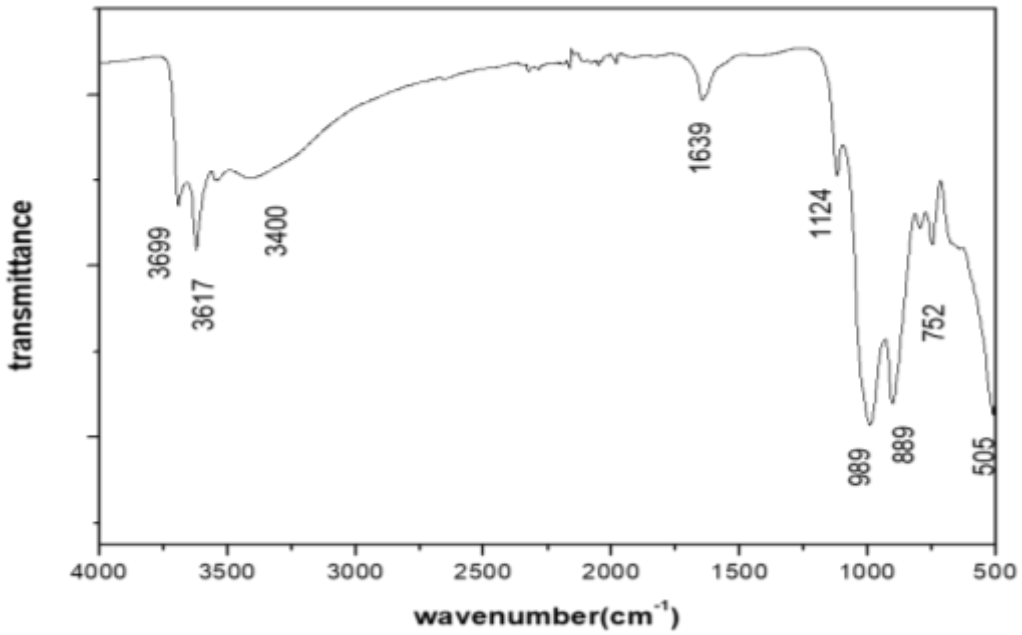

Figure III. 5 FITR spectra of HKDD3 clay

The halloysite HKDD3 spectra showed intense bands at 3622 cm^{-1} and 3690 cm^{-1} which are assigned to OH stretching vibrational groups **[13]** Stretching vibrations of hydroxyl groups are particularly allocated to this area. The signal at 1648 cm^{-1} was also assigned to OH deformation for the adsorbed water molecules. Intense peaks may be observed at 1120, 991, and 902 cm^{-1} Si-O stretching groups Al-O-Si, and Al-OH vibration groups, respectively [14]. the band at 511 cm^{-1} corresponds to Al-O-Si deformation **[15].**

Table III. 4 vibrational groups of HKDD3 cla

Groups	**Wavenumber (cm^{-1})**
Stretching vibration of the inner surface of O-H groups of halloysite	3,690 and 3,622
Interlayer water (adsorbed water)	1,648
Stretching of Si-O	1,112
Stretching vibration of Si-O-Si	1,030 and 470
The vibration of Al-O-Si	511
The vibration of the inner surface hydroxyl group	991 and 902

III.1.7 Thermogravimetric analysis (TGA)

The curve of variation of the mass as a function of the temperature of HKDD3 is displayed in **Figure III.6.** The HKDD3 clay has a first loss of mass of around 4%, which corresponds to adsorbed molecules of water on the surface of the HKDD3 clay. Then, in the range between 100° and 300°C, the loss of water is contained in the interfoliar space. This loss of mass reflects the structural transformation from halloysite to metahalloysite with a mass loss of 3.75%. At high temperatures, the weight loss of 15% is attributed to the dehydroxylation of structural aluminol groups.

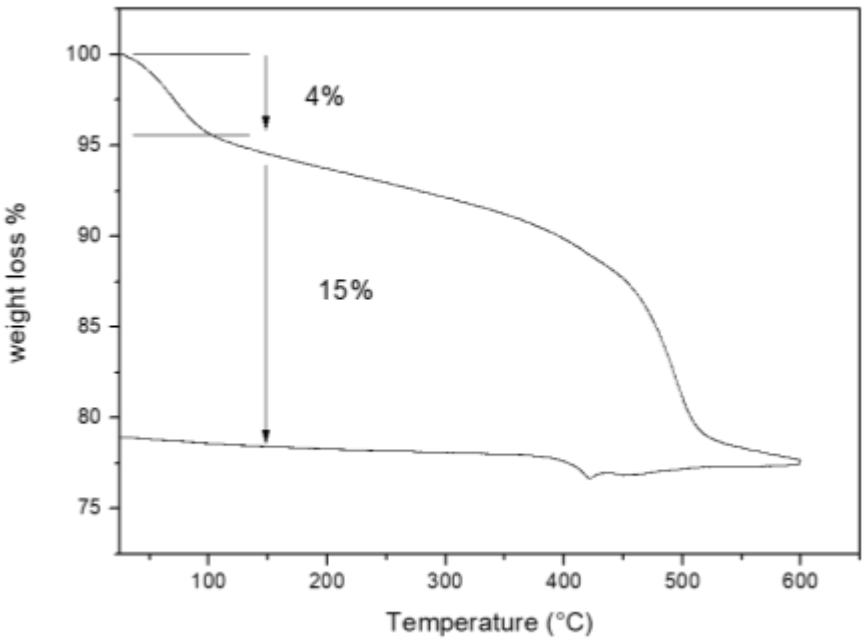

Figure III. 6 ATG curve of HKDD3 clay.

III.2 Adsorption study

III.2.1 Effect of initial dye concentration and contact time

Figure III.7 depicts the effect of initial dye concentration and contact time on the adsorption of the MB dye. As can be seen, the adsorption capacity increases as the initial dye concentration increases. The adsorption process happens in two stages, the first one is rapid for the first 20 min of contact to reach finally equilibrium within about 40 min. the adsorbed quantity reached 4.99, 8.29, 15, 22.3 mg/g for 5,10, 20, 40 $mg.L^{-1}$.

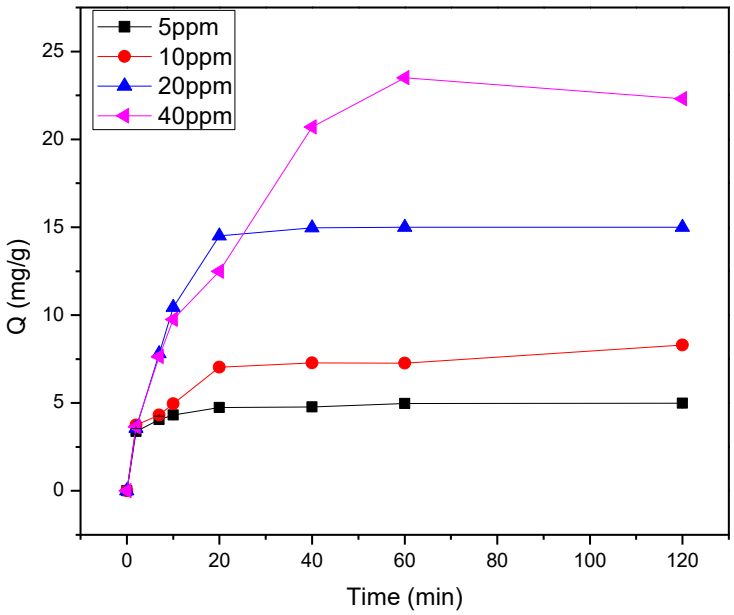

Figure III. 7 adsorption capacities in the uptake of MB dye as a function of time.

III.2.2 Effect of temperature

As shown in **figure III.8**. Adsorption experiments were conducted at 30, 40, and 50° C. the tests were carried out on a solution of 20 mg/L of methylene blue.

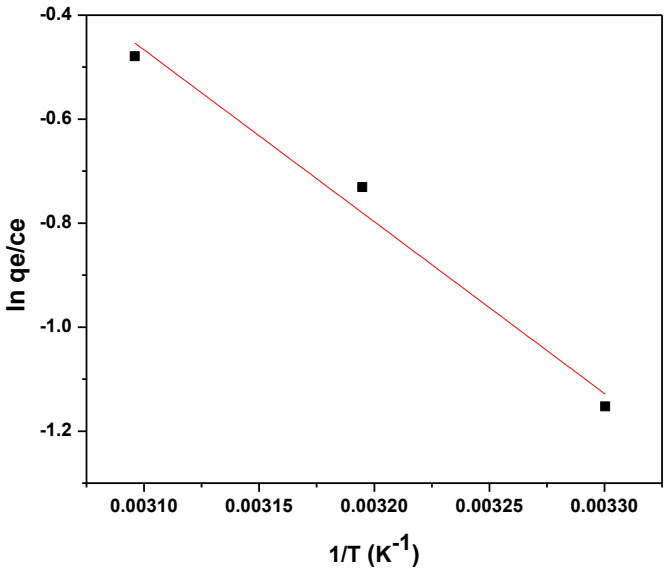

Figure III. 8 Temperature effect on the equilibrium thermodynamic constant (m=0.1g HKDD3 clay; 100 mL; 20 mg.L^{-1} of MB)

According to obtained results (**table III.5**), with the temperature rise, the MB adsorption capacity showed a significant increase. Despite this, the ΔG◦ values of the MB dye adsorption onto HKDD3 are positive. confirming that this adsorption is inhibited by charge heterogeneity **[16].** Furthermore, the adsorption of MB dye onto HKDD3 exhibited an endothermic nature because ΔH is around 27.47 kJ.mol^{-1} which is a positive value of standard enthalpy change; this value indicates that interactions between the dye molecules and adsorbent particles are electrostatic interaction type in this adsorption because ΔH^0 is ranged 20 and 80 kJ.mol^{-1} **[17]**. According to, the positive value of standard entropy changes ΔS^0 determined that the randomness is decreased at the interface solid-liquid when the adsorption occurred **[18].**

Table III. 5 Thermodynamic parameters

Parameters	**ΔG^0 (kJ.mol^{-1})**			**ΔH^0 (kJ.mol^{-1})**	**ΔS^0 (J.mol^{-1}. k^{-1})**	**R^2**
Temperature (K)	**303**	**313**	**323**	27.47	81.28	0.97
values	2.84	2.03	1.22			

III.2.3 Kinetic study

Interesting data about adsorption mechanisms are provided by applying the kinetic models. In this study, we used the major models to fit adsorption experiments which are: pseudo-first-order (PFO) and pseudo-second-order (PSO). **Figure.III.9** indicates that the plot was not linear over the range of time, which means that there is more than one process that affected the adsorption. As shown in the curve pattern there are two stages, external surface adsorption at the initial stage; is characterized by the rapid evolution of adsorption because the dye particles were adsorbed onto the external adsorbent surface. After the external surface has been saturated, the dye molecules slowly diffuse into the adsorbent pores in the second stage.

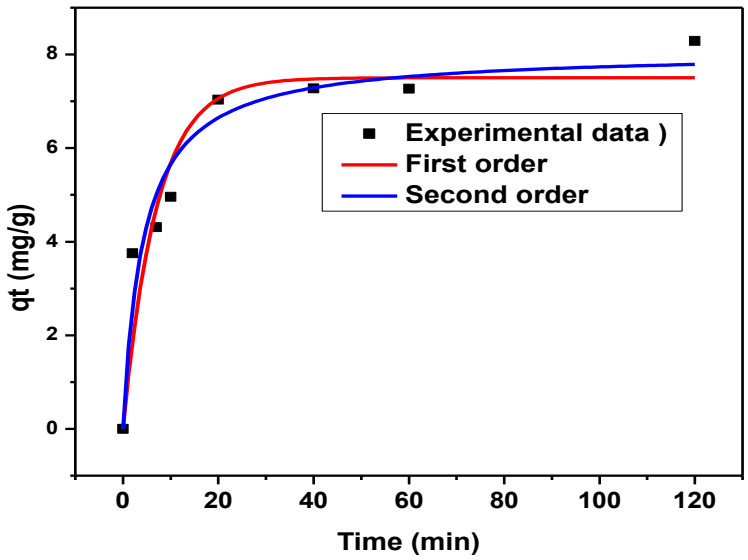

Figure III. 9 Adsorption kinetics of MB using HKDD3 and fitting curves of kinetic models (pH free; m=0.1 g of HKDD3 clay; 100 mL; 10 mg.L^{-1} of MB).

As can be observed (**Table III.6**), the pseudo-second-order equation fitted the data better than the first order. Furthermore, the pseudo-second-order model's calculated qe values are substantially consistent with the experimental results. These findings suggest that the adsorption magnitude may be attributed to a stronger driving force promoting the rapid transfer of MB molecules to the adsorbent particles' surface.

Table III. 6 kinetic study PFO and PSO.

Kinetic model	q_{exp} (mg/g)	$q_{e\ cal}$ (mg/g)	K	R^2
Pseudo-first-order	8.29	7.50	0.14	0.89
Pseudo-second-order	8.29	8.06	0.03	0.94

III.2.4 Adsorption isotherms

To explain the adsorption process, isotherm models of MB dye adsorption were applied by plotting q_e as a function of C_e at equilibrium. Among the major theoretical isotherms, Langmuir, and Freundlich models were used. The Langmuir model indicates that the adsorption occurred in a homogeneous phase. While Freundlich isotherm happened on the heterogeneous surface. Both equations of isotherms were mentioned in chapter II.

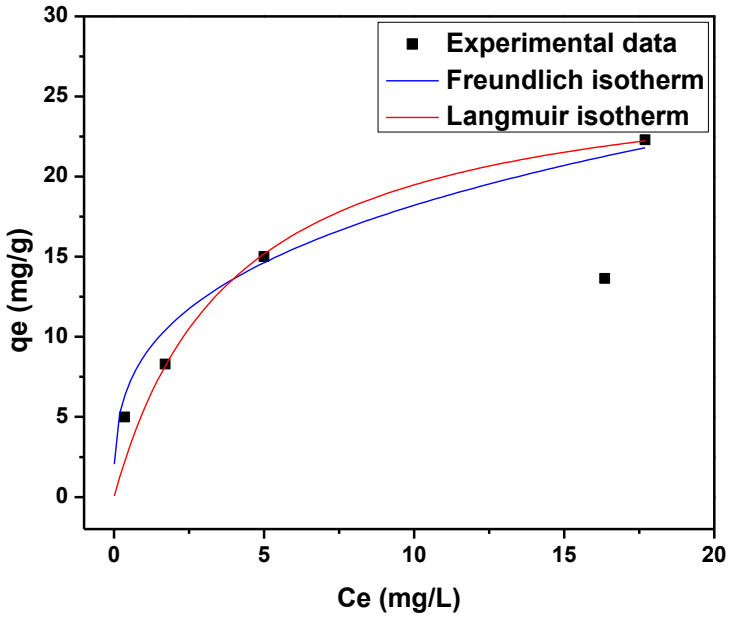

Figure III. 10 Isotherms model of MB adsorption onto HKDD3 clay.

According to the data summarized in **table III.7**, both the Langmuir and Freundlich adsorption isotherm models fit the equilibrium data well. The Freundlich isothermal model fitted well the experimental data than the Langmuir isothermal with higher R^2 0.99 and lower χ^2 0.71. The adsorption processes could be defined as reversible, not limited to monolayer formation, or as multilayer sorption with a non-uniform distribution of adsorption heat and affinities on a heterogeneous surface.

Table III. 7 Isotherm constant parameters for the adsorption of MB onto HKDD3 clay.

Isotherm	**Adsorption process**	
Langmuir	**q_m (mg.g^{-1})**	26.088
	K_L	0.298
	R_L	0.09-0.44
	R^2	0.968
	χ^2	2.386
Freundlich	**K_F**	7.476
	n	2.596
	R^2	0.990
	χ^2	0.710

III.3 Conclusion

In this chapter, HKDD3 clay was characterized by different techniques. Silica and alumina are the main constituent oxides of the HKDD3 clay. The TEM images of the halloysite show a hollow and opened tubular shape. Their external diameter varies from 50 nm to more than 100 nm. Batch adsorption experiments showed that the adsorption process followed the pseudo-second-order kinetic model and Freundlich isotherm. Furthermore, the thermodynamics parameters revealed that adsorption is endodermic.

References

[1] P. Pasbakhsh, G.J. Churchman, J.L. Keeling, Characterisation of properties of various halloysites relevant to their use as nanotubes and microfibre fillers, Applied Clay Science. 74 (2013) 47–57. https://doi.org/10.1016/j.clay.2012.06.014.

[2] T. Imai, T. Yamamoto, K. Urabe, H. Nakano, M. Ohyanagi, Structural Change of Fired Halloysite of the Democratic and People's Republic of Algeria, J. Ceram. Soc. Japan. 113 (2005) 620–625. https://doi.org/10.2109/jcersj.113.620.

[3] Y. He, W. Xu, R. Tang, C. Zhang, Q. Yang, pH-Responsive nanovalves based on encapsulated halloysite for the controlled release of a corrosion inhibitor in epoxy coating, RSC Adv. 5 (2015) 90609–90620. https://doi.org/10.1039/C5RA19296J.

[4] F. Chargui, M. Hamidouche, H. Belhouchet, Y. Jorand, R. Doufnoune, G. Fantozzi, Mullite fabrication from natural kaolin and aluminium slag, Boletín de La Sociedad Española de Cerámica y Vidrio. 57 (2018) 169–177. https://doi.org/10.1016/j.bsecv.2018.01.001.

[5] F. Chargui, M. Hamidouche, H. Belhouchet, Y. Jorand, R. Doufnoune, G. Fantozzi, Mullite fabrication from natural kaolin and aluminium slag, Boletín de La Sociedad Española de Cerámica y Vidrio. 57 (2018) 169–177. https://doi.org/10.1016/j.bsecv.2018.01.001.

[6] V. Amandine, M. Cédric, M. Sergio, D. Patricia, An ImageJ tool for simplified post-treatment of TEM phase contrast images (SPCI), Micron. 121 (2019) 90–98. https://doi.org/10.1016/j.micron.2019.01.006.

[7] K.S.W. Sing, R.T. Williams, Physisorption Hysteresis Loops and the Characterization of Nanoporous Materials, Adsorption Science & Technology. 22 (2004) 773–782. https://doi.org/10.1260/0263617053499032.

[8] R. Bardestani, G.S. Patience, S. Kaliaguine, Experimental methods in chemical engineering: specific surface area and pore size distribution measurements—BET, BJH, and DFT, Can. J. Chem. Eng. 97 (2019) 2781–2791. https://doi.org/10.1002/cjce.23632.

[9] W.O. Yah, A. Takahara, Y.M. Lvov, Selective Modification of Halloysite Lumen with Octadecylphosphonic Acid: New Inorganic Tubular Micelle, J. Am. Chem. Soc. 134 (2012) 1853–1859. https://doi.org/10.1021/ja210258y.

[10] J.L. Keeling, P.G. Self, M.D. Raven, Halloysite in Cenozoic sediments along the Eucla Basin margin, MESA Journal, 2010, vol. 59, p. 9-13..

[11] E. Joussein, S. Petit, J. Churchman, B. Theng, D. Righi, B. Delvaux, Halloysite clay minerals — a review, Clay Miner. 40 (2005) 383–426. https://doi.org/10.1180/0009855054040180.

[12] C.Y. Heah, H. Kamarudin, A.M. Mustafa Al Bakri, M. Bnhussain, M. Luqman, I. Khairul Nizar, C.M. Ruzaidi, Y.M. Liew, Kaolin-based geopolymers with various NaOH concentrations, Int J Miner Metall Mater. 20 (2013) 313–322. https://doi.org/10.1007/s12613-013-0729-0.

[13] R. Riahi-Madvaar, M.A. Taher, H. Fazelirad, Synthesis and characterization of magnetic halloysite-iron oxide nanocomposite and its application for naphthol green B removal, Applied Clay Science. 137 (2017) 101–106. https://doi.org/10.1016/j.clay.2016.12.019.

[14] E. Tierrablanca, J. Romero-García, P. Roman, R. Cruz-Silva, Biomimetic polymerization of aniline using hematin supported on halloysite nanotubes, Applied Catalysis A: General. 381 (2010) 267–273. https://doi.org/10.1016/j.apcata.2010.04.021.

[15] T. Tsoufis, F. Katsaros, B.J. Kooi, E. Bletsa, S. Papageorgiou, Y. Deligiannakis, I. Panagiotopoulos, Halloysite nanotube-magnetic iron oxide nanoparticle hybrids for the rapid catalytic decomposition of pentachlorophenol, Chemical Engineering Journal. 313 (2017) 466–474. https://doi.org/10.1016/j.cej.2016.12.056.

[16] A. Harrou, E. Gharibi, H. Nasri, M. El Ouahabi, Thermodynamics and kinetics of the removal of methylene blue from aqueous solution by raw kaolin, SN Appl. Sci. 2 (2020) 277. https://doi.org/10.1007/s42452-020-2067-y.

[17] A. Gürses, A. Hassani, M. Kıranşan, Ö. Açışlı, S. Karaca, Removal of methylene blue from aqueous solution using by untreated lignite as potential low-cost adsorbent: Kinetic, thermodynamic and equilibrium approach, Journal of Water Process Engineering. 2 (2014) 10–21. https://doi.org/10.1016/j.jwpe.2014.03.002.

[18] M. Abbas, Experimental investigation of titanium dioxide as an adsorbent for removal of Congo red from aqueous solution, equilibrium and kinetics modeling, Journal of Water Reuse and Desalination. 10 (2020) 251–266. https://doi.org/10.2166/wrd.2020.038.

CHAPTER IV
Characterization of Fe_3O_4-HKDD3 clay and its application for MB removal

This chapter is devoted to present the discussion of the results obtained from the various structural, textural, and microstructural characterizations obtained on magnetite-HKDD3 nanocomposite. Then, we present the results of the evaluation of the sono-adsorption and adsorption for methylene blue from an aqueous medium by studying several Physico-chemical parameters pH, adsorbent mass, temperature, and MB concentration.

IV.1 Characterization of M-HKDD3

IV.1.1 X-ray diffraction analysis

The XRD patterns of M-HKDD3 are displayed in **figure IV .1**. The peaks at positions 2 theta: 9.3, 11.8, 18.7, 19.8, 24.7, 34.8, 37.7, 48.2, 54.6, 62.3 were ascribed to halloysite and kaolinite **[1]**. Furthermore, the appearance of new peaks at 2θ values 30.1, 35.6, 43.3, 57.1, 62.7 refers to (220), (311), (400), (511), and (440) planes of reflections magnetite particles, respectively **[2]**. In addition, the peaks of clay were significantly weakened which proved that the magnetite (Fe_3O_4) particles were altered by modifying the composition of clay. Debye Scherrer equation **[3]** was applied to estimate the average size of Fe_3O_4-HKDD3

$$D = \frac{0.9\lambda}{\beta cos\theta} \qquad (1)$$

Where β (rad): the full width at half maximum (FWHM), θ (rad): The Bragg's diffraction angle, and $\boldsymbol{\lambda}$= 1.5406 A° (the wavelength of radiation copper). The estimated size of particles is around 43.8 nm.

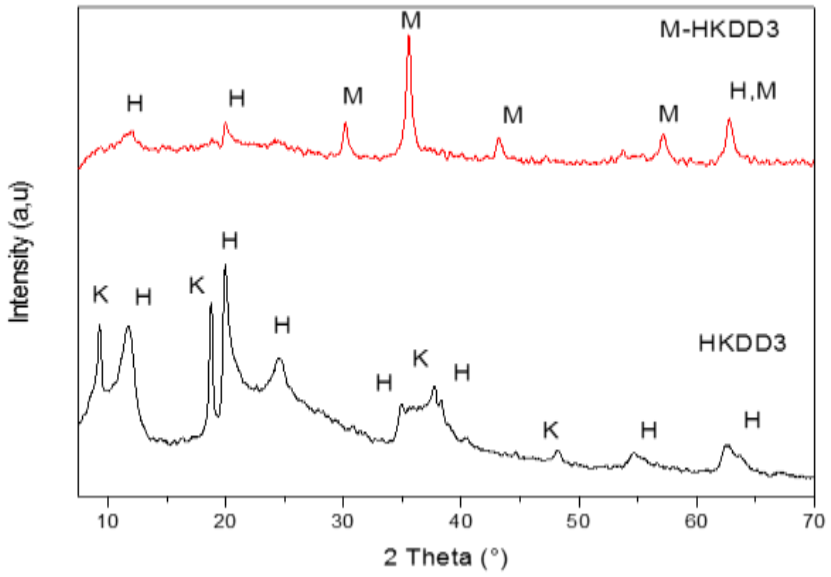

Figure IV. 1 X-ray diffraction patterns of HKDD3 and M-HKDD3

IV.1.2 Fourier transforms infrared spectroscopy

The infrared curve of M-HKDD3 was illustrated in **Figure IV.2**. the band at 1640 cm^{-1} is present, which is referred to the vibrations of the H-O-H bonds of the water molecules contained in the interfoliar space of the mineral halloysite **[4]**. The peaks at 3400, 3617 cm^{-1}, and 3699 cm^{-1} are

attributed to the stretching vibration of hydroxyl groups of clay **[5]**. In addition, the peak at 1124-989 cm^{-1} may be referred to as the silanol groups (Si-O-H, Si-O-Si stretching vibration) of silica **[6]**. The observed bands from 700 to 900 cm^{-1} are assigned to the deformation metal group Al-OH. For M-HKDD3 spectra, the intense and broadband at 3400cm^{-1} corresponded to stretching vibrations of hydroxyl (OH) groups from iron oxide (Fe_3O_4). The characteristic intense peak of magnetite (Fe_3O_4) at 580cm^{-1} could be overlapped by the band of Al-O-Si of HKDD3 clay at 536 cm^{-1}**[7]**.

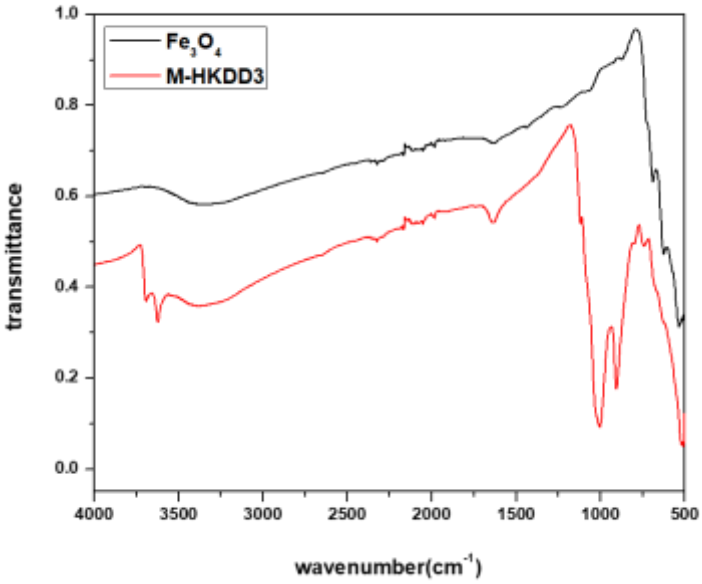

Figure IV. 2 FTIR spectra of M-HKDD3.

IV.1.3 High-resolution transmission electron microscopy

As presented in **Figure IV.3**, the morphology of clay M-HKDD3 was performed by HRTEM. The morphology of HKDD3 clay is a tubular shape (halloysite clay) with a length from 0.3 µm to 4 µm and a diameter between 30-50 nm. The magnetite nanoparticles were deposited on the surface of HKDD3 with a small size in the range from 5 to 50 nm with an average size of magnetite particles of 11.35 nm (using software Image J) **[8]**. As observed in the images the Halloysite (HKDD3) becomes rougher with irregular dispersion of spherical nanoparticles of magnetite **[9]**.

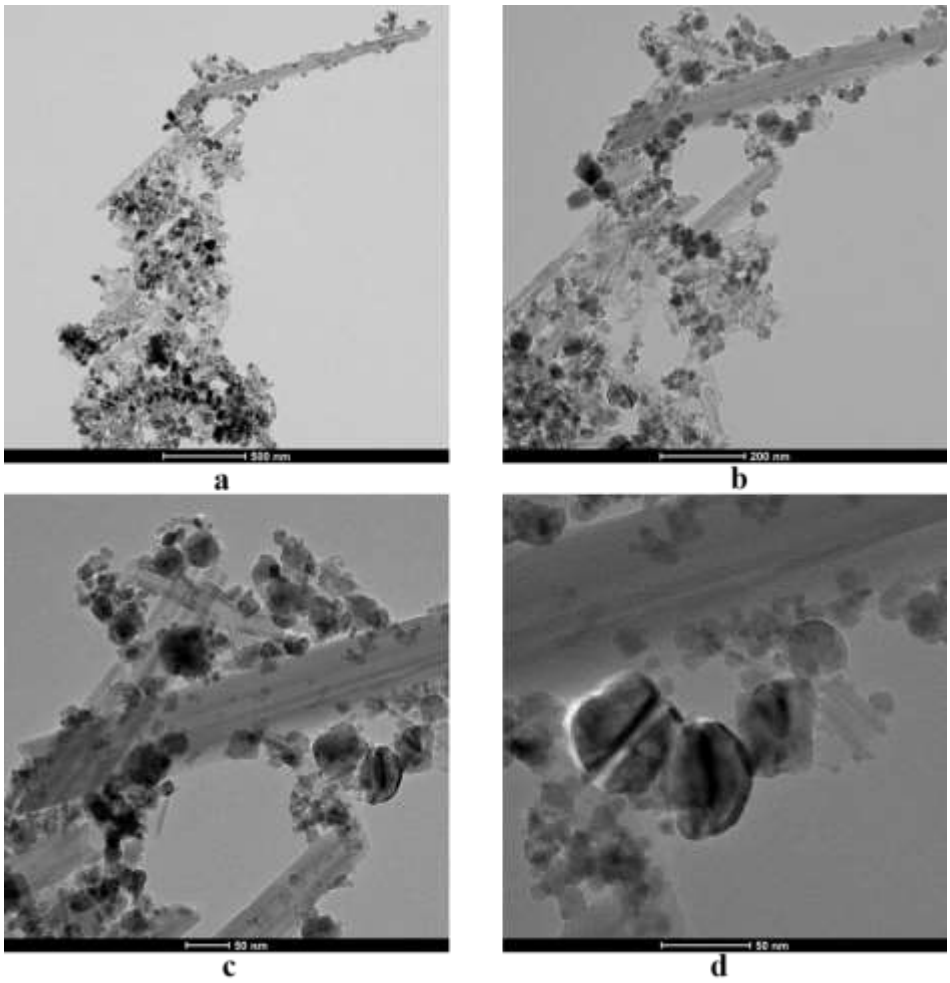

Figure IV. 3 HRTEM images of M-HKDD3

IV.1.4 SEM/EDX analysis

The SEM is screened in **figure IV.4**. It can be observed that the deposition of magnetite onto the surface of halloysite clay forms aggregate in some regions.

Halloysite has a variety of forms, including large-tubular, short-tubular, platy, and spheroidal shapes **[6]**. However, the most frequent form of halloysite is tubular morphology. The tubular shape can be represented by rolled kaolin sheets with inner diameters of 10-30 nm, outside diameters of 30-50 nm, and lengths ranging from 100–2000 nm **[7, 8]**. The halloysite's internal surface is made up of siloxane (Si–O–Si) groups, while the exterior is made up of gibbsite (Al–OH) groups. The major elements of Al, Si, and O, which are related to the halloysite chemical formula ($Al_2Si_2O_5.H_2O$), are seen in EDS spectra (**Figure IV.5**). Besides, these elements the Fe which is presented on Fe_3O_4 magnetite lattice.

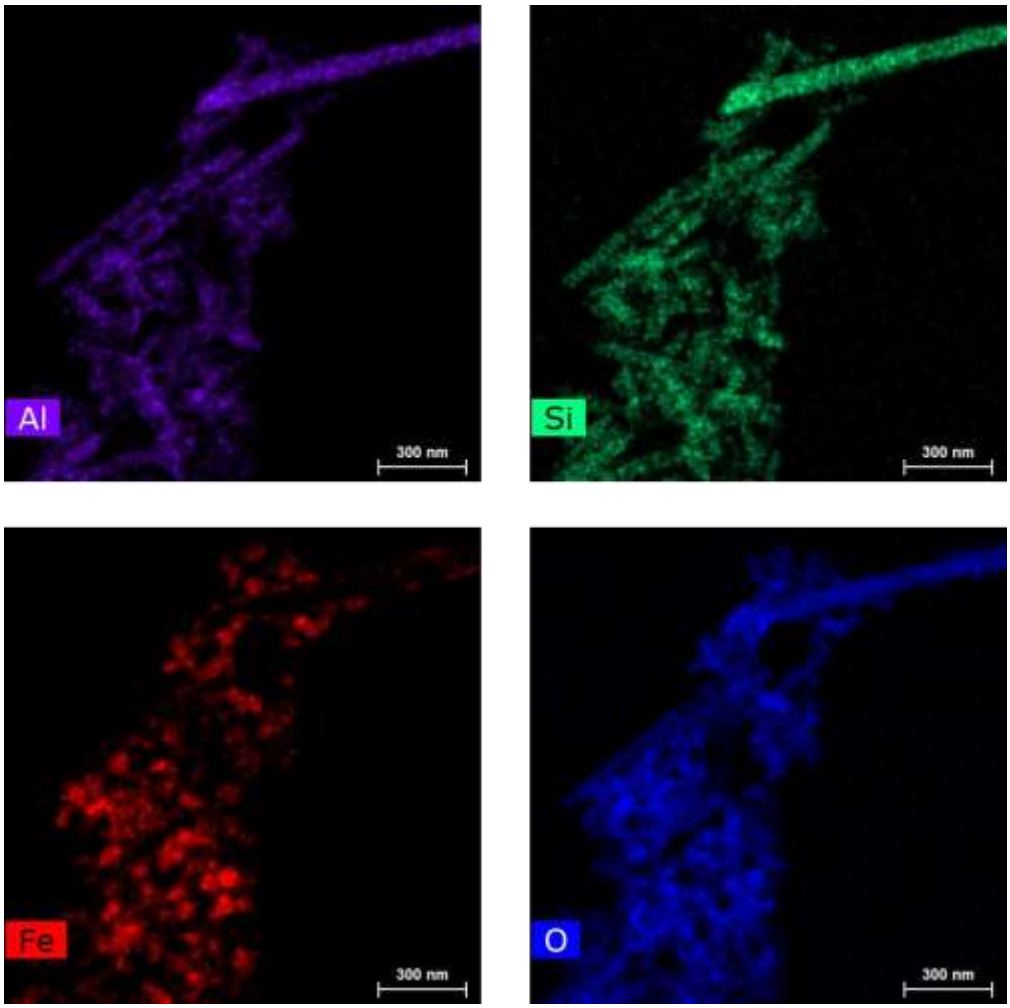

Figure IV. 4 SEM images of M-HKDD3

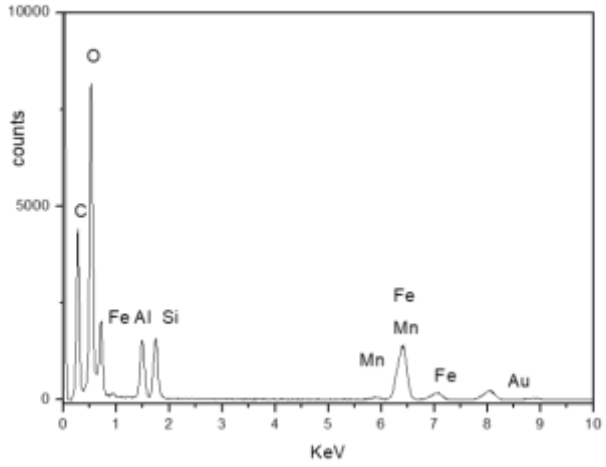

Figure IV. 5 EDS spectra of M-HKDD3

IV.1.5 BET analysis

BET study based on adsorption-desorption of N_2 gas measurement was carried out to determine the specific surface area **(figure IV.6)**. The isotherm exhibits a typical form for type II **[10]**, with an H3 type hysteresis loop **[11].** However, the BJH-determined pore size distribution **[12]**.

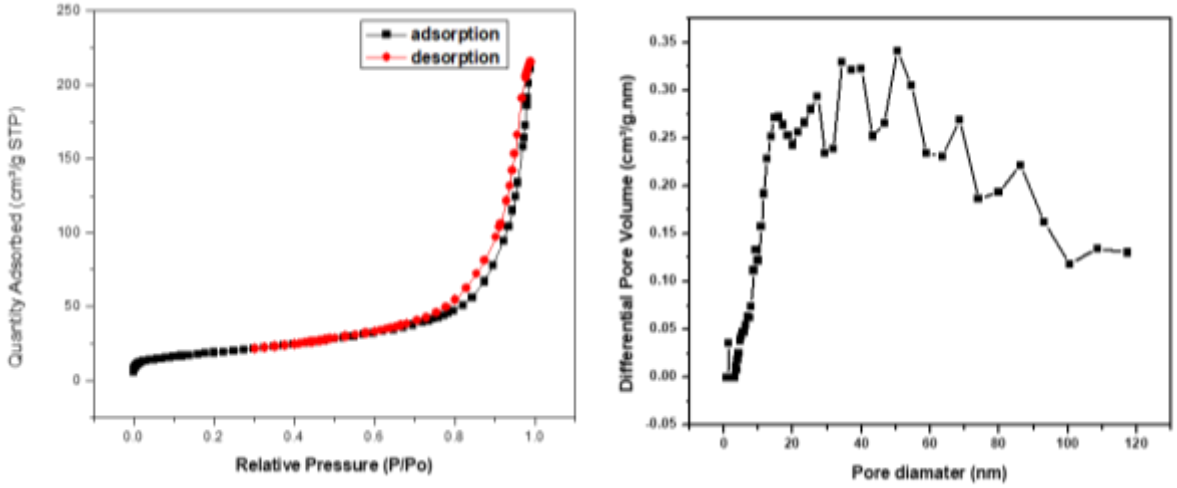

Figure IV. 6 Isotherms adsorption-desorption of N_2 (BET) and Pore size distribution of M-HKDD3.

After loading HKDD3 with magnetite nanoparticles, we observed a decrease in surface area, average volume, and diameter to be 67.42 m^2/g, 0.177 cm^3/g, and 10.54 nm, respectively (**Table IV.1**). It can be explicated by the deposition of magnetite nanoparticles onto the surface of HKDD3 clay. The M-HKDD3 nanocomposite shows the presence of mesopores and macropores.

Table IV.1 Textural characterization of HKDD3 and Fe_3O_4-HKDD3

adsorbent	S_{BET} (m^2/g)	Average pore volume (cm^3/g)	Average pore diameter (nm)
HKDD3	71.71	0.22	12.41
M-HKDD3	67.46	0.18	10.54

IV.2 Methylene blue adsorption and sono-adsorption studies

The purpose of this study was to see how effective M-HKDD3 nanocomposite was in removing methylene blue dye from an aqueous media. We conducted a comparison of adsorption and sono-adsorption procedures. The adsorbent mass, initial dye concentration, and time were 30 $mg.L^{-1}$, 0.1 g, and 120 minutes, respectively. Sono-adsorption was shown to be quicker and more effective than adsorption. For sono-adsorption and adsorption, the adsorption dye reached 18 mg/g and 10 mg/g,

respectively. Due to physical processes such as tiny turbulence, ultrasonic waves enhance the porosity of the M-HKDD3 surface adsorbent and mass transfer rate (liquid-solid interfaces) **[13]**.

A rapid rise corresponds to the first initial stage (20 min) when the MB adsorption rate is high due to the large accessible adsorbent surface area (pore size) and little dye-molecule competition **[14]**. After that, the second section (from 80 to 120 min) deals with slow adsorption induced by low concentration gradients, which takes around 60 minutes to reach equilibrium.

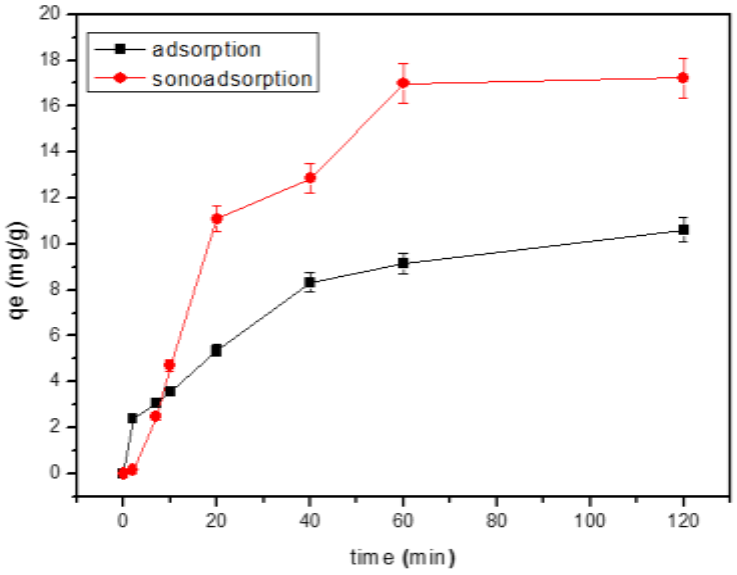

Figure IV. 7 Comparative adsorption and sono-adsorption for Methylene blue by M-HKDD3

IV.2.1 Effect of dye concentration

The adsorption and sono-adsorption efficiencies in the elimination of MB at different dye concentrations are shown in **Figure IV.8**. The adsorption and sono-adsorption equilibrium efficiencies improved as the MB concentration was increased. The adsorption and sono assisted-adsorption efficiencies of MB (10, 20, 30, and 40 $mg.L^{-1}$) were defined to be 8.63, 10.33, 10.60, and 11.70 mg/g and 9.54, 11.22, 17.23, 15.83 mg/g, respectively, after a 120-minute reaction period **[14]**. Due to the presence of ultrasonic irradiation, sono-adsorption efficiencies in the elimination of MB were found to be greater than adsorption efficiencies. By increasing mass transfer mechanisms like diffusion through micropores, ultrasound irradiation enhanced MB adsorption.

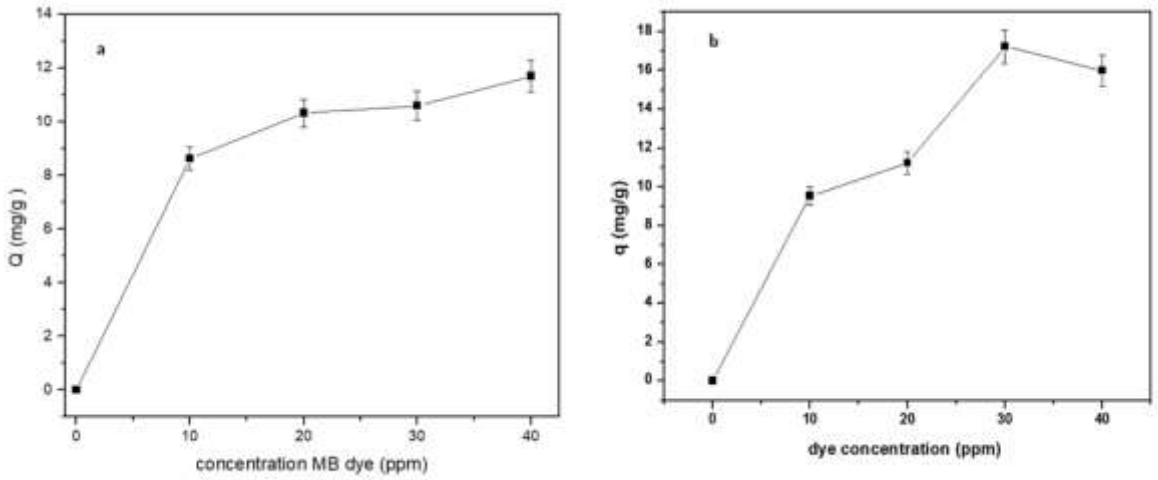

Figure IV. 8 adsorption (a) and sono-assisted adsorption (b) efficiencies in the uptake of MB dye as a function of MB dye concentration.

IV.2.2 Effect of pH

In this part of the study, the effect of the initial pH of MB solution was investigated, and the results are displayed in **figure IV.9**. The adsorption and sono-adsorption efficiencies of MB as a function of time at various pH (4, 7, 9). When the pH of the solution was raised from 4 to 9, the adsorption and sono-adsorption equilibrium efficiencies improved. The adsorption and sono-adsorption efficiencies of MB were defined as 9.77, 10.60, and 14.22 mg/g and 9.52, 17.23, and 18.78, respectively, when the pH of the solution was 4, 7, and 9. Due to the presence of ultrasonic irradiation, it was discovered that sono-adsorption efficiencies in the elimination of MB are greater than adsorption efficiencies.

In acidic conditions, pH <7, it was an unfavorable medium to adsorb MB dye owing to the electrostatic repulsion force between MB molecules and the surface of HKDD3 clay. Furthermore, there is a competition between H^+ ions and cationic dyes for migration to the active sites **[15].** By increasing pH, the OH^- ions are produced and the H^+ decreases in the solution **[16]**. The surface of the nanocomposite became more negatively charged, which improved the attraction of cationic methylene blue molecules, which caused the adsorption of MB in the active sites. As a result of the ultrasonic irradiation, reactive radicals ($OH^{\bullet}$ and $O2^{-\bullet}$) are produced on the surface of the magnetic clay, which may degrade the MB dye.

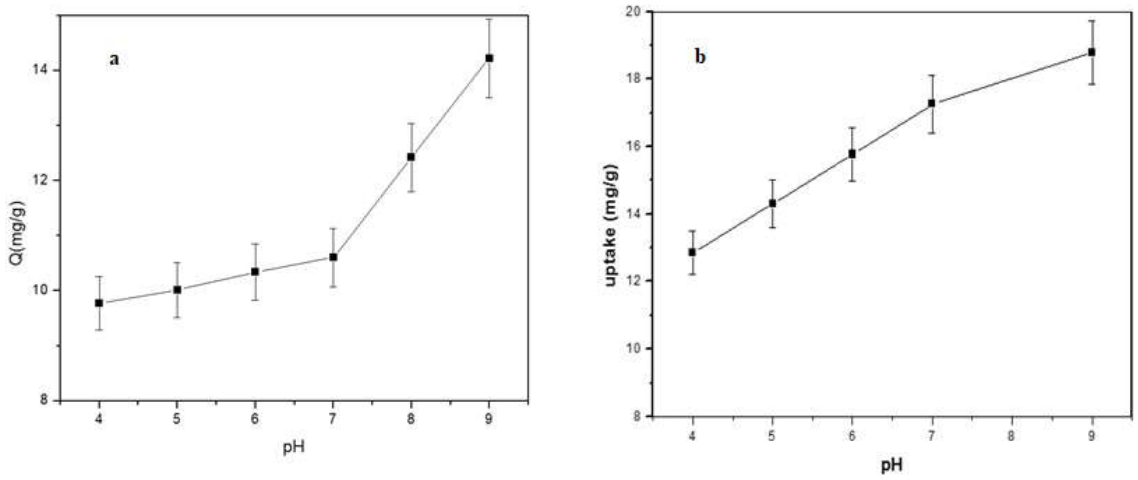

Figure IV. 9 Adsorption (a) and sono-assisted adsorption (b) the quantity adsorbed of MB dye as a function of pH variation (Co =30 mg.L^{-1}, T 25 °C).

IV.2.3 Effect of temperature

To study the influence of thermodynamic parameters, a series of experiments were conducted at different temperatures in the range of (303-323K°). The Gibbs free energy (ΔG), entropy (ΔS), and enthalpy (ΔH) were calculated by the equations **(seen in chapter II)**.

According to **Table VI.2,** the endothermic nature of the adsorption phenomena was confirmed by the positive value of standard enthalpy change ΔH°, besides the value of that parameter can give an idea about the type of interactions between adsorbate and adsorbent, therefore 36.38 and 31.94 kJ.mol^{-1} is higher than 20 kJ.mol^{-1} indicates that electrostatic interactions occurred between MB molecules and M-HKDD3 particles. The negative values of standard Gibbs ΔG° show decreasing with increasing temperature suggesting that the adsorption process was favorable, spontaneous, and enthalpy controlled, whereas the positive values of ΔS° exhibited the randomness at the solid-solution interface increased during the adsorption and sono-assisted adsorption process.

Table IV. 2 parameters of thermodynamic studies.

Sono-adsorption			
T (K°)	**ΔG (kJ mol^{-1})**	**ΔH (kJ mol^{-1})**	**ΔS (J/mol.K)**
303	-1.095	31.948	109.05
313	-2.116		
323	-3.073		
Adsorption			
T (K°)	**ΔG (kJ mol^{-1})**	**ΔH (kJ mol^{-1})**	**ΔS (J mol K^{-1})**
303	-0.575	36.831	123.54
313	-1.925		
323	-3.042		

IV.2.4 Kinetic study

The kinetic models provide us with information about the adsorption mechanism and the mode of solute transfer from the liquid phase to the solid phase. The literature reported several models such as the pseudo-first-order model (PFO), the pseudo-second-order kinetic model (PSO), and Weber and Morris model or intraparticle diffusion model. The nonlinear plots of data regression of PFO and PSO were represented to determine kinetics.

Results of kinetic modeling are presented in **Figure IV.10** and **Table IV.3**. For the pseudo-first-order model **[17]**, the adsorption rate constant K_1 is given by the following relation:

$$\frac{dq}{dt} = K_1 (q_e - q) \quad \textbf{(5)}$$

In the pseudo-second-order model **[18]**, the adsorption rate constant K_2 is given by the following relation: $K_2(qe-q)^2$

$$\frac{dq}{dt} = K_2 (q_e - q)^2 \quad \textbf{(6)}$$

Where; q_e is the quantity of dye adsorbed at equilibrium (g/mg); q_t is the quantity of dye adsorbed at time t (g/mg); t is the contact time (min); K_1 is the adsorption rate constant for the pseudo-first-order (min^{-1}); K_2 is the adsorption rate constant for pseudo-second-order (g/mg.min).

The intra-particle model **[19]** was defined by the equation $q_t = K_{id} * t^{0.5} + C$.

Where qt is the amount of adsorbate per unit weight of adsorbent.

C (mg/g) is a constant which gives information about the boundary layer and Kid ($mg.g^{-1}.min^{-1/2}$) is the intraparticle rate constant and t is time contact.

According to this model, internal diffusion would be the mechanism that controls adsorption kinetics if the capacity q (mg/g) varies linearly with the square root of time **[20]**. F**igure IV.10** showed that the curve is not linear. The first is fast owing to the unoccupied external sites of clay then we observed slow adsorption which referred to the diffusion molecules of MB into a sheet of clay. It means that the first region corresponds to the external diffusion mechanism that precedes the internal diffusion represented by the second region **[21]**. The intraparticle diffusion model for MB dye fitted the experimental kinetic results. Furthermore, the intercept value, C, is not zero indicating that the intraparticle diffusion mechanism does not entirely restrict the overall adsorption process.

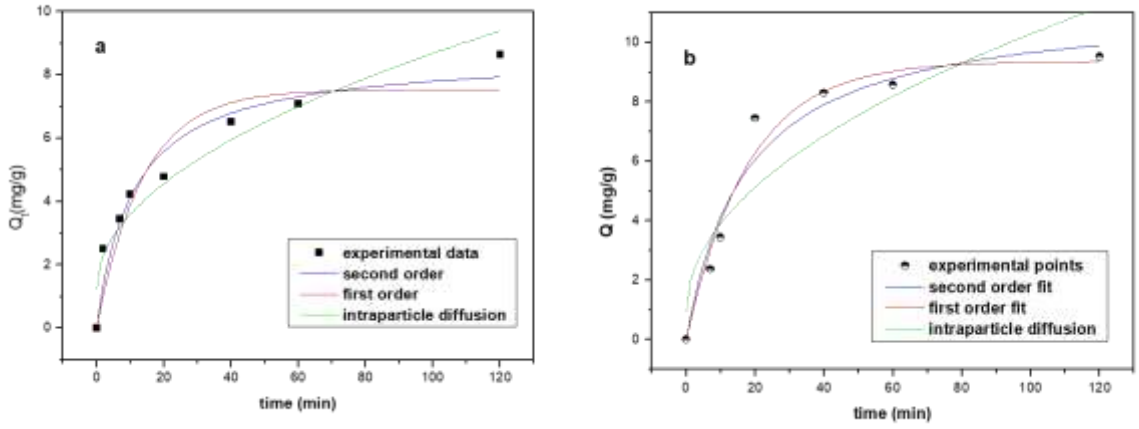

Figure IV. 10 Adsorption kinetics of MB using M-HKDD3 and fitting curves of kinetic models (C=10 $mg.L^{-1}$, T=20°C, m= 0,1 g, 100 ml (MB)).

As seen in **Table IV. 3**, the R^2 value for the pseudo-second-order kinetic equation was found to be greater than that of the pseudo-first-order kinetic equation for the adsorption process. The experimental qe (8.63 mg/g) was closer to the calculated qe (8.66 mg/g) for the pseudo-second-order model than the result for the pseudo-first-order (7.53 mg/g). Higher R^2 (0.941) and χ^2 lower (0.044) values revealed that the adsorption process matched the pseudo-second-order kinetic model. However, the obtained results indicate that the sono-assisted adsorption process follows pseudo-first order with R^2= 0.965 and low χ^2 (0.467). As well as the calculated quantity adsorbed reached 9.36 mg/g (from PFO) which is in agreement with experimental data (qe) 9.52 mg/g.

Table IV. 3 Parameters and error functions data for kinetic models studied for the adsorption of methylene blue onto M-HKDD3.

Kinetic model	Parameters	Adsorption	Sono-assisted adsorption
Pseudo first order (PFO)	qe_{exp} (mg/g)	8.63	9.52
	$q_{e\ cal}$ (mg/g)	7.53	9.36
	K_1	0.072	0.05
	R^2	0.885	0.965
	χ^2	0.870	0.467
Pseudo second order (PSO)	$q_{e\ cal}$ (mg/g)	8.66	11.34
	K_2	0.01	0.005
	R^2	0.941	0.947
	χ^2	0.446	0.711
Intraparticle diffusion (IPD)	Kip	0.74	0.934
	Ce	1.24	0.949
	R^2	0.934	0.814
	χ^2	0.500	2.521

IV.2.5 Isotherm of adsorption

The modeling of experimental isotherms is essential for understanding the adsorption process. By changing the initial concentration of MB (from 5 to 40 $mg.L^{-1}$) at 25 °C, the isotherm of MB dye adsorption was obtained. The plot of Qe = f(Ce) at equilibrium depicts the isotherm of MB adsorption onto M-HKDD3, which corresponds to Brunauer classification isotherm type I.

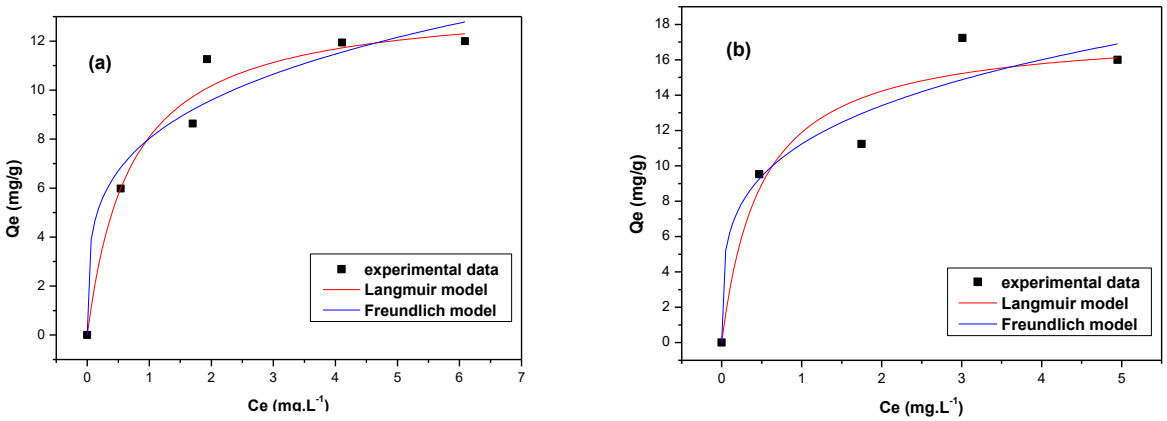

Figure IV. 11 Langmuir and Freundlich isotherms fitting nonlinear adsorption MB onto Fe_3O_4–HKDD3 nanocomposite (a), sono-adsorption of MB (b).

Figure IV.11 shows the experimental data fitted to Langmuir and Freundlich models. **Table IV.4** lists the correlation coefficients and isotherm constants with the experimental data. The Freundlich isotherm was selected as the best fitting model for the sono-adsorption process with a coefficient R^2 value of 0.96. the 1/n value is about 0.3 which confirms that the adsorption process is normal, favorable adsorption due to heterogeneity of adsorbent **[22]**. While the adsorption process follows Langmuir isotherm with a coefficient R^2 value of 0.97 and lower χ^2 **(0.68)**.

Table IV. 4 Parameters and error function data for adsorption isotherm models of MB onto M-HKDD3.

Isotherm	**Sono- assisted adsorption**		**Adsorption**
Langmuir	**q_m (mg/g)**	17.70	13.704
	K_L	2.043	1.439
	R_L	0.012-0.046	0.22-0.53
	R^2	0.95	0.968
	χ^2	2.885	0.686
Freundlich	**K_F**	11.23	8.020
	n	3.19	3.873
	R^2	0.96	0.944
	χ^2	2.343	1.228

IV.3 Conclusion

In summary, this study was focused on the modification of Algerian clay (HKDD3) by magnetite (Fe_3O_4) for the easier separation magnetic property. This work highlights the using a sono-adsorption method to eliminate methylene blue dye from the aqueous medium which is useful, rapid, and higher than the adsorption process. The adsorption capacity reached about 18.78 mg/g. Kinetics is influenced by the studied parameters: temperature, pH, and initial concentration. The adsorption behavior of M- HKDD3 for cationic MB could be well-described by the pseudo-second-order model. The thermodynamic studies showed endothermic and spontaneous adsorption processes. The application of ultrasound was proven to be effective in increasing the adsorption capacity.

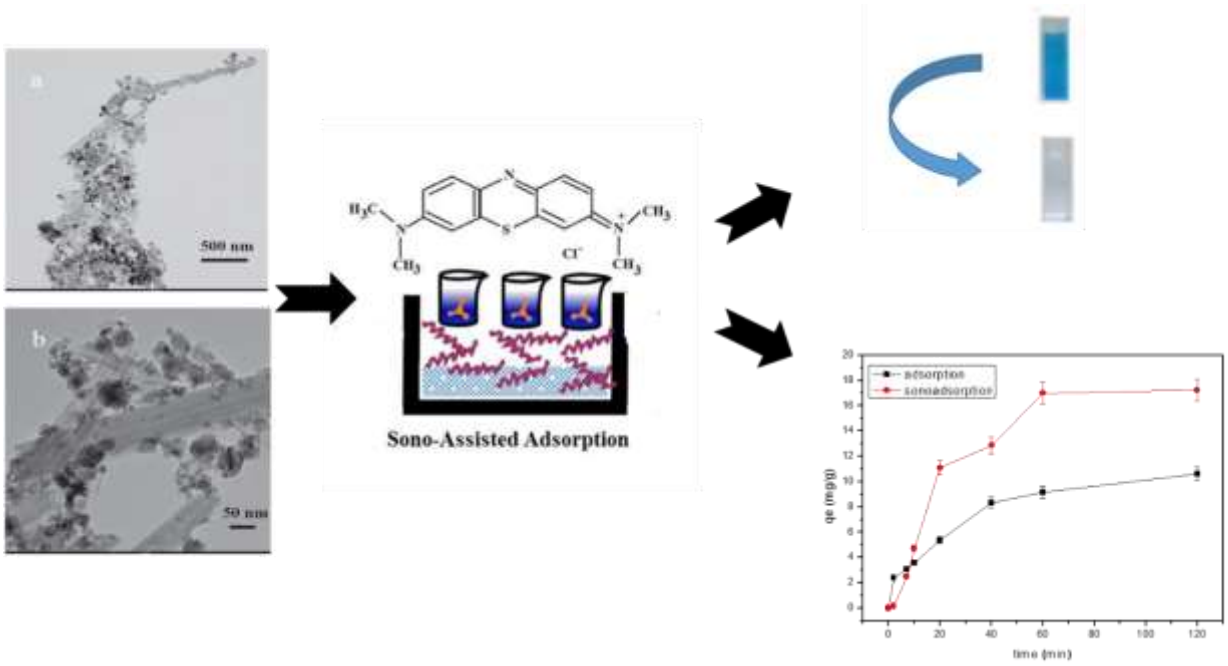

References

[1] F. Chargui, M. Hamidouche, H. Belhouchet, Y. Jorand, R. Doufnoune, G. Fantozzi, Mullite fabrication from natural kaolin and aluminium slag, Boletín de La Sociedad Española de Cerámica y Vidrio. 57 (2018) 169–177. https://doi.org/10.1016/j.bsecv.2018.01.001.

[2] P.K. Boruah, D.J. Borah, J. Handique, P. Sharma, P. Sengupta, M.R. Das, Facile synthesis and characterization of Fe 3 O 4 nanopowder and Fe 3 O 4 /reduced graphene oxide nanocomposite for methyl blue adsorption: A comparative study, Journal of Environmental Chemical Engineering. 3 (2015) 1974–1985. https://doi.org/10.1016/j.jece.2015.06.030.

[3] S. Mustapha, M.M. Ndamitso, A.S. Abdulkareem, J.O. Tijani, D.T. Shuaib, A.K. Mohammed, A. Sumaila, Comparative study of crystallite size using Williamson-Hall and Debye-Scherrer plots for ZnO nanoparticles, Adv. Nat. Sci: Nanosci. Nanotechnol. 10 (2019) 045013. https://doi.org/10.1088/2043-6254/ab52f7.

[4] R. Wang, G. Jiang, Y. Ding, Y. Wang, X. Sun, X. Wang, W. Chen, Photocatalytic Activity of Heterostructures Based on TiO $_2$ and Halloysite Nanotubes, ACS Appl. Mater. Interfaces. 3 (2011) 4154–4158. https://doi.org/10.1021/am201020q.

[5] Y. Du, P. Zheng, Adsorption and photodegradation of methylene blue on TiO2-halloysite adsorbents, Korean J. Chem. Eng. 31 (2014) 2051–2056. https://doi.org/10.1007/s11814-014-0162-8.

[6] T. Tsoufis, F. Katsaros, B.J. Kooi, E. Bletsa, S. Papageorgiou, Y. Deligiannakis, I. Panagiotopoulos, Halloysite nanotube-magnetic iron oxide nanoparticle hybrids for the rapid catalytic decomposition of pentachlorophenol, Chemical Engineering Journal. 313 (2017) 466–474. https://doi.org/10.1016/j.cej.2016.12.056.

[7] Y. Xie, D. Qian, D. Wu, X. Ma, Magnetic halloysite nanotubes/iron oxide composites for the adsorption of dyes, Chemical Engineering Journal. 168 (2011) 959–963. https://doi.org/10.1016/j.cej.2011.02.031.

[8] V. Amandine, M. Cédric, M. Sergio, D. Patricia, An ImageJ tool for simplified post-treatment of TEM phase contrast images (SPCI), Micron. 121 (2019) 90–98. https://doi.org/10.1016/j.micron.2019.01.006.

[9] R. Riahi-Madvaar, M.A. Taher, H. Fazelirad, Synthesis and characterization of magnetic halloysite-iron oxide nanocomposite and its application for naphthol green B removal, Applied Clay Science. 137 (2017) 101–106. https://doi.org/10.1016/j.clay.2016.12.019.

[10] M. Naderi, Surface Area, in Progress in Filtration and Separation, Elsevier, 2015: pp. 585–608. https://doi.org/10.1016/B978-0-12-384746-1.00014-8.

[11] K.S.W. Sing, R.T. Williams, Physisorption Hysteresis Loops and the Characterization of Nanoporous Materials, Adsorption Science & Technology. 22 (2004) 773–782. https://doi.org/10.1260/0263617053499032.

[12] E.P. Barrett, L.G. Joyner, P.P. Halenda, The Determination of Pore Volume and Area Distributions in Porous Substances. I. Computations from Nitrogen Isotherms, (2002). https://doi.org/10.1021/ja01145a126.

[13] A.R. Bagheri, Comparative study on ultrasonic assisted adsorption of dyes from single system onto Fe3O4 magnetite nanoparticles loaded on activated carbon: Experimental design methodology, Ultrasonics Sonochemistry. (2017) 11.

[14] M. Zhao, P. Liu, Adsorption behavior of methylene blue on halloysite nanotubes, Microporous and Mesoporous Materials. 1–3 (2008) 419–424. https://doi.org/10.1016/j.micromeso.2007.10.018.

[15] L.R. Bonetto, F. Ferrarini, C. de Marco, J.S. Crespo, R. Guégan, M. Giovanela, Removal of methyl violet 2B dye from aqueous solution using a magnetic composite as an adsorbent, Journal of Water Process Engineering. 6 (2015) 11–20. https://doi.org/10.1016/j.jwpe.2015.02.006.

[16] A. Khataee, M. Sheydaei, A. Hassani, M. Taseidifar, S. Karaca, Sonocatalytic removal of an organic dye using TiO2/Montmorillonite nanocomposite, Ultrasonics Sonochemistry. 22 (2015) 404–411. https://doi.org/10.1016/j.ultsonch.2014.07.002.

[17] A.S. Özcan, B. Erdem, A. Özcan, Adsorption of Acid Blue 193 from aqueous solutions onto BTMA-bentonite, Colloids and Surfaces A: Physicochemical and Engineering Aspects. 266 (2005) 73–81. https://doi.org/10.1016/j.colsurfa.2005.06.001.

[18] Y.S. Ho, G. McKay, Pseudo-second order model for sorption processes, Process Biochemistry. 34 (1999) 451–465. https://doi.org/10.1016/S0032-9592(98)00112-5.

[19] N.K. Gupta, Y. Ghaffari, J. Bae, K.S. Kim, Synthesis of coral-like α-Fe2O3 nanoparticles for dye degradation at neutral pH, Journal of Molecular Liquids. 301 (2020) 112473. https://doi.org/10.1016/j.molliq.2020.112473.

[20] Z. Cheng, X. Liu, M. Han, W. Ma, Adsorption kinetic character of copper ions onto a modified chitosan transparent thin membrane from aqueous solution, Journal of Hazardous Materials. 182 (2010) 408–415. https://doi.org/10.1016/j.jhazmat.2010.06.048.

[21] X. Hu, J. Wang, Y. Liu, X. Li, G. Zeng, Z. Bao, X. Zeng, A. Chen, F. Long, Adsorption of chromium (VI) by ethylenediamine-modified cross-linked magnetic chitosan resin: Isotherms, kinetics and thermodynamics, Journal of Hazardous Materials. 185 (2011) 306–314. https://doi.org/10.1016/j.jhazmat.2010.09.034.

[22] N.K. Gupta, M. Saifuddin, S. Kim, K.S. Kim, Microscopic, spectroscopic, and experimental approach towards understanding the phosphate adsorption onto Zn–Fe layered double hydroxide, Journal of Molecular Liquids. 297 (2020) 111935. https://doi.org/10.1016/j.molliq.2019.111935.

CHAPTER V
Characterization of titanium dioxide nanoparticles loaded on magnetic clay and its application for MB removal

In this chapter, we present the characterization results as well as photocatalytic tests of methylene blue dye from the aqueous medium, using TiO_2 and doped TiO_2 with silver and iron supported on the magnetic halloysite clay HKDD3. The TOC removal was carried out. Among the photocatalysts, the Ag-TiO_2-MHKDD3 is the best one in the photodegradation of methylene blue in comparison to other samples. For this reason, we studied different parameters such as concentration of dyes, catalyst mass, pH, and the effect of scavengers.

V.1 Characterization of prepared catalysts

V.1.1 XRD analysis

Figure V.1 represents the XRD patterns of prepared samples. Similar peaks are from Anatase TiO_2, Fe_3O_4, halloysite, and kaolinite clay.

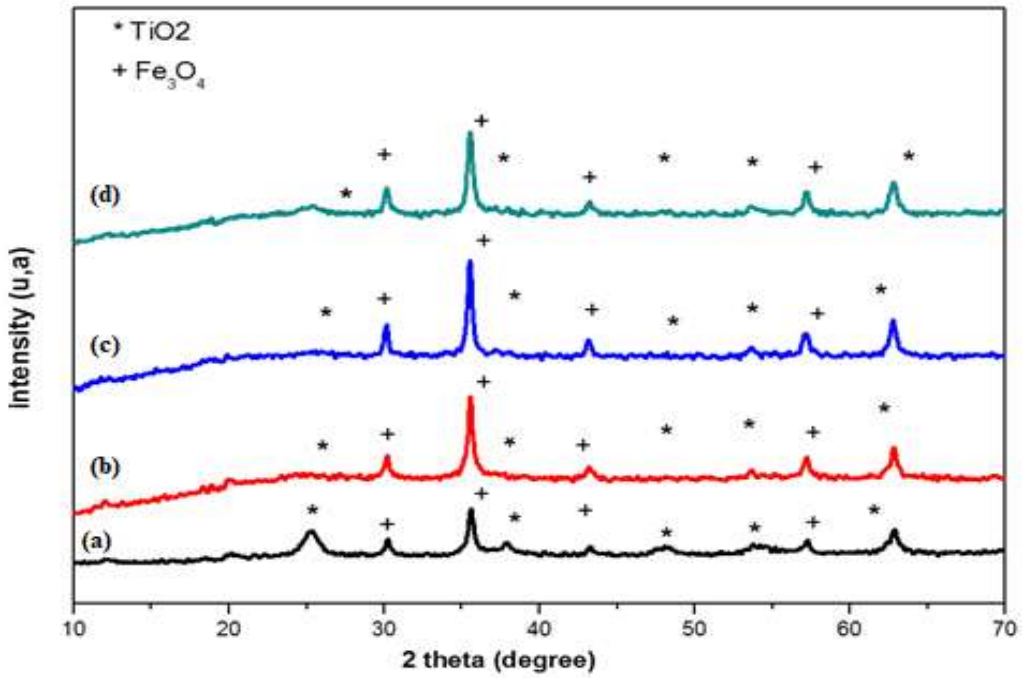

Figure V. 1 XRD patterns of prepared samples (a) TiO_2-MHKDD3, (b) Fe doped TiO_2-MHKDD3 (c) Ag doped TiO_2-MHKDD3 (d) Ag-Fe doped TiO_2-MHKDD3**.**

The presence of the other phases was not seen, owing to the low concentration of dopant silver (Ag^+) from silver nitrate and iron (Fe^{3+}) from nitrate iron precursors. Furthermore, the reflection peaks at 2θ values about 30.1, 35.6, 43.3, 57.1, and 62.7 refer to (220), (311), (400), (511), and (440) planes of magnetite particles. According to [JCPDS 86- 1157] file, the peaks were displayed at 2θ = 25.2, 37.9, 48.2, 54.7 and 62.8 with reflection planes (101), (004), (200), (105), and (204). After deposition by Fe_3O_4 and doped TiO_2 particles, the peaks of clay were significantly weakened as shown in the 2θ position: 9.41, 18.7, 19.8, which indicates that the particles immobilized on the surface of HKDD3 clay.

V.1.2 FTIR Characterization:

The FT-IR analysis is used to investigate the functional group and chemical bonds present on the surfaces of the material **(Figure V. 2)**. It is possible to observe intense bands at 3610 cm^{-1} and 3690 cm^{-1} which are assigned to OH stretching vibrational groups **[1]** of Halloysite Algerian clay. Besides, the signal at 1635 cm^{-1} can be attributed to OH deformation for the adsorbed molecules of water. It can be seen intense peaks at 1114, 987, and 907 cm^{-1}, which are referred to as the Si-O stretching group **[2]**, Al-O-Si, and Al-OH vibration groups, respectively **[3]**. The band 514 cm^{-1} corresponds to Al-O-Si deformation **[4]**. After the modification by TiO_2 and Fe_3O_4 nanoparticles, the same peaks were presented in other catalysts. However, the shifting of a Si-O band from 1000 cm^{-1} to 1025 cm^{1} and the decrease in intensity can be explained by the formation of hydrogen banding between TiO_2 and Si-OH (outer surfaces of HKDD3 clay) **[5]**. The characteristic band of Fe_3O_4 around 580 cm^{-1} can be overlapped by the Al-O-Si band of HKDD3 at 520 cm-^{1} **[6,7]**.

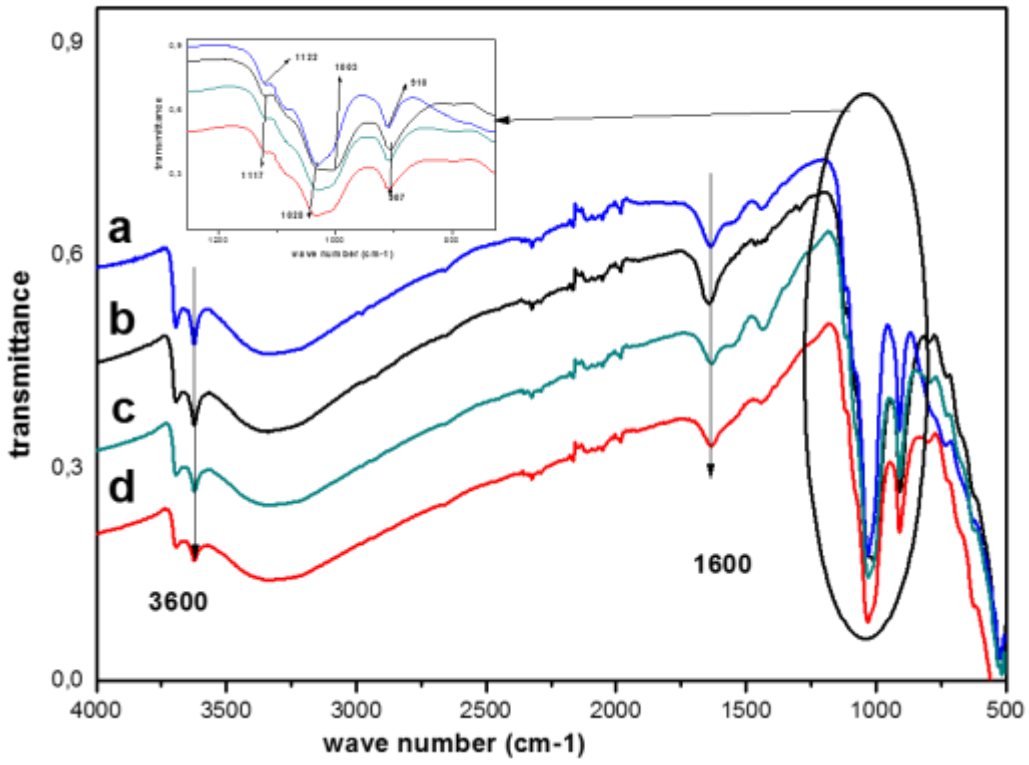

Figure V. 2 FTIR spectrum of different samples (a) Ag-doped TiO_2, (b) Ag-Fe doped TiO_2 (c) Fe doped TiO_2, (d) TiO_2-MHKDD3**.**

V.1.3 UV-Visible DRS analysis:

The absorption range of the samples is a crucial characteristic for studying photoactivity under UV and visible irradiation. Diffuse reflection spectroscopy was performed to characterize the photocatalysts' optical properties. The primary objective of metallic ion doping is to improve light absorption in the visible spectrum. The TiO_2 HKDD3 spectra exhibited an absorbance of 442 nm, as shown in **Figure V.3 (A)** after doping TiO_2 particles with silver nitrate and ferric nitrate, the onset absorption ranges from 400 to 600 nm with broadband in visible, especially for $FeTiO_2$-HKDD3, and Ag-Fe TiO2-HKDD3 due to the low bandgap. After using the Tauc plot equation (providing the direct bandgap) to determine the bandgap energy of each sample which is illustrated in **Figure V.3**.(**B**)

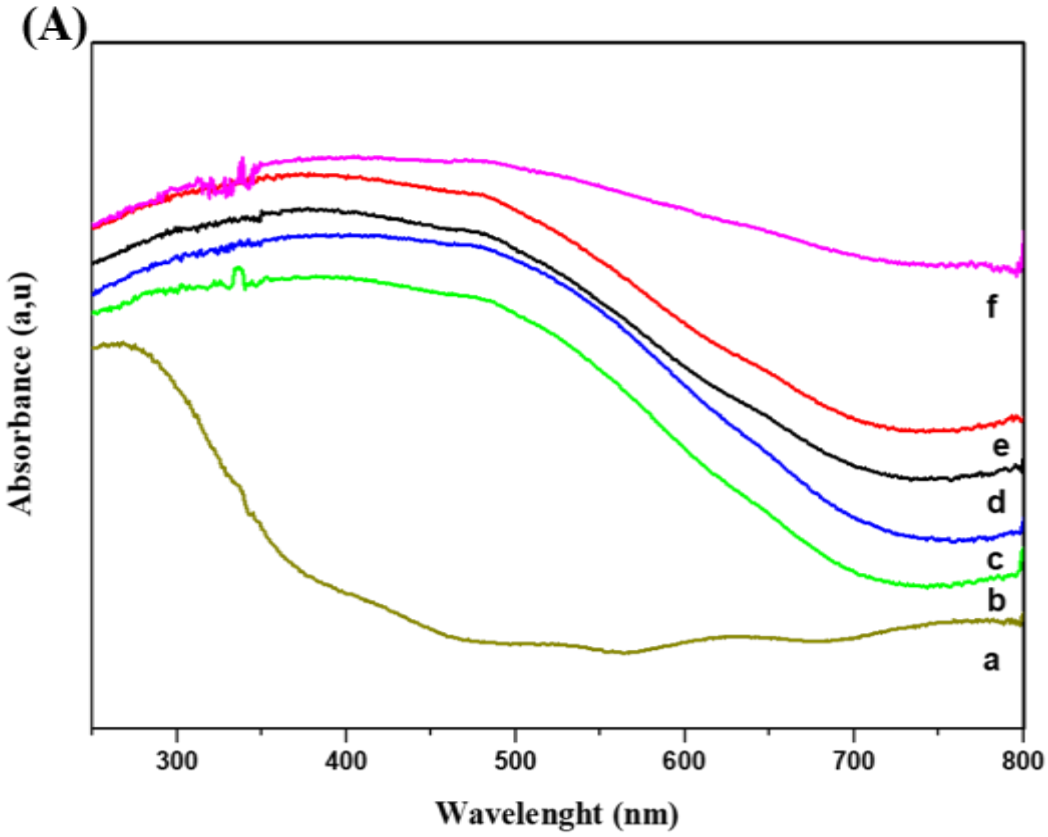

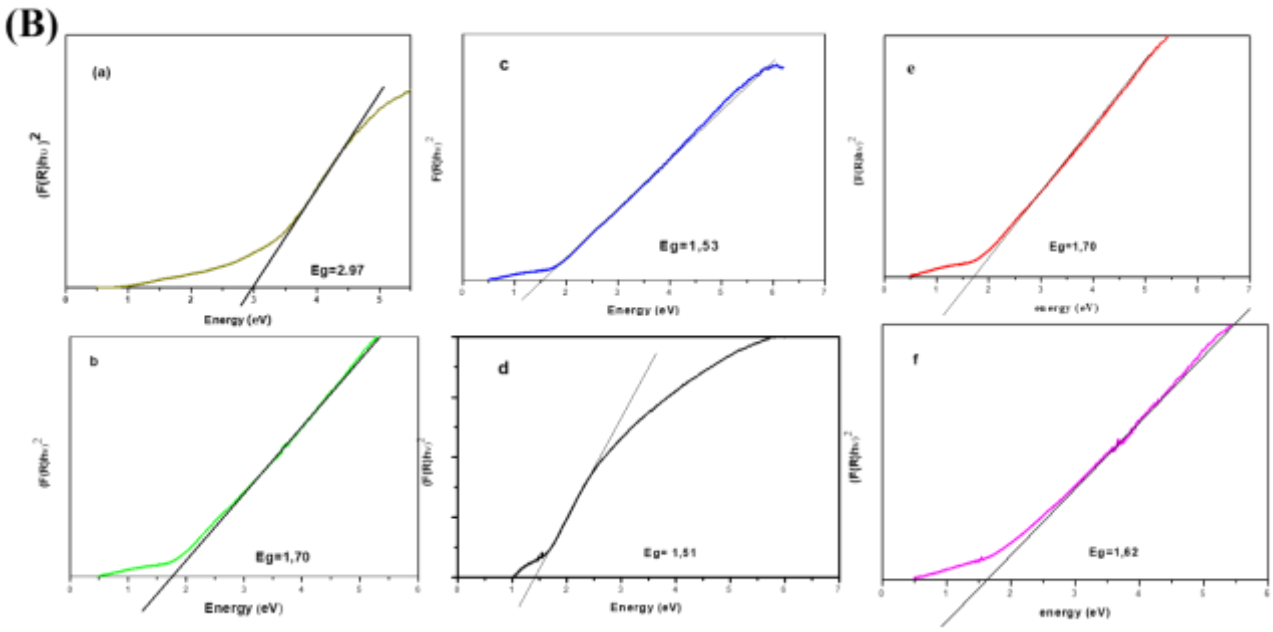

Figure V. 3 Uv- Visible DRS spectra of prepared samples (A) and their Tauc plots (B), (a) TiO_2HKDD3, (b) TiO_2 M-HKDD3, (c) Fe doped TiO_2 M-HKDD3, (d) Ag-Fe doped TiO_2 M-HKDD3,(e) Ag-doped TiO_2 M-HKDD3,(f) MHKDD3

As observed in **table V.1**, the bandgap energy is ordered as followed TiO_2HKDD3> Ag- TiO_2-Fe_3O_4-HKDD3> TiO_2-Fe_3O_4-HKDD3> Fe_3O_4-HKDD3> Fe- TiO_2-Fe_3O_4-HKDD3> Ag-Fe- TiO_2-Fe_3O_4-HKDD3. The iron oxide and doping TiO2 by silver and iron helped to decrease the bandgap energies. The decreased bandgap contributed to the generation of photon electron-hole pairs, which led to an increase in photocatalytic activity.

Table V. 1 values of bandgap energies after using Tauc plot equation.

Samples	Energy band gap (eV)
TiO_2-HKDD3	2.97
Fe_3O_4-HKDD3	1.62
Ag- TiO_2-Fe_3O_4-HKDD3	1.70
TiO_2-Fe_3O_4-HKDD3	1.67
Fe- TiO_2-Fe_3O_4-HKDD3	1.53
Ag-Fe- TiO_2-Fe_3O_4-HKDD3	1.51

V.1.4 TEM characterization

As shown in **figure V.4**, (as mentioned before in chapter III), the TEM images show that the morphology of the used clay (HKDD3) corresponds to the halloysite tubular shape. Fe_3O_4 –HKDD3 was attached with clusters of magnetite particles. The aggregates of Fe_3O_4 nanoparticles were constituted of even smaller subunits, showing that the smaller nanoparticles produced first and later agglomerated. After deposition of TiO_2 nanoparticles, the HKDD3 clay becomes rougher with irregular dispersion. As observed, there are a few aggregations of nanoparticles. Some TiO_2 nanoparticles were observed adhering to the HKDD3 hollow cavity walls. The attachment might be linked to HKDD3's structures, which include big pore volume and sufficient hydroxyl groups, allowing metal ions to reach and adsorb on the surface easily. It can be observed that the average particle size of TiO_2 loaded on clay is 10-50 nm. In the case of doping, the silver nanoparticles are not apparent in images due to the low concentration but the XPS results confirm their presence.

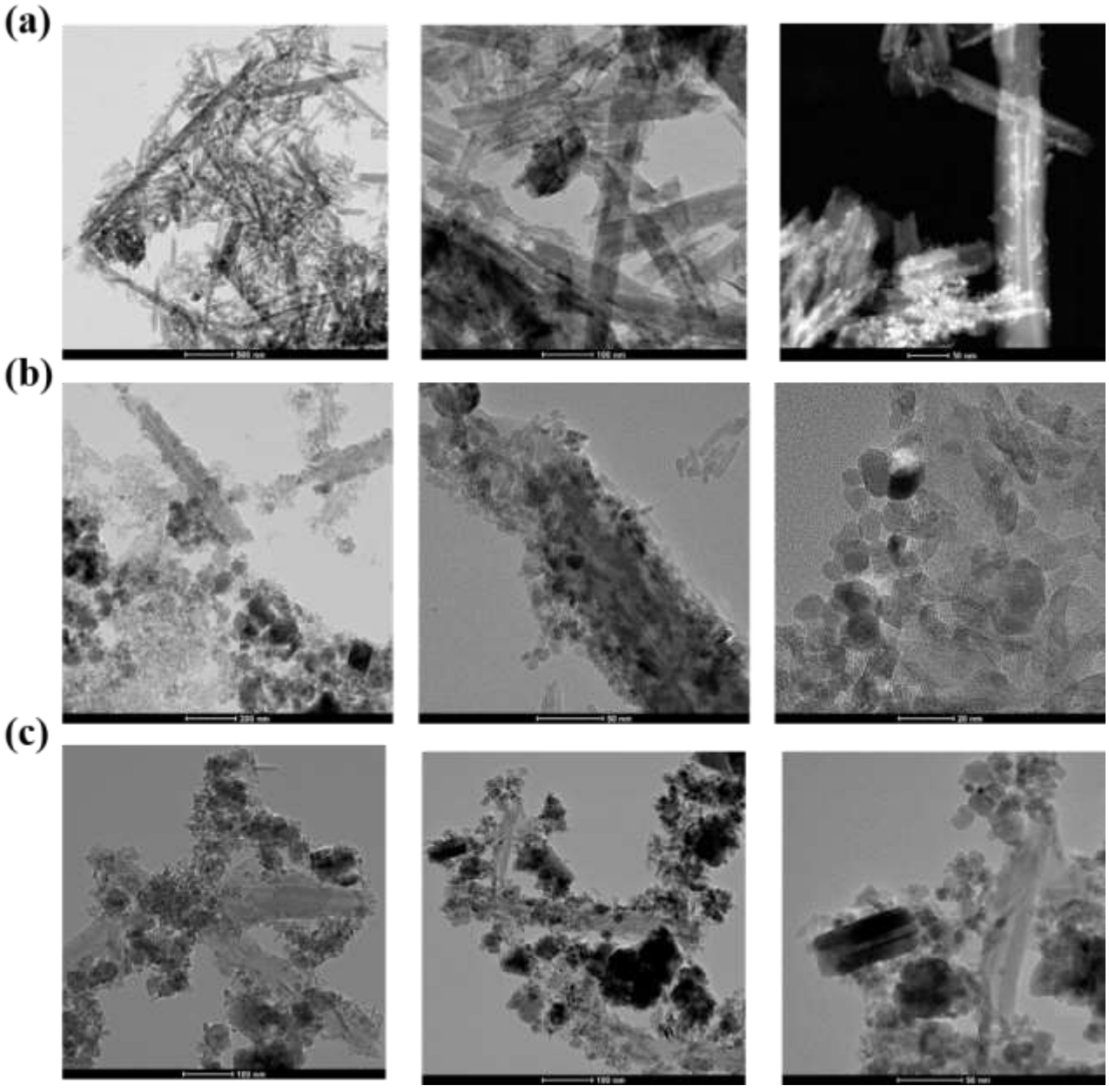
(a)
(b)
(c)

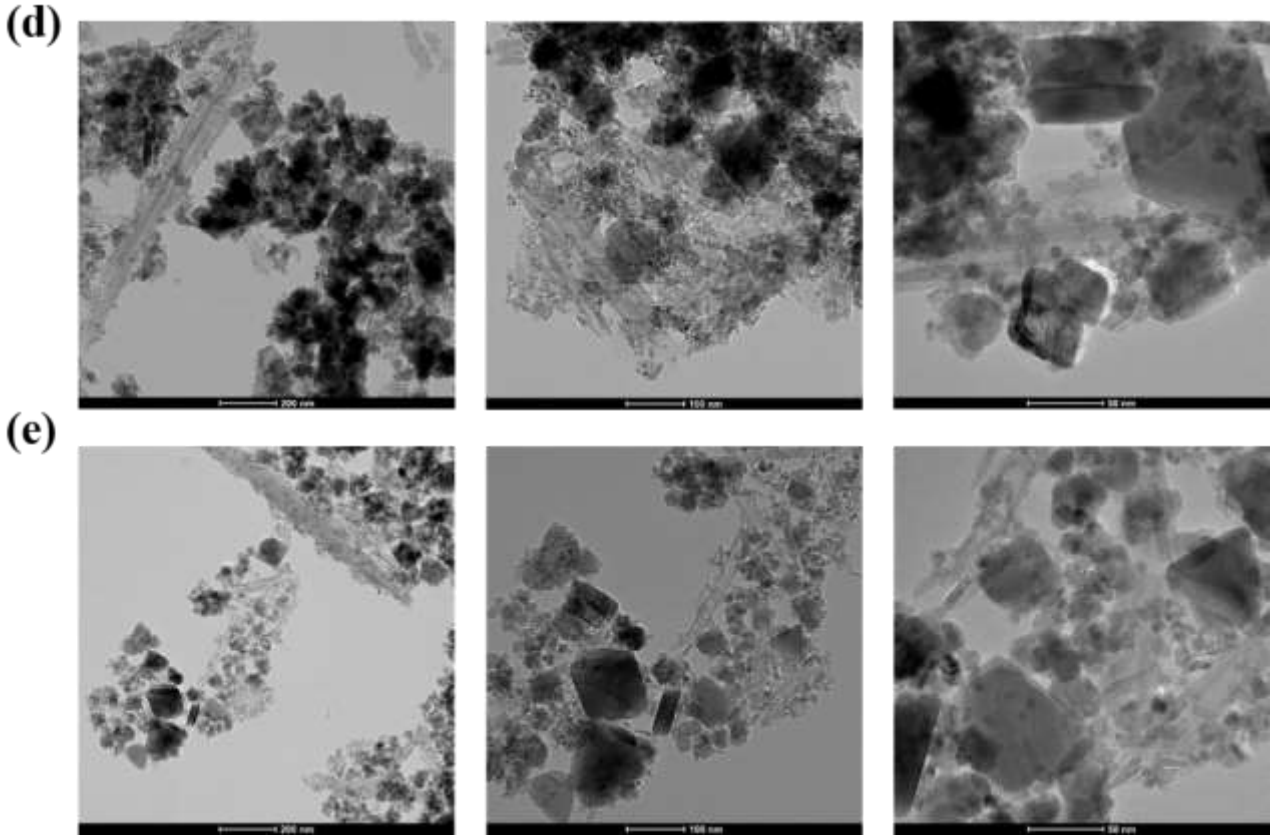

Figure V.4 TEM images of prepared samples (a) TiO_2-HKDD3, (b) TiO_2-M-HKDD3, (c) Ag-TiO_2 M-HKDD3, (d) Fe-TiO_2 M-HKDD3, (e) Ag-Fe-TiO_2 M-HKDD3.

V.1.5 BET analysis

The N_2 adsorption-desorption isotherms and pore size distribution plots of photocatalysts are shown in **Figure V.5**. All samples have type IV isotherms indicative of mesopores structure, except for the TiO_2-MHKDD sample, which has type III isotherms. The hysteresis loop appears to be of the H3 type, which is typical of materials with a large pore size distribution. The pore size distribution included one peak centered at around 20 nm, while the remaining peaks ranged from 50 nm to 100 nm, respectively.

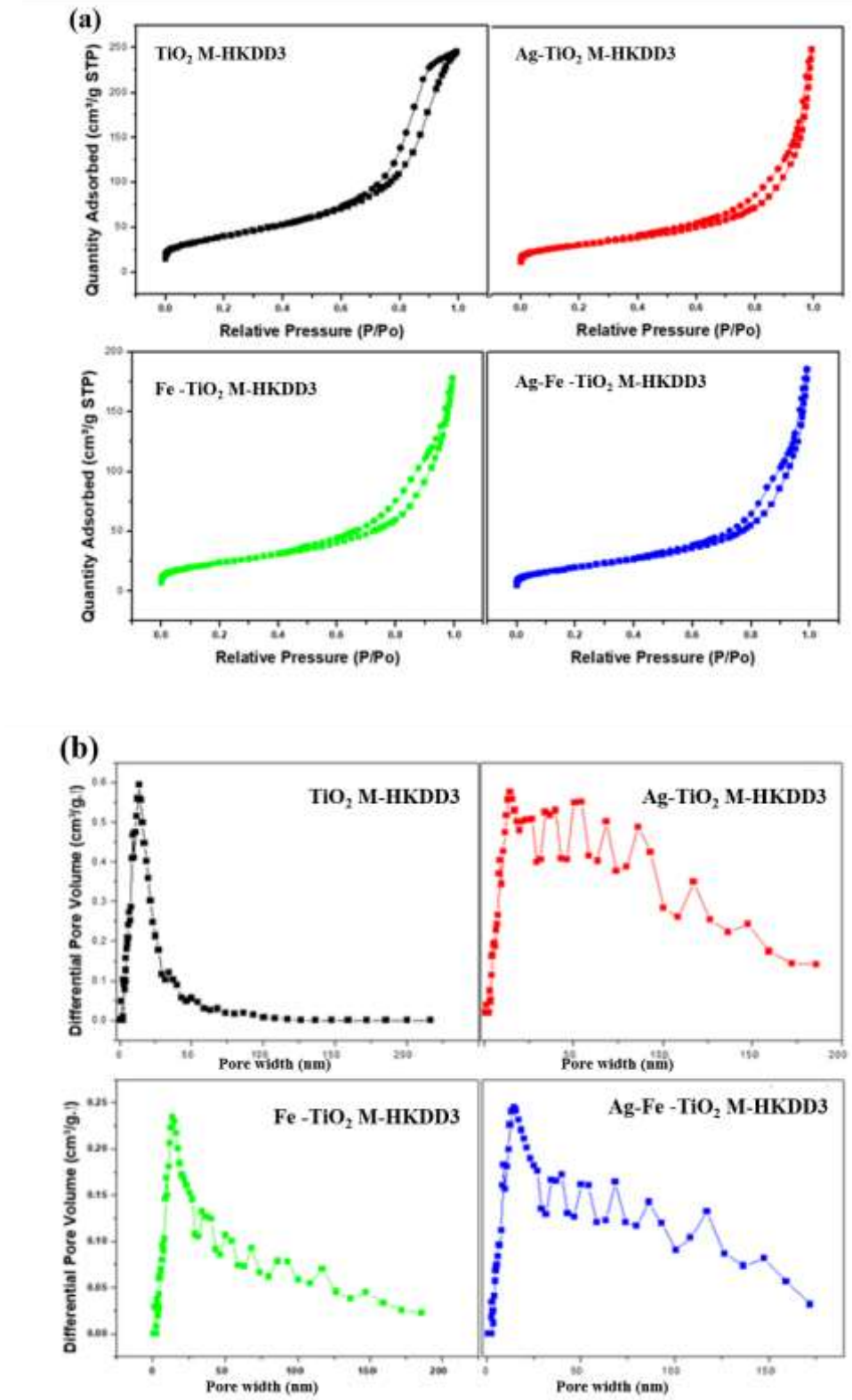

Figure V. 5 N_2 adsorption-desorption isotherms (a), pore size distribution plots of TiO_2-M-HKDD3, Ag-TiO_2 M-HKDD3, Fe-TiO_2 M-HKDD3, Ag-Fe-TiO_2 M-HKDD3.

The Surface specific area (SSA), pore volume, and area in pores of TiO_2- HKDD3 sample and doped are listed in **tableV.2.** It was found that the SSA for TiO_2- MHKDD3 composite (145 m^2/g) is 1.8 times than that of Ag- TiO_2- MHKDD3 (82 m^2/g) and 1.7 times than that of Fe-TiO_2- MHKDD3 (85.67 m^2/g) and 1.6 times than Ag- Fe-TiO_2- MHKDD3 89.37 m^2/g.

The porous nature of the samples and their large specific surface area may boost the adsorption capacity to organic contaminants, allowing fast diffusion of the reactants and so increasing the photocatalytic reaction rate **[8].**

Table V. 2 The physicochemical of as-prepared materials

sample	Volume in Pores cm^3/g (x 10^{-3})	Total Volume in Pores cm^3/g	Area in Pores m^2/g	Total Area in Pores m^2/g	BET Surface Area m^2/g
TiO_2M-HKDD3	9.34	0.35	6.57	75.77	145.01
TiO_2-HKDD3	0.80	0.29	17.97	63.25	98.67
Ag-TiO_2M-HKDD3	2.95	0.22	26.86	50.14	82.69
Ag-Fe-TiO_2-M-HKDD3	3.87	0.24	24.34	52.42	89.38
Fe-TiO_2-M-HKDD3	3.63	0.20	21.76	49.51	85.68

V.1.6 XPS analysis

XPS analysis was performed for prepared photocatalysts Fe doped TiO_2 M-HKDD3, Ag-doped TiO_2 M-HKDD3 Ag-Fe doped TiO_2 M-HKDD3 to determine the elements and their chemical state. This sample was composed of Si, Al, Fe, Ti, Ag, and O as shown in **Figure V.6**. The peak of C was seen due to the adventitious hydrocarbon from the XPS instrument **[9]**. The Si 2p XPS spectrum was located at 103 eV and assigned to SiO_2 which was the main composant of Algerian Halloysite clay. Peaks of Ti 2p3/2 and Ti 2p1/2 were observed at 458.81 and 464.56 eV, respectively **[10]**. These binding energies correspond to Ti^{4+}, which could indicate the formation of TiO_2. Besides, the binding energy of O1s was located at 533.92 eV, which is attributed to Ti-OH-and adsorbed molecules of

water on the surface of HKDD3 clay. As seen from **Figure 6. B** the existence of peaks with binding energy at 368.3 eV and 374.36 eV can be ascribed to Ag 3d 5/2 and Ag 3d3/2, respectively. The 6.0 eV difference between the two peaks also means that metallic Ag is presented **[11]**. As displayed in **Figure 6.C** Fe2P spectrum shows peaks at 711.11ev, 724.62ev for Fe2p3/2 and Fe2p1/2 respectively [**12**]. The gap of 13.6 eV between the peaks could be assigned to Fe, which was presented in Fe_2O_3. The satellite peak was exhibited at around 719 eV. These binding energies were referred to as the chemical state of Fe^{3+} (Fe_3O_4) **[13].**

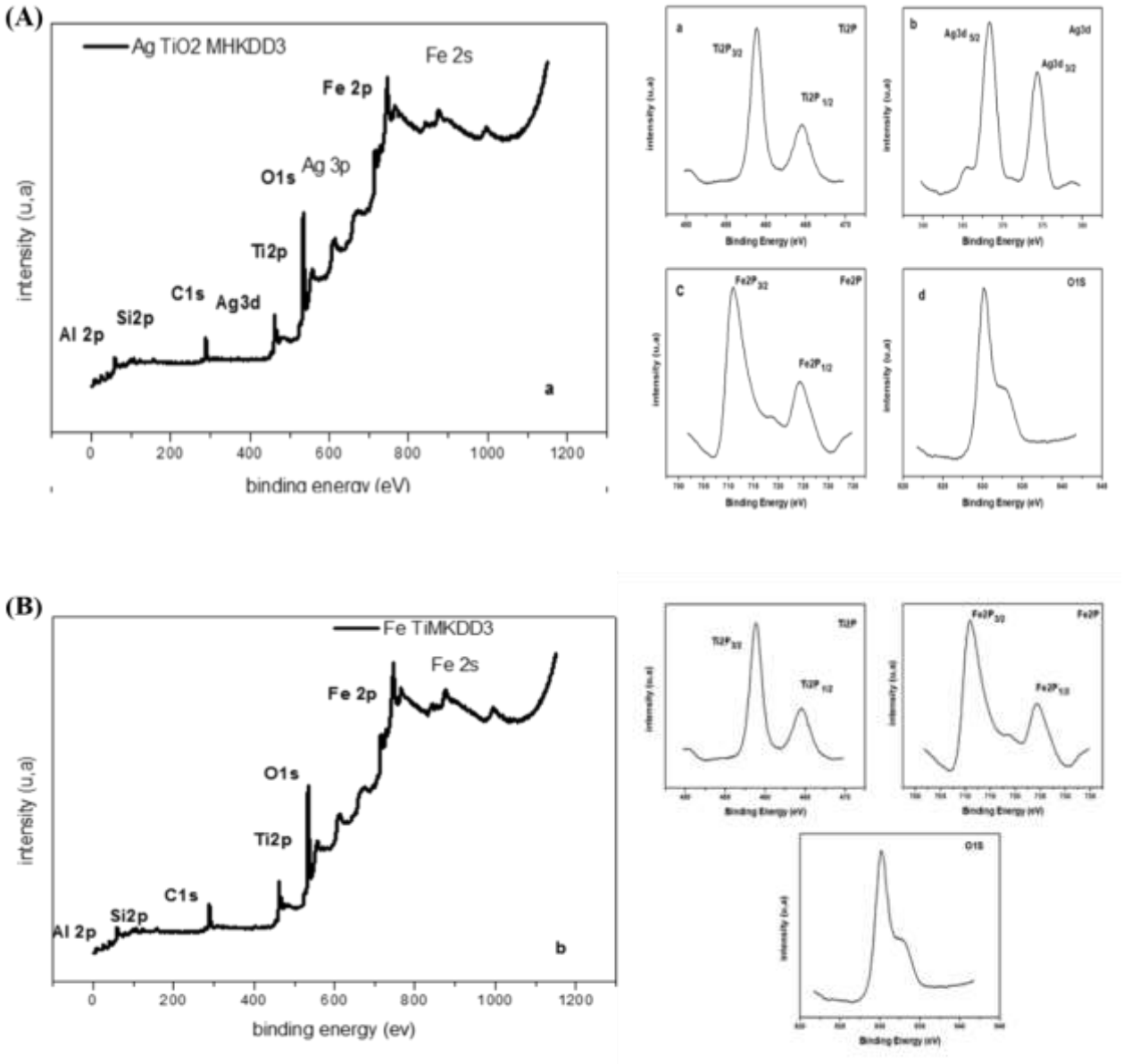

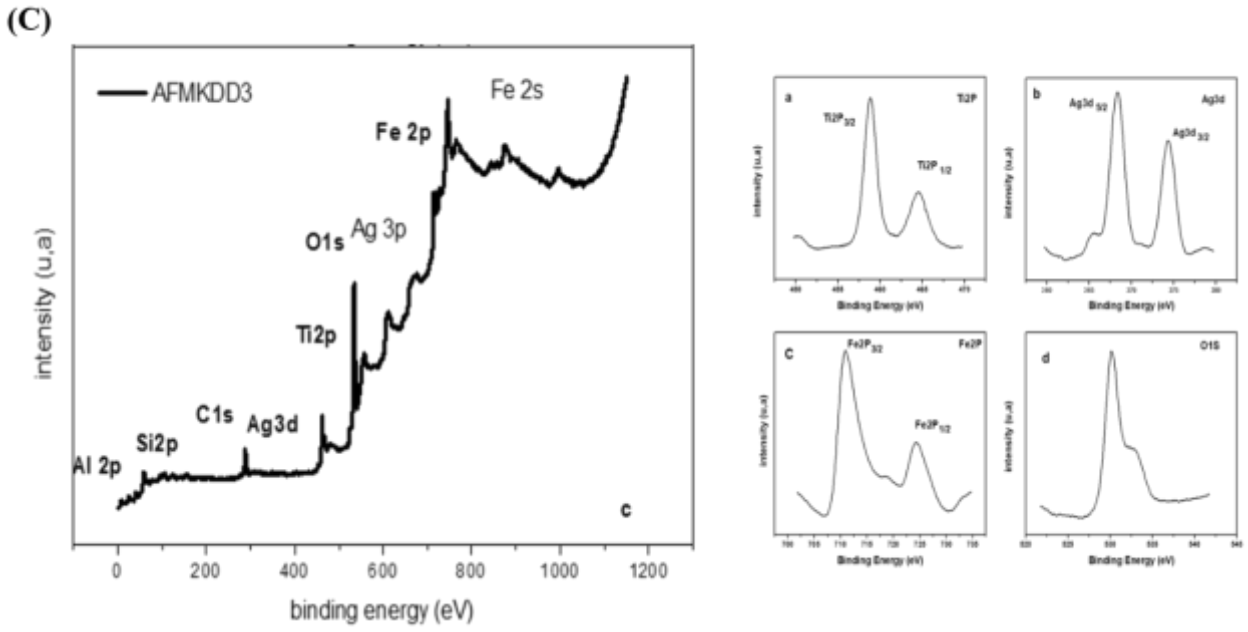

Figure V. 6 XPS spectra of Ag-TiO_2-MHKDD3 photocatalyst (A); Fe-TiO_2-MHKDD3 photocatalyst (B); Ag-Fe-TiO_2-MHKDD3 photocatalyst (C).

V.2 Photocatalytic activity for MB dye removal

The discoloration and mineralization of MB under visible light irradiation depicts in **Figure V.7**. Note that there is a strong decrease in the concentration of MB before irradiation and this corresponds to the adsorption of MB onto the surface of clay HKDD3. The best performance was obtained by the catalyst prepared using silver doping titanium dioxide nanoparticles. Consequently, we choose to test the latter for degradation of methylene blue dye with specific parameters such as concentration of the solution, mass loading catalyst, pH, and scavenger.

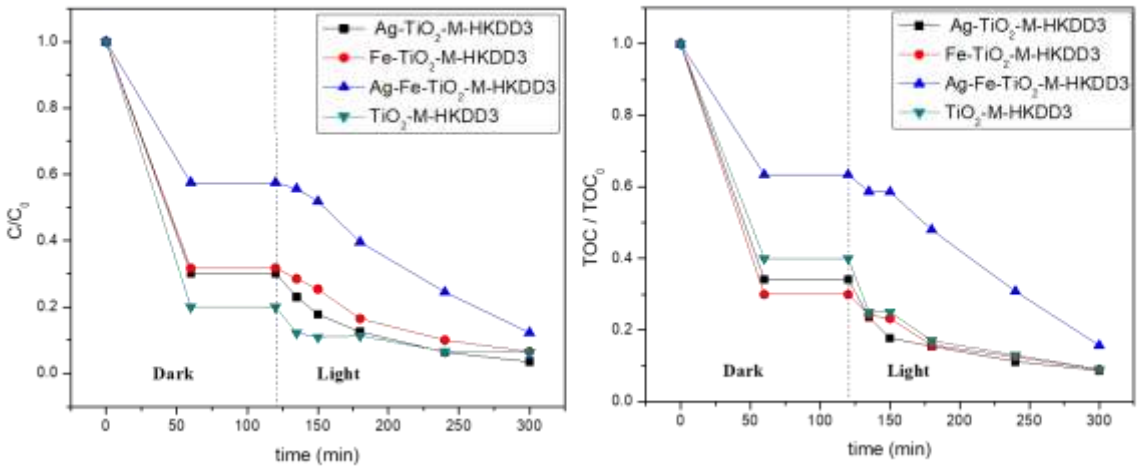

Figure V. 7 Photodegradation of methylene blue by catalysts: Ag-Fe-TiO_2- M-HKDD3, Fe-TiO_2-M-HKDD3, Ag-TiO_2-M-HKDD3, TiO_2- M-HKDD3.

The results show that the doping of TiO_2 with Ag, and Fe accelerates the degradation of methylene blue. The photocatalytic activity of the samples under visible light irradiation varies according to the following decreasing order: Ag-TiO_2-M-HKDD3> Fe-TiO_2-M-HKDD3> TiO_2-M-HKDD3>Ag-Fe- TiO_2-M-HKDD3. The metallic nanoparticles act as electron collectors and improve the charge separation. In addition, the reactivity of TiO_2 doped with Ag under visible light irradiation is attributed to the surface plasmon resonance of silver nanoparticles **[14]**.

The discoloration of MB dye is not enough to prove its mineralization; only the measurement of the total organic carbon (TOC) can prove it. The TOC removal rates achieved about 70% for both Fe-TiO_2-MHKDD3 and TiO_2-MHKDD3, 75% for Ag-Fe-TiO_2- MHKDD3, and Ag-TiO_2- MHKDD3 catalysts (**table V.3**.)

Table V. 3 Discoloration and mineralization of MB

catalysts	Quantity adsorbed (%)	Discoloration (%)	TOC removal (%)
Ag-TiO_2-M-HKDD3	70	92	75
Fe-TiO_2- M-HKDD3	68	90	70
Ag-Fe-TiO_2- M-HKDD3	43	88	75
TiO_2- M-HKDD3	80	89	70

The purpose of this study was to determine the effectiveness of photocatalytic activity in the presence of Ag-doped TiO_2 – Fe_3O_4 loaded on Algerian halloysite for the elimination of methylene blue (MB) dye from an aqueous solution under visible light irradiation. The impact of the following operational factors on photocatalytic activity was studied to identify the optimum conditions for cationic dye discoloration and mineralization: photocatalyst loading, starting concentration of MB contaminant, and initial pH. Additionally, photocatalytic tests with molecules able to scavenger the reactive oxygen species (ROS) were carried out to identify the main ROS involved in the degradation mechanism.

V.2.1 Photocatalyst loading

The effect of photocatalyst loading on the photocatalytic degradation process was investigated. It is a critical factor in photocatalysis because the number of active sites in the suspension and the photo-adsorption capacity of the catalyst employed can have a significant impact on photodegradation efficiency. Therefore, an Ag-TiO_2-M-HKDD3 concentration ranging from 0.312 to 1.25 g/L was used to investigate its influence on discoloration and mineralization efficiency, and to find out the optimal loading value. The tests were conducted using 80 mL of MB solution with an initial concentration of 7 mg/L. The results presented in **Figure V.8**, were shown that the photocatalytic activity is strongly influenced by the variation of the photocatalyst loading for MB dye. The catalyst mass affects both discoloration and mineralization efficiency. This is owing to the increased number of active Ag-TiO_2-M-HKDD3 catalyst sites **[13]**. The result is a clear saturation translated by a plateau where the discoloration and the mineralization of the photocatalyst remain

relatively constant, in agreement with the expected trend at the high level of concentration, where the photocatalyst particles screen themselves **[1]**.

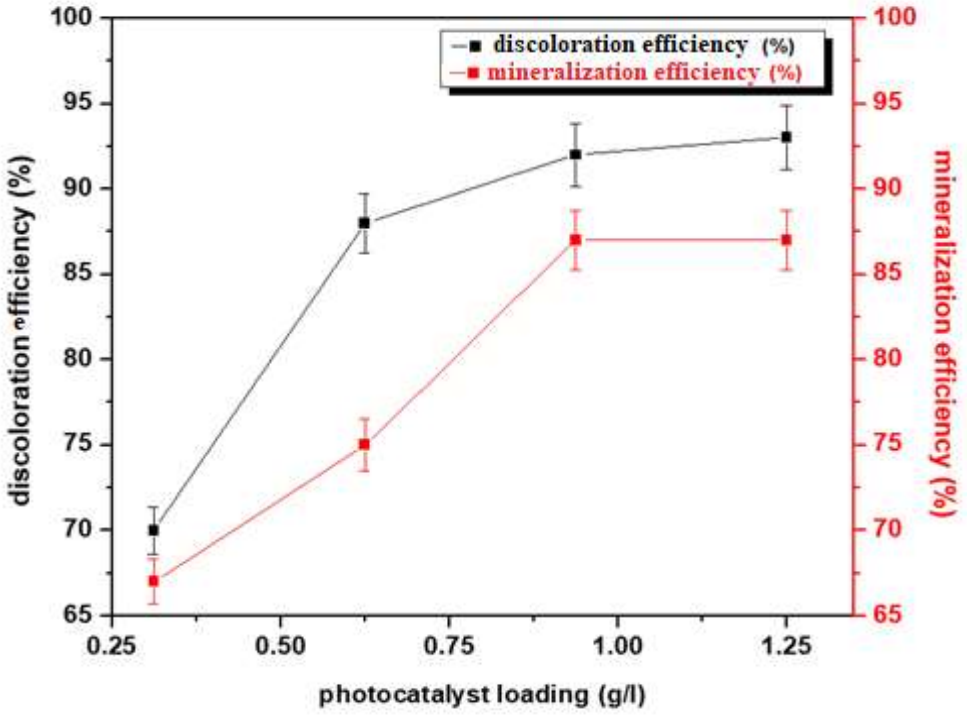

Figure V. 8 Effect of photocatalyst loading Ag-TiO_2-MHKDD3 on the discoloration and mineralization efficiency of MB dye.

It is noted that after three hours of visible light irradiation is sufficient to mineralize 87% of the dye for a photocatalytic loading of 0.937 and 1.25 g/l. On the other hand, the mineralization efficiency of 67 and 75% are obtained respectively for 0.3 and 0.9 g/l. Therefore, the optimal loading of the photocatalyst was at 0.9 g/l because this was the level of concentration useful to get the higher TOC removal, without the ineffective adding of further mass of photocatalyst.

V.2.2 Effect of Initial dye concentration

The influence of the initial concentration of the MB dye on the efficiency of photocatalysis was studied for different values ranging from 7 to 28 mg/l under visible light irradiation using the obtained optimal Ag-TiO_2-MHKDD3 dose of photocatalyst 0.937 g/l. According to the results shown in **Figure V.9**, it can be seen that the efficiency of the reaction is inversely proportional to the concentration; the

photocatalytic efficiency decreases with the increase of the concentration of MB dye **[15]**. The best efficiency is obtained with the lowest concentration (7 mg/l) with a discoloration efficiency of 92% and mineralization of 87%.

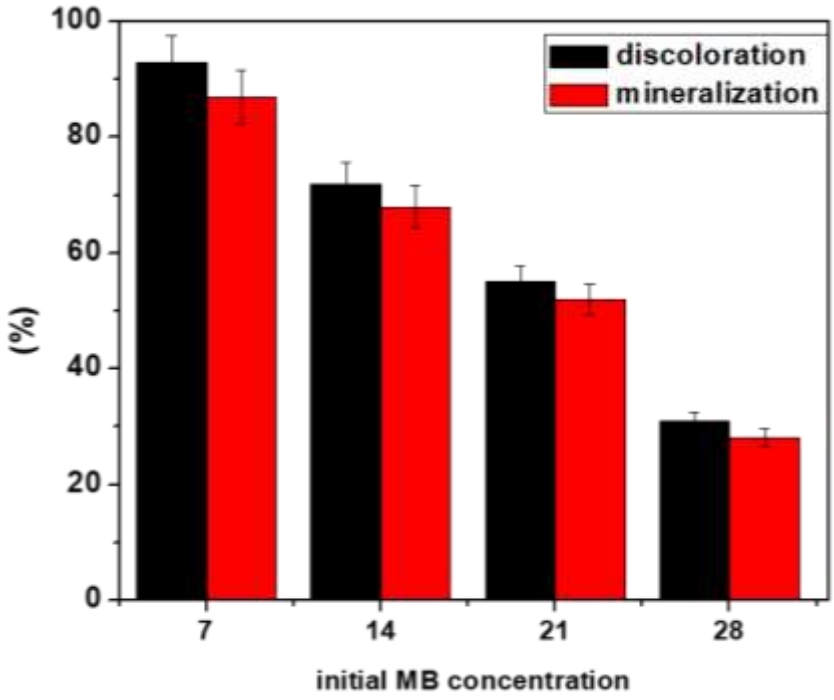

Figure V. 9 Effect of the initial MB concentration on photocatalytic discoloration and mineralization

The obtained results can be interpreted as follows: a high MB concentration leads to a high number of pollutant molecules adsorbed on the surface, reducing the generation of the reactive oxygen species (ROS), because the active sites of the photocatalyst were occupied by dye molecules **[16]**. In addition, the high dye concentration increases the opacity and turbidity of the solution, which reduces the penetration of light through the solution, and the absorption of photons by the catalyst particles was decreased, and consequently, the photocatalytic activity is reduced **[17]**.

V.2.3 Effect of pH

It was also found that the pH of the solution impacts the surface charge of the photocatalyst and the degree of MB ionization [18]. Its effect was examined by changing the initial pH solution at 5 and 8.63 using the optimal photocatalyst loading (0.937 g/l) and the optimal initial concentration of

MB (7 mg/l). The initial pH of the solution with an initial MB concentration of 7 mg/l was equal to 6.70.

Methylene blue is a cationic dye, therefore its absorption is favored for high pH values [19]. The catalyst surface is mainly negatively charged at high pH, resulting in a significant interaction between the photocatalysts surface and the cationic ions of the dye, resulting in strong adsorption. At low pH, however, both the surface of Ag-TiO_2-M-KDD3 and the dye molecules are positively charged, resulting in weak adsorption. Indeed, with an increase in pH, the adsorption of the MB on the photocatalyst surface increases, resulting in a higher degradation rate [20]. Nonetheless, for high alkaline pH, the hydroxyl radicals are rapidly scavenged, they do not have the opportunity to react with dyes and this leads to a decrease in photocatalytic activity.

Figure V.10 shows the effect of pH on the mineralization efficiency under 3 h of visible light irradiation and the apparent discoloration kinetic constant. The results highlight that a low photoactivity was obtained at a pH equal to 5; discoloration and mineralization efficiency are 75, and 71%, respectively. The optimal pH is equal to 6.7; it shows the highest K_{app} value (0.16 min^{-1}) with discoloration and mineralization efficiency of 92 and 87%. For this reason, we have opted to conduct the experiments at pH equal to 6.7.

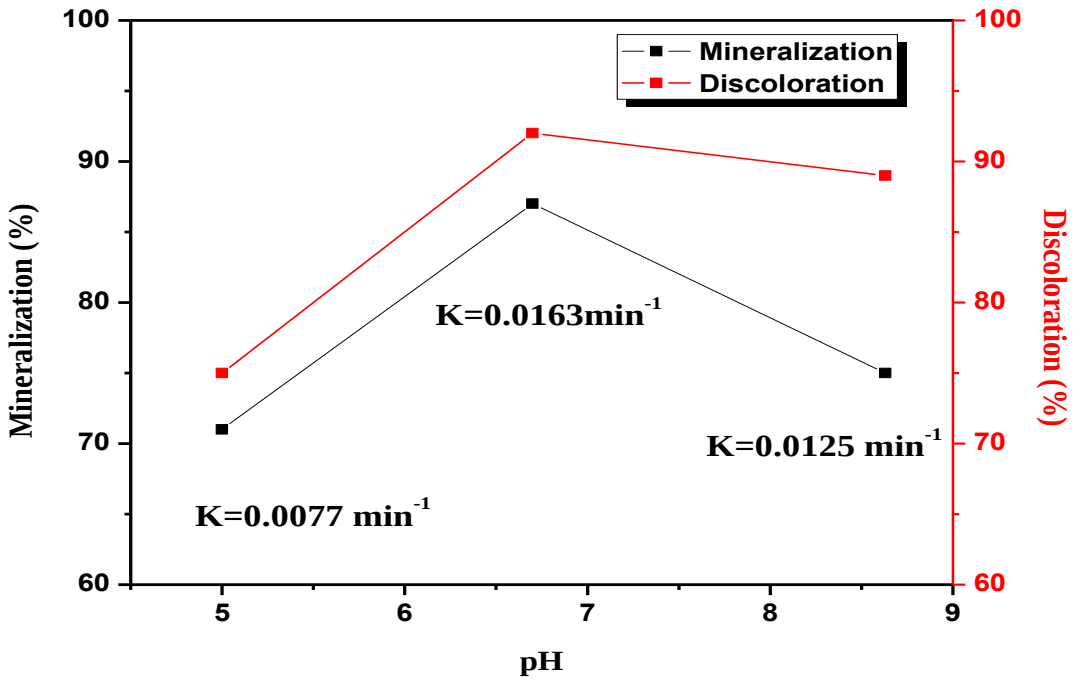

Figure V. 10 Effect of pH on the mineralization, and discoloration efficiency of MB dye and K_{app}.

V.2.4 Effect of Scavengers

During the MB photocatalytic discoloration process, the role of reactive oxygen species (ROS) such as hydroxyl radicals, superoxide, and positive holes was studied using Ag-TiO_2-MHKDD3 with its optimal loading (0.937 g/L) and optimal initial MB concentration (7 mg/L). Isopropanol (IPA, 10 mmol/L) for hydroxyl radicals, [21], benzoquinone (BQ, 1 mol/L) for superoxide, and disodium ethylenediamine tetraacetate (EDTA, 10 mmol/L) for positive holes were used as scavenger probe molecules **[22].**

As illustrated in **Figure V.11,** the use of benzoquinone and isopropanol shows lower photocatalytic efficiency compared to ethylenediamine tetra-acetate. In effect, the addition of BQ and IPA significantly inhibits the photocatalytic reaction; the discoloration efficiency registered results of 79 and 87%, respectively, instead of 92%, obtained for the reference solution without scavengers. On the other hand, when EDTA is added, removal rates of 91% are obtained. Based on the previous results, the photodegradation mechanism can be proposed mainly from two aspects: (i) the use of magnetic halloysite clay increases the adsorption properties due to its specific surface area and

porosity, (ii) doping TiO_2 with Ag nanoparticles improves the visible light absorbance owing to (SPR) effect. Electrons are excited from the valence band (VB) to the conductance band (CB) under visible light irradiation, resulting in the creation of a hole (h+) in the VB. The interaction of h+ and e- in each CB and VB with OH and O_2 creates superoxide and hydroxyl radicals $O_2^{\bullet -}$, $OH^{\bullet}$ from the reaction system, allowing the MB dye to be further oxidized [23]. These results are consistent with the literature reporting the role of ROS on visible-light-driven photodegradation of MB [23].

The proposed mechanism is as follows:

$$Ag\text{-}TiO_2\text{-}MHKDD3 + h\nu \rightarrow Ag\text{-}TiO_2\text{-}MHKDD3\ (h^+_{VB} + e^-_{CB}) \quad (3)$$

$$O_{2\ ads} + e^-_{CB} \rightarrow O_2^{\bullet -} \quad (4)$$

$$O_{2\ ads} + e^-_{CB} + H^+ \rightarrow HO^{\bullet}_2 \quad (5)$$

$$HO^{\bullet}_{2\ ads} + e^-_{CB} + H^+ \rightarrow H_2O_2 \quad (6)$$

$$2H_2O_{2\ ads} + e^-_{CB} \rightarrow 2OH^- + 2OH^{\bullet} \quad (7)$$

$$MB + (OH^{\bullet} \text{ and } O^{\bullet}_2{}^-) \rightarrow \text{intermediates} \rightarrow CO_2 + H_2O + \text{mineral salts} \quad (8)$$

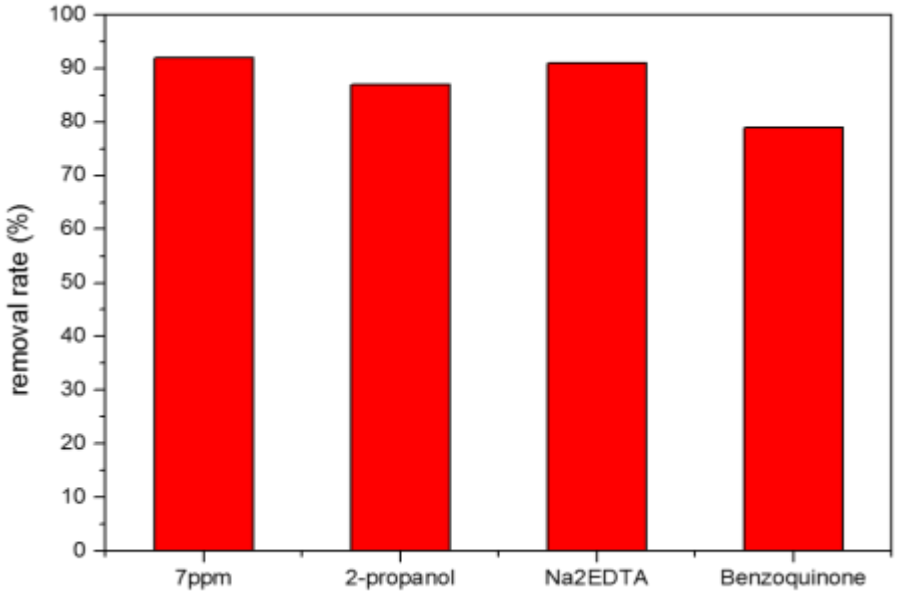

Figure V.11: Effect of different scavengers on MB photodegradation using photocatalyst under visible light irradiation

V.3 Conclusion

Different photocatalysts based on TiO_2, Ag-Fe doped TiO_2 supported on HKDD3 Algerian clay were synthesized via a solvothermal method. Various characterization techniques such as XRD, HRTEM, FTIR, BET, UV–Vis-DRS, and XPS were used. The prepared photocatalyst Ag-TiO2-MHKDD3 shows excellent performance for the removal of MB dye compared with other prepared materials, due to wide absorption on the visible region with a bandgap of 1.75 eV. After the photocatalytic process, the separation of catalyst from solution is easy owing to magnetite nanoparticles are sensitive to an applied magnetic field. According to the XPS results, the silver occurred in metallic form. The results highlight that the discoloration efficiency of dye reached 92% after 180 min of irradiation time with mineralization efficiency equal to 87% at pH 6.7. According to these results Ag-TiO_2- MHKDD3 photocatalyst exhibited higher photocatalytic performance. Due to the following factors, bandgap energy, pore distribution, and higher adsorption capacity. The main species responsible for the degradation of MB dye were hydroxyl $OH^{\bullet}$ and $O_2^{\bullet-}$ radicals.

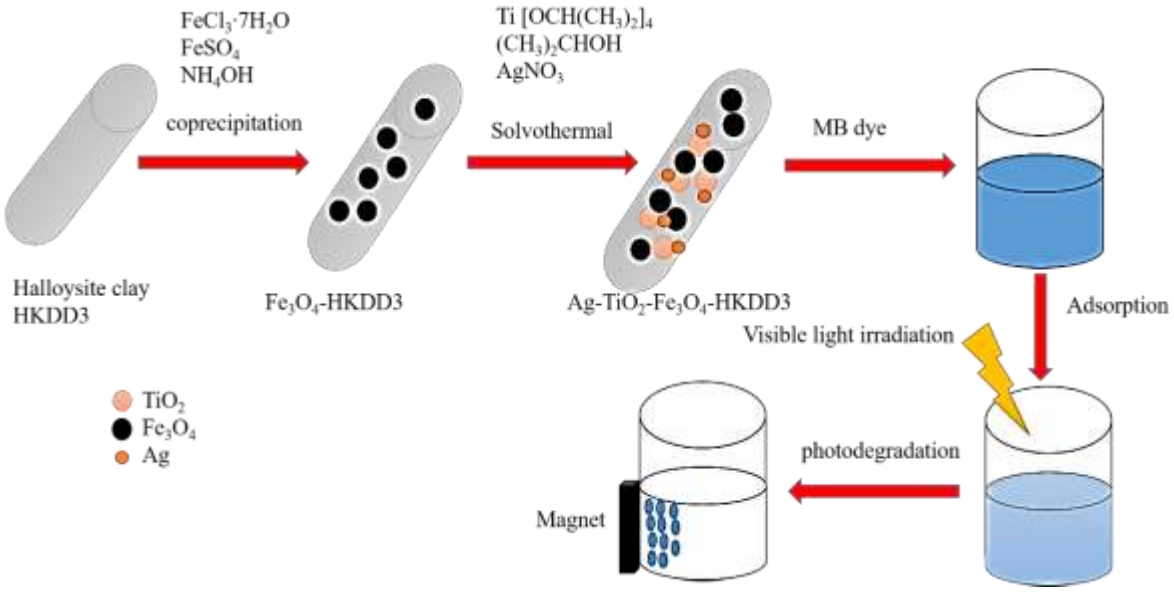

References

[1] R. Riahi-Madvaar, M.A. Taher, H. Fazelirad, Synthesis and characterization of magnetic halloysite-iron oxide nanocomposite and its application for naphthol green B removal, Applied Clay Science. 137 (2017) 101–106. https://doi.org/10.1016/j.clay.2016.12.019.

[2] E. Tierrablanca, J. Romero-García, P. Roman, R. Cruz-Silva, Biomimetic polymerization of aniline using hematin supported on halloysite nanotubes, Applied Catalysis A: General. 381 (2010) 267–273. https://doi.org/10.1016/j.apcata.2010.04.021.

[3] T. Tsoufis, F. Katsaros, B.J. Kooi, E. Bletsa, S. Papageorgiou, Y. Deligiannakis, I. Panagiotopoulos, Halloysite nanotube-magnetic iron oxide nanoparticle hybrids for the rapid catalytic decomposition of pentachlorophenol, Chemical Engineering Journal. 313 (2017) 466–474. https://doi.org/10.1016/j.cej.2016.12.056.

[4] Y. Xie, D. Qian, D. Wu, X. Ma, Magnetic halloysite nanotubes/iron oxide composites for the adsorption of dyes, Chem. Eng. J. 168 (2011) 959–963. https://doi.org/10.1016/j.cej.2011.02.031.

[5] R. Wang, G. Jiang, Y. Ding, Y. Wang, X. Sun, X. Wang, W. Chen, Photocatalytic Activity of Heterostructures Based on TiO2 and Halloysite Nanotubes, ACS Appl. Mater. Interfaces. (2011) 5 https://pubs.acs.org/doi/abs/10.1021/am201020q.

[6] N.V.S. Praneeth, S. Paria, Clay-Semiconductor Nanocomposites for Photocatalytic Applications, in: Clay Minerals: Properties, Occurrence and Uses, 2017.

[7] P. Zheng, Y. Du, X. Ma, Selective fabrication of iron oxide particles in halloysite lumen, Materials Chemistry and Physics. 151 (2015) 14–17. https://doi.org/10.1016/j.matchemphys.2014.11.075.

[8] Y. Ma, G. Zhang, Sepiolite nanofiber-supported platinum nanoparticle catalysts toward the catalytic oxidation of formaldehyde at ambient temperature: Efficient and stable performance and mechanism, Chemical Engineering Journal. 288 (2016) 70–78. https://doi.org/10.1016/j.cej.2015.11.077.

[9] Z. Ye, L. Kong, F. Chen, Z. Chen, Y. Lin, C. Liu, A comparative study of photocatalytic activity of ZnS photocatalyst for degradation of various dyes, Optik. 164 (2018) 345–354. https://doi.org/10.1016/j.ijleo.2018.03.030.

[10] C. Belver, M. Hinojosa, J. Bedia, M. Tobajas, M. Alvarez, V. Rodríguez-González, J. Rodriguez, Ag-Coated Heterostructures of ZnO-TiO2/Delaminated Montmorillonite as Solar Photocatalysts, Materials. 10 (2017) 960. https://doi.org/10.3390/ma10080960.

[11] F.C.S.M.R. Lopes, M. da G.C. da Rocha, P. Bargiela, H. Sousa Ferreira, C.A. de M. Pires, Ag/TiO2 photocatalyst immobilized onto modified natural fibers for photodegradation of anthracene, Chemical Engineering Science. 227 (2020) 115939. https://doi.org/10.1016/j.ces.2020.115939.

[12] L. Liu, W. Li, Z. Xiong, D. Xia, C. Yang, W. Wang, Y. Sun, Synergistic effect of iron and copper oxides on the formation of persistent chlorinated aromatics in iron ore sintering based on in situ XPS analysis, Journal of Hazardous Materials. 366 (2019) 202–209. https://doi.org/10.1016/j.jhazmat.2018.11.105.

[13] O. Fawzi Suleiman Khasawneh, P. Palaniandy, Removal of organic pollutants from water by Fe2O3/TiO2 based photocatalytic degradation: A review, Environmental Technology & Innovation. (2020) 101230. https://doi.org/10.1016/j.eti.2020.101230.

[14] K. Shoueir, S. Kandil, H. El-hosainy, M. El-Kemary, Tailoring the surface reactivity of plasmonic Au@TiO2 photocatalyst bio-based chitosan fiber towards cleaner of harmful water pollutants under visible-light irradiation, Journal of Cleaner Production. 230 (2019) 383–393. https://doi.org/10.1016/j.jclepro.2019.05.103.

[15] D. Rattan Paul, R. Sharma, S. P. Nehra, A. Sharma, Effect of calcination temperature, pH and catalyst loading on photodegradation efficiency of urea derived graphitic carbon nitride towards methylene blue dye solution, RSC Advances. 9 (2019) 15381–15391. https://doi.org/10.1039/C9RA02201E.

[16] J. Grzechulska, A.W. Morawski, Photocatalytic decomposition of azo-dye acid black 1 in water over modified titanium dioxide, Applied Catalysis B: Environmental. 36 (2002) 45–51. https://doi.org/10.1016/S0926-3373(01)00275-2.

[17] C.-C. Liu, Y.-H. Hsieh, P.-F. Lai, C.-H. Li, C.-L. Kao, Photodegradation treatment of azo dye wastewater by UV/TiO2 process, Dyes and Pigments. 68 (2006) 191–195. https://doi.org/10.1016/j.dyepig.2004.12.002.

[18] W.-Y. Wang, Y. Ku, Effect of solution pH on the adsorption and photocatalytic reaction behaviors of dyes using TiO2 and Nafion-coated TiO2, Colloids and Surfaces A: Physicochemical and Engineering Aspects. 302 (2007) 261–268. https://doi.org/10.1016/j.colsurfa.2007.02.037.

[19] C.-H. Weng, Y.-F. Pan, Adsorption of a cationic dye (methylene blue) onto spent activated clay, Journal of Hazardous Materials. 144 (2007) 355–362. https://doi.org/10.1016/j.jhazmat.2006.09.097.

[20] R.S. Dariani, A. Esmaeili, A. Mortezaali, S. Dehghanpour, Photocatalytic reaction and degradation of methylene blue on TiO2 nano-sized particles, Optik. 127 (2016) 7143–7154. https://doi.org/10.1016/j.ijleo.2016.04.026.

[21] Wei Zhang, Li Zhou, Jun Shi, Huiping Deng, Synthesis of Ag3PO4/G-C3N4 Composite with Enhanced Photocatalytic Performance for the Photodegradation of Diclofenac under Visible Light Irradiation, Catalysts. 8 (2018) 45. https://doi.org/10.3390/catal8020045.

[22] W. Zhang, L. Zhou, J. Shi, H. Deng, Fabrication of novel visible-light-driven AgI/g-C(3)N(4) composites with enhanced visible-light photocatalytic activity for diclofenac degradation, J Colloid Interface Sci. 496 (2017) 167–176. https://doi.org/10.1016/j.jcis.2017.02.022.

[23] W. Vallejo, A. Cantillo, C. Díaz-Uribe, Methylene Blue Photodegradation under Visible Irradiation on Ag-Doped ZnO Thin Films, International Journal of Photoenergy. 2020 (2020) 1–11. https://doi.org/10.1155/2020/1627498.

CHAPTER VI Characterization of FeS-HKDD3 clay and its application for MB removal

This chapter is devoted firstly to the presentation and discussion of the results of the various structural, textural and microstructural characterizations, obtained on FeS nanoparticles supported on the HKDD3. It denotes FeS-HKDD3. Then, we expose the results of the evaluation of the photocatalytic activity for the removal of MB in an aqueous medium. As a reminder, the synthesis of this composite photocatalyst has been described in chapter II.

VI.1 Characterization

VI.1.1 XRD analysis

The obtained XRD pattern of the prepared materials FeS and FeS-HKDD3 by the hydrothermal method are shown in **figure VI.1.**

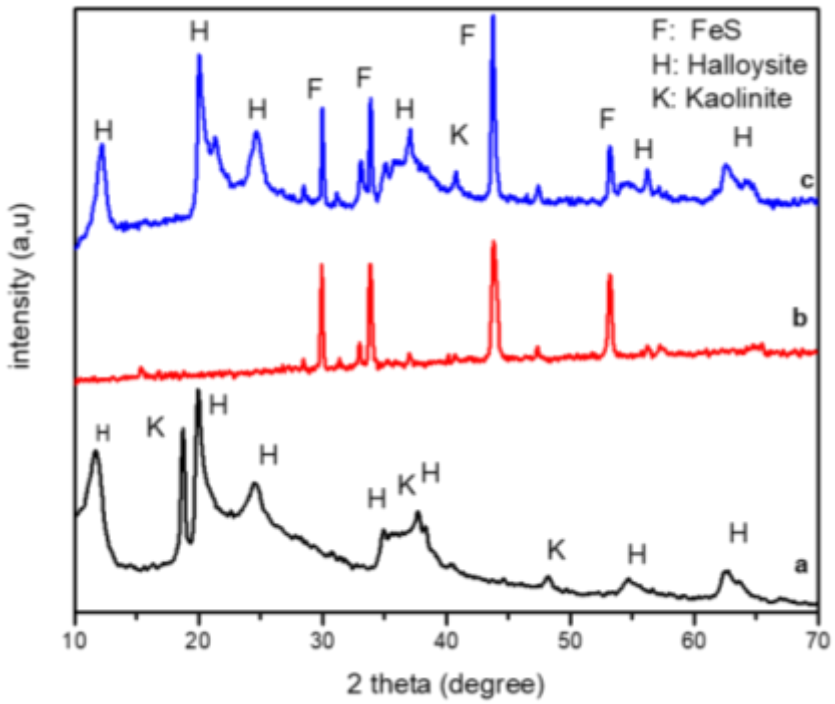

Figure VI. 1 XRD patterns of HKDD3 (a), iron sulfide FeS (b) and FeS-HKDD3 photocatalyst (c).

According to **figure VI.1.**, the diffraction peaks at position 2θ: 30.16, 31.49, 34.11, 44.04, 53.41, and 72 correspond to planes (010), (002), (011), (012), (110), (002) respectively. these diffraction peaks agree with the standard file FeS JCPDS no. 65-9124 **[1]**, which confirms the formation of a hexagonal phase of FeS. The XRD pattern peaks are very sharp, suggesting that FeS is well-crystallized sample [2]. Most of these peaks are partially overlapped by the peaks of HKDD3 clay at the position indexed into (JCPDS 29-1487) **[3]** and (JCPDS 80-0886) **[4]** which refers to Halloysite and Kaolinite respectively.

VI.1.2 STEM-EDS analysis

The morphology of FeS-HKDD3 photocatalyst was determined by STEM and some images are illustrated in **Figure VI.2**. The FeS crystals are dispersed as cubic-shaped form (**Figure VI.2**.**A) [5]** with an average diameter of 500 nm. As seen, in the composite, some particles formed aggregates, whereas others dispersed in a regular shape. **Figure VI.2.B** exhibited the distribution of FeS particles on tubular halloysite HKDD3. More particles have a nanometric dimension ranging from 25 nm to 80 nm, which due to the growth of FeS on the surface of HKDD3 tubes during the hydrothermal method.

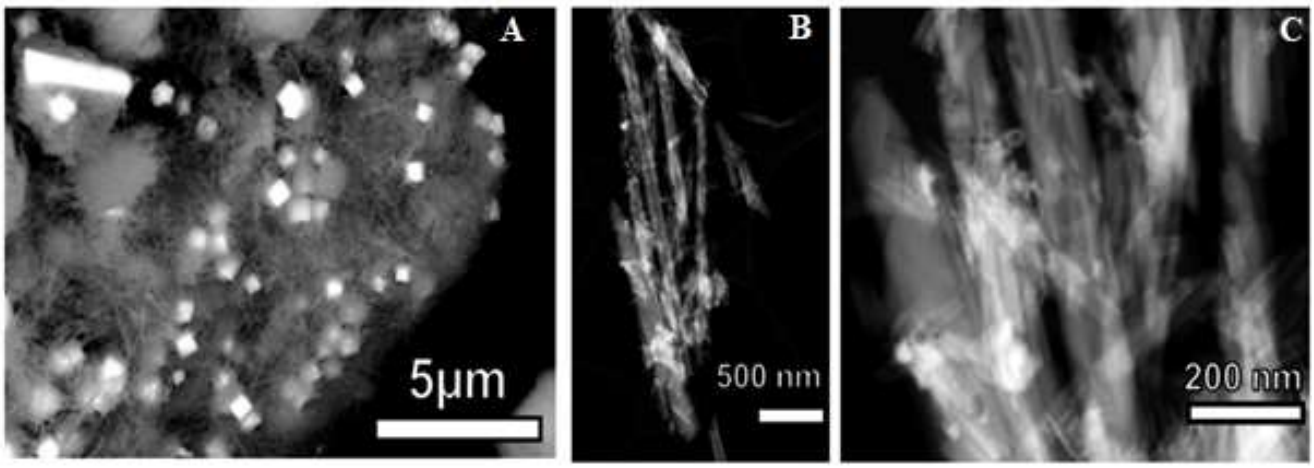

Figure VI. 2 STEM images of FeS-HKDD3 photocatalyst.

Moreover, mapping images of the sample are presented in **Figure VI.3** approving the good dispersion of each constituent element in the composite. The presence of characteristic elements from HKDD3 clay including Al, Si, and O, with little quantity of Fe and S which can be explicated the formation of iron sulfide particles.

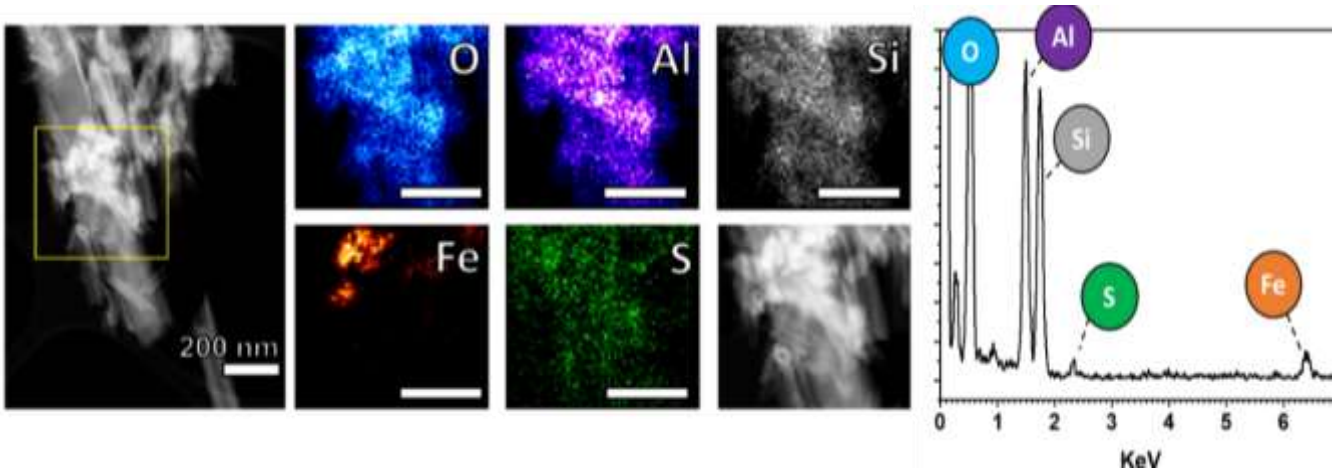

Figure VI. 3 STEM images and related elemental EDS MAP and elemental EDS analysis for selected elements of FeS-HKDD3 photocatalyst**.**

VI.1.3 BET analysis

The sorption-desorption of N_2 was applied to study the textual properties of FeS, HKDD3 clay, and FeS-HKDD3 catalyst. Results are listed in **table VI.1**, which exhibit that the specific surface area was 71.71 m^2/g, 61.16 m^2/g, and 1.59 m^2/g for HKDD3, FeS-HKDD3, and FeS particles, respectively. The BET surface area of FeS-HKDD3 is clearly increased compared to FeS particles due to the halloysite clay (HKDD3) support. It also shows that the average pore diameter is 17.35, 38.61, and 12.41nm, respectively. It can be explicated the mesoporous and microporous of prepared materials.

Table VI. 1 Texture analysis data for all the samples FeS, HKDD3, FeS-HKDD3.

Sample	Specific surface area (m^2/g)	Average pore diameter (nm)	Average pore volume (cm^3/g)
HKDD3	71.71	12.41	0.222
FeS	1.59	38.61	0.011
FeS/HKDD3	61.16	17.53	0.288

The **figure VI.4** showed the sorption-desorption of N_2 isotherms for FeS-HKDD3 and FeS. The isotherms were indicated the presence of macroporous and mesoporous structure, the isotherms followed type II with H3 hysteresis loops. The distribution of pore diameter ranging from 25 nm to 100 nm.

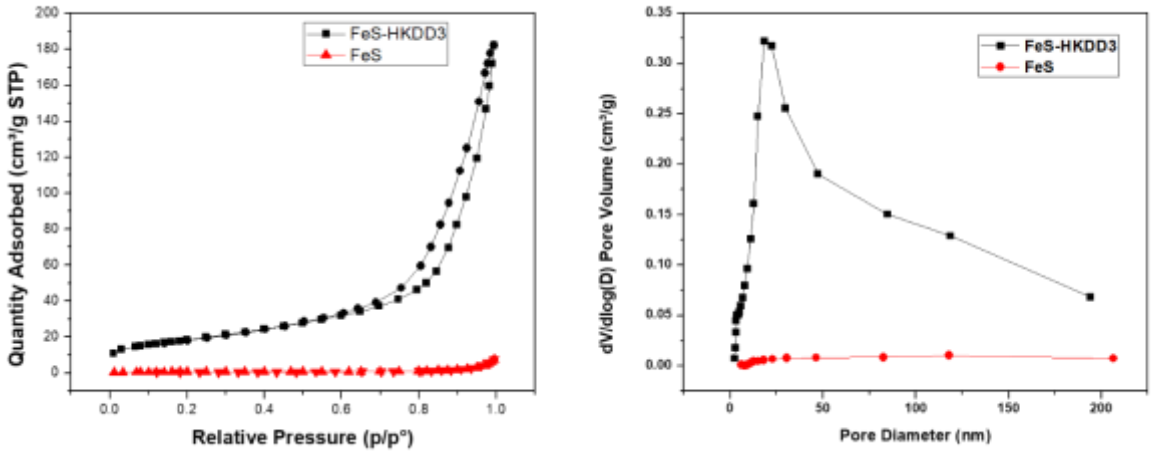

Figure VI. 4 isotherm of adsorption-desorption and pore diameter distribution of FeS and FeS-HKDD3**.**

VI.1.4 Uv-vis diffuse reflectance

The UV–vis diffuse reflectance spectra (DRS) of FeS and FeS-HKDD3 catalysts with their corresponding Tauc's plots are shown in fig 5. It can be seen that the onset band from 350 nm to 800 nm can confirm the absorption in the visible region. In addition, the Tauc's relation was used to estimate the bandgap according to the below equation [6]: $[(\alpha h\upsilon)^{1/n} = \beta (h\upsilon - E_g)]$ (4)

Where α is an absorption coefficient, hυ is the incident photon energy, 'β' is a constant, and 'n' is the exponent, Eg is the energy of bandgap. As FeS is a direct bandgap semiconductor, the value is 2. Consequently, The bandgap of FeS nanoparticles prepared is 1.87 eV which agrees with the light absorption properties of iron sulfide nanoparticles reported in the literature [7]. While FeS nanoparticles loaded on HKDD3 clay was calculated to be 1.60 eV.

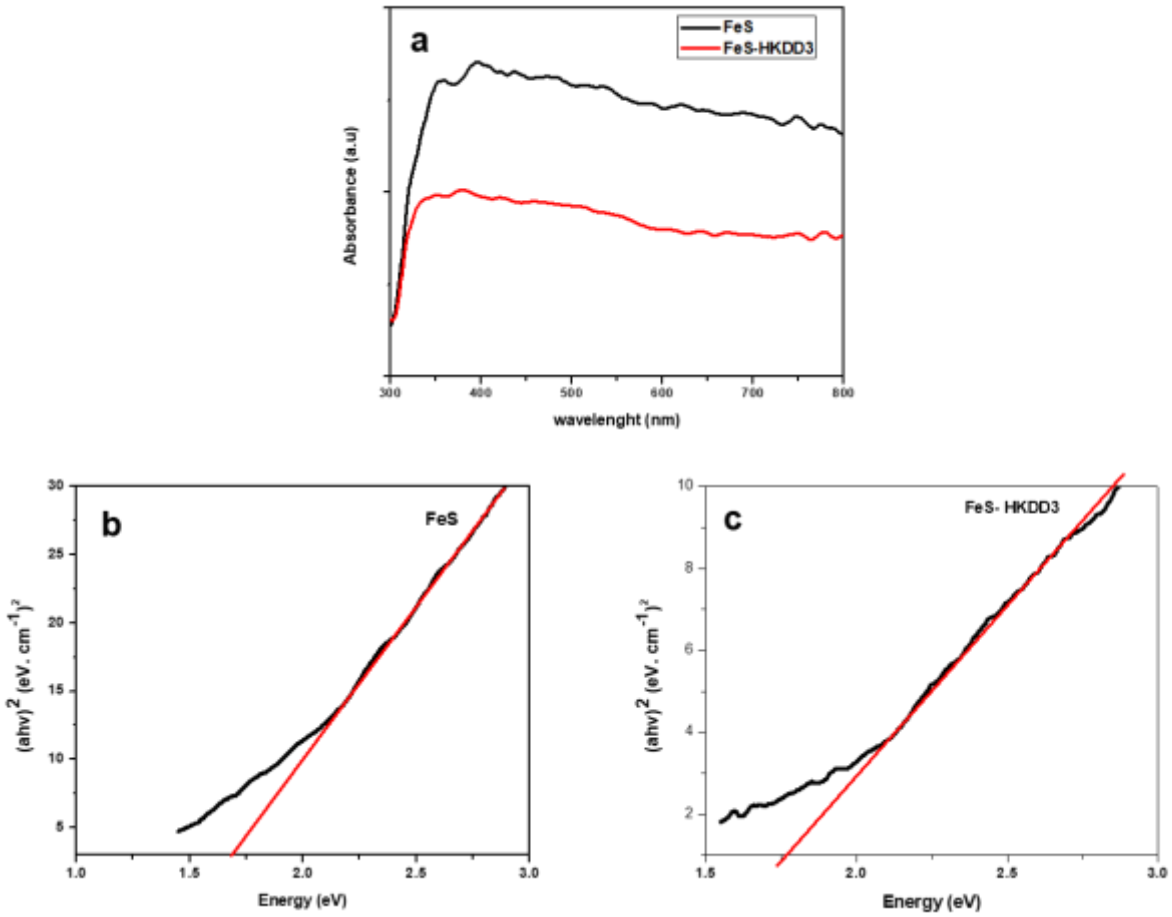

Figure VI. 5 Uv-vis diffuse reflectance spectra of FeS and FeS-HKDD3 photocatalyst (a), tauc plots using Kubelka-Munk relation to estimate band gap value of various sample FeS-HKDD3 (b); FeS (c).

VI.2 The point zero charge of FeS-HKDD3

The point zero charge (pH_{PZC}) is crucial in removal dye research because it provides a piece of important information about the types of interactions that might occur between the adsorbent and the adsorbate (attraction/repulsion). In a nutshell, the pH_{PZC} is the point at which the adsorbent surface charge's hydrogen pH potential equals zero (the sum of negative and positive charges of the surface sites equals zero). At a pH of around 4.5, the FeS-HKDD3 surface exhibits a net neutral charge, as shown in the **figure.VI.6**. When the pH of the solution is greater than the pH_{PZC} ($pH>pH_{PZC}$), the clay surface is negatively charged, and when the pH is lower than the pH_{PZC} ($pH<pH_{PZC}$), positively charged sites predominate on the clay adsorbent's surface.

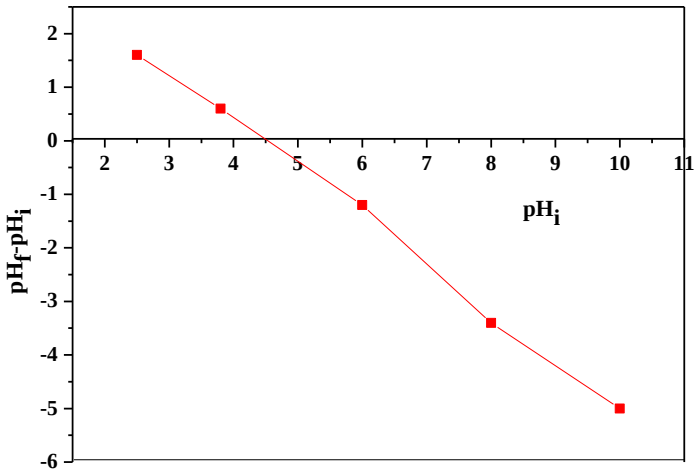

Figure VI. 6 pH_{PZC} Plot of FeS-HKDD3 catalyst.

VI.3 Photocatalytic activity

The photocatalytic performance of iron sulfide and FeS-HKDD3 catalyst was studied for the elimination of methylene blue under visible light irradiation. As seen from **Figure VI.7**, the removal rate adsorbed MB in the dark by FeS and FeS-HKDD3 reached 2 % and 74% respectively. After the irradiation of photocatalysts under visible light, the FeS-HKDD3 recorded a higher photocatalytic performance than FeS. The dye removal rate was attained by 90% and 20 %. It can be observed that the removal of methylene blue is a combination of adsorption and photodegradation. The lower efficiency of photodegradation of MB by iron sulfide could be explained by the lower surface specific area for iron sulfide and its high rate of recombination rate and wide-bandgap. However, The MB concentration decreased rapidly in the presence of HKDD3 clay. It could be ascribed to the adsorption effect of MB in the pores of halloysite clay nanotubes due to the higher specific surface area of 61.15 m^2/g. (HKDD3 clay acted as an adsorbent).

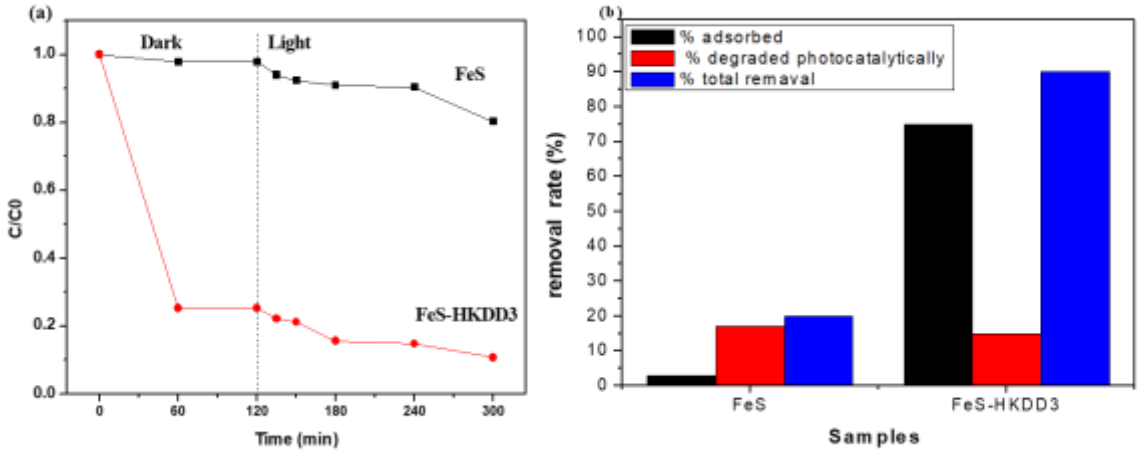

Figure VI. 7 (a) Photocatalytic removal of MB over FeS-HKDD3 photocatalyst under visible irradiation; **(b)** Summary of their performance (pH free; m=50 mg of FeS-HKDD3; 100 mL; 10 mg.L^{-1} of MB at 25°C)

VI.3.1 Kinetic study

The kinetic of MB removal by FeS-HKDD3 composite is fitted using the first order Langmuir–Hinshelwood model which is expressed by the following equation [8].

$$\frac{dc}{dt} = -k\,c \implies -ln\left(\frac{c}{c_0}\right) = k\ t \qquad (4)$$

The values of the apparent kinetic constant k are the slope of curves by plotting $-ln\left(\frac{c}{c_0}\right)$ as a function of the irradiation time (t). As seen in **Figure VI.8** the Kapp were 0.0038 min^{-1} and 0.0007 min^{-1} for FeS-HKDD3 and FeS photocatalysts, respectively. The rate of MB photodegradation using FeS-HKDD3 is about 11 times greater than the rate using FeS nanoparticles.

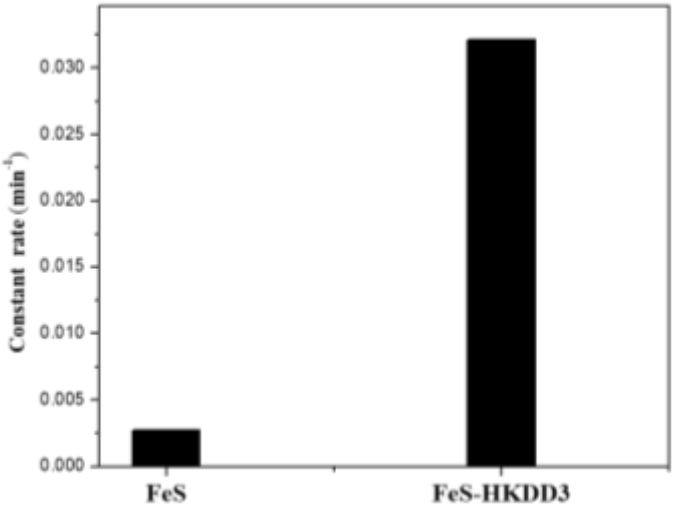

Figure VI. 8 constant rate removal of MB in the presence of FeS and FeS-HKDD3 catalysts.

VI.3.2 Effect of MB dye concentration

For the investigation of the effect of MB dye concentration, photocatalytic discoloration experiments were conducted with different MB dye concentrations ranging from 10 to 30 $mg.L^{-1}$. It can be shown in **Figure VI.9** that the degradation efficiency of MB solution decreases with an increase in MB concentration. For 10 $mg.L^{-1}$ dye concentration reached about 90% degradation. While, the removal efficiency of 20 and 30 $mg.L^{-1}$ were only 65 and 50%, respectively. It can be explained by the increasing concentration of MB which causes low transparency of the solution. the penetration of light is limited to reach effectively the surface of the photocatalyst which means less photocatalytic reactions **[9]**. On the other hand, the constant rate decrease with increasing of concentration MB dye (0.013 to 0.006 min^{-1}).

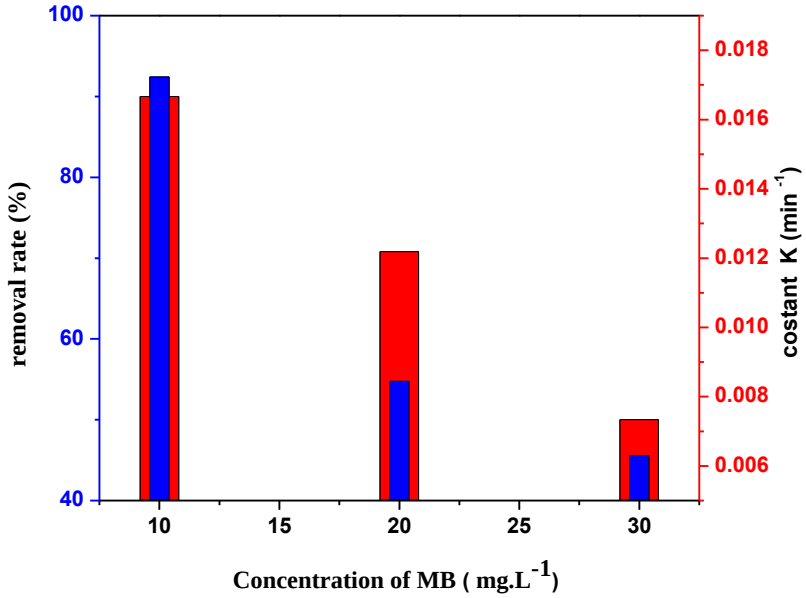

Figure VI. 9 effect of initial dye concentration on removal MB and constant rate of first order kinetics. (pH free
; m= 50 mg of FeS-HKDD3).

VI.3.3 Effect of catalyst mass

A series of photodegradation experiments were done with different FeS-HKDD3 mass from 25 to 100 mg. As expected, the obtained results are displayed in **Figure VI.10** which indicates that removal efficiency was increased with the increasing of catalyst amount. This can be attributed to the increase of catalyst active sites which led to the production of more reactive radicals OH^- which react with pollutant dye **[10]**.

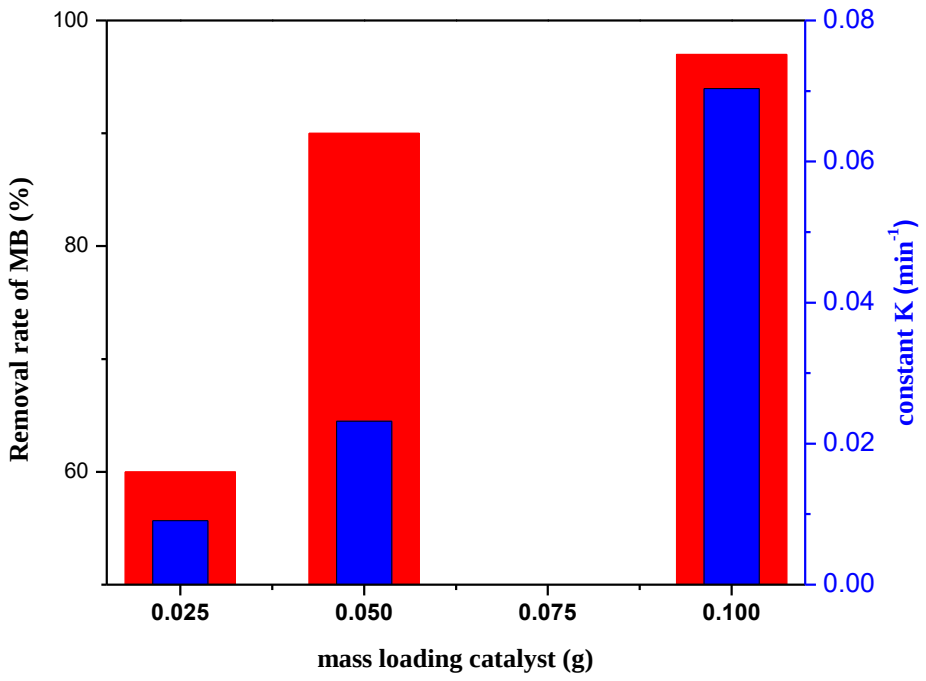

Figure VI. 10 effect of mass loading catalyst on MB removal and constant rate of first order kinetics (pH free; 100 mL; 10 mg.L^{-1} of MB at 25°C)

VI.3.4 Effect of pH

The obtained results were displayed in **Figure VI.11**. The removal efficiency was increased by increasing the pH. As seen at pH= 9, the rate of discoloration reached about 96% is higher than acidic and neutral conditions which attained 86% and 83%, respectively. The pHpzc of nanocomposite FeS-HKDD3 is around 4.46, which can be explained that the surface of nanocomposite was positive at pH levels lower than 4.46, causing the repulsion between the molecules of MB cationic dyes. While in the alkaline solution the surface became more negative which enhance the attraction force with MB dyes i.e. the improvement of combination between the MB on the surface of the nanocomposite **[11]**.

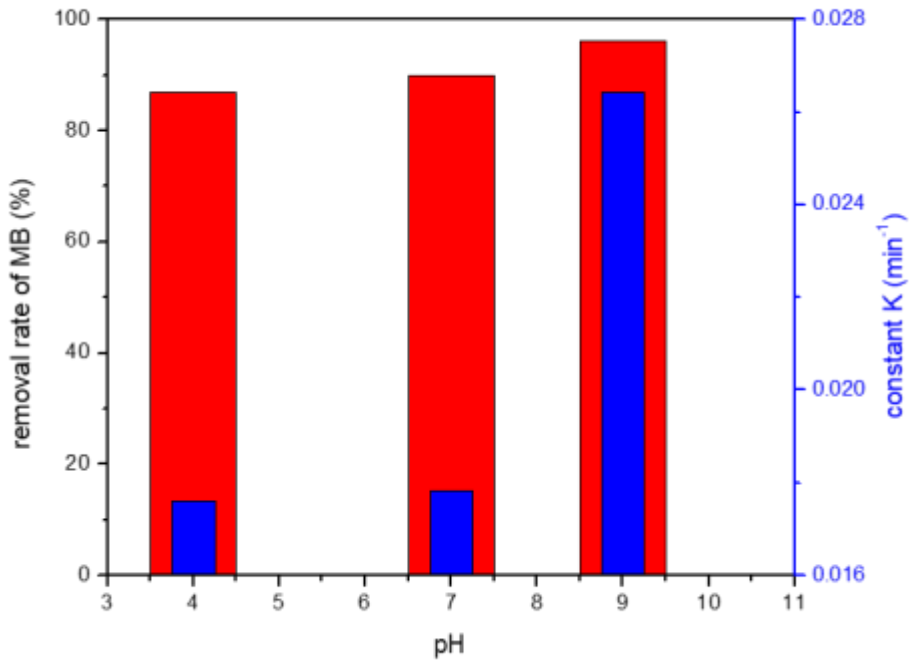

Figure VI. 11 Effect of pH of removal MB by FeS-HKDD3 clay and constant rate of first-order kinetics (pH=
4-9; m=50 mg of FeS; 100 mL; 10 mg.L^{-1} of MB at 25°C).

VI.4 Degradation mechanism of MB

Under the irradiation of photocatalyst iron sulfide by visible light, the electrons and holes were produced **(figure.VI.12).** The excited electron and the photo-generated holes were reacted to produce superoxide radicals (O_2^{-*}) and hydroxyl OH^*[12]., respectively, which oxidize MB dye. Furthermore, the photo-generated holes were trapped by negative charges on the surface of halloysite clay to react with MB adsorbed on the surface

$$FeS\text{-}HKDD3 + h\nu \rightarrow FeS\text{-}HKDD3\ (h^+_{BV} + e^-_{BC}) \quad (5)$$

$$FeS(e^-) + O_2 \rightarrow O_2^{\bullet -} \quad (6)$$

$$FeS(e^-) + HKDD3 \rightarrow FeS + HKDD3(e^-) \quad (7)$$

$$HKDD3(e^-) + O_2 \rightarrow O_2^{\bullet -} \quad (8)$$

$O2^{\bullet-} + H^+ \rightarrow OH^{\bullet}$ (9)

$h^+ + H_2O \rightarrow H^+ + OH^{\bullet}$ (10)

$MB + (h^+ + OH^{\bullet} + O_2^{-\bullet}) \rightarrow CO_2 + H_2O$ + other products (11)

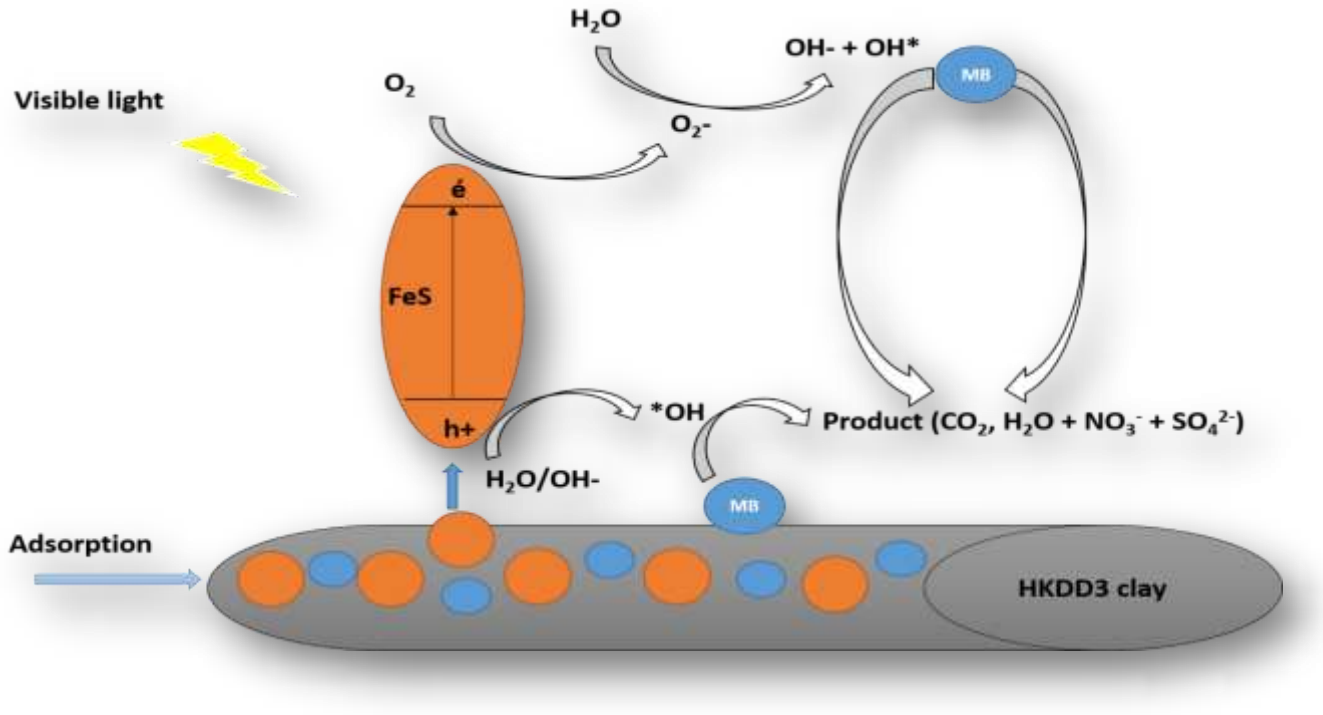

Figure VI. 12 proposed mechanism for photocatalytic degradation of MB dye by FeS-HKDD3.

VI.5 Conclusion

In summary, we have successfully synthesized the FeS particles loaded on Algerian Halloysite clay (HKDD3) by the hydrothermal method. The XRD pattern of FeS and FeS-HKDD3 confirms the hexagonal structure of FeS. Morphological analysis of prepared samples shows that FeS has a rods-morphology forming cubic aggregate on the surface of halloysite clay. An excellent photocatalytic efficiency to remove the MB dye under visible light which reached 96% in alkaline solution.

References

[1] Quanning Ma, Qianyu Zhuang, Jun Liang, Zhonghua Zhang, Jing Liu, Hongrui Peng, Changming Mao, Guicun Li, Novel Mesoporous Flowerlike Iron Sulfide Hierarchitectures: Facile Synthesis and Fast Lithium Storage Capability, Nanomaterials. 7 (2017) 431. https://doi.org/10.3390/nano7120431.

[2] X. Wen, X. Wei, L. Yang, P.K. Shen, Self-assembled FeS_2 cubes anchored on reduced graphene oxide as an anode material for lithium ion batteries, J. Mater. Chem. A. 3 (2015) 2090–2096. https://doi.org/10.1039/C4TA05575F.

[3] Y. He, W. Xu, R. Tang, C. Zhang, Q. Yang, pH-Responsive nanovalves based on encapsulated halloysite for the controlled release of a corrosion inhibitor in epoxy coating, RSC Adv. 5 (2015) 90609–90620. https://doi.org/10.1039/C5RA19296J.

[4] F. Chargui, M. Hamidouche, H. Belhouchet, Y. Jorand, R. Doufnoune, G. Fantozzi, Mullite fabrication from natural kaolin and aluminium slag, Bol Soc Esp Ceram Vidr. 57 (2018) 169–177. https://doi.org/10.1016/j.bsecv.2018.01.001.

[5] S.K. Maji, A.K. Dutta, P. Biswas, D.N. Srivastava, P. Paul, A. Mondal, B. Adhikary, Synthesis and characterization of FeS nanoparticles obtained from a dithiocarboxylate precursor complex and their photocatalytic, electrocatalytic and biomimic peroxidase behavior, Applied Catalysis A: General. 419–420 (2012) 170–177. https://doi.org/10.1016/j.apcata.2012.01.025.

[6] M. Nadimi, A. Ziarati Saravani, M.A. Aroon, A. Ebrahimian Pirbazari, Photodegradation of methylene blue by a ternary magnetic TiO2/Fe3O4/graphene oxide nanocomposite under visible light, Materials Chemistry and Physics. 225 (2019) 464–474. https://doi.org/10.1016/j.matchemphys.2018.11.029.

[7] D. Ayodhya, G. Veerabhadram, A review on recent advances in photodegradation of dyes using doped and heterojunction based semiconductor metal sulfide nanostructures for environmental protection, Materials Today Energy. 9 (2018) 83–113. https://doi.org/10.1016/j.mtener.2018.05.007.

[8] N.S. Moalej, S. Ahadi, S. Sheibani, Photocatalytic degradation of methylene blue by 2 wt.% Fe doped TiO2 nanopowder under visible light irradiation, J. Ultrafine Grained Nanostruct. Mater. 52 (2019). https://doi.org/10.22059/jufgnsm.2019.02.01.

[9] F. Han, V.S.R. Kambala, M. Srinivasan, D. Rajarathnam, R. Naidu, Tailored titanium dioxide photocatalysts for the degradation of organic dyes in wastewater treatment: A review, Applied Catalysis A: General. 359 (2009) 25–40. https://doi.org/10.1016/j.apcata.2009.02.043.

[10] A. Hassani, A. Khataee, S. Karaca, C. Karaca, P. Gholami, Sonocatalytic degradation of ciprofloxacin using synthesized TiO2 nanoparticles on montmorillonite, Ultrasonics Sonochemistry. 35 (2017) 251–262. https://doi.org/10.1016/j.ultsonch.2016.09.027.

[11] J. Rashid, S. Saleem, S.U. Awan, A. Iqbal, R. Kumar, M.A. Barakat, M. Arshad, M. Zaheer, M. Rafique, M. Awad, Stabilized fabrication of anatase-TiO_2/FeS_2 (pyrite) semiconductor composite nanocrystals for enhanced solar light-mediated photocatalytic degradation of methylene blue, RSC Adv. 8 (2018) 11935–11945. https://doi.org/10.1039/C8RA02077A.

[12] A. Mills, S. Le Hunte, An overview of semiconductor photocatalysis, Journal of Photochemistry and Photobiology A: Chemistry. 108 (1997) 1–35. https://doi.org/10.1016/S1010-6030(97)00118-4.

Conclusion

This thesis aims to evaluate the removal of methylene blue dye from aqueous solution by two methods adsorption and photocatalytic activity which are practical and low-cost processes. Furthermore, the contribution to the valorization of the abundant clay in Algeria kaolin Djebel Debbagh.

We are interested in the purification of HKDD3 clay and its characterization by physicochemical methods to follow their textural and structural evolution. The Algerian clay HKDD3 is a natural halloysite tubular shape with a length ranging from 500 nm to several micrometers and a diameter estimated from 50 nm to 100 nm. The main oxides are alumina content of 38.48%, and 36.11% of silica with SiO_2/Al_2O_3 mass ratio of about 0.94. In addition, it has a high surface area 71.71 m^2/g compared to other halloysite clay from the world.

We have conducted on the synthesis, characterization, and use of magnetic clay sorbent and its application for the removal of methylene blue. The synthesis of Fe_3O_4 – HKDD3 was carried out by the coprecipitation method. The results have shown that the nanoparticles of magnetite were about 50 nm and were well dispersed on the surface of HKDD3. A comparative study was carried out on the removal of MB dye by adsorption and sono-adsorption. A Series of experiments were determined to study the influence of contact time, initial concentration, pH, and temperature. The quantity adsorbed of methylene blue dye was increased with the increase of pH and concentration dye. The uptake dye reached 18.78 mg/g and 10 mg/g for sono-adsorption and adsorption respectively, due to the ultrasonic waves which improve the porosity of the M-HKDD3 surface adsorbent and mass transfer rate (liquid-solid interfaces) by physical phenomena such as microscopic turbulence, streaming and acoustic waves.

Secondly, we have elaborated different photocatalysts based on M-HKDD3: 30% TiO2-M-HKDD3, 2% Ag- TiO2-M-HKDD3, 1% Fe- TiO2-M-HKDD3, and 1%Fe -2% Ag- TiO2-M-HKDD3 via the solvothermal method, for the evaluation of the photocatalytic activity of methylene blue under visible light irradiation. Among these photocatalysts, the Ag- TiO2-M-HKDD3 sample exhibited the maximum removal rate of the dye.

Structural and morphological characterization indicated that magnetite (Fe_3O_4) and (TiO_2) sizes were estimated at around 50 nm and 30 nm, respectively. The photocatalytic performance was evaluated under visible light by changing different parameters including initial dye concentration, catalyst dosage, pH, and scavenger effect. The methylene blue discoloration was 92% with mineralization 87%, which was achieved at pH 6.7 with 0.9 g/l mass of catalyst. The O_2^- and $OH^\bullet$ species are the crucial species in the degradation of methylene blue dye.

Finally, we have successfully synthesized the FeS particles loaded on Algerian halloysite clay (HKDD3) by the hydrothermal method. The XRD pattern of FeS and FeS-HKDD3 confirms the hexagonal structure of FeS. The iron sulfide nanoparticles are shaped as cubes forming aggregates on the surface of the halloysite. Uv- Vis Drs results show strong absorption in the visible region with bandgap 1.60 eV. An excellent photocatalytic efficiency to remove the MB dye under visible light. It was observed that the removal rate reached 96% after 180 min under visible light irradiation.

All these conclusions demonstrate the excellent capacity of elimination of MB dye under simple conditions. In perspective, the study of the effectiveness of these photocatalysts in the treatment of dyeing effluents would be necessary. The regeneration of photocatalysts will be essential to confirm their stability and their efficiency in adsorption and photocatalytic performance.

Appendix I

The evolution of the concentration during the adsorption process was determined by a calibration curve, obtained from standards with different concentrations (Table.1). A series of samples were prepared to establish the calibration curve from the stock solution. The analysis by UV-visible absorption at λ_{max} =663 nm was carried out using a diluted solution in order to verify the Beer-lambert.

Table.1. Concentration values and their corresponding absorbance of the calibration curve.

Concentration C_0	0	2	4	6	8	10
Absorbance (A) of MB	0	0.484	0.906	1.240	1.498	1.917

The curve below (Figure 1) is linear in the range of the selected concentrations; so Beer - Lambert's law is verified.

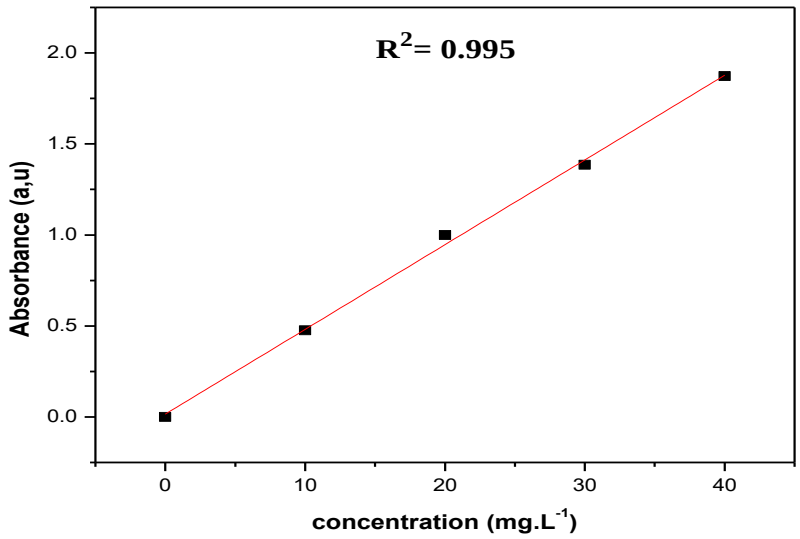

Figure.1 Calibration curve for MB.

Appendix II

In the following section the files of JCPDS used in thesis.

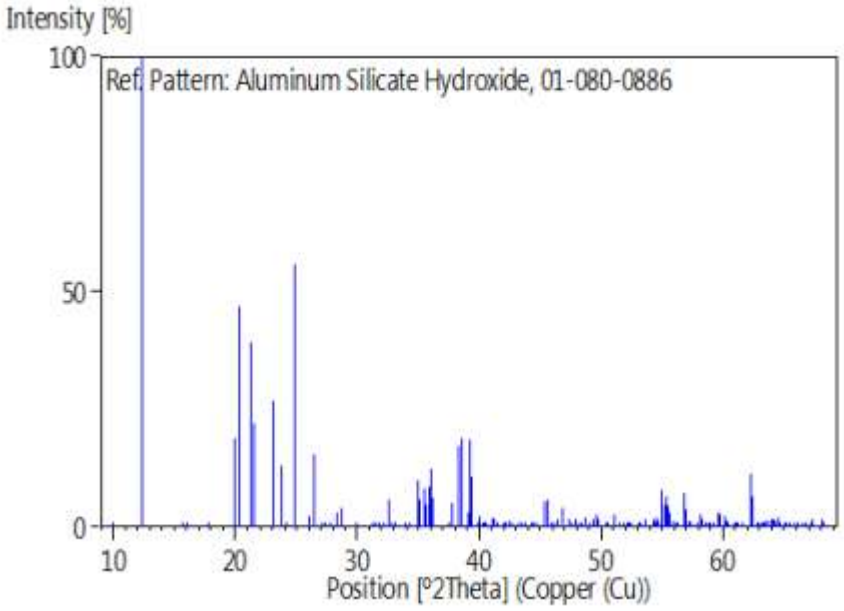

Figure 1: fiche JCPDS of kaolinite

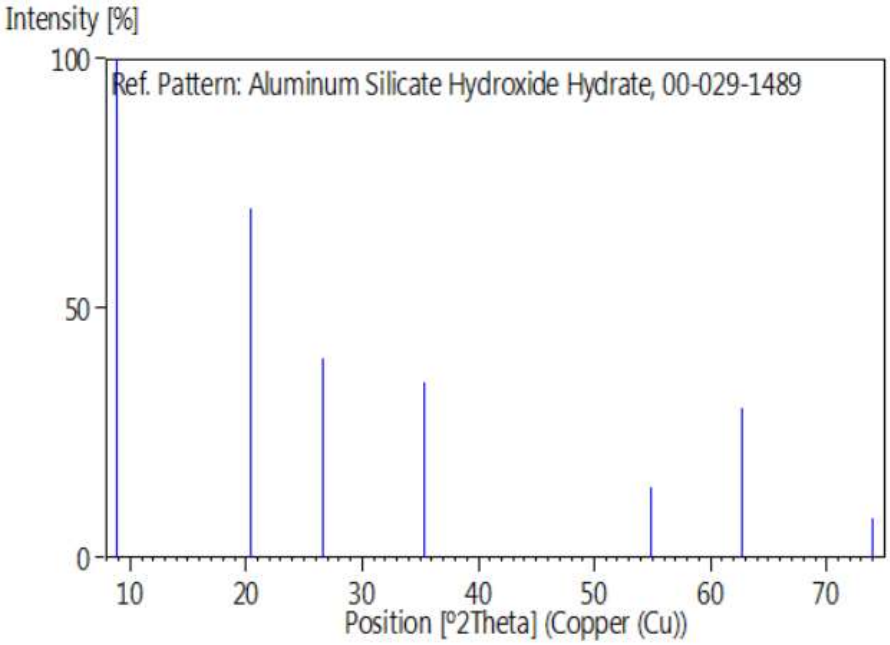

Figure 2: fiche JCPDS of halloysite

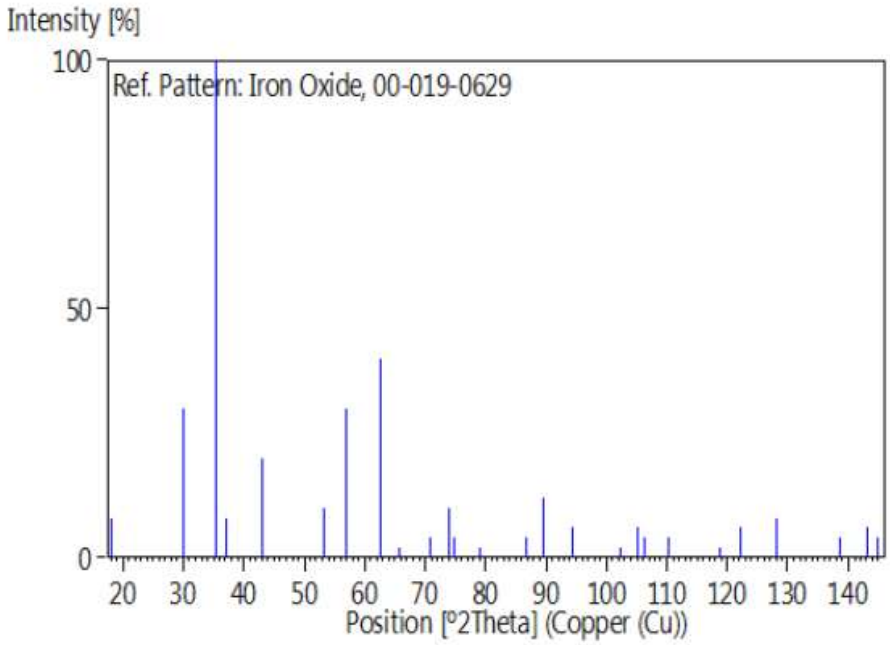

Figure 3: fiche JCPDS of magnetite

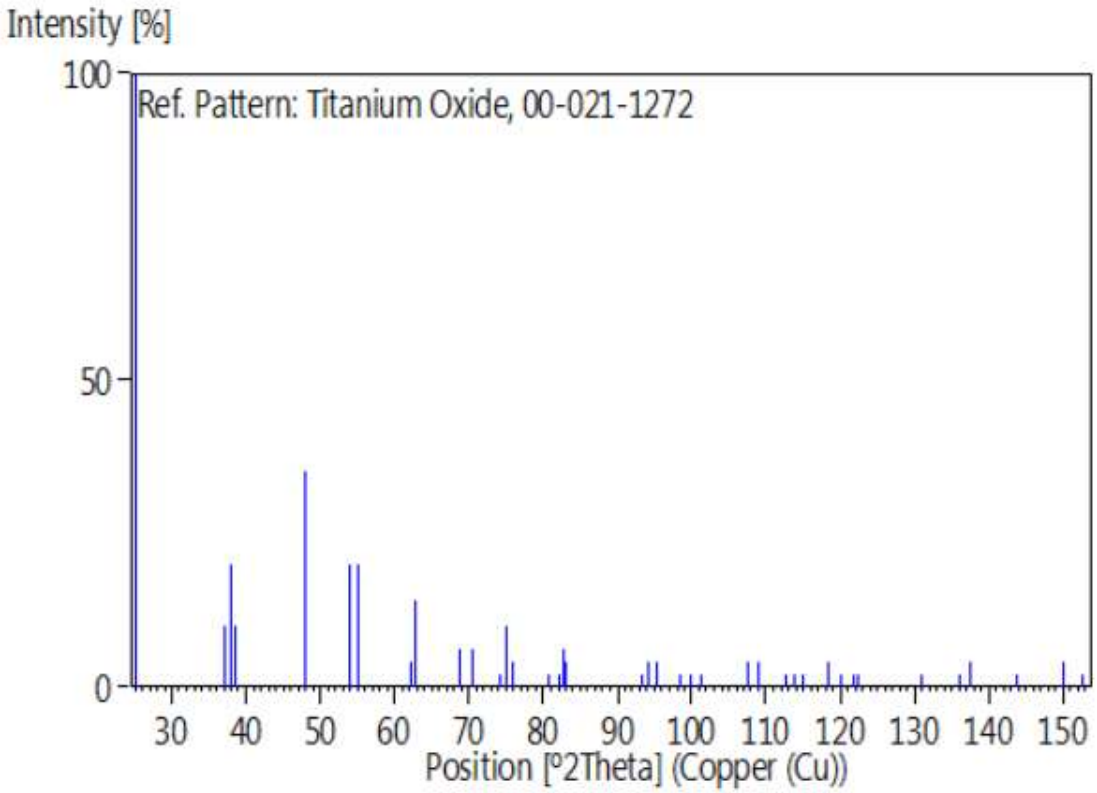

Figure 4: fiche JCPDS of TiO_2 Anatase.

Conferences and Publications

1. Conferences

International conference

- **A. Hayoune**, H. Akkari and A. Boudrouma, *"Adsorption of methylene blue onto purified clay KDD3*", Conference: International Symposium on Materials Chemistry, Boumerdes, Algeria, March, 19, 20 & 21, 2018
- **A. Hayoune,** H. Akkari and T. Mekhalif. *"comparative study on adsorption of methylene blue by KDD3-Fe_3O_4 magnetic composite and KDD3 purified clay",* Conference: International conference on materials science, Setif, Algeria, September 12-14,2018
- **A. Hayoune**, H. Akkari. *"preparation, characterization and application of Fe_3O_4-KDD3 nanocomposite"*, Conference: international conference on nanomaterials & renewable energies, Skikda, Algeria, October 15-17, 2018
- **A. Hayoune**, H. Akkari, N.Guettech, A. kaabche *"synthesis and characterization of magnetic iron oxide/clay composite and its application for water treatment"*, Conference: séminaire international environnement et toxicologie, costantine, Algeria, February 18-19, 2019

2. Publications

International journals

International journals

1. Synthesis and characterization of novel catalyst Ag-TiO2 loaded on magnetic Algerian halloysite clay (Fe3O4-HKDD3) for the photocatalytic activity of methylene blue dye in an aqueous medium Asma Hayoune, Hocine Akkari, Vincenzo Vaiano, Nicola Morante Diana Sannino, Farid Madjene. International Journal of Environmental Analytical Chemistry. Article DOI: 10.1080/03067319.2021.197442
2. Sono-assisted adsorption of methylene blue dye from aqueous medium using magnetic Algerian Halloysite clay (Fe3O4-HKDD3). Asma Hayoune, Hocine Akkari, Tahar Mekhalif and Francisco Martin. International Journal of Environmental Analytical Chemistry. Article DOI: 10.1080/03067319.2021.2020770

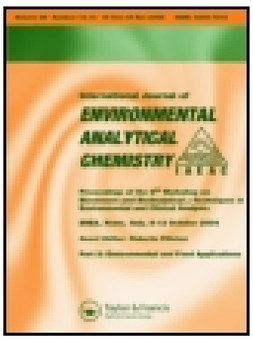

International Journal of Environmental Analytical Chemistry

ISSN: (Print) (Online) Journal homepage: https://www.tandfonline.com/loi/geac20

Synthesis and characterisation of novel catalyst Ag-TiO_2 loaded on magnetic Algerian halloysite clay (Fe_3O_4-HKDD3) for the photocatalytic activity of methylene blue dye in an aqueous medium

Asma Hayoune, Hocine Akkari, Vincenzo Vaiano, Nicola Morante, Diana Sannino & Farid Madjene

To cite this article: Asma Hayoune, Hocine Akkari, Vincenzo Vaiano, Nicola Morante, Diana Sannino & Farid Madjene (2021): Synthesis and characterisation of novel catalyst Ag-TiO_2 loaded on magnetic Algerian halloysite clay (Fe_3O_4-HKDD3) for the photocatalytic activity of methylene blue dye in an aqueous medium, International Journal of Environmental Analytical Chemistry, DOI: 10.1080/03067319.2021.1974425

To link to this article: https://doi.org/10.1080/03067319.2021.1974425

Published online: 22 Sep 2021.

INTERNATIONAL JOURNAL OF ENVIRONMENTAL ANALYTICAL CHEMISTRY
https://doi.org/10.1080/03067319.2021.1974425

Synthesis and characterisation of novel catalyst Ag-TiO_2 loaded on magnetic Algerian halloysite clay (Fe_3O_4-HKDD3) for the photocatalytic activity of methylene blue dye in an aqueous medium

Asma Hayoune[a], Hocine Akkari[b], Vincenzo Vaiano[c], Nicola Morante[c], Diana Sannino[c] and Farid Madjene[d]

[a]Groupe des matériaux fonctionnels, laboratoire LGMM, Université 20 aout 1955-Skikda, Algerie; [b]Département de Génie Industriel, Faculté de Technologie, Université Batna 2 Chahid Mostefa Ben Boulaid, Batna, Algérie; [c]Department of Industrial Engineering, University of Salerno, Salerno, Italy; [d]Unité de Développement des Equipements Solaires, UDES, Centre de Développement des Energies Renouvelables, CDER, Tipaza, Algérie

ABSTRACT

This work aimed to synthesise a magnetic photocatalyst based on Ag-TiO_2 nanoparticles supported on Algerian Halloysite clay (HKDD3) loaded with magnetite Fe_3O_4 through a solvothermal method. The prepared catalyst was characterised by X-ray diffraction (XRD), high-resolution transmission electronic microscopy (HRTEM), Fourier transform infrared spectroscopy (FTIR), Brunauer-Emmett-Teller (BET) surface area analysis, UV–vis-DRS Diffuse reflectance spectroscopy, and X-ray photoelectron spectroscopy (XPS). Structural and morphological characterisation exhibited that magnetite (Fe_3O_4) and (TiO_2) particles were on a nanometre scale and their sizes were estimated around 50 nm and 30 nm, respectively. DRS results demonstrated that the bandgap has shifted from 3 to 1.75 eV. The photocatalytic performance was evaluated under visible light by changing different operating parameters including photocatalyst loading, initial dye concentration, pH, and scavenger's effect. The methylene blue discoloration was 92% with mineralisation of 87%, which was achieved at pH 6.7 after 3 hours of irradiation visible light with a dosage of 0.937 g/l of catalyst. The photocatalyst can be easily separated due to the action of an external magnetic field. The $^{\bullet}O_2^-$ and $^{\bullet}OH$ species are the main ones responsible for the photodegradation of methylene blue dye.

ARTICLE HISTORY
Received 11 July 2021
Accepted 18 August 2021

KEYWORDS
Ag-TiO_2; Fe_3O_4-HKDD3; clay-photocatalyst; methylene blue

1. Introduction

Wastewater treatment is the biggest challenge because of the discharge of several industries sectors such as textile, rubber, food, cosmetics, etc [1]. Which contains different inorganic and organic contaminants that are very toxic, harmful, and non-biodegradable [2]. In this aspect, advanced oxidation processes (APOs) are the most suitable to remove these pollutants, transforming the organic pollutants into CO_2 and

CONTACT Asma Hayoune hayoune.asma@gmail.com; Farid Madjene faridmadjene@yahoo.fr; madjene.farid@udes.dz

water. Heterogeneous photocatalysis is one of the APOs based on the use of semiconductors under solar or artificial irradiation for degradation and mineralisation of contaminants that can be done by using the catalyst in the form of suspended or supported particles [3]. The use of photocatalysts in powder form poses problems of agglomeration of their ultrafine particles in larger particles, less active due to the lower exposed surface area, generating a decrease in photocatalytic activity [4], as well as including the requirement of catalysts separation, the needing the use of expensive microfiltration for their separation from the treated water [5]. One of the solutions to these problems is to immobilise the photocatalyst on inert support easily separable. Nevertheless, it has been shown that the immobilisation of TiO_2 on supports typically reduces the efficiency of the whole process due to the decrease in the surface area of the photocatalyst under irradiation. At present, studies are being carried out on the search for new supports [6], such as clays, zeolites, and carbonaceous materials [7]. Clays are abundant and low-cost materials including montmorillonite [8], halloysite [9], sepiolite [10], and kaolinite [11]. Halloysite is affordable mineral clay with different surface chemical properties which endow to facilitate modification and grow functional materials onto their surface [12]. On the other hand, titanium dioxide is one of the well-known catalysts owing to its non-toxicity, abundance, and low cost [13]. However, the main drawback of TiO_2 is that like nanomaterial, is difficult to separate from simple sedimentation and it is active only in UV which accounts only for 5% of the total solar light. Different papers focus on doping TiO_2 with metals [14–16] and non-metals [17,18] or coupling with other semiconductors [19] to improve absorption of visible light [20]. On the other hand, it must be considered that with the use of an external magnetic field, photocatalyst coupled with magnetic support could be easily recovered. Recently it was found the TiO_2 can be readily combined with clay and recovered under an external magnetic field [21]. To prevent agglomeration, there is a certain interest to use natural clay as a support for loading metal-doped TiO_2 nanoparticles. Although there have been several studies on TiO_2 /halloysite or Ag/TiO2, few reports focused on the preparation of Ag-TiO2/halloysite composite to enhance photocatalytic activity. In light of these findings, for the first time, we developed a novel Ag-TiO_2-Fe_3O_4 composite photocatalyst using a simple solvothermal method.

The purpose of this research was to evaluate the efficiency of the photocatalytic activity under visible light irradiation in the presence of Ag-doped TiO_2 – Fe_3O_4 loaded on Algerian halloysite for the removal of methylene blue (MB) dye from an aqueous medium. A novel magnetic photocatalyst was prepared based on natural clay for the purpose to investigate natural abundant sources which are low cost. The loading of Ag-TiO2 into halloysite clay to ease the separation of photocatalyst from the bulk solution. Also, doping TiO2 with Ag in small portions of 2% enhance photocatalytic activity through the inhibition of electron recombination. The use of visible light sensitisation is efficient photocatalysis mechanism that saves energy. To determine the best conditions of cationic dye discoloration and mineralisation, the influence of the following operating parameters on the photocatalytic activity was analysed: photocatalyst loading, initial concentration of MB contaminant, initial pH of the solution. Additionally, photocatalytic tests with molecules able to scavenger the reactive oxygen species (ROS) were carried out in order to identify the main ROS involved in the degradation mechanism.

2. Material and methods

2.1. Chemicals and materials

The halloysite clay was obtained from KDD3 mountain (Djebel Debbagh) Guelma city, Algeria. It denoted HKDD3. The chemical composition of HKDD3 clay was performed by fluorescence X analysis, it was found to be as follows: 38.48% Al_2O_3; 36.11% SiO_2; 0.13% Fe_2O_3, 0.42% CaO, 0.16% MgO, 0.26% Na_2O. Iron (III) chloride hexahydrate ($FeCl_3{\cdot}6H_2O$), Iron (II) sulphate heptahydrate ($FeSO_4{\cdot}7H_2O$), and ammonia used for the synthesis of Fe_3O_4 were provided from sigma Aldrich. For preparation 2% Ag-doped TiO_2 supported on HKDD3 loaded with Fe_3O_4, Titanium isopropoxide (TTIP, 97%), isopropanol (99%), acetic acid, silver nitrate were used. All reagents were analytical grade and used without further purification. The prepared catalyst Ag-TiO_2 loaded on Fe_3O_4-HKDD3 clay was labelled Ag-TiO_2-MHKDD3 catalyst.

2.2. Preparation of samples

To prepare the catalyst 2% Ag-TiO_2-MHKDD3 were employed in two steps. **The first one** is the synthesis of magnetic clay nanocomposite (M-HKDD3) through the coprecipitation method by dissolving 1.2 g of $FeCl_3{\cdot}7H_2O$ and 0.6 g of $FeSO_4$ with molar ration 2:1 in distilled water under stirring then 0.5 g of HKDD3 clay was added. A volume of NH_4OH was dropped slowly to the mixture under N_2 inert gas for the formation of magnetite particles. The black solution was kept under stirring for 4 h at 70°C. The obtained powder was washed several times and dried in the oven at 80°C. **The second step** is to prepare the Ag-TiO_2-M-HKDD3 photocatalyst. An amount of 0.25 g of magnetic clay (M-HKDD3) was dispersed in 9.6 ml of isopropanol $(CH_3)_2CHOH$ under sonication for 15 min. Then 0.40 ml of TTIP (Ti $[OCH(CH_3)_2]_4$) was added dropwise. A quantity of silver nitrate ($AgNO_3$) was added to the solution to attain 2 wt% of silver on TiO_2. The pH of the solution was adjusted to 4 by acid acetic (CH_3COOH). Then, the solution was transferred into a Teflon-lined stainless steel autoclave 23 ml, followed by a solvothermal treatment at 160°C for 24 h. The obtained powders were cooled at room temperature. Subsequently, they were washed with deionised water five times and dried in a vacuum oven at 100°C.

2.3. Photocatalyst characterisation techniques

X-ray diffraction (XRD) patterns were collected on a PANanalytical X'Pert Pro automated diffractometer. Powder patterns were recorded in Bragg-Brentano reflection configuration by using a Ge(111) primary monochromator (Cu Kα) and the X'Celerator detector with a step size of 0.0167° (2θ). The powder patterns were recorded between 4 and 70 ° in 2θ with an equivalent counting time of ~60 s/step. The Fourier transform infrared (FTIR) spectrum was carried out by Bruker model Vertex70 in the mid and near-infrared range from 4000–500 cm^{-1}. UV–vis diffuse reflectance spectrophotometry (DRS) was obtained by Cary 5000 spectrometer from Varian with an integrating Spectralon sphere with high resolution from 170 to 3300 nm. High-resolution transmission electron microscopy (HRTEM) and selected area electron diffraction (SAED) was achieved with an FEI TALOS

F200X microscope operated at 200 kV. The textural properties of nanocomposites were performed by sorption desorption measurements of N_2 at −196°C using a Micrometrics (TriStar II 3020).

2.4. Photocatalytic activity tests under visible light

The photocatalytic experiments were carried out with a Pyrex cylindrical reactor (ID = 2.6 cm, L_{TOT} = 41 cm, and V_{TOT} = 200 mL) equipped with an air distributor device (flowrate of 142 N cm^3 min^{-1}). Visible-LEDs strip (nominal power: 10 W; provided by LED lighting hut; emission in the range 400–800 nm; light intensity: 13 mW cm^{-2}) was positioned in contact with the external surface of the photoreactor. The solution of MB dye was exposed under visible light irradiation for 3 hours after keeping it for 2 hours in the dark to reach the adsorption-desorption phenomenon. At different times, about 3 mL of the suspension was withdrawn from the photoreactor and centrifuged to remove the catalyst particle. UV-Vis spectrophotometer (Thermo scientific Evolution 201) was used to analyse the aqueous solution. In detail, the removal of MB dye was evaluated by measuring the maximum absorbance value at 663 nm. The mineralisation level was determined by measuring the treated solutions' total organic carbon (TOC) content. TOC of solutions was measured from CO_2 obtained by the high temperature (680°C) catalytic combustion [22].

The TOC removal (mineralisation efficiency) and MB discoloration efficiency at the generic irradiation time were evaluated using the following relationship:

$$Mineralization\ efficiency(t) = \left(1 - \frac{TOC(t)}{TOC_0}\right)100 \tag{1}$$

$$Discoloration\ efficiency(t) = \left(1 - \frac{c(t)}{c_0}\right)100 \tag{2}$$

Where *TOC(t)* is the total organic carbon at the generic irradiation time (mg/l), TOC_0 is the initial total organic carbon (mg/l), *c(t)* is the MB concentration at the generic irradiation time (mg/l), c_0 is the initial MB concentration (mg/l).

The Langmuir–Hinshelwood model is usually used to describe the kinetics of the photocatalytic process [23]. The derivation is based on the degradation rate (*r*), which is expressed as follows:

$$r = -\frac{dc}{dt} = \frac{k_r K_{ad} c}{1 + K_{ad} c} \tag{3}$$

Where k_r, K_{ad}, and *c* are the intrinsic kinetic constant, adsorption equilibrium constant and, dye concentration, respectively.

Assuming that adsorption is weak and the concentration of compounds is low, the equation above can be simplified to the first-order kinetics expression with an apparent discoloration kinetic constant (K_{app}):

$$\ln\left(\frac{c_0}{c}\right) = k_r K_{ad}\ t = K_{app} t \tag{4}$$

The value of the apparent discoloration kinetic constant can be calculated by the slope of the zero-passing straight line obtained from plotting $ln(c_0/c)$ vs time t.

3. Result and discussions

3.1. XRD patterns

The X-ray diffraction spectra showed that the kaolin Djebel Debbagh (HKDD3) includes kaolinite (JCPDS 80–0886) [24] and halloysite (JCPDS 29–1489) [25]. Furthermore, new peaks appeared at 2θ values 30.1, 35.6, 43.3, 57.1, 62.7, which referred to (220), (311), (400), (511), and (440) planes of magnetite particles [26]. Besides, after functionalization of clay by Ag-doped TiO_2 particles other characteristics peaks were displayed at 2θ values25.2, 37.9, 48.2, 54.7 and 62.8 with reflection planes (101), (004), (200), (105), and (204), respectively [27]. These peaks are attributed to the TiO_2 anatase phase. However, there are no peaks related to Ag particles meanings that the quantity of silver(2%) is not appropriate to have its characteristic peaks in pattern [28,29]. The average crystalline size of TiO_2, Fe_3O_4 were calculated by the Debye Scherrer equation; it was estimated to be 24 nm and 46 nm, respectively. After deposition of Fe_3O_4 and doped TiO_2 particles, the clay peaks were significantly weakened, as shown from the intensity of the signal at 2θ: 9.41, 18.7, 19.8 (Figure 1), which indicates that TiO_2 particles well present in a mixture with clay.

3.2. FTIR

The FTIR analysis is used to investigate the functional group and chemical bonds present on the surfaces of the material. The FTIR spectra for natural Algerian HKDD3 and Ag-TiO_2 MHKDD3 are displayed in Figure 2. It is possible to observe intense bands at 3622 cm^{-1}

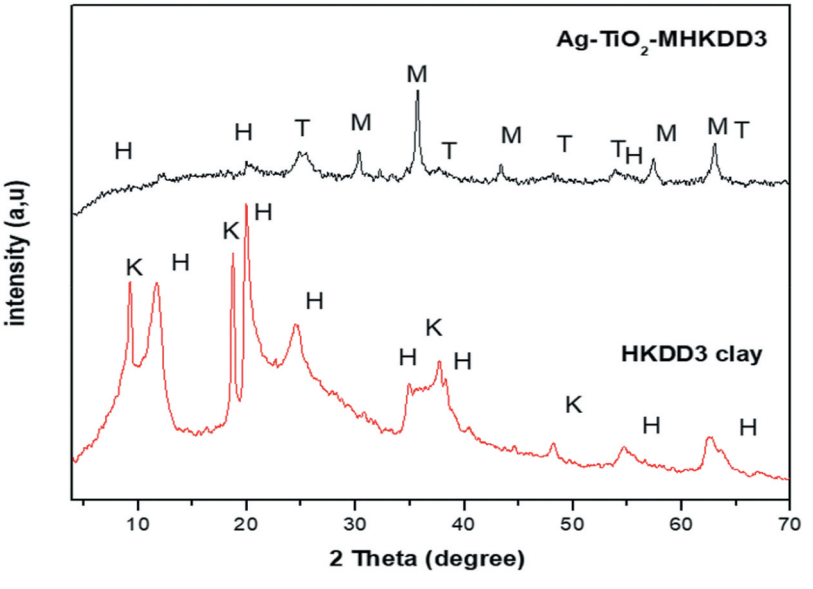

Figure 1. XRD patterns for HKDD3 and Ag-TiO2-MHKDD3 (H: halloysite, K: kaolinite, M: Fe_3O_4, T: TiO_2).

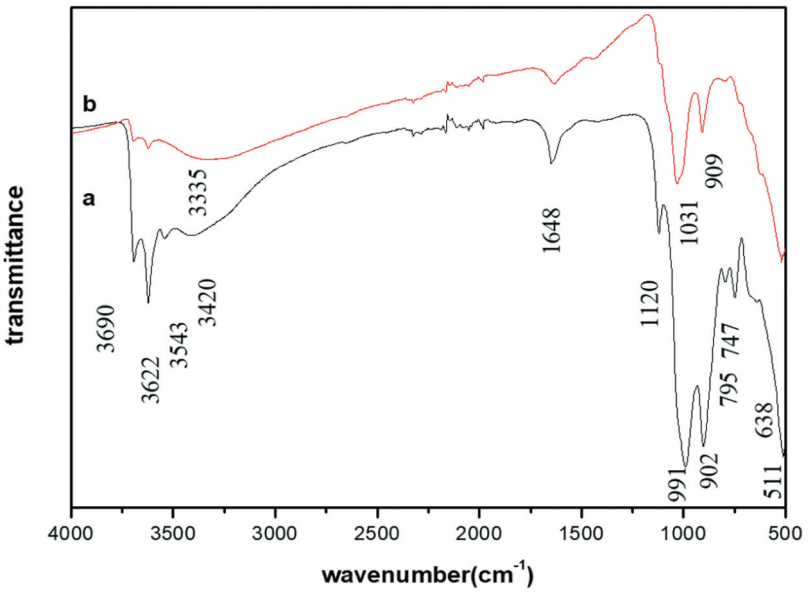

Figure 2. FTIR spectrum HKDD3 (a), Ag TiO_2 MHKDD3 catalyst (b).

and 3690 cm^{-1} which are assigned to OH stretching vibrational groups [30] of halloysite Algerian clay. Besides, the signal at 1648 cm^{-1}, attributed to OH deformation for the adsorbed molecules of water. Intense peaks can be seen at 1120, 991, 902 cm^{-1}, which are referred to as in-plane Si-O stretching groups [31], Al-O-Si and Al-OH vibration groups respectively [32]. The band 511 cm^{-1} corresponds to Al-O-Si deformation [33]. After the modification by Fe_3O_4 and TiO_2 nanoparticles, the same peaks were seen in the Ag-TiO_2 -M-HKDD3 catalyst. However, the shifting of a Si-O band from 1000 cm^{-1} to 1025 cm^{-1} and the decrease of intensity can be explained by the formation of hydrogen banding between TiO_2 and Si-OH groups of HKDD3 clay [27]. The characteristic band of Fe_3O_4 around 580 cm^{-1} does not appear clearly but like a shoulder, because overlapped by the storn Al-O-Si bands of HKDD3 at 511 cm^{-1} [34,35].

3.3. UV – visible DRS analysis

Diffuse reflectance spectroscopy (DRS) was performed to analyse the absorption properties of catalysts. as seen from Figure 3, it was clear that the HKDD3 clay has an absorption very wide and featureless throughout the entire spectrum area [36]. The modification of clay with TiO_2 nanoparticles emerged the appearing an absorption edge at about 400 nm corresponding to 3 eV bandgap by constructing the tauc plot. After deposition of magnetite (Fe_3O_4) [37] and Ag- TiO_2 nanoparticles, it can be observed a redshift to the visible light region (broadband in the visible region from 250 to 700 nm). This redshift is due to the transition of the charge transfer between the electrons of the nanoparticles of magnetite Fe_3O_4 and the TiO_2 conduction band (or valence band) [38] and to the presence of plasmonic absorptions of silver nanoparticles. Iron oxide nanoparticles can

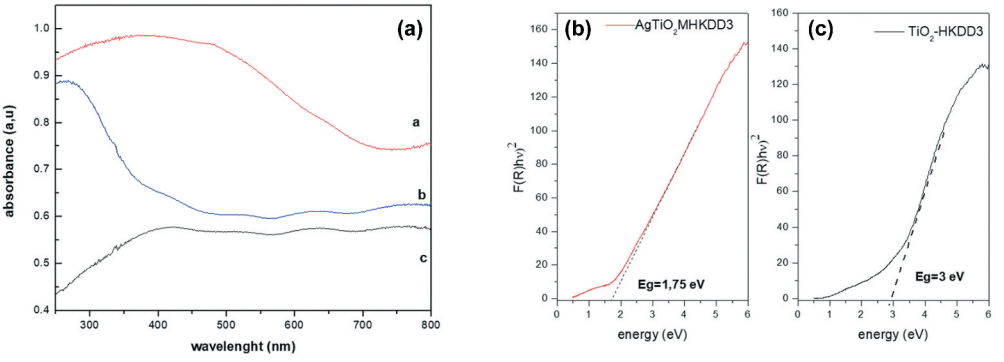

Figure 3. UV visible spectra of catalysts, (a) Ag-TiO_2-MHKDD3 (b) TiO_2-HKDD3 (c) HKDD3 and their optical band gap energy plot.

increase the energy spacing between the TiO_2 conduction band, allowing the quantisation of energy levels and lead to the absorption of visible light [39]. In addition, increased light absorption will increase the number of photogenerated electrons and holes involved in the photocatalytic reaction and photocatalytic performance enhancement. After using the Tauc plot equation (providing the direct bandgap), it can be estimated that the bandgap value is around 1.75 eV [40].

3.4. HRTEM

The images of HRTEM show the morphology and the distribution of magnetite and titanium dioxide particles doped with silver supported on Algerian halloysite clay (HKDD3) (Figure 4). The halloysite clay HKDD3 can be individuated by its tubular shape with length from 0.3 um to 3 um and inner diameter between 15 nm and 50 nm. After deposition of magnetite and titanium dioxide nanoparticles, the clay becomes rougher with irregular dispersion of particles forming aggregates loaded onto the surface of M-HKDD3 clay. As presented in Figure 4(a-d), It can also be observed that the average particle size of TiO_2 and Fe_3O_4 nanoparticles are ranging from 10 to 30 nm and from 20 to 50 nm, respectively.

3.5. BET analysis

To determine the textural properties of clay functionalised by Ag-TiO_2-MHKDD3 catalyst, the adsorption-desorption measurements N_2 were performed at 77.35k (Figure 5). According to the classification of IUPAC, TiO_2-M-HKDD3 and Ag TiO_2-M-HKDD3 catalysts show type IV and II, respectively, with an H3 hysteresis loop [41]. As seen in Table 1, the average pore volume and diameter was calculated by the DFT method [42] the decrease of specific surface area (SSA), pore-volume, and diameter could be explained by the filling of vacant pores of TiO_2-M-HKDD3 catalyst by Ag nanoparticles [40].

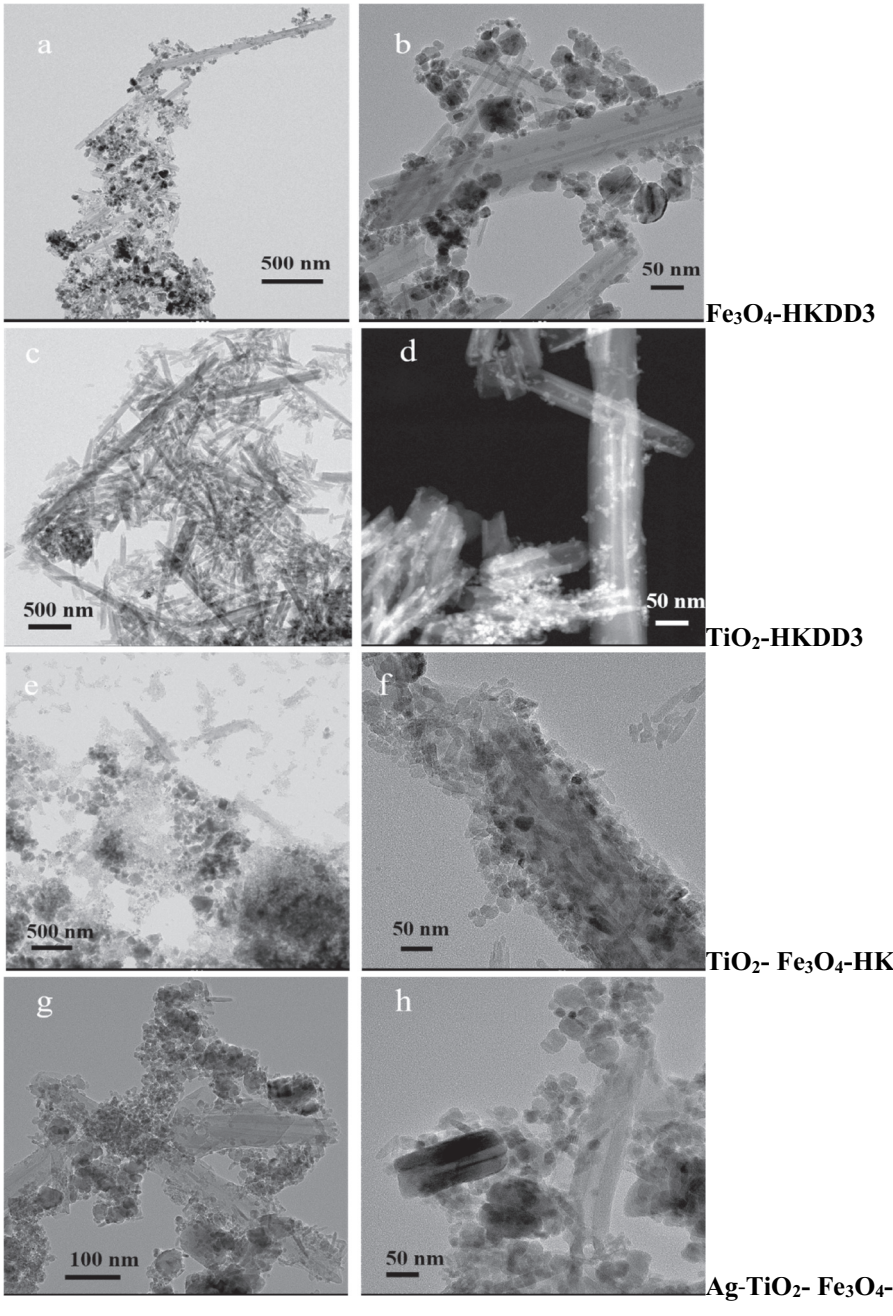

Figure 4. HRTEM images of as-prepared (a and b) Fe_3O_4-HKDD3, (c and d) TiO_2- HKDD3, (e and f) TiO_2- Fe_3O_4-HKDD3, (g and h) Ag-TiO_2-MHKDD3 catalysts.

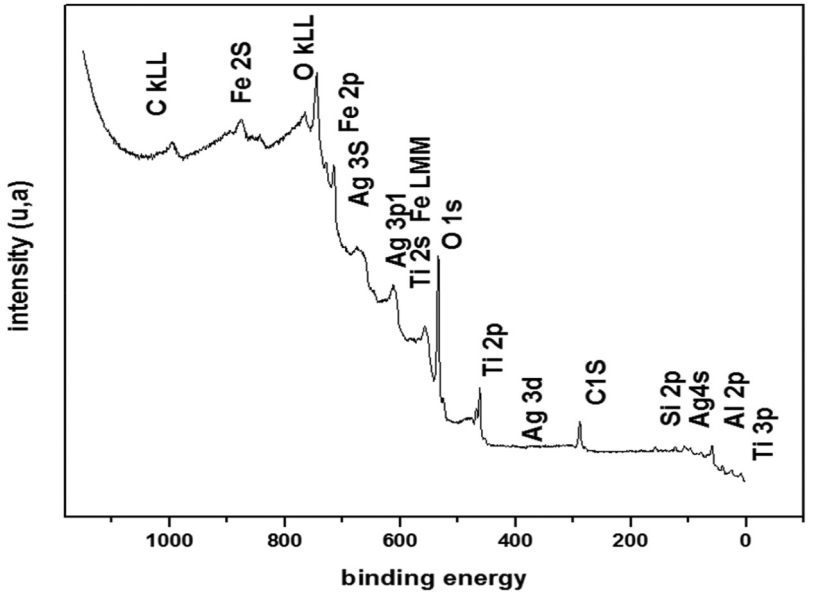

Figure 5. XPS spectra of Ag-TiO2-MHKDD3 photocatalyst.

Table 1. Textural properties of TiO_2-M-HKDD3 and Ag-TiO_2-MHKDD3 catalyst.

Sample	S_{BET} (m^2/g)	Average pore volume(cm^3/g)	Average pore diameter (nm)
TiO_2-M-HKDD3	145	0.34	9.36
Ag-TiO_2-M-HKDD3	83	0.18	8.65

3.6. XPS analysis

XPS analysis was performed for Ag-TiO_2-MKDD3 photocatalyst to determine the elements and their chemical state. This sample was composed of Si, Al, Fe, Ti, Ag, and O as shown in Figure 5. The peak of C was seen due to the adventitious hydrocarbon from the XPS instrument [43]. The Si 2p XPS spectrum was located at 103 eV assigned to SiO_2 that was the main corposant of Algerian halloysite clay. According to peaks of Ti 2p3/2 and Ti 2p1/2 were observed at 458.81 and 464.56 eV, respectively (Figure 6(a)) [44]. These binding energy corresponding to Ti^{4+}, which could indicate the formation of TiO_2. Besides, the binding energy of O1s was located at 533.92 eV, which is attributed to Ti-OH-and adsorbed molecules of water on the surface of HKDD3 clay. As seen from Figure 6(b) the existence of peaks with binding energy at 368.3 eV and 374.36 eV were revealed to Ag 3d 5/2 and Ag 3d3/2, respectively. The 6.0 eV difference between the two peaks also means that metallic Ag is presented [45]. As displayed in Figure 6(c) Fe2P spectrum shows peaks at 711.11 ev, 724.62 ev for Fe2p3/2 and Fe2p1/2 respectively [46]. The gap of 13.6 eV between the peaks could be assigned to Fe, which was presented in Fe_2O_3. The satellite peak was exhibited at around 719 eV. These binding energies were referred to the chemical state of Fe^{+3} (Fe_3O_4) [47].

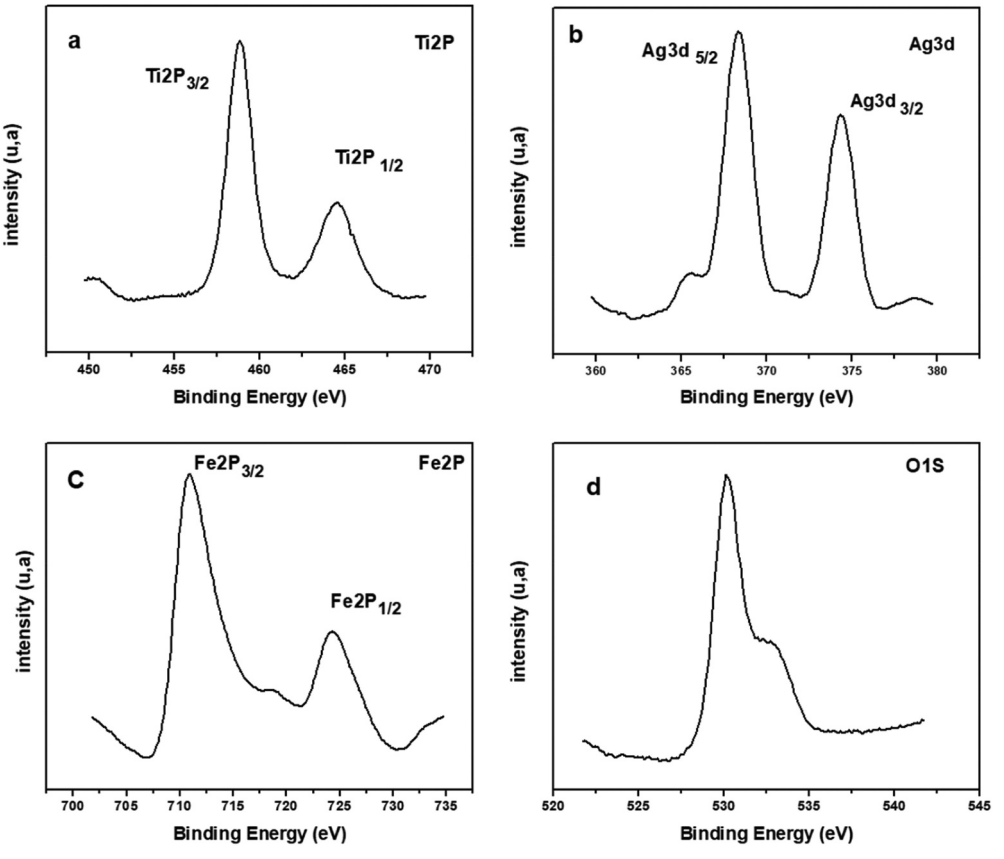

Figure 6. XPS spectrum of Ag-TiO2-MHKDD3 photocatalyst. (a) O1s, (b) Ag3d, (c) Fe2p, (d) Ti2p.

3.7. Photocatalytic activity results under visible light

Initially, a preliminary test was carried out to evaluate the photocatalytic activity under visible light of the prepared Ag-TiO_2-MHKDD3. It was conducted with a photocatalyst loading equal to 0.625 g/l and an initial MB concentration of 7 mg/l. Figure 7 highlights that discoloration and mineralisation occur simultaneously under visible light irradiation of photocatalyst and that the catalyst presents an interesting activity being well activated by the visible irradiation. The sorption of MB dye reached 60% after 120 min in the dark. By the way, the discoloration reached more than 90% after 180 min of irradiation, meanwhile, the mineralisation was, as showed by TOC removal, at 75%.

3.7.1. Photocatalyst loading

The effect of photocatalyst loading on the photocatalytic degradation process was studied because the optimum photocatalyst dosage could maximise the photocatalytic performance and minimise the cost and energy consumption. Indeed it is an important factor in photocatalysis because the photodegradation efficiency could be strongly affected by the number of active sites present in the suspension and photo-adsorption ability of the catalyst used. Therefore, an Ag-TiO_2-M-HKDD3 dosage ranging from 0.312 to

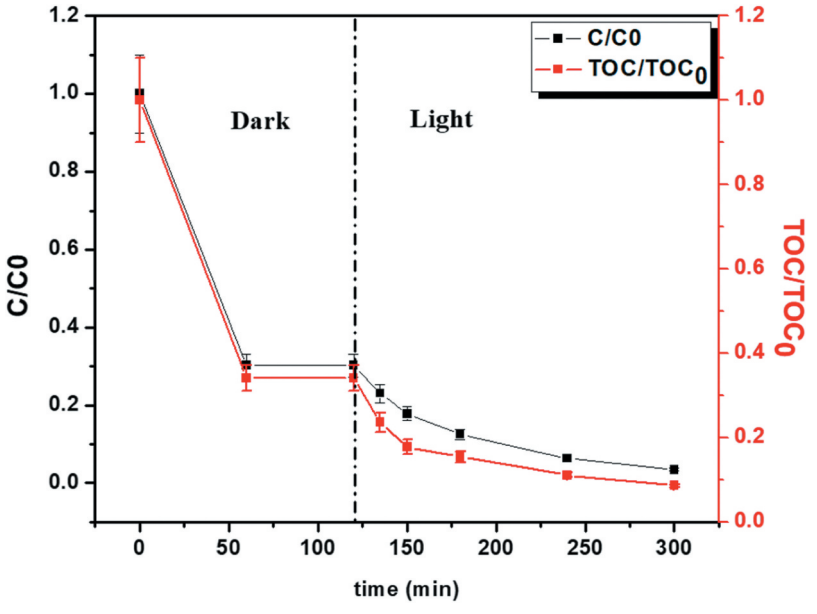

Figure 7. Photocatalytic discoloration and mineralisation of Ag-TiO2-MKDD3 photocatalyst for preliminary test under visible light irradiation.

1.25 g/l was used to investigate its influence on discoloration and mineralisation efficiency, and to find out the optimal loading value. The tests were conducted using 80 ml of MB solution with an initial concentration of 7 mg/l. The results presented in Figure 8, show that the photocatalytic activity is strongly influenced by the variation of the photocatalyst loading for MB dye. Both discoloration efficiency and mineralisation efficiency are proportional to the catalyst dosage, this is due to the increasing number of active sites of Ag-TiO_2 -M-HKDD3 catalyst. Thus to a higher photon reception surface and consequently to an increasing concentration of the reactive species formed contributing to the photocatalysis process [48]. The result is a clear saturation translated by a plateau where the discoloration and the mineralisation of the photocatalyst remain relatively constant, in agreement with the expected trend at the high level of dosage, where the photocatalyst particles screen themselves [49].

It is noted that after three hours of visible light irradiation is sufficient to mineralise 87% of the dye for a photocatalytic loading of 0.937 and 1.25 g/l. On the other hand, the mineralisation efficiency of 67 and 75% are obtained respectively for 0.3 and 0.9 g/l. Therefore, the optimal loading of the photocatalyst was at 0.9 g/l because this was the level of dosage useful to get the higher TOC removal, without the ineffective adding of further mass of photocatalyst.

3.7.2. Initial dye concentration

The influence of the initial concentration of the MB dye on the efficiency of photocatalysis was studied for different values ranging from 7 to 28 mg/l under visible light irradiation using the obtained optimal Ag-TiO2-MHKDD3 dose of photocatalyst 0. 937 g/l. According to the results shown in Figure 9, it can be seen that the efficiency of the reaction is

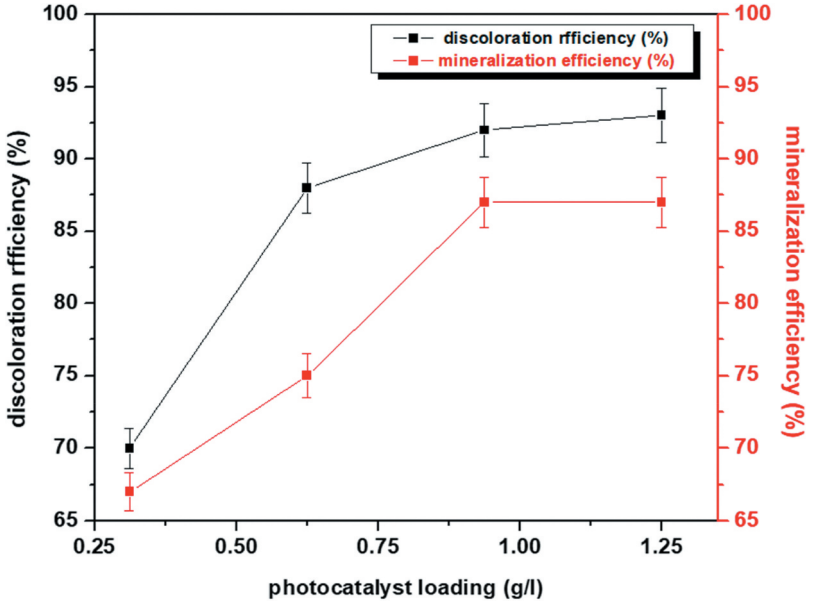

Figure 8. Effect of Ag-TiO2-MHKDD3 dosage on the discoloration efficiency and mineralisation efficiency measured after 3 h under visible light irradiation.

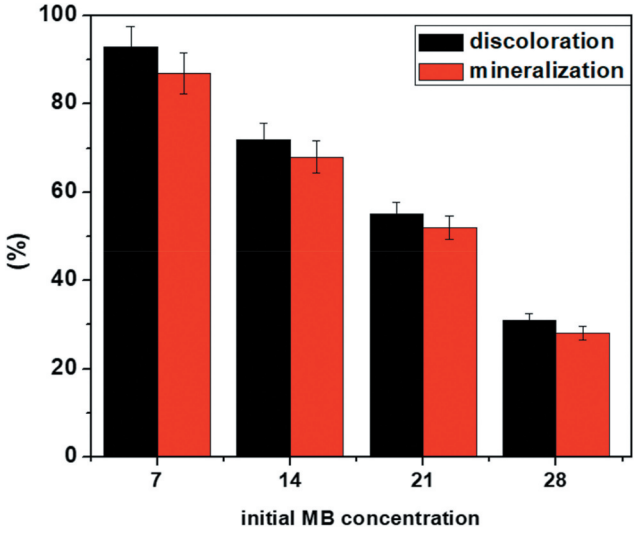

Figure 9. Effect of initial MB concentration on photocatalytic discoloration and mineralisation.

inversely proportional to the concentration; the photocatalytic efficiency decreases with the increase of the concentration of MB dye [50]. The best efficiency is obtained with the lowest concentration (7 mg/l) with the discoloration efficiency of 93% and mineralisation of 87%. The probable formation of reactive oxygen species (ROS), such as hydroxyl radicals, superoxide, and positive holes on the semiconductor surface and their subsequent interaction with dye molecules determine the degradation mechanism [51]. The obtained results can be interpreted as follows: a high MB concentration leads to a high number of pollutant molecules adsorbed on the surface reducing down the generation of the reactive oxygen species (ROS) because the active sites of the photocatalyst were occupied by dye molecules [52]. In addition, the high dye concentration increases the opacity and turbidity of the solution, which reduces the penetration of light through the solution, and the absorption of photons by the catalyst particles decrease, and consequently, the photocatalytic activity is reduced [53].

3.7.3. pH

It was also reported that the pH value is another parameter that influences the surface charge of photocatalyst and the degree of MB ionisation in the solution [54]. Its effect was examined by changing the initial pH solution at 5 and 8.63 using the optimal photocatalyst loading (0.937 g/l) and the optimal initial concentration of MB (7 mg/l). The initial pH of the solution with an initial MB concentration of 7 mg/l was equal to 6.70. The values of pH were modified with an aqueous solution of HCl or NaOH.

Methylene blue is a cationic dye therefore its absorption is favoured for high pH values [55]. At high pH, the catalyst surface is predominantly negatively charged, and a strong interaction occurs between the photocatalysts surface and the cationic ions of the dye, resulting in strong adsorption. At low pH, however, both the surface of Ag-TiO_2-M-KDD3 and the dye molecules are positively charged, resulting in weak adsorption. Thus, it is reasonable that with an increase in pH, the adsorption of the MB on the photocatalyst surface increases, resulting in a higher degradation rate [56]. But for high alkaline pH, the hydroxyl radicals are rapidly scavenged, they do not have the opportunity to react with dyes and this leads to a decrease in photocatalytic activity.

Figure 10 shows the effect of pH on the mineralisation efficiency under 3 h of visible light irradiation and the apparent discoloration kinetic constant. The results highlight that a low photoactivity was obtained at pH equal to 5 K_{app} discoloration and mineralisation efficiency are 0.77 min^{-1}, 75, and 71%, respectively. The optimal pH is equal to 6.7; it shows the highest K_{app} value (0.16 min^{-1}) with the discoloration, mineralisation efficiency of 92 and 87%. For this reason, we have opted to conduct the experiments at pH equals to 6.7.

3.7.4. Scavengers

The possible role of reactive oxygen species (ROS), such as hydroxyl radicals, superoxide and positive holes has been investigated during the MB photocatalytic discoloration process using Ag-TiO2-MHKDD3 with its optimal loading (0.937 g/l) and optimal initial MB concentration (7 mg/l). The scavenger probe molecules were isopropanol (IPA, 10 mmol/l) for hydroxyl radicals [57], benzoquinone (BQ, 1 µmol/l) for superoxide [58] and disodium ethylenediamine tetra-acetate (EDTA, 10 mmol/l) for positive holes.

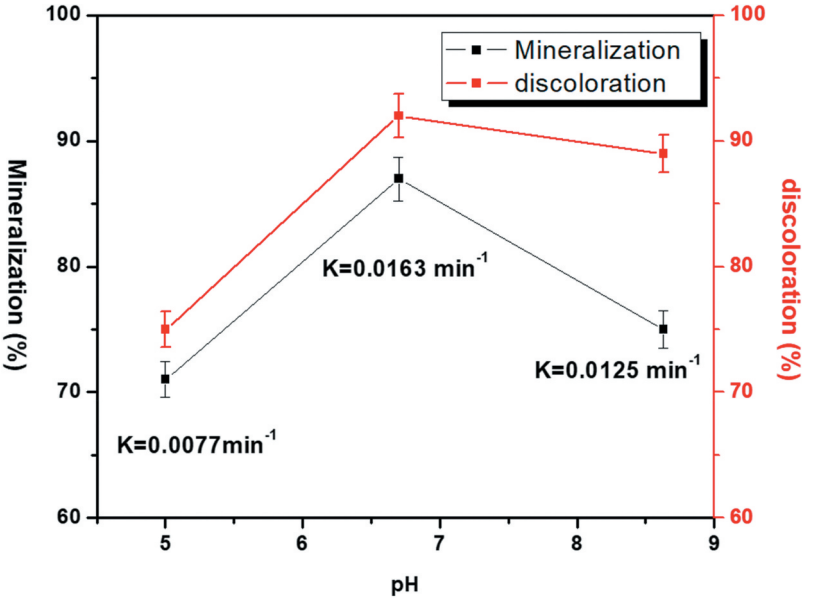

Figure 10. Effect of pH on the mineralisation, discoloration efficiency measured after 3 h and K_{app} under visible light irradiation.

As illustrated in Figure 11, the use of benzoquinone and isopropanol shows lower photocatalytic efficiency compared to ethylenediamine tetra-acetate. In effect, the addition of BQ and IPA significantly inhibits the photocatalytic reaction; the discoloration efficiency registered results 79 and 87%, respectively, instead of 92%, obtained for the reference solution without scavengers. On the other hand, when EDTA is added, removal rates of 91% are obtained. Based on the previous results, the photodegradation mechanism can be proposed mainly from two aspects: (i) the use of magnetic halloysite clay increases the adsorption properties due to its specific surface area and porosity, (ii) doping TiO_2 with Ag nanoparticles improves the visible light absorbance owing to (SPR) effect. Electrons are excited from the valence band (VB) to the conductance band (CB) under visible light irradiation, resulting in the creation of a hole (h+) in the VB. The interaction of h+ and e- in each CB and VB with OH and O_2 creates superoxide and hydroxyl radicals O2•-, •OH from the reaction system, allowing the MB dye to be further oxidised [59]. These results are consistent with the literature reporting the role of ROS on visible-light-driven photodegradation of MB [60].

The proposed mechanism is as follows:

$$Ag - TiO_2 - MHKDD3 + h\nu \rightarrow Ag - TiO_2 - MHKDD3\left(h^+_{VB} + e^-_{CB}\right) \quad (5)$$

$$O_{2ads} + e^-_{CB} \rightarrow O_2^{\bullet -} \quad (6)$$

$$O_{2ads} + e^-_{CB} + H^+ \rightarrow HO^{\bullet}_2 \quad (7)$$

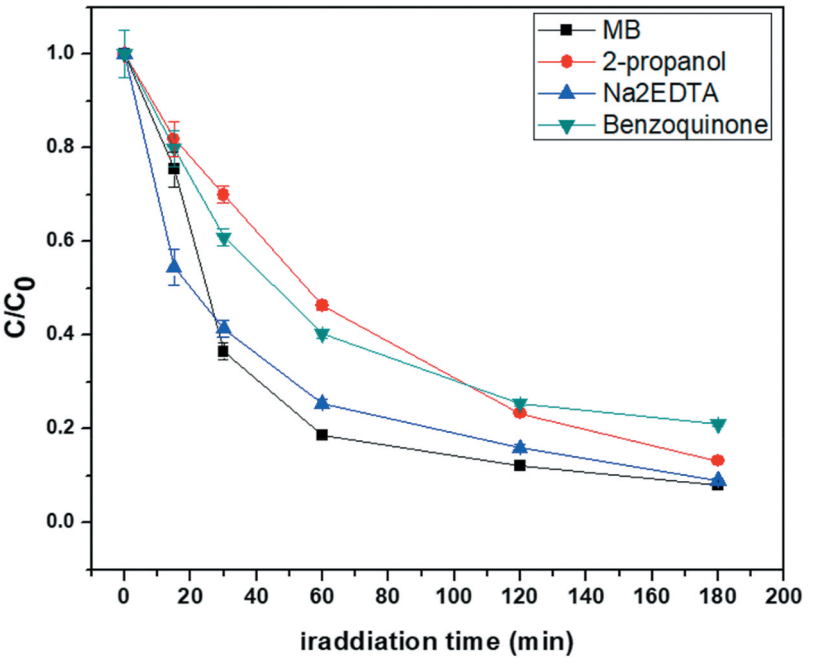

Figure 11. Effects of different scavengers on MB photodegradation using photocatalyst under visible light irradiation.

$$HO^{\bullet}_{2ads} + e^{-}_{CB} + H^{+} \rightarrow H_2O_2 \quad (8)$$

$$2H_2O_{2ads} + e^{-}_{CB} \rightarrow 2OH^{-} + 2OH^{\bullet} \quad (9)$$

$$MB + (OH^{\bullet} \text{ and } O^{\bullet}{}_2^{-}) \rightarrow \text{intermediates} \rightarrow CO_2 + H_2O + \text{mineral salts} \quad (10)$$

4. Conclusion

In summary, a novel photocatalyst was synthesised based on natural Algerian clay via a solvothermal method. Various characterisation techniques such as XRD, HRTEM, FTIR, BET, UV–vis-DRS, and XPS were used for its structure evaluation. The prepared photocatalyst Ag-TiO_2-MHKDD3 shows a wide absorption on the visible region with a bandgap of 1.75 eV. After the photocatalytic process, the separation of catalyst from solution is easy owing that magnetite nanoparticles are sensitive to an applied magnetic field. According to the XPS results, the silver existed in metallic form. The results highlight that the discoloration efficiency of dye reached 92% after 180 min of irradiation time with mineralisation efficiency equal to 87% at pH 6.7. According to these results Ag-TiO_2- MHKDD3 photocatalyst exhibited higher photocatalytic performance due to the following factors, bandgap energy, pore distribution, and higher adsorption capacity. The main species responsible for the degradation of MB dye were hydroxyl $OH^{\bullet}$ and $O_2^{\bullet-}$ radicals.

Disclosure statement

No potential conflict of interest was reported by the author(s).

References

[1] J. Gloser and G.T. Miller, Biol. Plantarum. **45** (1), 128 (2002). doi:10.1023/A:1015199330106.
[2] F. Han, V.S.R. Kambala, M. Srinivasan, D. Rajarathnam and R. Naidu, Appl. Catal. A. **359** (1–2), 40 (2009). doi:10.1016/j.apcata.2009.02.043.
[3] F. Madjene, M. Assassi, I. Chokri, T. Enteghar and H. Lebik, Water Environ.Res **92** (1), 11 (2020). doi:10.1002/wer.1360.
[4] H. Mohammed, M. Saidi, D. Tabet, P. Pichat and H. Khalaf, Amer. J. Appl.Sci **2**, 1140 (2005). doi:10.3844/ajassp.2005.1136.1140.
[5] J. Liu, M. Dong, S. Zuo and Y. Yingchun, Appl. Clay Sci. **43** (2), 159 (2009). doi:10.1016/j.clay.2008.07.016.
[6] N. Yahya, F. Aziz, N.A. Jamaludin, M.A. Mutalib, A.F. Ismail, W.N.W. Salleh, J. Jaafar, N. Yusof and N.A. Ludin, J. Environ.Chem. Eng **6** (6), 7425 (2018). doi:10.1016/j.jece.2018.06.051.
[7] B. Szczepanik, Appl. Clay Sci. **141**, 239 (2017). doi:10.1016/j.clay.2017.02.029.
[8] L. Cottet, C.A.P. Almeida, N. Naidek, M.F. Viante, M.C. Lopes and N.A. Debacher, Appl. Clay Sci. **95**, 31 (2014). doi:10.1016/j.clay.2014.03.023.
[9] D. Papoulis, S. Komarneni, D. Panagiotaras, E. Stathatos, D. Toli, K.C. Christoforidis, M. Fernández-García, H. Li, S. Yin, T. Sato and H. Katsuki, Appl Catal B **132–133**, 422 (2013). doi:10.1016/j.apcatb.2012.12.012.
[10] F. Zhou, C. Yan, H. Wang, S. Zhou and S. Komarneni, Appl. Clay Sci. **146**, 253 (2017). doi:10.1016/j.clay.2017.06.010.
[11] A. Magdy, Y.O. Fouad, M.H. Abdel-Aziz and A.H. Konsowa, J. Indu. Eng. Chem **56**, 311 (2017). doi:10.1016/j.jiec.2017.07.023.
[12] D. Wu, J. Li, J. Guan, C. Liu, X. Zhao, Z. Zhu, C. Ma, P. Huo, C. Li and Y. Yan, J. Indu. Eng. Chem **64**, 218 (2018). doi:10.1016/j.jiec.2018.03.017.
[13] M. Ge, C. Cao, J. Huang, S. Li, Z. Chen, K.Q. Zhang, S.S. Al-Deyab and Y. Lai, J. Mater. Chem. A **4**, 6801 (2016). doi:10.1039/C5TA09323F.
[14] P. Karuppasamy, N.R.N. Nisha, A. Pugazhendhi, S. Kandasamy and S. Pitchaimuthu, J. Environ. Chem. Eng **9** (4), 105254 (2021). doi:10.1016/j.jece.2021.105254.
[15] N. Wei, H. Cui, Q. Song, L. Zhang, X. Song, K. Wang, Y. Zhang, J. Li, J. Wen and J. Tian, Appl Catal B **198**, 90 (2016). doi:10.1016/j.apcatb.2016.05.040.
[16] T. Ali, A. Ahmed, U. Alam, I. Uddin, P. Tripathi and M. Muneer, Mater. Chem. Phys. **212**, 335 (2018). doi:10.1016/j.matchemphys.2018.03.052.
[17] W.C. Huang and J.-M. Ting, Ceramics Int. **43**, 9997 (2017). doi:10.1016/j.ceramint.2017.05.012.
[18] Z.-L. Cheng and W. Sun, J. Mater. Eng. Perform. **24** (10), 4095 (2015). doi:10.1007/s11665-015-1699-3.
[19] Y. Xin, Z. Li, W. Wu, B. Fu and Z. Zhang, ACS Sustainable Chem. Eng **4** (12), 6667 (2016). doi:10.1021/acssuschemeng.6b01533.
[20] M. Wang, J. Ioccozia, L. Sun, C. Lin and Z. Lin, Energy Environ. Sci **7**, 2202 (2014). doi:10.1039/C4EE00147H.
[21] D. Mehta, S. Mazumdar and S.K. Singh, J. Water Process Eng. **7**, 265 (2015). doi:10.1016/j.jwpe.2015.07.001.
[22] P. Franco, O. Sacco, I. De Marco and V. Vaiano, Catalysts **9** (346), 346 (2019). doi:10.3390/catal9040346.
[23] C.-H. Wu and J.-M. Chern, Ind. Eng. Chem. Res **45**, 6457 (2006). doi:10.1021/ie0602759.
[24] F. Chargui, M. Hamidouche, H. Belhouchet, Y. Jorand, R. Doufnoune and G. Fantozzi, Bol. Soc. Esp. Ceram. **57** (4), 177 (2018). doi:10.1016/j.bsecv.2018.01.001.
[25] Y. He, W. Xu, R. Tang, C. Zhang and Q. Yang, RSC Adv. **5**, 90620 (2015). doi:10.1039/C5RA19296J.

[26] J. Chang, J. Ma, Q. Ma, D. Zhang, N. Qiao, M. Hu and H. Ma, Appl. Clay Sci. **119**, 140 (2016). doi:10.1016/j.clay.2015.06.038.
[27] R. Wang, G. Jiang, Y. Ding, Y. Wang, X. Sun, X. Wang and W. Chen, ACS Appl. Mater. Interfaces **3**, 4158 (2011). doi:10.1021/am201020q.
[28] M. Valenzuela, S. Flores, O. Bernÿ, E. Albiter and S. Alfaro, *Molecular Photochemistry - Various Aspects* (InTech, 2012). doi:10.5772/38891.
[29] M.T. Aytekin Aydın, H.L. Hoşgün, A. Dede and K. Güven, Spectro. Acta A. **205**, 507 (2018). doi:10.1016/j.saa.2018.07.063.
[30] R. Riahi-Madvaar, M.A. Taher and H. Fazelirad, Appl. Clay Sci. **137**, 106 (2017). doi:10.1016/j.clay.2016.12.019.
[31] E. Tierrablanca, J. Romero-García, P. Roman and R. Cruz-Silva, Appl. Catal. A. **381** (1–2), 273 (2010). doi:10.1016/j.apcata.2010.04.021.
[32] T. Tsoufis, F. Katsaros, B.J. Kooi, E. Bletsa, S. Papageorgiou, Y. Deligiannakis and I. Panagiotopoulos, Chem. Eng. J. **313**, 474 (2017). doi:10.1016/j.cej.2016.12.056.
[33] Y. Xie, Chem. Eng. J. **168** (2), 963 (2011). doi:10.1016/j.cej.2011.02.031.
[34] N.V.S. Praneeth and S. Paria, *Clay-Semiconductor Nanocomposites for Photocatalytic Applications, Clay Minerals: Properties, Occurrence and Uses: Chapter 5* (Nova Science Publishers, Inc., USA, 2017).
[35] P. Zheng, Y. Du and X. Ma, Mater. Chem. Phys. **151**, 17 (2015). doi:10.1016/j.matchemphys.2014.11.075.
[36] W. Xing, Appl. Surf. Sci. **259**, 704 (2012). doi:10.1016/j.apsusc.2012.07.102.
[37] T. Ws and D. Wa, ACS Appl. Mater. Interfaces **1**, 2461 (2009). doi:10.1021/am900418q.
[38] X. Chen and Y. Mao, Chem. Rev. **107**, 959 (2007). doi:10.1021/cr0500535.
[39] W. Wu, X. Xiao, S. Zhang, F. Ren and C. Jiang, Nanoscale Res. Letters **6** (1), 533 (2011). doi:10.1186/1556-276X-6-533.
[40] A. Mishra, A. Mehta, M. Sharma and S. Basu, J. Environ. Chem. Eng **5**, 651 (2017). doi:10.1016/j.jece.2016.12.042.
[41] K.S.W. Sing and R.T. Williams, Adsorption Sci. Technol **22** (10), 782 (2004). doi:10.1260/0263617053499032.
[42] P.I. Ravikovitch, G.L. Haller and A.V. Neimark, Adv. Coll. Inter. Sci. **76–77**, 226 (1998). doi:10.1016/S0001-8686(98)00047-5.
[43] X. Zhao, Y. Du, C. Zhang, L. Tian, X. Li, K. Deng, L. Chen, Y. Duan and K. Lv, Chinese J. Catal **39**, 746 (2018). doi:10.1016/S1872-2067(18)63039-6.
[44] C. Belver, M. Hinojosa, J. Bedia, M. Tobajas, M. Alvarez, V. Rodríguez-González and J. Rodriguez, Materials **10** (8), 960 (2017). doi:10.3390/ma10080960.
[45] F.C.S.M.R. Lopes, M.G.C. Da Rocha, P. Bargiela, H.S. Ferreira and C.A.M. Pires, Chem. Eng. Sci. **227**, 115939 (2020). doi:10.1016/j.ces.2020.115939.
[46] O.F.S. Khasawneh and P. Palaniandy, Environ. Technol. Innov 2020, 101230. doi:10.1016/j.eti.2020.101230
[47] H. Singh, J.K. Rajput, G. Govil, P. Arora and J. Badhan, Appl. Organometal. Chem. **32** (10), e4514 (2018). doi:10.1002/aoc.4514.
[48] H. Singh, J.K. Rajput, N. Dogra, G. Jain, A. Gupta and S. Garg, J. Aust. Ceram. Soc **57** (3), 848 (2021). doi:10.1007/s41779-021-00592-3.
[49] D.R. Paul, R. Sharma, S.P. Nehra and A. Sharma, RSC Adv. **9** (27), 15391 (2019). doi:10.1039/C9RA02201E.
[50] H. Singh and J.K. Rajput, J. Iran. Chem. Soc **16** (11), 2432 (2019). doi:10.1007/s13738-019-01710-6.
[51] M. Stylidi, Appl. Catal. B. **47** (3), 201 (2004). doi:10.1016/j.apcatb.2003.09.014.
[52] J. Grzechulska and A.W. Morawski, Appl. Catal. B **36** (1), 51 (2002). doi:10.1016/S0926-3373(01)00275-2.
[53] -C.-C. Liu, Y.-H. Hsieh, P.-F. Lai, C.-H. Li and C.-L. Kao, Dyes and Pigments **68** (2–3), 195 (2006). doi:10.1016/j.dyepig.2004.12.002.
[54] W.-Y. Wang and Y. Ku, Colloids and Surfaces A **302**, 268 (2007). doi:10.1016/j.colsurfa.2007.02.037.

[55] C.-H. Weng and Y.-F. Pan, J. Hazard. Mater **144** (1–2), 355 (2007). doi:10.1016/j.jhazmat.2006.09.097.
[56] R.S. Dariani, A. Esmaeili, A. Mortezaali and S. Dehghanpour, Optik **127** (18), 7154 (2016). doi:10.1016/j.ijleo.2016.04.026.
[57] W. Zhang, L. Zhou, J. Shi and H. Deng, Catalysts **8** (2), 45 (2018). doi:10.3390/catal8020045.
[58] W. Zhang, L. Zhou, J. Shi and H. Deng, J. Colloid Interface Sci. **496**, 176 (2017). doi:10.1016/j.jcis.2017.02.022.
[59] Y.M. Xia, Z.M. He, J.B. Su, S. Zhu and B. Tang, J. Electron. Mater. **49** (5), 3268 (2020). doi:10.1007/s11664-020-08022-z.
[60] W. Vallejo, A. Cantillo and C. Díaz-Uribe, Intern. J. Photoener **2020**, 11 (2020). doi:10.1155/2020/1627498.

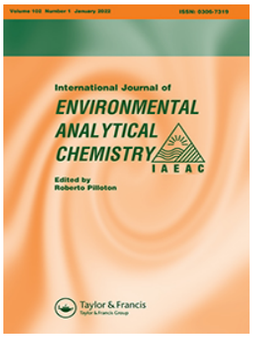

International Journal of Environmental Analytical Chemistry

ISSN: (Print) (Online) Journal homepage: https://www.tandfonline.com/loi/geac20

Sono-assisted adsorption of methylene blue dye from aqueous medium using magnetic Algerian Halloysite clay (Fe_3O_4-HKDD3)

Asma Hayoune, Hocine Akkari, Tahar Mekhalif & Francisco Martin

To cite this article: Asma Hayoune, Hocine Akkari, Tahar Mekhalif & Francisco Martin (2022): Sono-assisted adsorption of methylene blue dye from aqueous medium using magnetic Algerian Halloysite clay (Fe_3O_4-HKDD3), International Journal of Environmental Analytical Chemistry, DOI: 10.1080/03067319.2021.2020770

To link to this article: https://doi.org/10.1080/03067319.2021.2020770

Published online: 04 Jan 2022.

INTERNATIONAL JOURNAL OF ENVIRONMENTAL ANALYTICAL CHEMISTRY
https://doi.org/10.1080/03067319.2021.2020770

Taylor & Francis
Taylor & Francis Group

Sono-assisted adsorption of methylene blue dye from aqueous medium using magnetic Algerian Halloysite clay (Fe_3O_4-HKDD3)

Asma Hayoune[a,b], Hocine Akkari[c], Tahar Mekhalif[d] and Francisco Martin[e]

[a]Laboratoire de Recherche Sur La Physico-chimie Des Surfaces Et Interfaces, Faculté Des Sciences, Université 20 Août 1955, Skikda, Algérie; [b]Groupe Des Matériaux Fonctionnels, Laboratoire Lgmm, Université 20 Août 1955, Skikda, Algérie; [c]Département de Génie Industriel, Faculté de Technologie, Université Batna 2 Chahid Mostefa Ben Boulaid, Batna, Algeria; [d]Laboratoire de Biochimie Appliquée, Faculté Des Sciences de La Nature Et de La Vie, Université Ferhat Abbes de Sétif, Algérie; [e]Department of Chemical Engineering, University of Malaga, Málaga, Spain

ABSTRACT

In this study, magnetite (Fe_3O_4) nanoparticles were prepared successfully to synthesise magnetic Algerian halloysite sorbent by the coprecipitation approach. The Algerian halloysite was collected from Kaolin Djebel Debbagh (KDD3) in Guelma (east of Algeria). Different analysis including Brunauer Emmett-Teller (BET), high-resolution transmission electronic microscopy (HRTEM), scanning electron microscopy with energy-dispersive X-ray spectroscopy (SEM/EDX), Fourier transform infrared spectroscopy (FTIR), and X-ray diffraction (XRD) were performed to characterise the prepared magnetic sorbent. The Algerian halloysite is a tubular shape with a length from 0.3 µm to 2 µm and a diameter between 30 and 50 nm. The magnetite particles were well dispersed on the surface of HKDD3 which have a small size in the range 5–50 nm. The nanocomposite Fe_3O_4-HKDD3 was used for the removal of cationic dye methylene blue from an aqueous solution by sono-assisted adsorption. The quantity adsorbed of methylene blue dye was increased with increasing pH and concentration dye. The equilibrium time and maximum adsorption capacity were determined to be about 60 min and 18.78 $mg.g^{-1}$, respectively. The removal of methylene blue is well described by the first pseudo-order. Isotherm models indicate that the sonosorption is represented perfectly by Freundlich. Moreover, thermodynamic studies have shown that the process of adsorption was spontaneous and endothermic.

ARTICLE HISTORY
Received 18 November 2021
Accepted 9 December 2021

KEYWORDS
Fe_3O_4-HKDD3; nanocomposite; sono-assisted adsorption; methylene blue

1. Introduction

Water pollution is a great problem in the world, over the decades and now. Dyes are very toxic, harmful, and non-biodegradable, which are used in several industries, such as textiles, cosmetics, food, plastics, and so on [1]. Several physical and chemical processes have been developed for wastewater treatment, including photocatalytic degradation [2], ozonation [3], ion exchange [4], and adsorption [5]. The last method has gained more interest in the elimination of various contaminants due to their effectiveness, and

CONTACT Asma Hayoune hayoune.asma@gmail.com; a.hayoune@univ-skikda.dz

affordable approach. Recently more works have reported the combination of the adsorption process with ultrasound irradiation [6] owing to improve the removal of organic contaminants by creation more sites on the surface of the adsorbent and accelerate the mass transfer by ultrasounds waves [7].

Over the past decade, there is an increasing interest in environmental implications and applications of magnetic nanoparticles (MNPs) [8]. MNPs are attractive materials for environmental contamination problems owing to their paramagnetism properties that help the ease separation from the environment and recyclability of use [9]. There has been a great interest in using raw clay materials for their capacity to adsorb inorganic and organic pollutants due to the high surface specific area, pore-volume, and low cost [10]. Previous papers were focused on a combination of clay by iron oxide including bentonite [11], momorillonite [12], sepiolite [13], kaolinite [14], and halloysite [15] for elimination pollutants from wastewater. Halloysite is one of the aluminosilicate types (1/1) of the kaolin family which has a great interest owing to their hollow tubular morphology, high surface area, physical and chemical properties [16]. In recent years, there has been an increasing interest in sono-assisted adsorption, Hamza et al. used sono-assisted sorption to remove crystal violet (CV) onto raw Tunisian smectite clay. Sono-assisted adsorption was carried by using an ultrasonic bath with a low frequency of 50 Hz. The quantity adsorbed was reached 86.54 $mg.g^{-1}$ at pH 8 [17]. Sobhy M. Yakout et al. used a combined ultrasound/activated charcoal process resulted in a higher CV decolourisation than using sorption or sonolysis alone at high frequency 40 kHz. The maximum monolayer sorption capacity was reached 50.1 mg/g [18]. The present research explores, for the first time, the using of magnetic Algerian halloysite (Fe_3O_4-HKDD3) for sonosorption of methylene blue dye from an aqueous medium. A Series of factors, such as initial concentration of MB dye, pH; and temperature were studied. Besides, isotherms and kinetic studies were applied to evaluate sono-assisted adsorption.

2. Experimental details

2.1. Materials

The clay has been taken from the mountain of Guelma Djbel Dbbegh (zone3) which is located in the east of Algeria. It is labelled HKDD3. The chemical composition of the HKDD3 clay was found to be as follows: 38.48% Al_2O_3; 36.11% SiO_2; 0.13% Fe_2O_3, 0.42% CaO, 0.16% MgO, 0.26% Na_2O [19]. Ferrous sulphate heptahydrate ($FeSO_4.7H_2O$) and ferric chloride hexahydrate ($FeCl_3.6H_2O$) were purchased from Sigma Aldrich. Methylene blue abbreviated as MB (chemical formula: $C_{16}H_{18}N_3SCl$), molecular weight: 319.85 g/mol, λ_{max} = 664 nm) was applied from Biochem Chemopharma. These reagents were used without further purifications, all aqueous solutions were prepared using distilled water.

2.2. Preparation of Fe_3O_4-HKDD3 nanocomposite

The crude clay was treated with hydroxide oxygen for the elimination of the organic matter, and then HKDD3 clay was obtained by sedimentation for 1 hour and dried at room temperature.

The functionalization of HKDD3 clay by magnetite was performed by the co-precipitation method [19]. A quantity of HKDD3 clay was dispersed in 200 mL of a solution containing 1.16 g $FeCl_3.6H_2O$ and 0.6 g $FeSO_4.7H_2O$ dissolved in distilled

water. Then, 20 ml of ammonia solution was added dropwise. The mixture was stirred for 3 h at 70°C under inert gas (N_2). After that, the black prepared nanocomposite was washed several times and dried at 100°C in the oven. The obtained Fe_3O_4 – HKDD3 nanocomposite was labelled M-HKDD3

2.3. Characterisation

A PAN analytical X'Pert Pro automated diffractometer with a primary monochromator (Cu Kalfa1) and the X'Celerator detector with a step size of 0.0167° (2θ) was used to get XRD patterns of both HKDD3 and Fe_3O_4- HKDD3. The powder patterns were captured at a rate of 4 to 70 o in 2 with a 60 s/step counting time. In the mid and near-infrared ranges of 4000–500 cm^{-1}, a Bruker model Vertex 70 was used to do Fourier transform infrared (FTIR) analysis. High-resolution transmission electron microscopy (HRTEM) and selected area electron diffraction (SAED) was achieved with an FEI TALOS F200X microscope operated at 200 kV. The FESEM images of the nanocomposite were obtained by using a HITACHI SU 3500 electron microscope. Energy dispersive X-ray spectroscopy (EDX) was performed by employing an energy-dispersive X-ray analyser (Bruker, X Flash detector 410-M) coupled to SEM. At 77 K, a Micrometrics BET study (nitrogen adsorption) was performed (TriStar II 3020).

2.4. Methylene blue adsorption study

To carry out the sono-sorption experiments on the nanocomposite, we prepared a stock solution of MB dye. The effect of MB initial concentration on dye concentration removal was performed at a fixed adsorbent dosage 0.1 g, at room temperature (±25°C), pH free. Different initial concentrations of dye ranging from 10 to 40 $mg.L^{-1}$ for 120 min. a sample was separated by centrifugation and analysed in a UV–vis spectrophotometer using suitable calibration curves at appropriate wavelengths, corresponding to λmax = 663 nm the maximum absorbance. For ultrasonic bath used in this study was with a frequency of 50/60 Hz and a power of 80 W (D-78224 Singen/Htw Elma).

The adsorption capacity at time t, q_t (mg/g) was calculated using the following expression:

$$q_t = \frac{(C_0 - C_t) * V}{m} \quad (1)$$

Where C_o and C_t are the initial concentration and the concentration at time (t) of adsorbate solution, respectively (mg/L); V is the volume of dye solution (L) and m is the weight of the used adsorbent (g).

3. Results

3.1. Characterisation of samples

3.1.1. X-ray diffraction analysis

The HKDD3 and M-HKDD3 were characterised by XRD as displayed in Figure 1. The XRD spectra of purified clay HKDD3 exhibit the peaks at positions 2 theta: 9.3, 11.8, 18.7, 19.8, 24.7, 34.8, 37.7, 48.2, 54.6, 62.3 were ascribed to halloysite and kaolinite [19]. Furthermore,

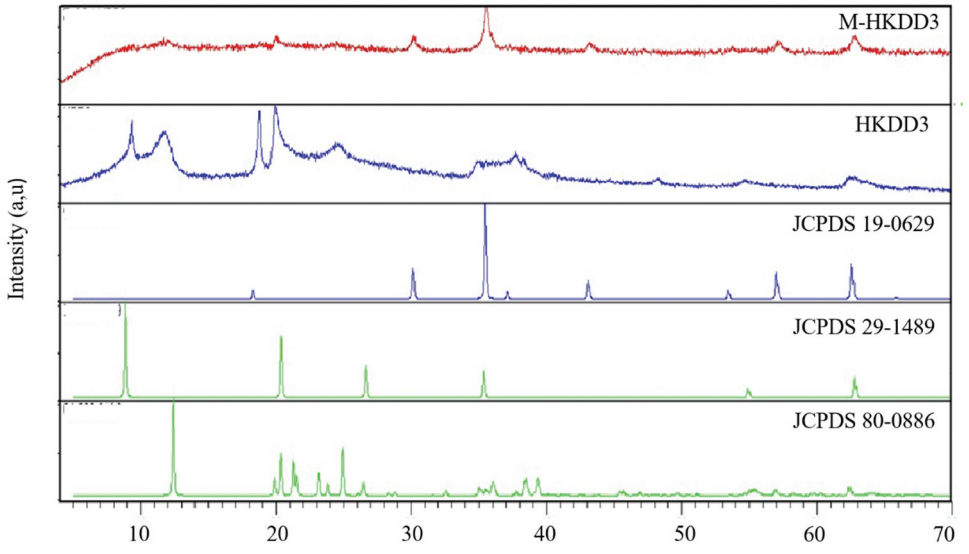

Figure 1. X-ray diffraction patterns of HKDD3 and M-HKDD3 nanocomposite.

the appearance of new peaks at 2θ values 30.1, 35.6, 43.3, 57.1, 62.7 refers to (220), (311), (400), (511), and (440) planes of reflections magnetite particles, respectively [20]. In addition, the peaks of clay were significantly weakened as was shown in HKDD3 spectra which proved that the magnetite (Fe_3O_4) particles were altered by modifying the composition of clay. Debyee Scherrer formula [21] was applied to estimate the crystalline size of M-HKDD3

$$D = \frac{0.9\lambda}{\beta cos\theta} \tag{2}$$

Where β (rad): the full width at half maximum (FWHM), θ (rad): angle of diffraction and λ = 1.540 A° (the wavelength of radiation copper). The estimated crystallite size is around 43.8 nm.

3.1.2. Fourier transforms infrared spectroscopy

The infrared spectrum of Fe_3O_4 and M-HKDD3 were illustrated in Figure 2. The peak at 580 cm^{-1} in Fe_3O_4 is attributed to Fe-O bond; while 3349 cm^{-1} is referred to O-H in the magnetite. For M-HKDD3 spectra, the band at 1640 cm^{-1} is present in which is attributed to the vibrations of the H-O-H bonds of the water molecules contained in the interfoliar space of the mineral halloysite [22]. The peaks at 3400, 3617 $cm^{-1,}$ and 3699 cm^{-1} were assigned to the stretching vibration of hydroxyls OH groups of HKDD3 clay [23]. Moreover, the peak at 1124–989 cm^{-1} may be referred to as the silanol groups (Si-O-H, Si-O-Si stretching vibration) of silica [24]. The observed bands from 700 to 900 cm^{-1} are assigned to the deformation metal group Al-OH. The intense and broadband at 3400 cm^{-1} corresponded to stretching vibrations of hydroxyl (OH) groups from (Fe_3O_4). The characteristic intense peak of magnetite (Fe-O) at 580 cm^{-1} could be explained by overlapping the band of Al-O-Si (HKDD3 clay) at 536 cm^{-1} [25].

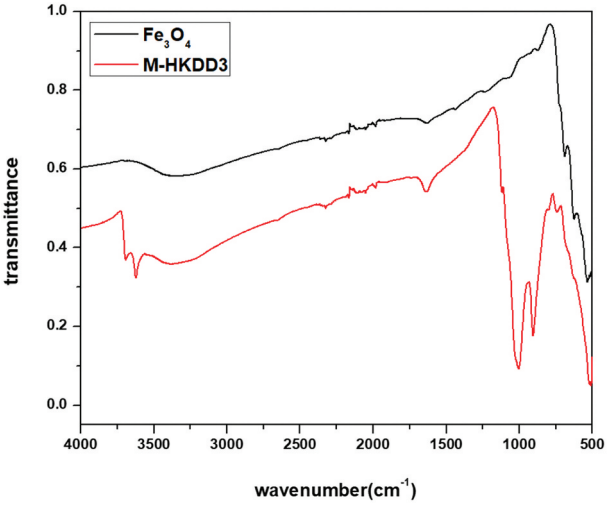

Figure 2. FTIR spectra of Fe_3O_4 and M-HKDD3 nanocomposite.

3.1.3. High-resolution transmission and scanning electronic microscopy with energy dispersive X-ray spectroscopy

The morphology of HKDD3 clay is a tubular shape (halloysite clay) with a length from 0.3 µm to 3 µm and a diameter between 15 and 50 nm [19]. The iron oxide particles were dispersed on the surface of HKDD3 which have a small size in the range from 20 to 50 nm with the average size of magnetite particles 12 nm (using software Image J). As observed in the images (Figure 3.**A**) the HKDD3 clay becomes rougher with irregular dispersion of spherical magnetite nanoparticles [26]. Energy dispersive X-ray spectroscopy (EDX) elemental mappings of O, Si, Al, and Fe elements with corresponding SEM images (Figure 3.**B**) further demonstrated the distribution of magnetite nanoparticles in the whole nanocomposite. The major elements of Al, Si, and O, which are related to the halloysite chemical formula ($Al_2Si_2O_5.H_2O$), are seen in EDX spectra. Besides, these elements the Fe which is presented on Fe_3O_4 magnetite lattice.

3.1.4. BET analysis

Surface Area analysis of HKDD3 and M-HKDD3 was carried out using the BET technique (Figure 4). The isotherms adsorption-desorption of N_2 gas measurement have a typical shape of mesoporous and macroporous materials that belong to type II [27], with a hysteresis loop of H3 type [28]. However, the pore size distribution, determined by the BJH [29]. As listed in Table 1, the specific surface area, pore diameter, and volume were around 67.42 m^2/g, 12.41 nm, and 0.222 cm^3/g respectively. After loading of HKDD3 clay by magnetite nanoparticles, we observed a decrease for surface area, average volume, and diameter to be 67.42 m^2/g; 0.177 cm^3/g and 10.54 nm, respectively. It can be explicated by deposition of magnetite nanoparticles onto the surface of HKDD3 clay.

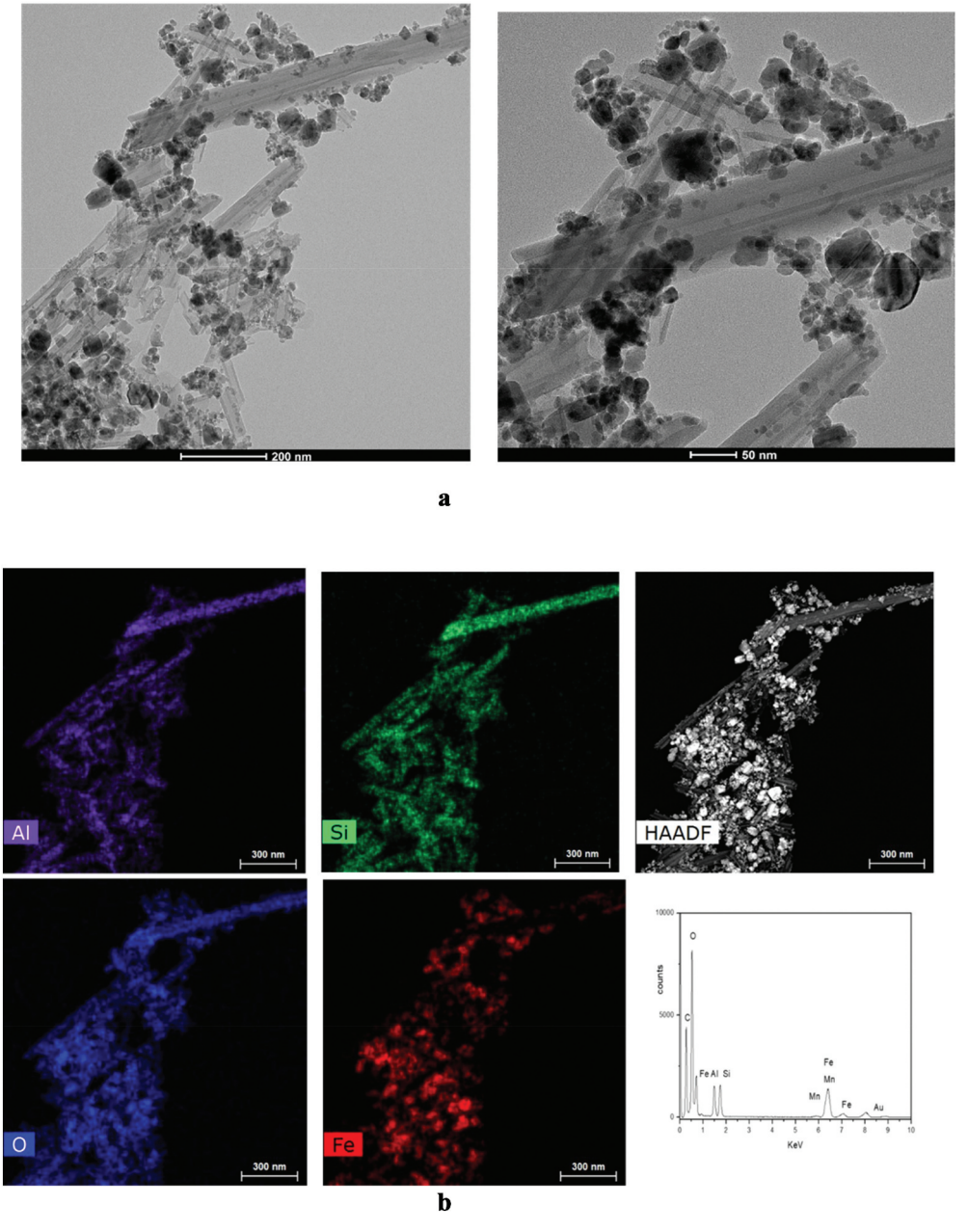

Figure 3. HRTEM images of M-HKDD3 nanocomposite (A); SEM-EDX mapping of M-HKDD3 nanocomposite (B).

3.2. Methylene blue sorption studies

In order to evaluate the efficiency of removal methylene blue dye from an aqueous medium by using M-HKDD3 nanocomposite as an adsorbent. For this study, we performed a comparative study between adsorption and sono-sorption processes. The initial dye, the

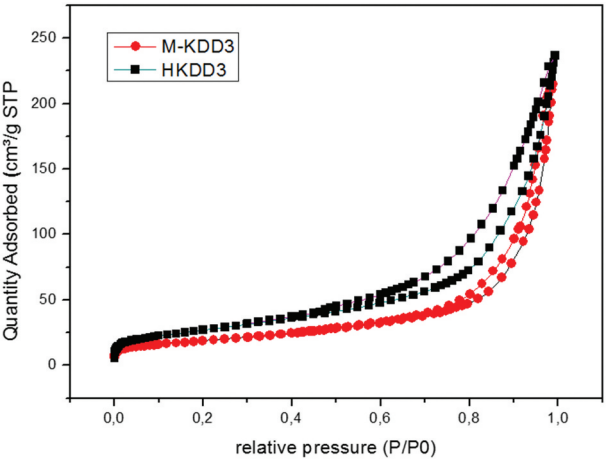

Figure 4. Isotherm nitrogen N_2 adsorption-desorption of HKDD3 and M-HKDD3 nanocoposite.

Table 1. Textural characterisation of HKDD3 and Fe_3O_4-HKDD3.

Adsorbent	S_{BET} (m^2/g)	Average pore volume (cm^3/g)	Average pore diameter (nm)
HKDD3	71.71	0.22	12.41
M-HKDD3	67.46	0.18	10.54

mass of adsorbent, and time were adjusted to 30 $mg.L^{-1}$, 0.1 g, and 120 min, respectively. According to Figure 5, the results showed that the sono-sorption was faster and effective than classic adsorption. The uptake dye was reached 18.78 mg/g and 10 mg/g for sono-sorption and adsorption, respectively. Due to the ultrasonic waves which improve the porosity of the M-HKDD3 surface adsorbent and mass transfer rate (liquid-solid interfaces) by physical phenomena, such as microscopic turbulence, streaming, and acoustic waves [30].

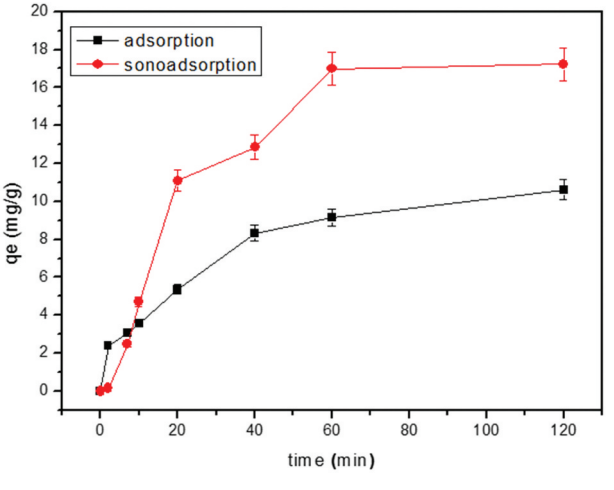

Figure 5. Comparative adsorption and sono-adsorption for Methylene blue by M-HKDD3 (m = 0.1 g of Fe_3O_4-HKDD3; 100 mL and 30 $mg.L^{-1}$ of MB; pH free at room temperature).

3.2.1. Effect of dye concentration and contact time

The initial dye concentration and contact time have a great effect on the removal of MB by M-HKDD3 which is shown in Figure 6. Clearly, the adsorption process occurs in two stages, a rapid increase corresponds to the MB adsorption rate is high due to the available pore size of M-HKDD3 nanocomposite and limited competition between the MB dye molecules [31]. The second part indicates slow adsorption caused by a low concentration of MB dye, in the last phase (from 60 to 120 minutes) the equilibrium was achieved wherein a plateau was seen. As it is observed, the quantity adsorbed increases from 9.54 to 17.27 mg/g with increasing of initial dye concentration from 10 to 40 mg. L^{-1} for an adsorbent 0.1 g. it means that it is related to the increase in the driving force of concentration by diffusion of dyes on the pores of HKDD3 clay [17].

3.2.2. Effect of pH

In order to study the effect of pH on MB adsorption on M-HKDD3, experiments were carried with 30 mg.L^{-1} initial dye concentration at varying pH range of 4.0 to 9.0 in presence of 0.1 g adsorbent particles at room temperature (±25°C).

As observed from Figure 7 with increasing pH the quantity adsorbed increased from 9.77 to 14.23 mg/g. In acidic conditions, pH < 7 was an unfavourable medium to adsorb MB dye owing to the electrostatic repulsion force between MB molecules and the surface of HKDD3 clay. Furthermore, there is a competition between H^+ ions and cationic dyes for migration to the active sites [32]. By increasing pH, the OH^- ions are produced and the H^+ decreases in the solution [33]. The surface of nanocomposite became more negatively which improve the attraction of cationic methylene blue molecules which caused the adsorption of MB in the active sites. Moreover, due to the effect of ultrasound irradiation, reactive radicals as OH• and $O_2^{-\bullet}$ are generated over the surface of magnetic clay, which could degrade MB molecules dye.

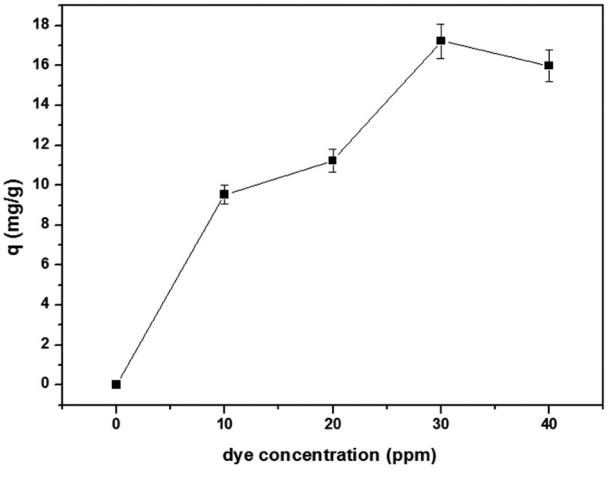

Figure 6. Influence of MB concentration using M-HKDD3 nanocomposite. (m = 0.1 g of Fe_3O_4-HKDD3; C = 10–40 mg.L^{-1} of MB; at room temperature).

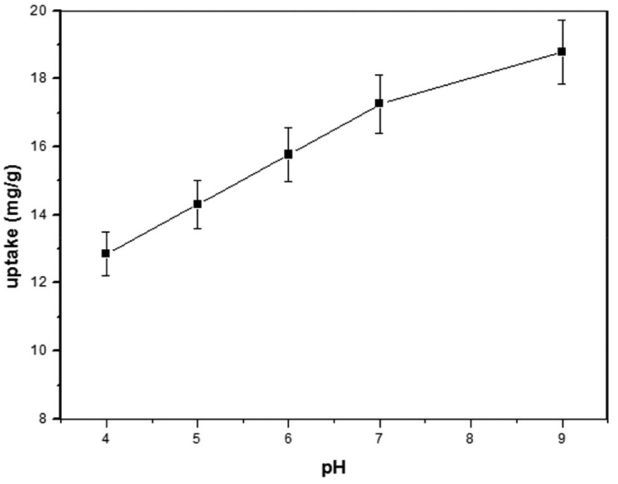

Figure 7. Influence of pH on sono-sorption of MB dye using M-HKDD3 nanocomposite (m = 0.1 g of Fe_3O_4-HKDD3; 100 mL and 30 mg.L^{-1} of MB; pH 4–9 at room temperature).

3.2.3. Thermodynamic study

The thermodynamic study was carried out in the range of (303–323 K°) to estimate standard Gibbs free energy change (ΔG), standard enthalpy change (ΔH), and standard entropy change (ΔS). The different energies can be related to each other by the following equations [34].

$$\Delta G^{\circ} = -RTlnK_e \tag{3}$$

$$\Delta G^{\circ} = \Delta H^{\circ} - T\Delta S^{\circ} \tag{4}$$

$$lnK_e = -\frac{\Delta H^{\circ}}{RT} + \frac{\Delta S^{\circ}}{R} \tag{5}$$

Where R is the universal gas constant (8.314 J/mol K) and T is the absolute temperature (K). K_e is the adsorption equilibrium constant.

The thermodynamics parameters for the sono-assisted adsorption process are represented in Table 2. The quantity adsorbed by the M-HKDD3 adsorbent increase with increasing of temperature. The positive value ΔH confirmed the endothermic nature of sono-sorption. The negative values of standard Gibbs ΔG° show decreasing with increasing temperature suggesting that the adsorption process was favourable,

Table 2. Thermodynamic parameters of MB adsorption on Fe_3O_4-HKDD3 nanocomposite.

T (K°)	ΔG (kJ/mol)	ΔH (kJ/mol)	ΔS (J/mol.K)
303	−1.095	31.948	109.054
313	−2.116		
323	-3.073		

spontaneous, and enthalpy controlled, where the positive values of ΔS° exhibited the randomness at the solid-solution interface increased during the sorption and sono-assisted sorption process [35].

3.2.4. Kinetic modelling

The kinetic models provide us information about the adsorption mechanism and the mode of solute transfer from the liquid phase to the solid phase. The literature reported a number of models, such as the pseudo-first-order model (PFO), the pseudo-second-order kinetic model (PSO), and Weber and Morris model or intraparticle diffusion model. They were applied to describe the mechanism and the potential rate-controlling steps by distinct processes, such as transfer of mass, and diffusion of particles for the sono-sorption of MB dye.

Results of kinetic modelling are presented in Figure 8A and Table 3. For the pseudo-first-order model [36], the adsorption rate constant K_1 is given by the following relation:

$$\mathbf{q} = \boldsymbol{q_e}\left(1 - \mathbf{e}^{-\mathbf{Kt}}\right) \tag{6}$$

In the pseudo-second-order model proposed by Ho and Mckay [37], the adsorption rate constant K_2 is given by the following relation: K_2 (qe-q)^2

$$\frac{\boldsymbol{dq}}{\boldsymbol{dt}} = \boldsymbol{K}_1(\boldsymbol{q_e} - \boldsymbol{q})^2 \tag{7}$$

Where; q_e is the quantity of dye adsorbed at equilibrium (g/mg); q_t is the quantity of dye adsorbed at time t (g/mg); t is the contact time (min); K_1 is the adsorption rate constant for the pseudo-first-order (min^{-1}); K_2 is the adsorption rate constant for pseudo-second-order (g/mg.min). The intra-particle model [2] was defined by equation

$$\boldsymbol{q_t} = \boldsymbol{K_{id}} * \boldsymbol{t}^{0.5} + \boldsymbol{C} \tag{8}$$

where qt is the amount of adsorbate per unit weight of adsorbent.

C (mg/g) is a constant which gives information about the boundary layer and K_{id} (mg. g^{-1}.$min^{-1/2}$) is the intraparticle rate constant and t is time contact.

The sono-assisted sorption process follows first order with R^2 = 0.965 and low χ^2 (0.467). As well as the calculated quantity adsorbed reached 9.36 mg/g (from PFO) which is in agreement with experimental data (qe) 9.52 mg/g.

Figure 8**B** showed that the curve is not linear. It means that the adsorption has happened in two-stage. The first is fast owing to the unoccupied external sites of M-HKDD3 clay then we observed slow adsorption which referred to the diffusion molecules of MB into sheets of HKDD3 clay.

3.2.5. Isotherm of sono-sorption

An adsorption isotherm is a variation of the adsorbed quantity qe ($mg.g^{-1}$) on a solid as a function of the Ce concentration ($mg.L^{-1}$), that is, the interaction adsorbate with adsorbent. In this study, the adsorption equilibrium is analysed by application of the Langmuir and Freundlich models (Figure 9) which are commonly used [38].

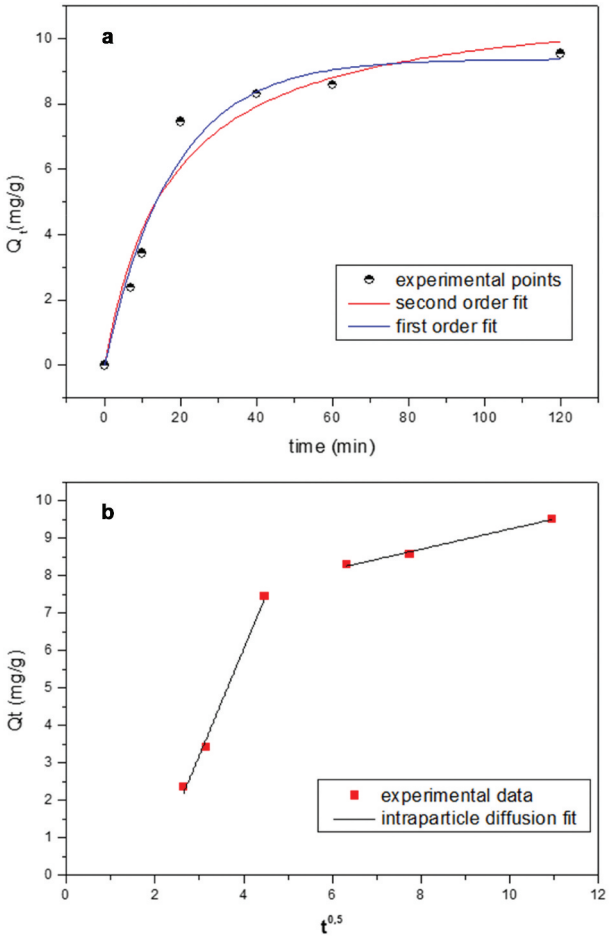

Figure 8. Kinetic models of adsorption MB onto M-HKDD3 (A); intra-particle diffusion of MB dye onto M-HKDD3 nanocomposite (B).

Table 3. Kinetic parameters for MB sono-sorption on M-HKDD3 nanocomposite.

Kinetic model	Parameters	Sono-assisted sorption
Pseudo first order	qe_{exp} (mg/g)	9.52
(PFO)	$q_{e\ cal}$ (mg/g)	9.36
	K_1	0.05
	R^2	0.965
	χ^2	0.467
Pseudo second order	$q_{e\ cal}$ (mg/g)	11.34
(PSO)	K_2	0.005
	R^2	0.947
	χ^2	0.71133
Intraparticle diffusion	K_{ip1}	2.83
(IPD)	Ce	5.31
First step	R^2	0.988
Intraparticle diffusion	K_{ip2}	0.26
(IPD)	Ce	6.55
Second step	R^2	0.983

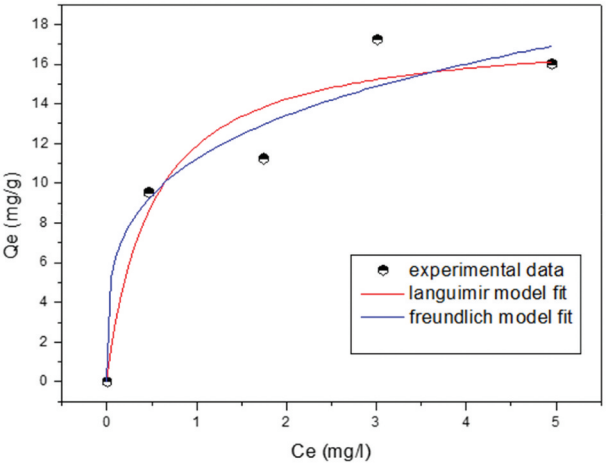

Figure 9. Isotherm models of sono-assisted adsorption of MB onto Fe_3O_4-HKDD3 nanocomposite.

The Langmuir model suggests that the adsorption takes place on a homogeneous phase, the nonlinear form of the Langmuir equation is given by the following equation:

$$\mathbf{q} = \frac{\boldsymbol{q_e K_l C_e}}{\mathbf{1} + \boldsymbol{K_l C_e}} \tag{9}$$

Where qe ($mg.g^{-1}$) represents the maximum monolayer adsorption capacity; K_l is the Langmuir constant; C_e is the equilibrium concentration (mg/L). The favourability of adsorption can be confirmed using the dimensionless parameter, which is defined as

$$\boldsymbol{R_l} = \frac{\mathbf{1}}{\mathbf{1} + \boldsymbol{K_l} * \boldsymbol{C_0}} \tag{10}$$

The value of R_L indicates that the type of isotherm can be irreversible if (R_L = 0), unfavourable if (R_L>1), linear if (R_L = 1), and favourable while (0< R_L<1).

The Freundlich model assumes that the multilayer adsorption takes place on a heterogeneous surface of the adsorbent. This model is given as follows [39]:

$$\mathbf{qe} = \mathbf{K_f Ce}^{1/\mathbf{n}} \tag{11}$$

where K_F is the equilibrium constant relative to the Freundlich model (L/g); 1/n is the heterogeneity factor is ranging between 0.1 and 1. Table 4 lists the correlation coefficients and isotherm constants with the experimental data. The Freundlich isotherm was selected as the best fitting model for the sono-sorption process with a coefficient R^2 value of 0.96. The 1/n value is about 0.3 which confirms that the adsorption process is normal, favourable adsorption due to heterogeneity of adsorbent [40].

Adsorption capacities were compared in Table 5. Various adsorbents were used for adsorption cationic dyes such as methylene blue and crystal violet. The Algerian halloysite Fe_3O_4-HKDD3 is a good adsorbent in comparison with other adsorbents.

Table 4. Isotherm model parameters of the sono-assisted adsorption of MB onto M–HKDD3 nanocomposite.

Isotherm		Sono-sorption
Langmuir	q_m **(mg/g)**	17.70
	K_L	2.043
	R_L	0.012–0.046
	R^2	0.95
	χ^2	2.885
Freundlich	K_F	11.23
	n	3.19
	R^2	0.96
	χ^2	2.343

Table 5. Comparison of methylene blue sono-assisted adsorption using M-HKDD3 nanocomposite with other works.

Adsorbent	Quantity adsorbed (mg/g)	adsorbate	pH	Reference
Nanomagnetic iron oxide	16.15	CV	<7	[41]
Moroccan clay	12.19	CV	6	[42]
HNTs-Fe_3O_4	18.44	MB	-	[25]
Tunisian clay	86.54	CV	8	[17]
Magnetic NAY zeolite	2.04	MB	10.3	[43]
M-HKDD3	18.78	MB	9	This work

4. Conclusion

In summary, this study was focused on the functionalization of Algerian clay (HKDD3) by magnetite (Fe_3O_4) for the easier separation magnetic property. This work highlights the using a sono-sorption method to eliminate methylene blue dye from an aqueous medium which is useful, rapid, and higher than the adsorption process. The adsorption capacity reached about 18.78 mg/g. Kinetics is influenced by the studied parameters: temperature, pH, and initial concentration. The adsorption behaviour of M-HKDD3 for cationic MB could be well described by the pseudo-second-order model. The thermodynamic studies showed endothermic and spontaneous adsorption processes.

Disclosure statement

No potential conflict of interest was reported by the author(s).

References

[1] K.G. Pavithra, S.K. P., J. V. and S.R. P., J. Ind. Eng. Chem. **75**, 1 (2019). doi:10.1016/j.jiec.2019.02.011.
[2] N.K. Gupta, Y. Ghaffari, J. Bae and K.S. Kim, J. Mol. Liq. **301**, 112473 (2020). doi:10.1016/j.molliq.2020.112473.
[3] S. Khuntia, S.K. Majumder and P. Ghosh, J. Environ. Chem. Eng. **4** (2), 2250 (2016). doi:10.1016/j.jece.2016.04.005.
[4] M. Wawrzkiewicz, Ind. Eng. Chem. Res. **53** (29), 11838 (2014). doi:10.1021/ie501992n.
[5] I. Ali, Chem. Rev. **112** (10), 5073 (2012). doi:10.1021/cr300133d.
[6] Y. Rashtbari, M. Abazari, L. Arfaeinia, A. Gholizadeh, S. Afshin, Y. Poureshgh and M. Alipour, Biomass Convers. Biorefinery 2021. doi:10.1007/s13399-021-01773-7

[7] R. Foroutan, Env. Sci. Pollut Res. **26** (19), 2019, 17.
[8] P. Xu, G.M. Zeng, D.L. Huang, C.L. Feng, S. Hu, M.H. Zhao, C. Lai, Z. Wei, C. Huang, G.X. Xie et al. Sci. Total Environ. **424**, 1 (2012). doi:10.1016/j.scitotenv.2012.02.023.
[9] C. Su, J. Hazard. Mater **322** (Pt A), 48 (2017). doi:10.1016/j.jhazmat.2016.06.060.
[10] A.A. Adeyemo, I.O. Adeoye and O.S. Bello, Appl. Water Sci. **7** (2), 543 (2017). doi:10.1007/s13201-015-0322-y.
[11] Q.U. Ain, U. Rasheed, M. Yaseen, H. Zhang and Z. Tong, J. Hazard. Mater **397**, 122758 (2020). doi:10.1016/j.jhazmat.2020.122758.
[12] J. Chang, J. Ma, Q. Ma, D. Zhang, N. Qiao, M. Hu and H. Ma, Appl. Clay Sci. **119**, 132 (2016). doi:10.1016/j.clay.2015.06.038.
[13] R. Dabiri and E. Amiri Shiraz, J. Min. Environ. **9** (4), 1049 (2018). doi:10.22044/jme.2018.7201.1572.
[14] A. Magdy, Y.O. Fouad, M.H. Abdel-Aziz and A.H. Konsowa, J. Ind. Eng. Chem. **56**, 299 (2017). doi:10.1016/j.jiec.2017.07.023.
[15] B. Mu, W. Zhang and A. Wang, J. Mater. Sci. **49** (20), 7181 (2014). doi:10.1007/s10853-014-8426-6.
[16] Y. Zhang and H. Yang, Appl. Clay Sci. **56**, 97 (2012). doi:10.1016/j.clay.2011.11.028.
[17] W. Hamza, N. Dammak, H.B. Hadjltaief, M. Eloussaief and M. Benzina, Ecotoxicol. Environ. Saf. **163**, 365 (2018). doi:10.1016/j.ecoenv.2018.07.021.
[18] S.M. Yakout, M.R. Hassan, A.A. Abdeltawab and M.I. Aly, J. Clean. Prod. **234**, 124 (2019). doi:10.1016/j.jclepro.2019.06.164.
[19] A. Hayoune, H. Akkari, V. Vaiano, N. Morante, D. Sannino and F. Madjene, Int. J. Environ. Anal. Chem. 2021, 1. doi:10.1080/03067319.2021.1974425
[20] P.K. Boruah, D.J. Borah, J. Handique, P. Sharma, P. Sengupta and M.R. Das, J. Environ. Chem. Eng. **3** (3), 1974 (2015). doi:10.1016/j.jece.2015.06.030.
[21] S. Mustapha, M.M. Ndamitso, A.S. Abdulkareem, J.O. Tijani, D.T. Shuaib, A.K. Mohammed and A. Sumaila, Adv. Nat. Sci. Nanosci. Nanotechnol. **10** (4), 045013 (2019). doi:10.1088/2043-6254/ab52f7.
[22] R. Wang, G. Jiang, Y. Ding, Y. Wang, X. Sun, X. Wang and W. Chen, ACS Appl. Mater. Interfaces **3** (10), 4154 (2011). doi:10.1021/am201020q.
[23] Y. Du and P. Zheng, Korean J. Chem. Eng **31** (11), 2051 (2014). doi:10.1007/s11814-014-0162-8.
[24] T. Tsoufis, F. Katsaros, B.J. Kooi, E. Bletsa, S. Papageorgiou, Y. Deligiannakis and I. Panagiotopoulos, Chem. Eng. J. **313**, 466 (2017). doi:10.1016/j.cej.2016.12.056.
[25] Y. Xie, D. Qian, D. Wu and X. Ma, Chem. Eng. J. **168** (2), 959 (2011). doi:10.1016/j.cej.2011.02.031.
[26] R. Riahi-Madvaar, M.A. Taher and H. Fazelirad, Appl. Clay Sci. **137**, 101 (2017). doi:10.1016/j.clay.2016.12.019.
[27] X. Wang, H. Cheng, P. Chai, J. Bian, X. Wang, Y. Liu, X. Yin, S. Pan and Z. Pan, Energy Fuels **34** (10), 12204 (2020). doi:10.1021/acs.energyfuels.0c01922.
[28] K.S.W. Sing and R.T. Williams, Adsorpt. Sci. Technol. **22** (10), 773 (2004). doi:10.1260/0263617053499032.
[29] E.P. Barrett, L.G. Joyner and P.P. Halenda, J. Am. Chem. Soc. **73** (1), 373 (1951). doi:10.1021/ja01145a126.
[30] A.R. Bagheri, M. Ghaedi, A. Asfaram, A.A. Bazrafshan and R. Jannesar, Ultrason. Sonochem. **34**, 294 (2017). doi:10.1016/j.ultsonch.2016.05.047.
[31] M. Zhao and P. Liu, Microporous Mesoporous Mater **112** (1–3), 419 (2008). doi:10.1016/j.micromeso.2007.10.018.
[32] L.R. Bonetto, F. Ferrarini, C. de Marco, J.S. Crespo, R. Guégan and M. Giovanela, J. Water Process Eng. **6**, 11 (2015). doi:10.1016/j.jwpe.2015.02.006.
[33] A. Khataee, M. Sheydaei, A. Hassani, M. Taseidifar and S. Karaca, Ultrason. Sonochem. **22**, 404 (2015). doi:10.1016/j.ultsonch.2014.07.002.
[34] A.Q. Alorabi, M.S. Hassan, M.M. Alam, S.A. Zabin, N.I. Alsenani and N.E. Baghdadi, Nanomaterials **11** (11), 2789 (2021). doi:10.3390/nano11112789.
[35] M. Bhowmik, M. Kanmani, A. Debnath and B. Saha, Powder Technol. **354**, 496 (2019). doi:10.1016/j.powtec.2019.06.009.

[36] A.S. Özcan, B. Erdem and A. Özcan, Colloids Surf. Physicochem. Eng. Asp. **266** (1), 73 (2005). doi:10.1016/j.colsurfa.2005.06.001.
[37] Y.S. Ho and G. McKay, Process Biochem. **34** (5), 451 (1999). doi:10.1016/S0032-9592(98)00112-5.
[38] K.Y. Foo and B.H. Hameed, Chem. Eng. J. **156** (1), 2 (2010). doi:10.1016/j.cej.2009.09.013.
[39] R. Ezzati, Chem. Eng. J. **392**, 123705 (2020). doi:10.1016/j.cej.2019.123705.
[40] N.K. Gupta, M. Saifuddin, S. Kim and K.S. Kim, J. Mol. Liq. **297**, 111935 (2020). doi:10.1016/j.molliq.2019.111935.
[41] A. Debrassi, A.F. Corrêa, T. Baccarin, N. Nedelko, A. Ślawska-Waniewska, K. Sobczak, P. Dłużewski, J.-M. Greneche and C.A. Rodrigues, Chem. Eng. J. **183**, 284 (2012). doi:10.1016/j.cej.2011.12.078.
[42] Y. Miyah, A. Lahrichi, M. Idrissi, S. Boujraf, H. Taouda and F. Zerrouq, J. Assoc. Arab Univ. Basic Appl. Sci. **23** (1), 20 (2017). doi:10.1016/j.jaubas.2016.06.001.
[43] M. Shirani, A. Semnani, H. Haddadi and S. Habibollahi, Water. Air. Soil Pollut. **225** (8), 2054 (2014). doi:10.1007/s11270-014-2054-2.

Abstract

The present thesis focuses on the preparation and characterization of different catalysts based on local kaolin Djebel Debbagh (KDD3) for the removal of methylene blue as a cationic dye from aqueous solution by adsorption and photocatalytic processes. The prepared materials were characterized by X-ray diffraction (XRD); Fourier transform infrared spectroscopy (FTIR); Brunauer-Emmett-Teller (BET), transmission electron microscopy (TEM), Uv-DRS Diffuse reflectance spectroscopy, and X-ray photoelectron spectroscopy (XPS). The thesis involves three different axes:

The first part is to synthesize Fe_3O_4- HKDD3 composite (M-HKDD3) by coprecipitation method, and its application for adsorption and sono-adsorption of methylene blue dye. The results show that the magnetite Fe_3O_4 was efficiently formed into HKDD3 clay. The Algerian clay HKDD3 is a natural halloysite tubular shape with a length ranging from 500 nm to 4 um and a diameter was estimated from 50 nm to 100 nm. The mean crystallite size of magnetite particles is about 45 nm. Several factors as contact time, pH, initial concentration and temperature were studied to evaluate the removal of MB dye via adsorption and sono-adsorption. The adsorption efficiencies reached about 18.78 and 10.5 mg/g for sono-adsorption and adsorption, respectively. The adsorption behavior of Fe_3O_4- HKDD3 for cationic MB could be well-described by the pseudo-second-order model. The thermodynamic studies showed endothermic and spontaneous adsorption process. The separation of nanocomposite from solution is easy owing that magnetite nanoparticles are sensitive to an applied magnetic field.

The second part aimed to the preparation of 30% TiO_2-M-HKDD3, 2% Ag- TiO_2-M-HKDD3, 1% Fe-TiO_2-M-HKDD3, and 1%Fe -2% Ag- TiO_2-M-HKDD3 by solvothermal route, for the photocatalytic activity of methylene blue under visible light irradiation. The average crystallite size of TiO_2 particles is about 30 nm. The results of this study show that the efficiency follows this order: Ag- TiO_2-M-HKDD3 (92%) > Fe- TiO_2-M-HKDD3 (90%) > TiO_2-M-HKDD3 (89%) > Fe -Ag- TiO_2-M-HKDD3 (88%) with TOC removal 75%, 70% and 72% respectively. According to these results Ag-TiO_2-MHKDD3 photocatalyst exhibited higher photocatalytic performance due to the following factors, bandgap energy, pore distribution, and higher adsorption capacity. The main species responsible for the degradation of MB dye were hydroxyl $OH^{\bullet}$ and $O_2^{\bullet-}$ radicals.

The third part was based on the functionalization of HKDD3 clay by iron sulfide FeS through a hydrothermal route and explore its capacity for removal of methylene blue under visible light irradiation. The iron sulfide crystals are dispersed as cubic shaped form forming aggregates on the surface of the HKDD3. Uv-Drs results show strong absorption in the visible region with bandgap 1.60 eV. The results exhibit an excellent degradation of about 96% after 90 min using 10 $mg.L^{-1}$ of methylene blue and 50 mg of catalyst.

Keywords: Fe_3O_4-HKDD3, (Ag-Fe)-TiO_2-Fe_3O_4-HKDD3, FeS-HKDD3, photocatalyst, adsorption, photodegradation, methylene blue

Résumé

La présente thèse se base sur la préparation et la caractérisation de différents catalyseurs à base de kaolin Djebel Debbagh pour l'élimination du bleu de méthylène à partir d'une solution aqueuse par adsorption et par activité photocatalytique sous irradiation de la lumière visible. La caractérisation des catalyseurs préparés a été effectuée par diffraction des rayons X (DRX), spectroscopie infrarouge à transformée de Fourier (IRTR), Brunauer-Emmett-Teller (BET), microscopie électronique à transmission (TEM), Uv-DRS Spectroscopie par réflectance diffuse, et spectroscopie photoélectronique à rayons X (XPS). La thèse comprend trois axes différents :

La première étude a été consacrée à la synthèse du composite Fe_3O_4- HKDD3 (M-HKDD3) par la méthode de coprecipitation, pour objectif de adsorption et sono- adsorption du bleu de méthylène. Les résultats montrent que la magnétite Fe_3O_4 a été bien formée et dispersée sur la surface de halloysite HKDD3. L'argile HKDD3 est sous forme tubulaire avec une longueur allant de 500 nm à 4 um et un diamètre qui a été estimé de 50 nm à 100 nm. La taille moyenne des cristallites des particules de magnétite est d'environ 45 nm. Plusieurs facteurs comme le temps de contact, le pH, la concentration initiale et la température ont été étudiés pour évaluer l'élimination du colorant MB par adsorption et sono-adsorption. La quantité adsorbée a atteint environ 18.78 et 10.5 mg/g pour la sono-adsorption et l'adsorption, respectivement. Le comportement d'adsorption du M- HKDD3 pour le MB cationique a été bien décrit par le modèle de pseudo-second ordre. Les études thermodynamiques ont montré que le processus d'adsorption est endothermique et spontané. La séparation du nanocomposite est facile grâce à la sensibilité des nanoparticules de magnétite à un champ magnétique appliqué.

La deuxième partie visait sur la préparation des dopant de TiO_2 (Ag, Fe) supportée sur l'argile HKDD3 :30% TiO_2-M-HKDD3, 2% Ag- TiO_2-M-HKDD3, 1% Fe- TiO_2-M-HKDD3, et 1%Fe -2% Ag- TiO_2-M-HKDD3 par voie solvothermal. Les résultats de cette étude montrent que l'efficacité suit cet ordre : Ag-TiO_2-M-HKDD3 (92%) > Fe-TiO_2-M-HKDD3 (90%) > TiO_2-M-HKDD3 (89%) > Fe -2% Ag- TiO_2-M-HKDD3 (88%) avec une élimination du carbone organique total COT de 75%, 70% et 75%, respectivement. Selon ces résultats, le photocatalyseur Ag-TiO_2-MHKDD3 a présenté une performance photocatalytique plus élevée en raison des facteurs suivants : énergie de la bande

interdite, distribution des pores et capacité d'adsorption plus élevée. Les espèces responsables de la dégradation du colorant MB étaient les radicaux hydroxyles $OH^{\bullet}$ et $O_2^{-\bullet}$.

La troisième partie a était basée sur la fonctionnalisation de l'argile HKDD3 par le sulfure de fer par voie hydrothermale et l'exploration de sa capacité à éliminer le bleu de méthylène sous irradiation de lumière visible. Les cristaux de sulfure de fer sont dispersés sous forme cubique qui ils sont formé des agrégats à la surface du HKDD3. Les résultats de l'Uv-Drs montrent qu'il y a une forte absorption dans la région visible avec une bande interdite de 1,60 eV. Les résultats montrent une excellente dégradation d'environ 96% après 90 min en utilisant 10 $mg.L^{-1}$ de bleu de méthylène et 50 mg de catalyseur.

Mots-clés : Fe_3O_4-HKDD3, (Ag-Fe)-TiO_2-Fe_3O_4-HKDD3, FeS-HKDD3, photocatalyseurs, adsorption, photodégradation, bleu de méthylène.

ملخـص

تحضير و توصيف محفزات من طين كاولن جبل دباغ مثبث فيه اكسيد الحديد وحفازات ضوئية لازالة ازرق المتيلين

الهدف من هذه الاطروحة هو إعداد و توصيف محفزات جديدة ترتكز على تغيير خصائص طين كاولن جبل دباغ 3 المحلي لإزالة صبغة الميتيلين الأزرق عن طريق الامتزاز والتحفيز الضوئي تحت اشعاعات الضوء المرئي. تم توصيف المركبات المحضرة باستعمال حيود الأشعة السينية (XRD) ؛ مطيافية فوريه لتحويل الأشعة تحت الحمراء (FTIR) إلى جانب Brunauer-Emmett-Teller (BET) والفحص المجهري الإلكتروني بالإضافة إلى مطيافية الانعكاس المنتشر(Uv-DRS) والتحليل الطيفي الكهروضوئي للأشعة السينية (XPS). لهذا تطرقنا إلى ثلاثة محاور رئيسية :

(1) خصصت الدراسة الاولى لتحضير مركب أكسيد الحديد-هالوزيت (كاولن جبل دباغ) بطريقة الترسيب ثم تطبيق الامتزاز و الامتزاز الصوتي لصبغة الميثيلين الزرقاء من الماء . أظهرت النتائج أن أكسيد الحديد الأسود تم تشكيله بكفاءة في طين الكاولن . الطين الكاولن الجزائري ذو شكل أنبوبي بطول يتراوح من 500 نانومتر إلى عدة ميكرومترات ويقدر قطره من 50 نانومتر إلى 100 نانومتر. يبلغ متوسط الحجم البلوري لجزيئات أكسيد الحديد الأسود حوالي 45 نانومتر. تهدف الدراسة المقارنة للامتزاز والامتزاز الصوتي إلى مناقشة آثار وقت التلامس ودرجة الحموضة والتركيز الأولي للمذاب . بلغت كفاءة الامتزاز حوالي 18.78 و 10.5 مغ / غ للامتزاز الصوتي والامتزاز على التوالي. يمكن وصف سلوك حركة الامتزاز بواسطة نموذج الدرجة الثانية. أظهرت الدراسات الديناميكية الحرارية عملية امتصاص ماص للحرارة وتلقائية. يعد فصل المركب النانوي عن المحلول أمرًا سهلاً نظرًا لأن الجسيمات النانوية للمغنتيت حساسة للمجال المغناطيسي المطبق.

(2): الجزء الثاني يهدف إلى تحضير 30٪ TiO_2-M-HKDD3 و 2٪ Ag- TiO_2-M-HKDD3 و 1٪ Fe- TiO_2-M-HKDD3 و 1٪ Fe -2٪ Ag- TiO_2-M -HKDD3 عن طريق التحليل المائي الحراري لتقييم نشاط التحفيز الضوئي لأزرق الميثيلين. تظهر نتائج هذه الدراسة أن كفاءة المحفزات تتبع هذا الترتيب: Ag-Fe-TiO_2 M- Fe-TiO_2- M-HKDD3 < Ag- TiO_2-M-HKDD3 <HKDD3مع إزالة الكربون العضوي الكلي 75٪ و 70٪ و 72٪ على التوالي. وفقًا لهذه النتائج ، أظهر المحفز الضوئي Ag- TiO_2-M-HKDD3 أداء تحفيزيًا أعلى بسبب العوامل التالية توزيع المسام ، والامتصاص العالي. كانت الأنواع الرئيسية المسؤولة عن تحلل صبغة المتيلين الأزرق هي جذور الهيدروكسيل •OH و O_2•- .

(3): اعتمد الجزء الثالث على تثبيث كبريتيد الحديد(FeS) على طين الهالوزيت من خلال هيدروتارمل. استكشاف قدرته على إزالة الميثيلين الأزرق تحت إشعاع الضوء المرئي. تتثبت بلورات كبريتيد الحديد على شكل مجاميع مكعبة الشكل على سطح الهالوزيت. تظهر نتائج امتصاصًا قويًا في المنطقة المرئية ذات فجوة الحزمة 1.60 eV . أظهرت النتائج تحللاً ممتازًا لحوالي 96٪ بعد 90 دقيقة باستخدام 10 مغ/ل من الميثيلين الأزرق و 50 مغ من المحفز.

الكلمات المفتاحية: Fe_3O_4-HKDD3، Fe_3O_4-HKDD3 -(Ag-Fe) -TiO_2-Fe_3O_4-HKDD3، FeS-HKDD3، الحفز الضوئي، الامتزاز ، التحلل الضوئي، أزرق الميثيلين.